JAERI-M
85-081

JAPANESE CONTRIBUTIONS TO IAEA INTOR WORKSHOP, PHASE TWO A, PART 2 CHAPTER IX : ENGINEERING

July 1985

Hiromasa IIDA, Masahiro SEKI, Yoshio SAWADA,
Katsuyuki EBISAWA[*1], Mikihiko GOTO[*1], Akiyoshi HATAYAMA[*1],
Yutaka IMAMURA[*2], Shin-ichi ITOH[*3], Yutaka ITOU[*3],
Masao KASAI[*2], Kazunori KITAMURA[*1], Shinzaburo MATSUDA,
Nobuharu MIKI[*1], Tadanori MIZOGUCHI[*3], Hideo NAKAJIMA,
Satoshi NISHIO, Ryuta SAITOH, Susumu SHIMAMOTO,
Kichiro SHINYA[*1], Tatsuzo TONE, Takaho UCHIDA[*1]
and Masao YAMADA[*2]

日本原子力研究所
Japan Atomic Energy Research Institute

JAERI-Mレポートは，日本原子力研究所が不定期に公刊している研究報告書です。

入手の問合わせは，日本原子力研究所技術情報部情報資料課（〒319－11茨城県那珂郡東海村）あて，お申しこしください。なお，このほかに財団法人原子力弘済会資料センター（〒319-11茨城県那珂郡東海村日本原子力研究所内）で複写による実費頒布をおこなっております。

JAERI-M reports are issued irregularly.

Inquiries about availability of the reports should be addressed to Information Division, Department of Technical Information, Japan Atomic Energy Research Institute, Tokai-mura, Naka-gun, Ibaraki-ken 319-11, Japan.

編集兼発行　日本原子力研究所
印　　刷　日立高速印刷株式会社

JAERI-M 85-081

Japanese Contributions to IAEA INTOR Workshop, Phase Two A, Part 2 Chapter IX : Engineering

Hiromasa IIDA, Masahiro SEKI, Yoshio SAWADA,
Katsuyuki EBISAWA[*1], Mikihiko GOTO[*1], Akiyoshi HATAYAMA[*1],
Yutaka IMAMURA[*2], Shin-ichi ITOH[*3], Yutaka ITOU[*3], Masao KASAI[*2],
Kazunori KITAMURA[*1], Shinzaburo MATSUDA, Nobuharu MIKI[*1],
Tadanori MIZOGUCHI[*3], Hideo NAKAJIMA[+1], Satoshi NISHIO,
Ryuta SAITOH, Susumu SHIMAMOTO[+1], Kichiro SHINYA[*1],
Tatsuzo TONE, Takaho UCHIDA[*1] and Masao YAMADA[*2]

Department of Large Tokamak Research,
Naka Fusion Research Establishment, JAERI

(Received May 31, 1985)

This report corresponds to Chapter IX of Japanese contribution report to IAEA INTOR Workshop, Phase Two A, Part 2. Data base assessment are made for systems engineering, magnet systems, torus systems, and NBI heating systems. R&D programme and impact on INTOR design are also specified. In addition to the data base assessment, studies have been made for several new tasks.

Keywords: INTOR, Engineering, Data Base, Systmes Engineering, Magnet, Torus System, NBI

+1 Department of Thermonuclear Fusion Research
*1 Toshiba Corp.
*2 Mitsubishi group
*3 Hitachi Ltd.

JAERI－M 85－081

IAEA INTORワークショップ，フェーズⅡA，パート2報告書
第Ⅸ章：工　学

日本原子力研究所那珂研究所臨界プラズマ研究部

飯田　浩正・関　昌弘・沢田　芳夫・海老沢克之[*1]・後藤　幹彦[*1]
畑山　明聖[*1]・服部　泰秀[*2]・今村　豊[*2]・伊藤　新一[*3]・伊藤　裕[*3]
笠井　雅夫[*2]・喜多村和憲[*1]・松田慎三郎・三木　信晴[*1]・溝口　忠憲[*3]
中島　秀夫[+1]・西尾　敏・斉藤　龍太・島本　進[+1]・新谷　吉郎[*1]
東稔　達三・内田　孝穂[*1]・山田　政男[*2]

（1985年5月31日受理）

この報告書は，IAEA主催のINTORワークショップ，フェーズⅡA，パート2の日本の報告書の第Ⅸ章に相当するものである。

システム工学，超電導磁石システム，トーラスシステム，NBI加熱システムに関するデータベース評価を行った。

データベース評価とともに，例えばRFによる電流立上げなど個々の設計変更がINTOR全体設計に及ぼす影響について検討した。

+1）　核融合研究部
*1）　㈱東芝
*2）　三菱グループ
*3）　㈱日立

Contents

目　　次

1. Data Base Assessment

1.1 Introduction

The current data base in Japan has been compiled mainly focusing on the superconducting magnet development and JT-60 project at JAERI.

The data base for magnet system has greatly advanced since the Phase 0 data base assessment through the LCT and CTP(Cluster Test Program) projects and the TMC(Test Module Coil)-I experiment. R & D requirements for the INTOR design data base are identified.

Satisfactory test results of the JT-60 NBI Prototype have also demonstrated a great advance particularly in energy, power and pulse length since the Phase 0 data base assessment. Problematic areas in R & D requirements for the INTOR-NBI system is being reduced.

1.2 System Engineering

S. Nishio, T. Tone

1.2.1 Analytical Tools

Data Base Assessment

A FORTRAN code named "TORSAC" (Tokamak Reactor System Analysis Code) has been developed to evaluate a design concept and to make a sensitivity analysis. The basic structure of "TORSAC" is shown in Fig. 1.2.1. The code calculates configuration parameters, weight of components, required capacity of a power supply system, and performance as a function of main plasma parameters and machine parameters.

For conducting a parametric study the code is capable of redesigning automatically reactor components according to variations from the standard design parameters input in a consistent way.

The system code is being upgraded to have a function of performing an automatic design starting from basic design parameters input. The flow diagram of the code is shown in Fig. 1.2.2. A main effort is being made on deciding PF coil locations automatically in accordance with plasma parameters.

R & D Requirements

A further great effort is required for developing a more functional and reliable code for implementing trade-off studies for fusion reactor systems from near-term fusion device to commercial reactors. For this purpose a data base of cost assessment should be provided and the improvement of each program element in its accuracy and of the whole program logic should be made. A function of computer graphics will be important for performing a computer-aided design.

Impact

A system code will be a useful tool for assessing and selecting a reactor design through trade-off study analysis.

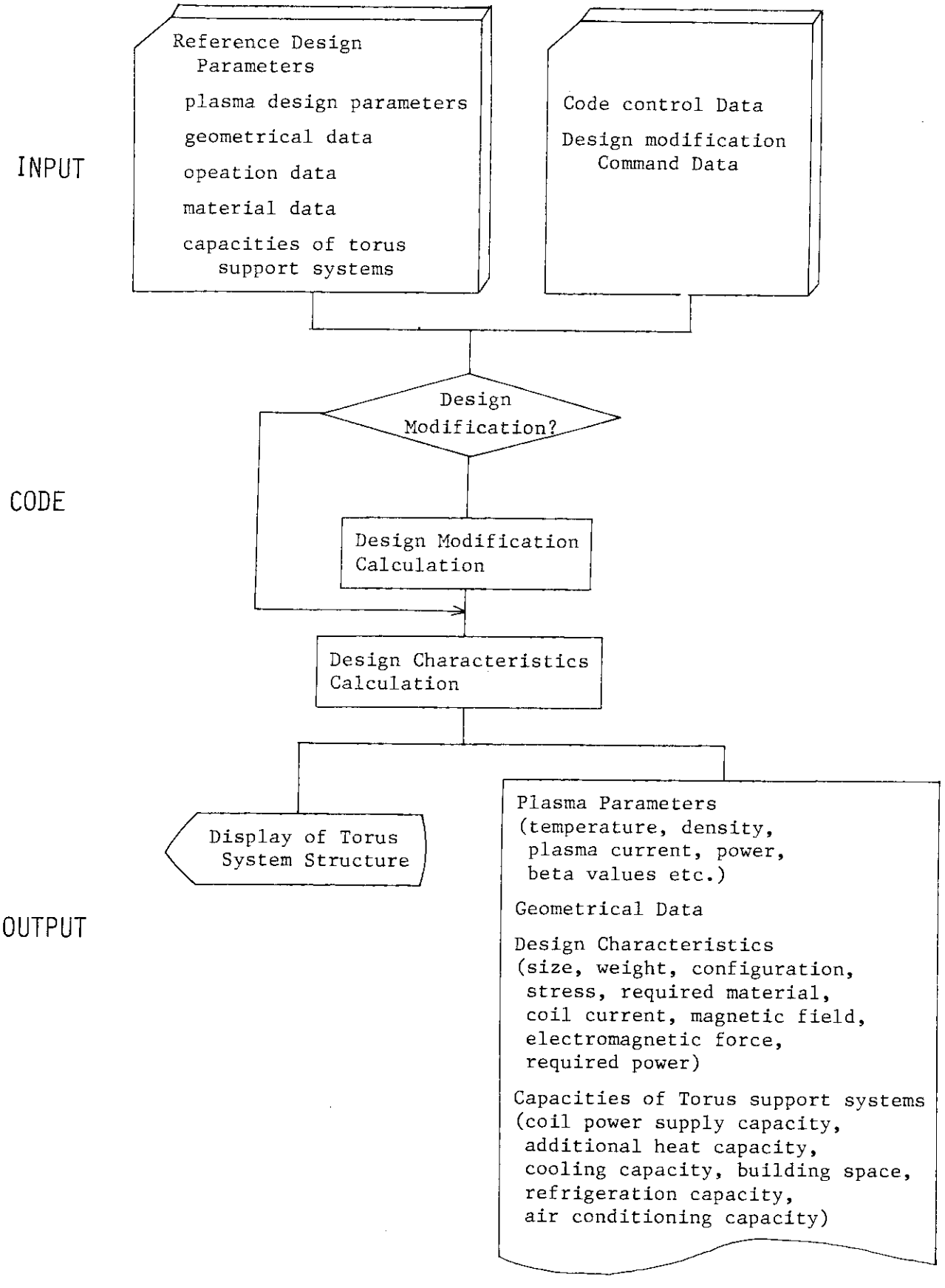

Fig. 1.2.1 Basic code structure of the "TORSAC"

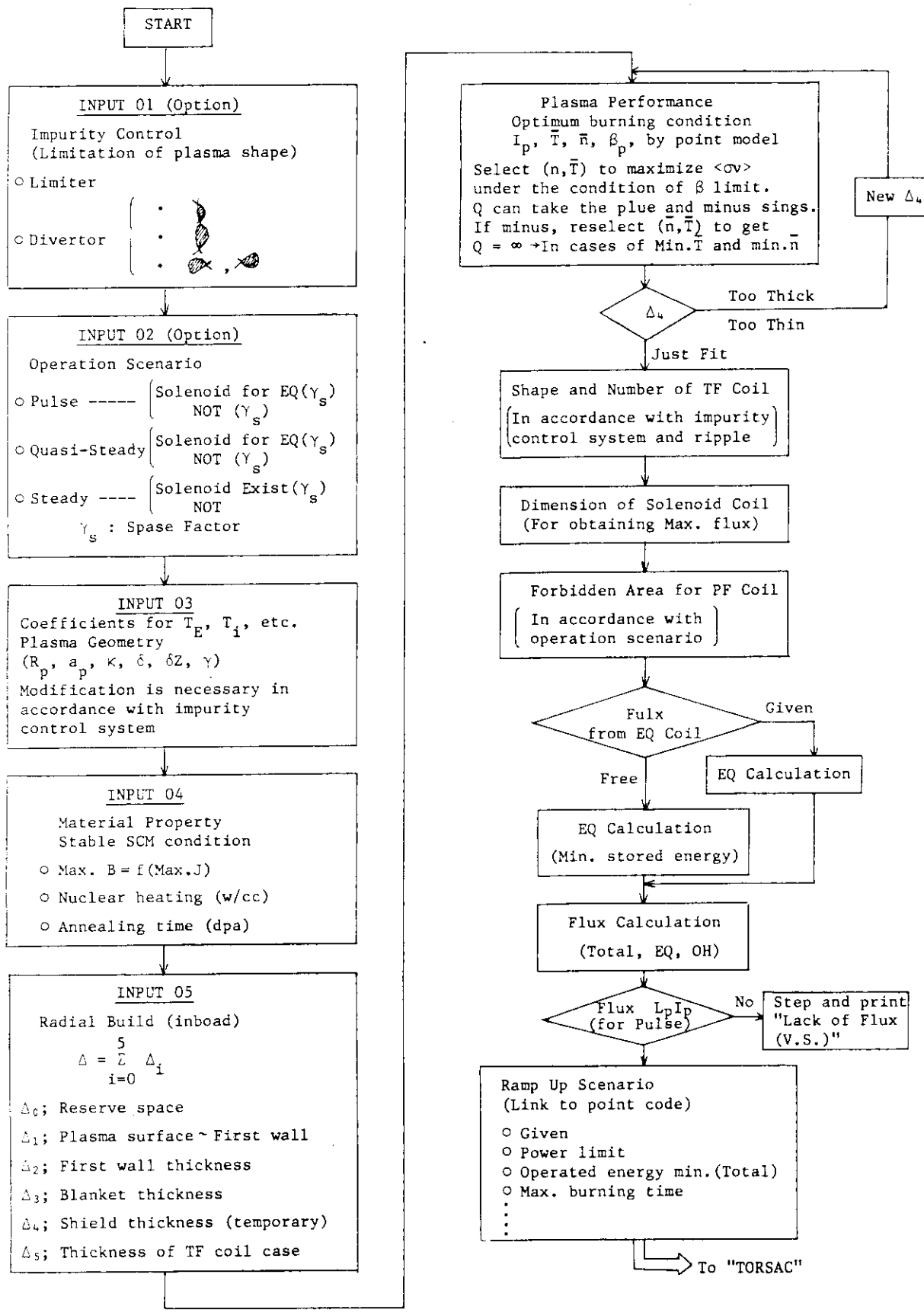

Fig. 1.2.2 Flow diagram for new code

1.3 Magnet systems

S. Shimamoto, H. Nakajima,
Y. Hattori, M. Seki

1.3.1 Design Requirements

Specifications in INTOR

(1) Toroidal Coil

o Size of the coil	6.6 x 1.3 m (D-shape)
o Maximum filed intensity	12 T
o Operation current	15 - 20 kA
o Average current density	15 - 20 A/mm^2

(2) Poloidal Coil

o Size of the coil (max)	20 m (circular)
o Maximum field intensity	8 T
o Operation current	30 - 50 kA
o Average current density	10 - 15 A/mm^2
o Rate of change of the field	10 T/s

Current status in Japan

(1) Toroidal Coil [1,2,3,4,5,6]

o Size of the coil	3.5 x 4.5 m	(LCT)
o Maximum field intensity	11 T	(TMC-1)
o Operation current	10.2 kA	(LCT9
o average current density	30 A/mm^2	(TMC-1)

(2) Poloidal Coil [10]

o Size of the coil	1 m dia	(Pulser-C)
o Maximum field intensity	7 T	(Pulser-D)
o Operation current	30 kA	(JA-50)
o Average current density	17 A/mm^2	(JA-50)
o Rate of change of the field	10 T/s	(Pulser-D)

1.3.2 Structures

1.3.2.1 Mechanical characteristics

Data Base Assessment

1. A data base for mechanical characteristics of stainless steel as a structural material has been generated through the projects of LCT and CTP(Cluster Test Program) [1].

2. A data base for tensile strength, impact strength, fracture toughness, crack growth, etc. of SS304LN at low temperatures has been produced. Yield strength was 830 MPa, and fracture toughness was 250 MPa $\sqrt{m}$ [1].

3. A reasonable data base exists on mechanical characteristics (tensile strength, compressive strength, shearing stress, Young's modulus) of particular structures such as conductors, turn-to-turn insulators, layer-to-layer insulators, etc. which constitute windings.

R & D Requirements

1. Development of high performance structural materials for SCM of FER have been continued at JAERI which are required to simultaneously satisfy the following specifications. Some materials including industrial-scale produced materials have already attained a part of the targets. [Fig.1.3.1] [10]

a) Yield stress (0.2% proof stress) > 1200 MPa
b) Charpy absorbed energy > 100 J
c) Fracture toughness K_{IC} > 200 MPa $\sqrt{m}$

2. Generation of a data base for the high strength stainless steels now under development is needed. A data base on weld preparations is also required as well as base materials. R & D is now in progress at JAERI.

3. Generation of a data base on mechanical characteristics of cable-type conductors for PF coils is needed especially for bi-axial (longitudinal and transverse directions) stresses.

4. A limited data base exists on embrittlement and debonding strength between different materials of epoxy resins. Generation of the data base is required.

1.3.2.2 Quality control techniques

Data Base Assessment

1. Acoustic emission (AE) techniques and strain measurements are applicable for on-line quality control of structures. Strain gauges should be attached on locations where maximum stress or stress concentration is expected by prior stress calculations.

2. Since there are a number of factors to produce measuring errors in both AE and strain measurements, verification of the measuring methods is required prior to the adoption of the methods as a part of a quality control system.

R & D Requirments

1. These measuring techniques should be improved.

1.3.2.3 Radiation effects

Data Base Assessment / R & D Requirements

1. Some data base exists on radiation effects on mechanical characteristics of stainless steels from nuclear fission reactors. The data suggests that stainless steels can be used in magnet structures of fusion reactors.

2. A data base is now being generated on radiation effects on FRP and epoxy resins which are promising candidates for winding pack insulators. The data reveals that a matrix structure of polyimids has a good radiation resistance. An additional data base is necessary.

3. Low temperature irradiation data is required. Measurements should be made without intermediate warm-up.

1.3.3 Conductor

1.3.3.1 Critical current characteristics

Data Base Assessment

1. An extensive data base exists on the critical current characteristics of NbTi and Nb_3Sn conductors in strand-size from the projects of CTP and LCT.

2. A reasonable data base exists on the dependence of a critical current on stress and strain, but limited data are available on the effect of fatigure. An additional data base is required.

R & D Requirements

1. A bata base is required for a full-size conductor.

2. A limited data base exists on the deterioration of critical current due to manufacturing wires into bundle and cable conductors. JAERI is planing to make R & D on this effect.

1.3.3.2 Thermal and electrical characteristics

Data Base Assessment / R & D Requirements

1. A reasonable data base exists on thermal and electrical characteristics of particular materials which constitute conductors. In future a data base is required on whether these paticular characteristics are superimposable or not when the materials are assembled into conductors.

1.3.3.3 Heat transfer

Data Base Assessment

1. An extensive data base exists on heat transfer characteristics of bath-cooled conductors from the projects of LCT and CTP.

2. A high performance heat transfer surface with three times as much heat transfer capability as former one was employed in Japanese LCT conductors.

3. An additional data base is required for bath-cooled cable-typed conductors (not solid-typed) which are expected to be employed in PF coils.

4. In LCT the stability criteria of "recovery from normalization in half-a-turn" was adopted as a design criteria. On-going LCT experiments will prove propriety of the criteria.

5. The Japanese LCT coil was successfully kept stable against disturbance of an energy of 1 J/cm^3. It was experimentally confirmed that the superconducting state was recovered in two seconds after generation of a normal zone of half-a-turn.

6. Fundamental data exists on forced-cooled heat transfer characteristics in a simple geometry such as a single tube.

R & D Requirements

1. Few data exists on the characteristics of full-size forced-cooled conductors. An additional data base is required for the full-size conductors along with development of high-current forced-cooled conductors.

2. An additional data base is required on transient heat transfer characteristics.

3. A data base on heat transfer is one of the most important data bases for the design of superconducing coils. Generation of a data base on heat transfer characteristics of a large-scale conductor set-up is needed for both steady and transient states when the INTOR design is boiled down.

4. Little data exists for estimation of how much disturbance energy will be generated in an actual SCM. Generation of a data base is required on sources of instability in relation to mechanical instability of a SCM.

1.3.3.4 Analytical tools

Data Base Analysis

1. Many analytical tools and experimental data exist for transverse AC losses. It is required to define applicability of the tools and to improve accuracy by comparing the analytical results with experimental data.

2. Satisfactory computer codes exist for predicting stability in both bath-cooled and forced-cooled conductors. A level of the analysis is different according as which initial condition is given in the codes; that is, (1) temperature rise given, of (2) disturnbance energy given.

The model with distrubance energy given as an initial condition is more realistic. In this case, parameters such as (1) thermal properties of materials surrounding a location where disturbance is generated, (2) transient heat transfer characteristics, (3) time-dependence of disturnbance, should be given as inputs. Thus data bases on these characteristics are necessary.

3. For stress analysis many generalized FEM codes exist and are used to calculate electromagnetic and thermal stresses.

4. Generalized FEM codes exist for thermal analysis and are used to calculate temperatures during initial cool-down and warm-up. However, for thermohydraulic analyses of quenching and of a initial cool-down stage of forced-cooled conductors, it is desirable to develop special-purpose codes in order to improve accuracy and to save computation time.

5. A generalized code for predicting eddy current exists, which is capable of computing eddy current losses in structures.

R & D Requirements

1. Few analytical tools exist on longitudinal AC losses. Generation of an experimental data base is required for a first step.

2. One of the critical issues in stress analysis by FEM lies in modeling of coil-winding and coil-to-vessel coupling; that is, how to evaluate stiffness of coils. Generation of a data base is required on the evaluation of the stiffness by both experiment and theory.

1.3.3.5 Manufacturing technology

Data Base Assessment / R & D Requirements

1. There is a reasonable manufacturing data base for large-scale bath-cooled conductors up to 11 T. Generation of a data base on technology for large-scale forced-cooled conductors is required.

1.3.3.6 Radiation effects

Data Base Assessment

1. A data base on the influence of radiation on critical current of NbTi and Nb_3Sn, and on electric resistance of stabilizers is not sufficient. However, it appears that the effect is not a limiting factor.

R & D Requirements

1. Generation of a data base on nuclear heating is required because

nuclear heating affects cooling loads and stability of coils.

1.3.4 Insulator

1.3.4.1 Electrical properties

Data Base Assessment / R & D Requirements

1. A data base exists on dielectric breakdown strength of organic insulators. But a limited data base exists for insulators under mechanical stresses (tension, compression, cyclic) and radiation. Generation of the data base is required.

2. Development of a data base on the influence of neutron and gamma ray irradiation on deterioration of withstanding voltage characteristics of organic materials is very important. The test facility should be quickly installed.

1.3.4.2 Thermomechanical properties

Data Base Assessment

1. A reasonable data base exists on thermomechanical properties such as tensile strength, thermal expansion and contraction. There is a limited data base on influence of irradiation on the thermomechanical properities.

1.3.4.3 Manufacturing technology

Data Base Assessment

1. A reasonable manufacaturing data base has been generated through manufacturing coils of large projects.

1.3.5 Refrigeration

Data Base Assessment

1. An extensive data base exists for refrigeration through CTP, LCT, and development and demonstration tests of large components.

1.3.6 Demonstration Coil Projects

1. Following projects are being discussed in Japan.
(1) 20 MJ coils for PF coils
(2) 100 MJ coils for PF coils
(3) TMC(Test Module Coil)-II coils for TF coils
(4) STTA (Superconducting Tokamak Test Assembly --- medium size machine)

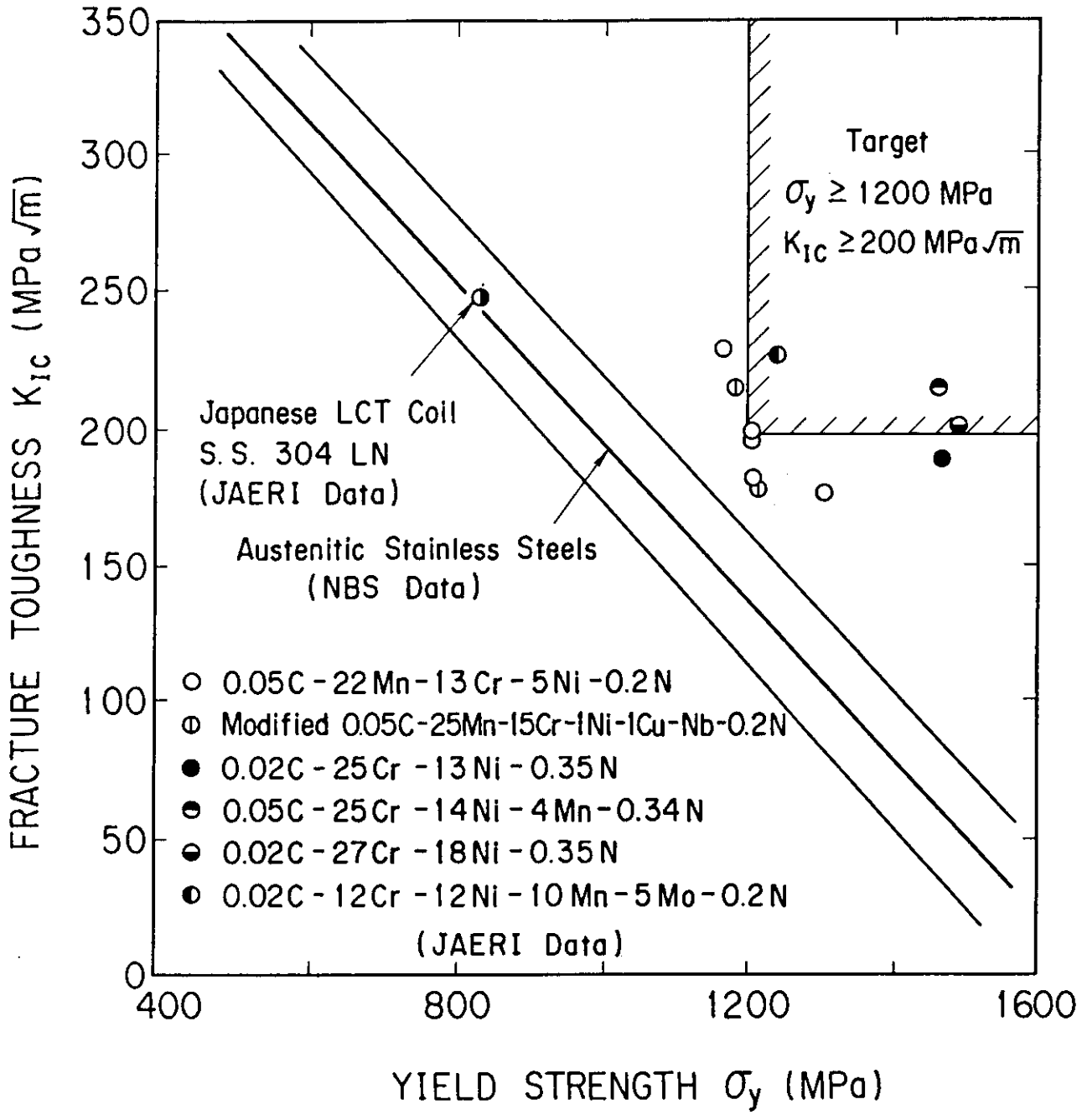

Fig. 1.3.1 Fracture toughness vs. yield strength

1.4 Torus system

M. Goto, K. Kitamura, K. Ebisawa

1.4 Torus System			1. Summary of INTOR requirements (Phase IIA)	2. Data base assessment		3. R & D Programs			4. Impact of new data on INTOR reference design
				Review of previous assessment	New data/ New results	Ongoing and planned programs	Required programs	Required new data	
1.4.2 Insulating Joint of Vacuum Enclosure	1.4.2.1 Bellows in Torus Structure	1.4.2.1.1 Material	Type 316L S.S	Type 316L S.S	Inconel 625				
		1.4.2.1.2 Mechanical Properties	To endure external atmospheric pressure and electromagnetic force at plasma disrutption.	Seems to exceed the allowable stress of 316S.S. (210 MPa at R.T)	Sufficiently below allowable stress of Inconel (530 MPa at R.T)		Detailed stress analysis of bellows	Mechanical properties of irradiated Inconel	
		1.4.2.1.3 Vacuum Properties	To assure high vacuum tightness and negligible outgas rate on the surface ($\sim 10^{-11}$ Torr.ℓ/sec.cm^2)	Negligible small (10^{-12} Torr.ℓ/sec.cm^2 of S.S. outgas rate)	Negligible small (10^{-12} Torr.ℓ/sec.cm^2 of Inconel outgas shield)				
		1.4.2.1.4 Radiation Behavior	Low BDDT and slow fatigue crack growth rate are required	be satisfied if placed behind the shield	be satisfied if placed behind the shield				
		1.4.2.1.5 Electrical Properties	Required one-turn resistance of torus structure is more than 0.2 mΩ	Larger than required resistance	Larger than required resistance				
	1.4.2.2 Ceramic Break for port Joint	1.4.2.2.1 Material	Alumina ceramics	Alumina ceramics					
		1.4.2.2.2 Mechanical Properties	To withstand the electromagnetic force at plasma disruption	Seems to be less than the allowable shear stress (90 MPa at R.T)		Mechanical tests for the feed through of JT-60 ICRF	Detailed stress analysis of ports joint around ceramic break	Mechanical properties of irradiated ceramics	
		1.4.2.2.3 Vacuum Properties	Required outgas rate of ceramics is considered to be $\sim 10^{-9}$ Torr.ℓ/sec.cm^2 because ceremics surface area is smaller compared to bellows surface	Seems to satisfy for same order as ceramic outgas rate of 3.5×10^{-9} Torr.ℓ/sec.cm^2					
		1.4.2.2.4 Radiation Behavior	Small swelling and little change of conductivity are required	marginal			Systematic irradiation experiments	tanδ, swelling	
		1.4.2.2.5 Electrical Properties	To have enough electrical resistance	Seems to satisfy				Break down voltage test of irradiated ceramics	

1.4 Torus System			1. Summary of INTOR requirements(Phase IIa)	2. Data base assessment		3. R & D Programs			4. Impact of new data on INTOR reference design
				Review of previous assessment (Phase 0, 1 ,2a)	New data/ results	Ongoing and planned programs	Major test facilities	Required new programs	
1.4.3. Vacuum Technology	1.4.3.1 Vacuum Pumps	1.4.3.1.1 Pumping speed for different atomic species (D,T,D_2,T_2,DT, He)	for D,T,D_2,T_2,DT, effective pumping speed at vacuum chamber seff=1.5×10^5ℓ/s for He, Seff=2×10^5ℓ/s (5×10^4ℓ/s/1 pump)	Same as Phase IIa addition Pumping speed: ℓ/s.cm^2 Condensation: 7~10 (for D,T, D_2,T_2,DT) Cryosorption:1.5~3.5 (for He) (or 2.0)	Pumping speed of compound cryopump at TSTA Condensation: 6.6 (for D_2) ℓ/s.cm^2 Cryosorption: 2.0 (for He) ℓ/s.cm^2	TSTA at LASL in USA	TSTA	Pumping speed of compound cryopump will be satisfied with INTOR requirements.	
		1.4.3.1.2 Regeneration time	Regeneration time should be minimized in order to reduce tritium inventoty in the reactor. Estimated regeneration time is 2 hours.	Same as Phase IIa	Regeneration time of compound cryo-pump at TSTA is 4.5 hrs.	ditto	ditto	It'll be necessary to certify if failure of cryoupump due to thermal cycles will be happended during long term life test.	
		1.4.3.1.3 Tritium compatibility (containment, seals, etc.)	Double containment Estimated range of tritium release from pumps Normal 10^{-2}~10^{-1}Ci.d^{-1}, Maintenance, <50 Ci.d , Accident 10^{-2}~10^5 Ci Tritium inventory of cryopumps for 2 hrs. is 120 g.	Double containment Tritium inventoty of cryopumps for 2 hrs. is 120 g.	Secondary con-tainment Metallic seal Magnetic bearing turbomolecular pump Metallic mechani-cal pumps (e.g., spiral booster pump metal bellows pump at TSTA)	ditto	ditto	It'll be necessary to develop large scale magnetic bearing t.m.p. and matallic mechanical pumps.	
		1.4.3.1.4 Maintenance considerations			At TSTA maintente-nance will only be performed as a consequence of system performance degradation. Requirements for the repair or replacement of components should be infrequent by virture of the design of these items.	ditto	ditto	It'll necessitate to certify the reliability of pumps through long term life test and to develop remote handling tools for the repair or replacement of pumps.	

1.4 Torus System			1. Summary of INTOR requirement (Phase IIa)	2. Data base assessment		3. R & D Programs			4. Impact of new data on INTOR reference design
				Review of previous assessment (Phase 0, 1, 2a)	New data/ results	Ongoing and planned programs	Major test facilities	Required new programs	
1.4.3 Vacuum Technology	1.4.3.2 Valves	1.4.3.2.1 Tritium compatibility (as above)	·Double containment	·Double containment	·Secondary containment ·Metallic seal ·All remote control valves at TSTA	TSTA at LASL in USA	TSTA	It'll necessitate to certify the tritium compatibility of 1.0-1.2 m ida. all metallic gate valve.	
		1.4.3.2.2 Duct size and cross section	·An exhaust duct of 1.0 to 1.2 m diameter	·Same as Phase IIa	·All metallic gate valve of 0.6 m diameter is available in Japan	R&D for developing large size all metallic gate valve is proceeding for JT-60 project. (0.6m dia. gate value)		It'll take about 4~5 years in order to develop all metallic gate valve of 1.0~1.2 m diameter.	
		1.4.3.2.3 Maintenance considerations			Same as the item 3.6.1.4	TSTA at LASL in USA	TSTA	Same as the item 3.6.1.4, except using "valves" instead of "pumps".	

1.4 Torus System		1. Summary of INTOR requirement (Phase IIa)	2. Data base assessment		3. R & D Programs			4. Impact of new data on INTOR reference design
			Review of previous assessment	New data/ new results	Ongoing and planned programs	Required programs	Required new data	
1.4.4 Insulating Joint of Support Structure	1.4.4.1 Ceramic break between blanket module	Same as item 1.4.2.2						

1.5 Heating and Fueling Systems

S. Matsuda, M. Seki

1.5.1 Summary of INTOR Phase IIA Design Requirements

1.5.1.1 Requirements for NBI system at Phase I

1.5.1.1.1 Positive Ions

1.5.1.1.1.1	Overall	
1.5.1.1.1.1.1	Total Power/NBI	18.7 MW/NBI
1.5.1.1.1.1.2	Power Density	15.6 MW/m^2 average
1.5.1.1.1.1.3	Energy	175 keV
1.5.1.1.1.1.4	Pulse Length	10 s
1.5.1.1.1.1.5	Species Mix	$H^+ : H_2^+ : H_3^+$
	- Ion Fraction	80 : 12 : 8 (%)
	- Power Fraction	62 : 28 : 10 (%)
1.5.1.1.1.1.6	Efficiency	
	- Full Energy	22 %
	- All Energies	35 %
1.5.1.1.1.2	Ion Source	
1.5.1.1.1.2.1	Number/NBI	4/NBI
1.5.1.1.1.2.2	Size (HxW)	16 cm x 32 cm/grid
1.5.1.1.1.2.3	Divergence	< 1.5°
1.5.1.1.1.2.4	Current	68 A
1.5.1.1.1.2.5	Type of Grid Cooling	Active Cooling/water
1.5.1.1.1.3	Beam Line	
1.5.1.1.1.3.1	Type of Ion Deposition	
	- Beam Dump Energy Density	
	- Direct Recovery Efficiency	
1.5.1.1.1.3.2	Cryopumps (drift and gas cell regions)	
	- Type	H and isotopes
	- Pumping Speed	
	- Pressure	
1.5.1.1.1.3.3	Valves	

1.5.1.2 Requirements for fueling system

Number of injectors		2 (dual channel)
Pellet size (diameter)		3 mm
Tritium pellet	0.00679 g	1.36×10^{21} T_2 atoms
Deuterium pellet	0.00426 g	1.28×10^{21} D_2 atoms
Pellet composition		
Tritium pellet		> 90 % T_2
Deuterium pellet		> 90 % D_2
Pellet velocity		2 km/s
Injection rate range		0 - 15/s
Pellets per injection period		3000 (max)
Injection distance from plasma		> 6 m
Magnetic field		< 0.2 T

1.5.2 Neutral Beam Heating System

1.5.2.1 Positive ions

1.5.2.1.1 Overall

1.5.2.1.1.1 Total power/NBI

Data Base Assessment

1.5 MW/NBI for up to 100 keV H^+. However, if the beam energy is limited to 175 keV with D^+, it is possible to design a system of about 3 MW/NBI with the same degree of technical difficulty.

R & D Programs

Needs : High Power Plate ... cooling capability of several kW/cm^2.

Test Facility : JT 60 NBI Prototype ... several kW/cm^2.

1.5.2.1.1.2 Power density

Data Base Assessment

7.6 MW/m^2 average. As in 1.5.2.1.1, this number can be doubled, if the system is designed in such a way that the maximum beam energy is 175 keV D^+.

No beam choking effect was found in the JT-60 NBI Prototype experiments.

1.5.2.1.1.3 Energy

Data Base Assessment

No problem for handling high energy beam up to 200 keV.

100 keV H^+ 80 A at JT-60 NBI Prototype

200 keV He^+ 3.5 A at JT-60 He diagnostic system

Beam energy is changeable during a pulse.

JT-60 NBI : 50 to 100 keV within 1.5 sec

Impact

Heat load on NBI shine through region of the first wall will be decreased by controlling the beam energy according to plasma density.

1.5.2.1.1.4 Pulse length

Data Base Assessment

No problem to handle quasi-continuous beam

10 sec at JT-60 NBI prototype

The system which can handle more than several second pulse length beam (= quasi-stationary beam) has a capability equivalent to continuous rating system.

1.5.2.1.1.5 Species mix

Data Base Assessment

$H^+ : H_2^+ : H_3^+ = 92:5:3$

Impact

The design D^+ fraction can be increased since we have already achieved much higher percentage.

1.5.2.1.1.6 Efficiency

Data Base Assessment

Design requirements are almost uniquely determined from the beam energy and the species ratio. Therefore, it is not meaningful to compare with the recent data. Namely, if we operate our system with a reduced species ratio, we get the same number with the design value.

1.5.2.1.2 Ion source

1.5.2.1.2.1 Number/NBI

Data Base Assessment

2/NBI at JT-60 NBI

No particular difficulty is found to put four sources per NBI

1.5.2.1.2.2 Size (HxW)

Data Base Assessment

12 cm x 27 cm/grid for 40 A extraction

No particular problem is foreseen to build up to 100 A source.

R & D Programs

Needs : development of large ceramic insulators

Facility : JT-60 NBI prototype

1.5.2.1.2.3 divergence

Data Base Assessment
1.0 for H^+ at JT-60 NBI
0.24 for He^+ at JT-60 He_0 diagnostic system
The design requirements are too loose.

1.5.2.1.2.4 Current

Data Base Assessment
45 A H^+ at JT-60 NBI Prototype
No problem is foreseen to build up to 100 A sources.

1.5.2.1.2.5 Type of grid cooling

Data Base Assessment
Active cooling/water

1.5.2.1.2.6 Reliability

Data Base Assessment
Once extractor grids are well conditioned, they will scarcely encounter breakdowns. Moreover, even if some breakdowns take place, the control system can compensate almost completely.

1.5.2.1.3 Beam Line

1.5.2.1.3.1 Type of ion deposition

o Beam dump energy density

Data Base Assessment
5 MW/m^2 at the peak point (JT-60 NBI)

o Direct recovery efficiency

Data Base Assessment
To increase overall power efficiency up to 50 % , it is absolutely necessary to develop direct recovery system with efficiencies higher than 80 - 90 %.

R & D Program
Needs : Development of a direct recovery system
Facility : ITS-2

Impact
Capacity of a power supply system for NBI will be largely decreased with increasing efficiency through development of a direct recovery system.

1.5.2.1.4 Cryopumps

Data Base Assessment
o Type : He pool
o Pumping speed : 1.42×10^6 l/s

o Pressure : $5 \times 10^{-6} - 2 \times 10^{-5}$ torr

R & D Program
Needs : Development of He pump

1.5.2.1.4 Valves

Data Base Assessment
At JT-60 NBI Prototype unit
600 dia : bakable up to 250 C
closed baking is possible
Life : 500 cycles

R & D Program
Needs : Development of a large diameter valve

1.5.2.2 Negative Ions

Data Base Assessment
12 mA with volume production type source

R & D Program
Present R & D : searching for higher current density with source plasma confinement structure
Needs : source development; beam acceleration; beam transport; neutralization
Facility : ITS-2 75 kV, 40 A, test stand

Impact
Capacity of a power supply system for NBI will be largely decreased with the development of a negative ion injection system.

1.6 Radiation Hardened diagnostics

1.6.1 Summary of INTOR Requirements

The basic requirements for diagnostics were established during Phase 1 studies. Table 1.6.1 and 1.6.2 sumerize the major disgnostic requirements.

TABLE 1.6.1 SEQUENCE OF CONTROL OPERATIONS

	Phase (duration)	Control purpose	Feedback control time constant (reasoning)[a]	Actuators			Diagnostics (sensors)
				Magnetic fields	Fueling	Heating	
Start-up	Ionization and current initiation (~100 ms)	Loop voltage Plasma current Minor radius Ionization	10 ms (Joule loss)	Transformer Transformer Divertor	Filling pressure	Pulsive	One-turn loop Rogowski coil X-ray intensity profile Multi-channel interferometer
	Current rise and Ohmic heating (2 ~ 4 g)	Plasma current Current profile Elongation Electron temp. Density	100 ms ~ 1 s (Joule loss) 100 ms~1 s(τ_p)	Transformer Divertor Shaping field Transformer	Gas injection	Pulsive	Rogowski coil FIR polarimeter X-ray intensity profile Cyclotron radiation Multi-channel interferometer
	Additional heating (~ 5 s)	Plasma current Ion and electron temp. Density Density profile	100 ms~1 s 100 ms~1 s(τ_E) 100 ms~1 s(τ_p)	Transformer	Gas injection or pellets	Continuous	Rogowski coil Doppler broadening(?) Multi-channel interferometer
Burn (100~200s)		Plasma current Density Helium accumulation	~1 s(Joule loss) ~1 s(τ_p)	Transformer Divertor	Gas injection or pellets		Rogowski coil Multi-channel interferometer Charge-exchange measurement Fluorescence spectroscopy Residual gas analyser Triton density measurement
	Sub-ignition Marginally ignited Ignited state	Burn control Compress.-decompress. Reactivity Field ripple limit	~1 s (burn confinement time)	Vertical field Toroidal field Shaping field	Gas injection	Pulsive Pulsive	Neutron measurement Doppler booadening(?) Multi-channel interferometer Cyclotron radiation Bolometer
Shut-down (5 s)	Burn termination	Ripple enhancement Reactivity lowering Impurity injection Decompression	100 ms ~ 1 g	Toroidal field Vertical field	Gas injection Impurity pellets		
	Cooling and current run-down	Plasma current Cooling	100 ms~1 s	Transformer	Impurity pellets		Same as in the current rise and Ohmic heating phase

[a] Feedback is unnecessary unless specified.

Table 1.6.2 INSTABILITY CONTROL

Control	Control measures	Feedback control		Actuators	Diagnostics (sensors)
		Time const.	Reasonings		
MHD instability and disruption	m = 2/n = 1 mode suppression	1 ms	MHD growth rate	Helical windings	X-ray, ω_{ce}, neutrons magnetic probes
	Feed-forward control by disruption precursor	10 ms	Time delay between precursor and disruption	?	X-ray, ω_{ce} neutrons, magnetic probes
	Avoidance of dangerous regime				
	Impurity			Divertor	Spectroscopy
	Density lowering	10 ms		Injection speed	Multi-channel interferometer
	Speed of density increase	?			
	Speed of I_p increase			Transformer	Rogowski coil
	Current profile	10 ms?		Pulsive heating, gas injection	Multi-channel FIR polarimeter
Equilibrium control	Horizontal, vertical and shape control	0.5-1s	Time constant of eddy current in the blanket	Vertical and shaping magnetic fields	X-ray intensity profile magnetic probes

REFERENCE

(1) Shimamoto, S., et al., "Japanese Design of a Test Coil for the Large Coil Task," Proc. of the 8th Symposium on Engineering Problem of Fusion Research, p.1174
(2) Shimamoto, S., et al., "Domestic Test Results of the Japanese LCT Coil," IEEE Trans., Mag-11. No.3, p.851
(3) Shimamoto, S., et al., "Cluster Test Facility Construction and Its Future Perspective," Proc. of 8th symposium on Engineering Problem of Fusion Research, p.261
(4) Shimamoto, S., et al., "Construction and Operation of the Cluster Test facility," IEEE Trans., Mag-17, No.1, p.41.
(5) Ando, T., et al., "Experiment of 10-T, 60-cm Bore Nb3Sn Test Module Coil for the Cluster Test Program," IEEE Trans., Mag-11. No.3, p.312
(6) Ando, T., et al., "Up Grading of the Cluster Test Facility and an Extended Test on TMC-I," A paper presented at ICEC 10, July-August (Helsinki)
(7) Takahashi, Y., et al., "Development of 12T-10kA Al Stabilized Nb3Sn Conductor for TMC-II," A paper presented at 11.4 Applied Superconductivity Conference (San Diego, USA)
(8) Shimamoto, S., et al., "Design and Verification Test for a 20 MJ Pulsed Poloidal Coil," 10th Symposium on Fusion Engineering Proceedings, p.1358
(9) Takahashi, Y., et al., "Mechanical Evaluation of Nitrogen strengthened Stainless Steels at 4K," Advances in Cryogenic Engineering, Vol. 28, p.73
(10) Nakajima, H., et al., "Development of the New Cryogenic structural Material for Fusion experimental Reactor," Advances in Cryogemnic Engineering, Vol.30, p.219

Appendix Selected Data for Magnet Systems
Figures and Tables

Table 1 Chemical compositions and heat-treatment of the steels tested

No.	Chemical Compositions (%)									Plate Thickness (mm)	Heat Treatment
	C	Si	Mn	P	S	Ni	Cr	N	Others		
A1	0.04	0.09	22.30	0.001	0.009	5.09	12.23	0.225	-	15	AR
A2	0.02	0.40	3.70	0.009	0.005	19.33	24.32	0.250	Mo: 2.87	20	ST
B1	0.61	0.32	17.35	0.010	0.006	2.93	7.89	0.041	Cu: 1.50	20	ST
B2	0.57	0.26	24.13	0.008	0.007	5.10	3.47	0.130	-	20 20	AR ST
C1	0.05	0.23	0.56	0.002	0.001	9.09	-	-	-	22	QT
C2	0.001	0.007	0.005	0.001	0.003	18.08	-	-	Mo:1.92 Al:0.09 Ti:1.47	20	ST
D	0.03	0.52	1.66	0.004	0.005	8.94	18.24	0.120	-	20	ST

A1, A2, C2, D : 90kg vacuum-melting
B1, B2 : 90kg air-induction-melting
} forging → hot-rolling to plates

Table 2 Mechanical properties and magnetic permeability of the steels

No.	Material	Heat Treatment	Test temperature (K)	Tensile Properties			Impact Properties		Magnetic[a] Permeability
				0.2%YS (MPa)	TS (MPa)	El (%)	vE (J)	LE (mm)	
A1	22Mn-5Ni-12Cr-0.22N	AR	293	443	697	53	213	-	< 1.01
			77	1036	1455	50	81	-	< 1.01
			4	1429	1742	23	77	0.7	1.02 ~ 1.15
A2	3.5Mn-24Cr-20Ni-3Mo-0.25N	ST	293	438	802	52	246	-	< 1.01
			77	915	1397	54	171	-	< 1.01
			4	1275	1703	37	174	1.6	< 1.01
B1	0.6C-18Mn-1.5Cu-3Ni-8Cr	ST	293	394	846	79	247	-	< 1.01
			77	881	1349	50	149	-	< 1.01
			4	1349	1688	43	122	1.4	< 1.01
B2	0.6C-24Mn-5Ni-3Cr-0.1N	AR	293	517	960	58	272	-	< 1.01
			77	1020	1490	37	113	-	< 1.01
			4	1501	1814	32	64	0.8	< 1.01
		ST	293	389	800	69	318	-	< 1.01
			77	883	1329	51	189	-	< 1.01
			4	1384	1640	40	112	1.5	< 1.01
C1	9% Ni Steel	QT	293	681	720	25	253	-	-
			77	989	1051	32	234	-	-
			4	1300	1368	19	180	1.8	-
C2	Co-free Maraging Steel	ST	293	834	971	18	216	-	-
			77	1373	1476	16	105	-	-
			4	1442	1642	13	55	0.5	-
D	SUS304LN	ST	293	309	623	56	234	-	< 1.01
			77	627	1491	44	178	-	> 2.5
			4	735	1721	40	147	-	> 2.5

[a] measured at fracture surface of tensile specimen

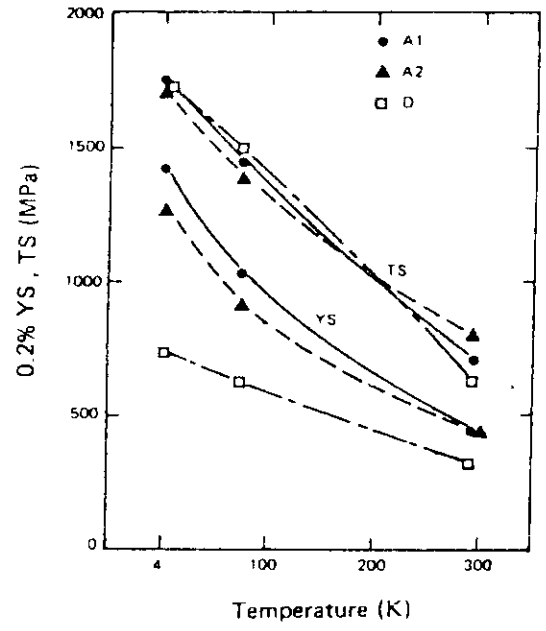

a) Tensile and yield strengths

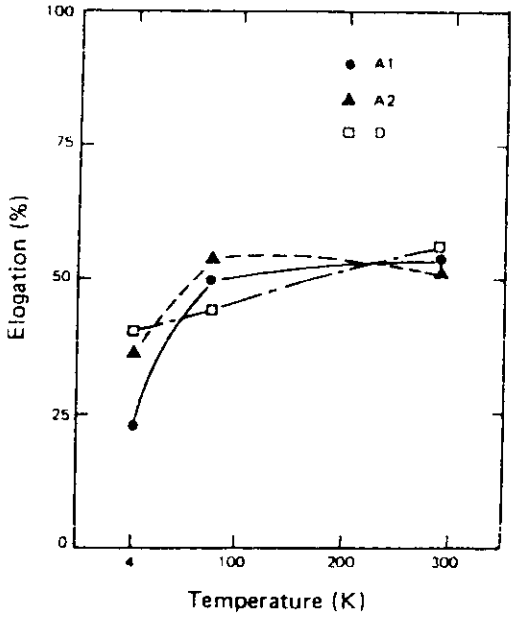

b) Elongation

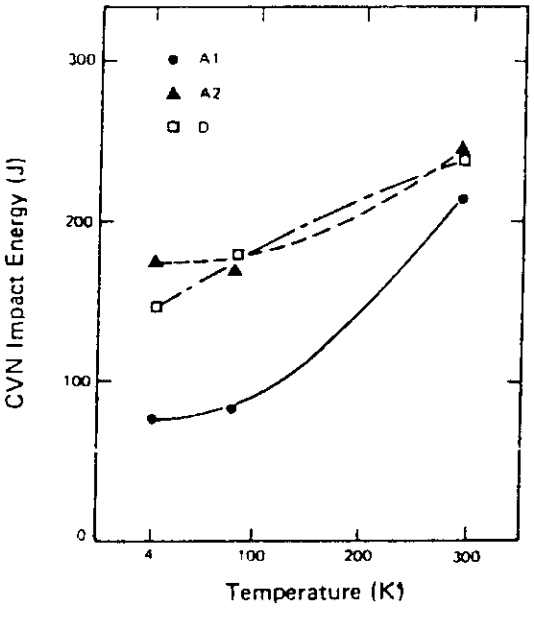

c) Impact toughness

A1 22Mn-12Cr-5Ni-0.22N
A2 3.5Mn-24Cr-20Ni-3Mo-0.25N
D SUS 304 LN

Fig. 1. Mechanical properties of nitrogen-strengthened high-manganese austenitic stainless steels and SUS304LN as a function of temperature

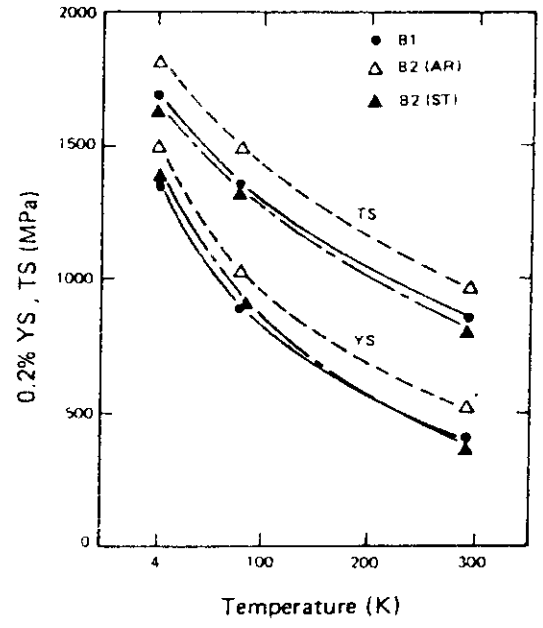

a) Tensile and yield strengths

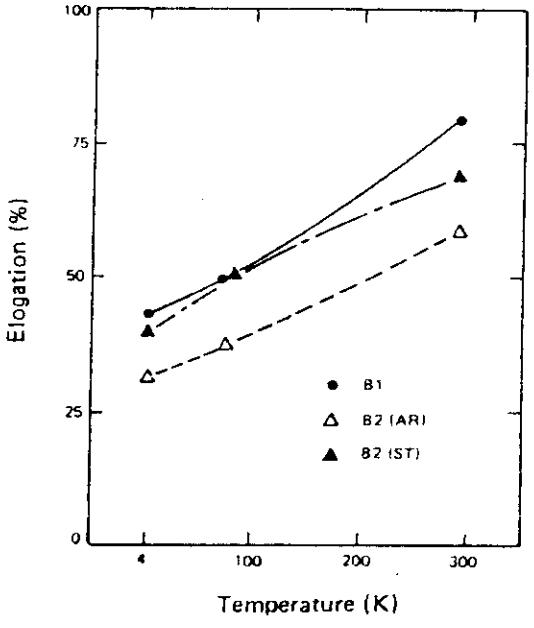

b) Elongation

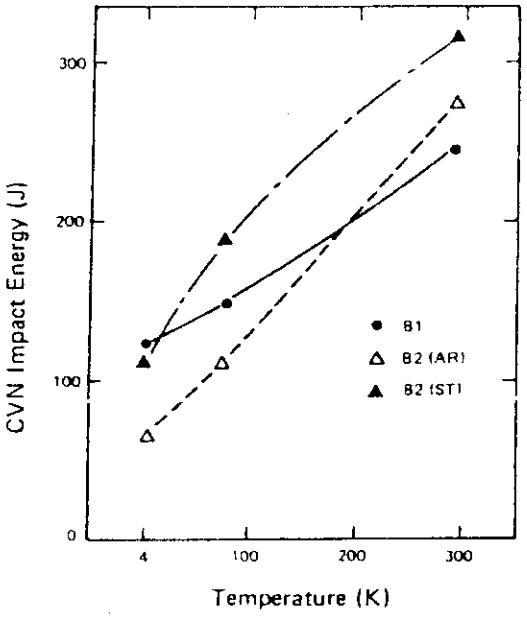

c) Impact toughness

B1 : 0.6C-18Mn-1.5Cu-3Ni-8Cr
B2(AR), B2(ST) } 0.6C-24Mn-5Ni-3Cr-0.1N

Fig. 2 Mechanical properties of carbon-strengthened high-manganese austenitic steels as a function of temperature

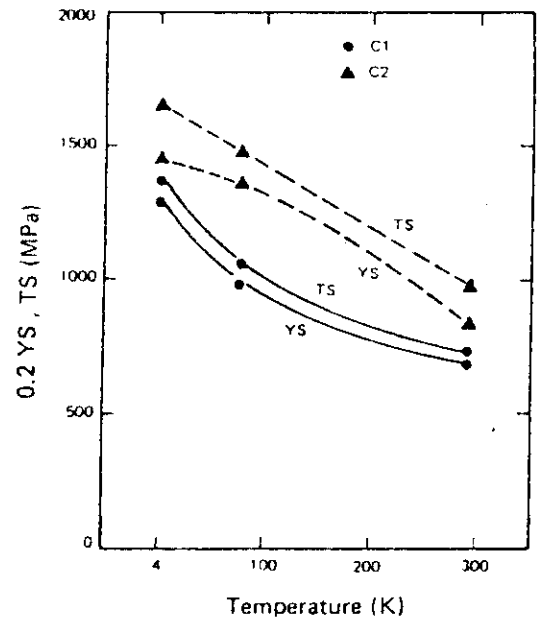

a) Tensile and yield strengths

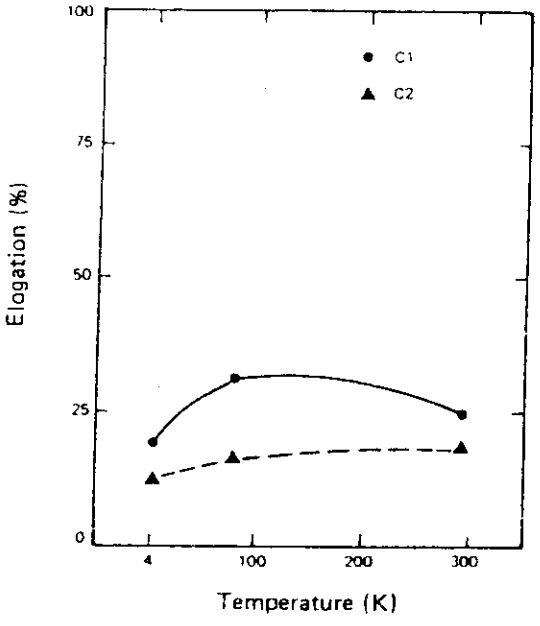

b) Elongation

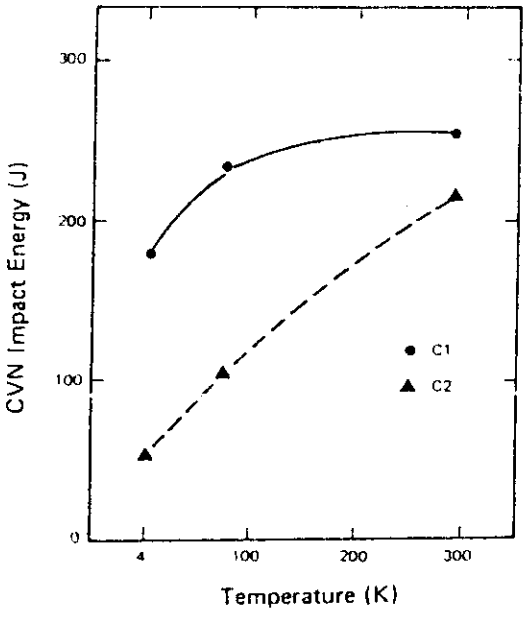

C1 : 9% Ni Steel
C2 : Co-free Maraging Steel

c) Impact toughness

Fig. 3 Mechanical properties of ferritic steels as a function of temperature

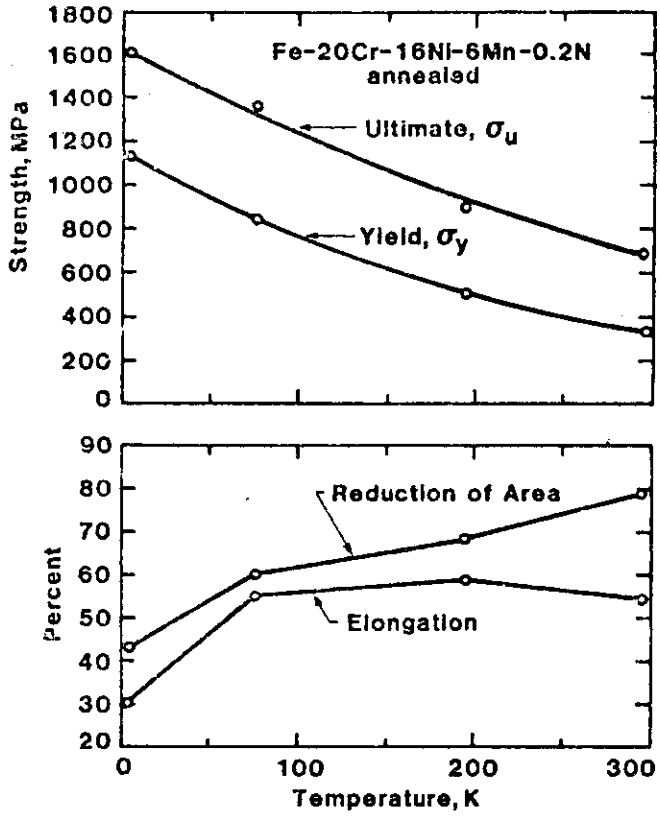

Fig. 4 Tensile properties at 295, 195, 75, and 4 K of Fe-20Cr-16Ni-6Mn-0.2N steel

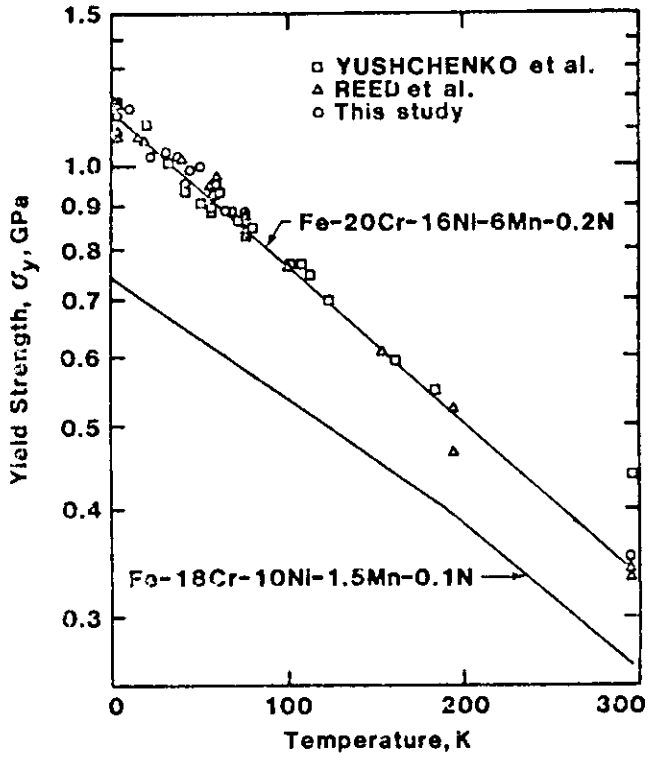

Fig. 5 Yield strength versus temperature for Fe-20Cr-16Ni-6Mn-0.2N steel, with data summarizing from this study and other studies. Average data for Fe-18Cr-10Ni-1.5Mn-0.1N steel are included.

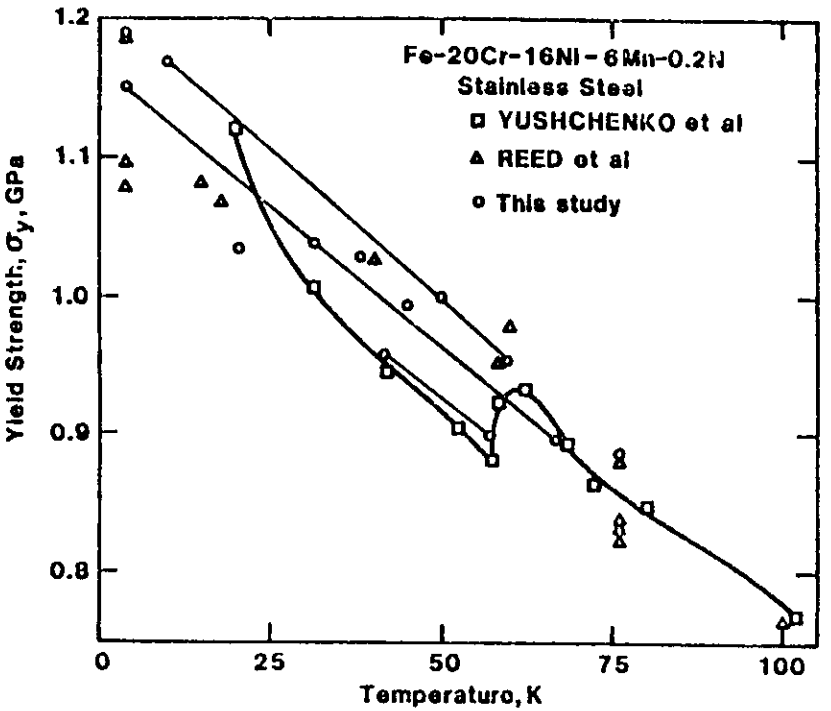

Fig. 6 Yield strength data for Fe-20Cr-16Ni-6Mn-0.2N steel at cryogenic temperatures, showing specimen-to-specimen variabiulity and trend, as trend, as reported by other studies

Table 3 Yield Strength Measurements* for Fe-20Cr-16Ni-6Mn-0.2N Steel.

Temperature (K)	Yield Strength, σ_y (MPa)
20	1122
31	1008
42	946
51	904
57	880
58	923
62	934
68	893
72	863
80	848
102	770
108	769
114	748
123	700
162	595
184	550
300	~340?

* USSR data [1-3]; taken using ruler and interpolation from published graphs.

Table 4 Chemical composition by weight percent of the studied alloys and a previously studied alloy.

Designation	Fe	Cr	Ni	Mn	N	C	Mo	Si	S	P	Nb	V	Cu	Co
Fe-18Cr-3Ni-13Mn	bal	18.09	3.26	13.22	.37	.038	.12	.52	.005	.029	---	---	---	---
Fe-21Cr-12Ni-5Mn	bal	21.15	12.37	4.96	.31	.041	2.17	.49	.015	.026	18	15		
Fe-19Cr-9Ni-2Mn	bal	18.65	9.49	1.88	.12	.048	.52	.38	.024	.019	---	.03	.07	.06
Fe-21Cr-6Ni-9Mn	bal[a]	19.75	7.16	9.49	.28	.019	---	.15	.003	.004	---	---	---	---

[a]Reported in Reference 5.

Table 5 Tensile properties of the nitrogen-strengthened stainless steels used in the present study and a previously tested material.

	Temperature (K)	Yield Strength 0.2 offset MPa	Tensile Strength MPa	Flow Strength[a] MPa	Elongation 2.5 cm gage length ( )	Reduction of Area ( )
Fe-18Cr-3Ni-13Mn	295	421	787	604	54	63
		459	803	632	56	63
		440	796	618	56	63
	76	1154	1522	1338	19	32
		1134	1516	1325	18	25
		1144	1519	1331	19	29
	4	1572	1807	1689	5	23
		1509	1815	1662	4	29
		1540	1811	1676	4	26
Fe-21Cr-12Ni-5Mn	295	534	845	689	35	64
		522	840	681	35	59
		528	842	685	35	61
	76	1164	1584	1373	28	36
		1178	1591	1384	29	31
		1171	1587	1379	28	34
	4	1472	1898	1685	9	34
		1422	1889	1655	9	32
		1446	1893	1670	9	33
Fe-19Cr-9Ni-2Mn	295	310	654	482	61	70
		290	644	467	60	69
		300	649	474	60	70
	76	633	1512	1073	48	66
		676	1502	1089	48	67
		655	1507	1081	48	66
	4	846	1663	1255	37	42
		743	1647	1195	32	47
		794	1655	1225	34	44
Fe-21Cr-12Ni-5Mn-X (special anneal)	4	1307	1842	1575	16	36
		1353	1853	1604	15	41
		1330	1848	1589	16	38
Fe-21Cr-6Ni-9Mn[b]	295	350	696	523	61	79
		357	705	531	61	78
		353	701	527	61	78
	76	0.913	1462	1188	42	32
		0.886	1435	1176	43	41
		0.899	1474	1187	43	37
	4	1250	1633	1446	16	40
		1224	1634	1429	--	--
		1241	1634	1438	16	40

[a]Flow strength is taken as the average of the tensile and yield strengths.

[b]Data from Reference 5.

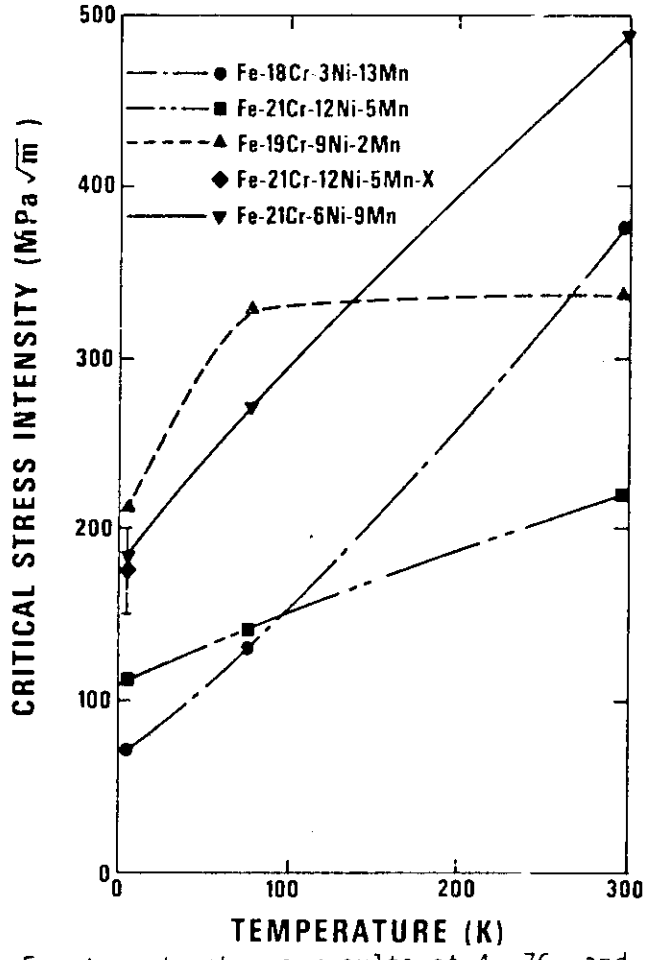

Figure 7 Fracture toughness results at 4, 76, and 295 K for nitrogen-strengthened stainless steels used in the present study.

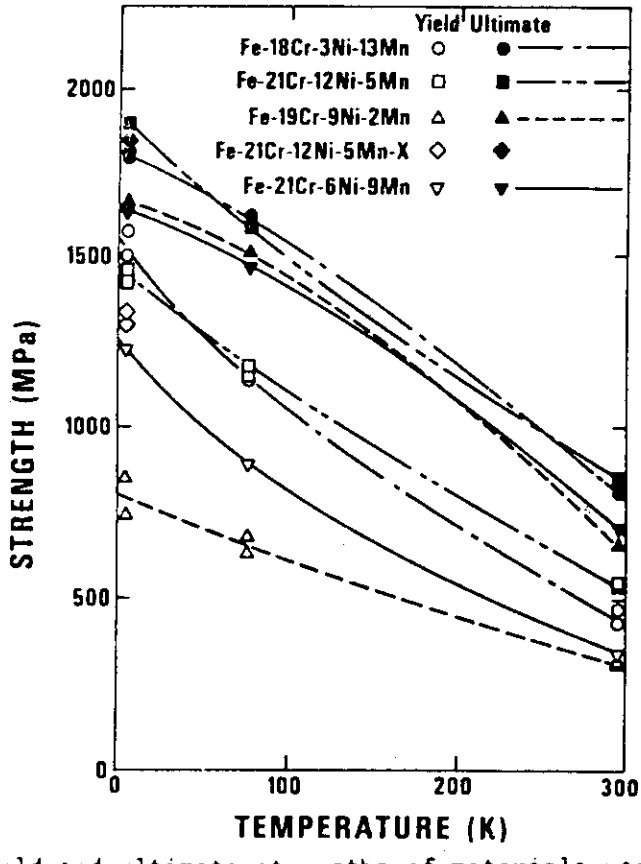

Figure 8 .Yield and ultimate strengths of materials used in the present study.

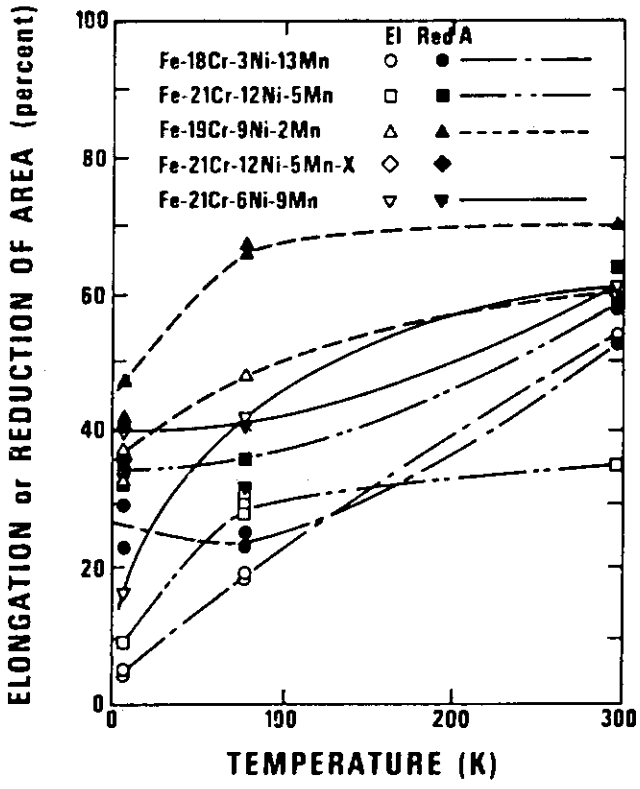

Figure 9 .Elongations and reduction of areas of the materials used in the present study.

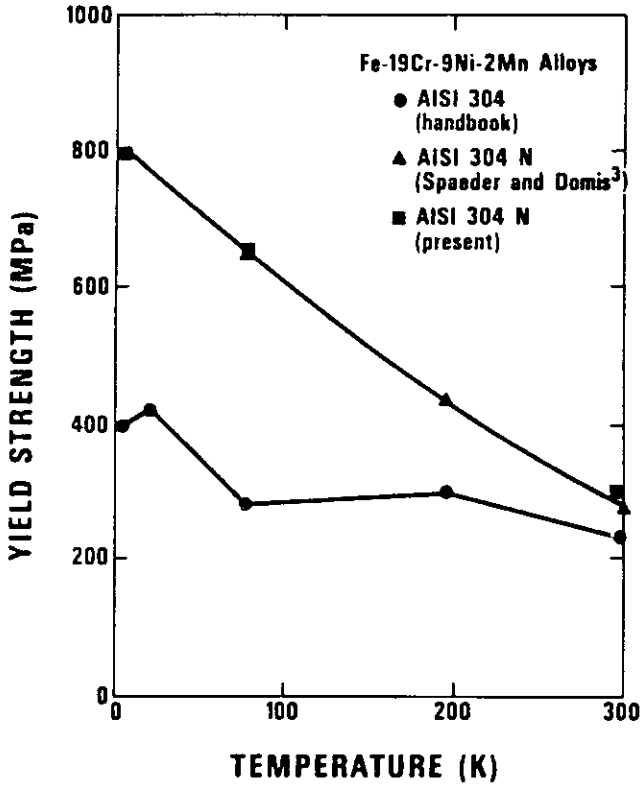

Figure 10 .Yield strengths of AISI 304 and AISI 304N (Fe-19Cr-9Ni-2Mn) between 4 and 300 K.

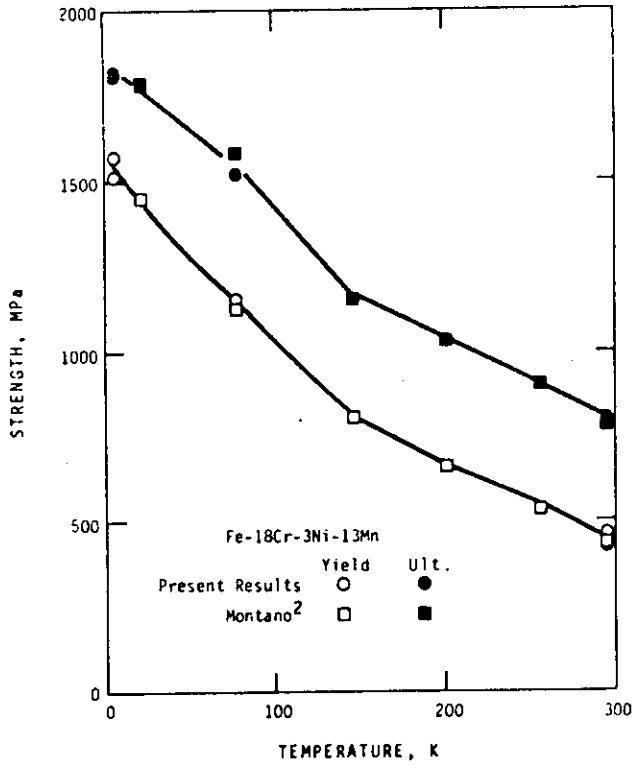

Figure 11 .Strength property data for Fe-18Cr-3Ni-13Mn from the present study and from Montano.[2]

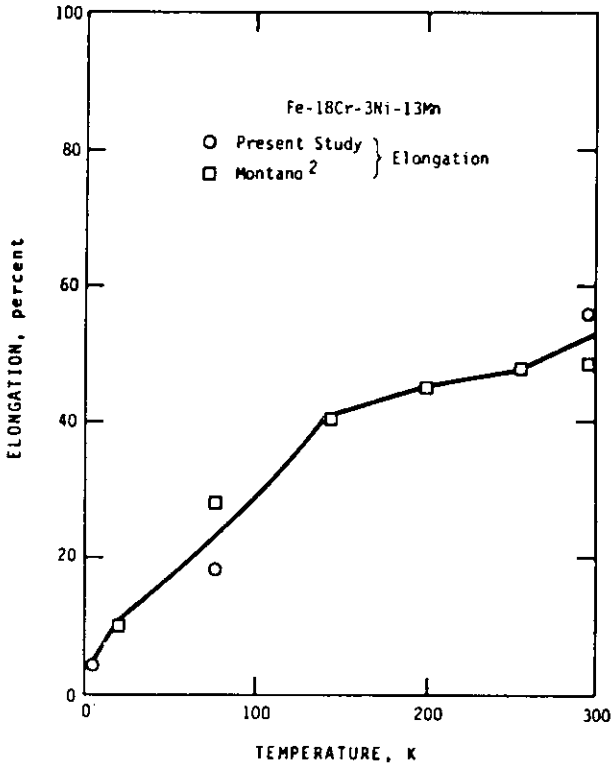

Figure 12 .Elongation data for Fe-18Cr-3Ni-13Mn from the present study and from Montano.[2]

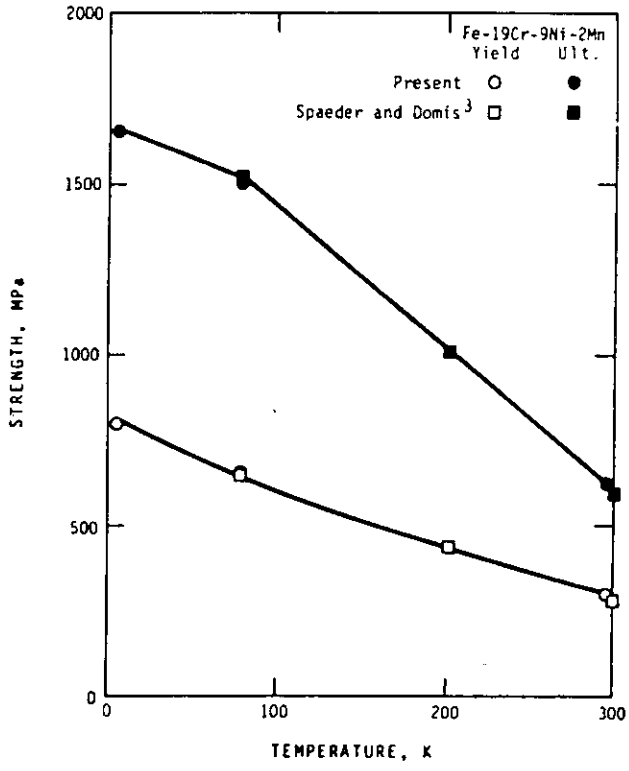

Figure 13 .Strength property data for Fe-19Cr-9Ni-2Mn from the present study and from Spaeder and Domis.[3]

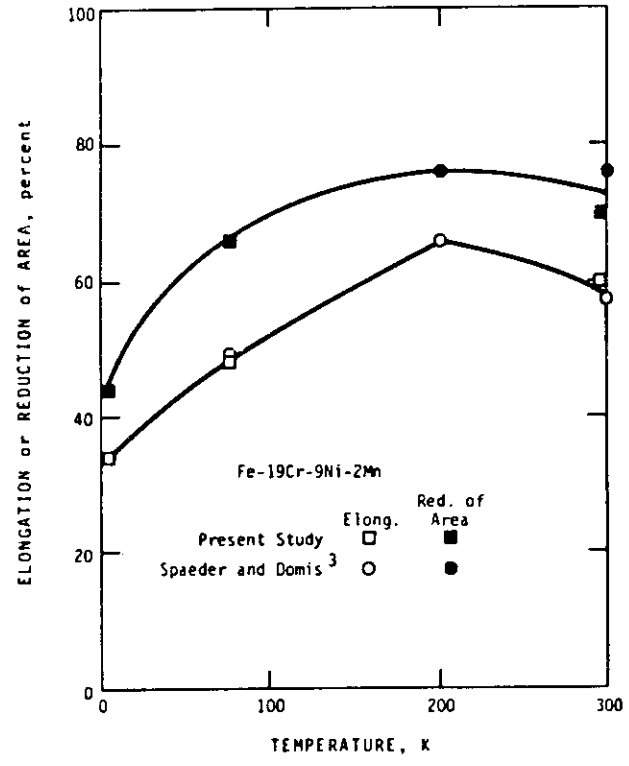

Figure 14 .Elongation and reduction of area data for Fe-19Cr-9Ni-2Mn from the present study and from Spaeder and Domis.[3]

2.1.1.1.2 Shear stress versus shear strain curve

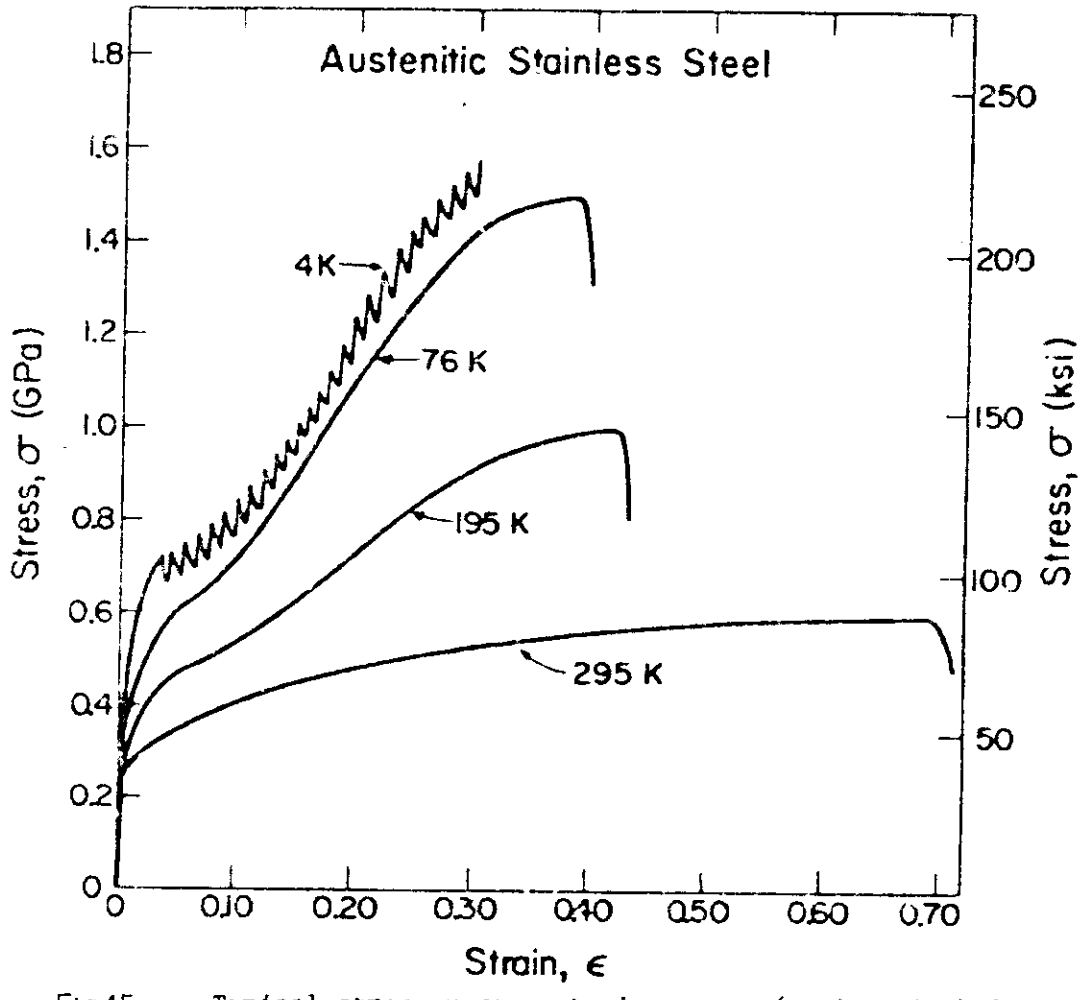

Fig.15 Typical stress versus strain curves (engineering) for polycrystalline Fe-18Cr-8Ni austenitic stainless steel.

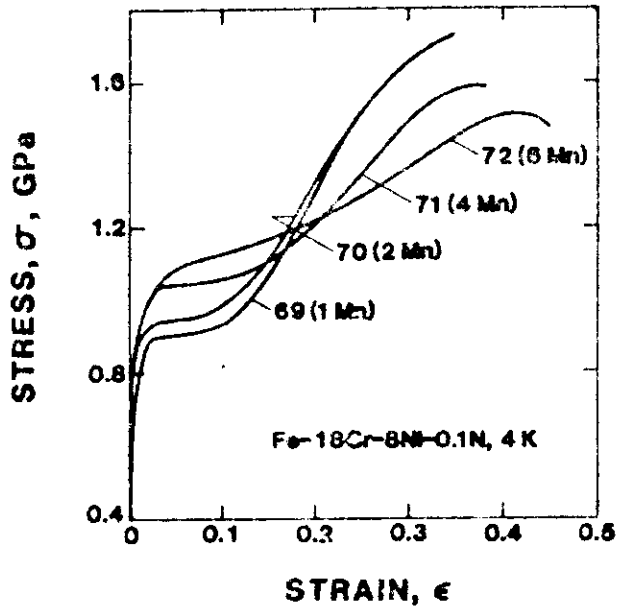

Fig.16 Stress-strain curves at 4 K for series of Fe-18Cr-8Ni-0.1N alloys with 1-6 wt% Mn.

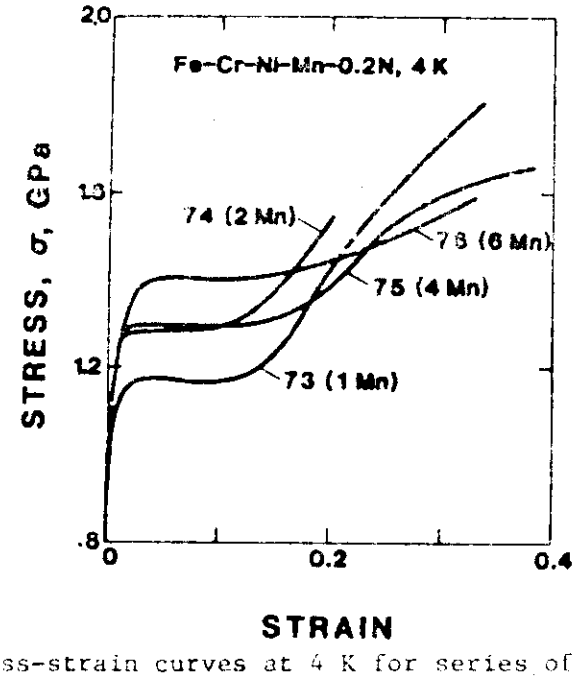

Fig. 17 Stress-strain curves at 4 K for series of Fe-18Cr-8Ni-0.2N alloys with 1-6 wt% Mn.

2.1.1.2 Fatigue Characteristics

2.1.1.2.1 Curve of failure stress versus number of cycles to failure

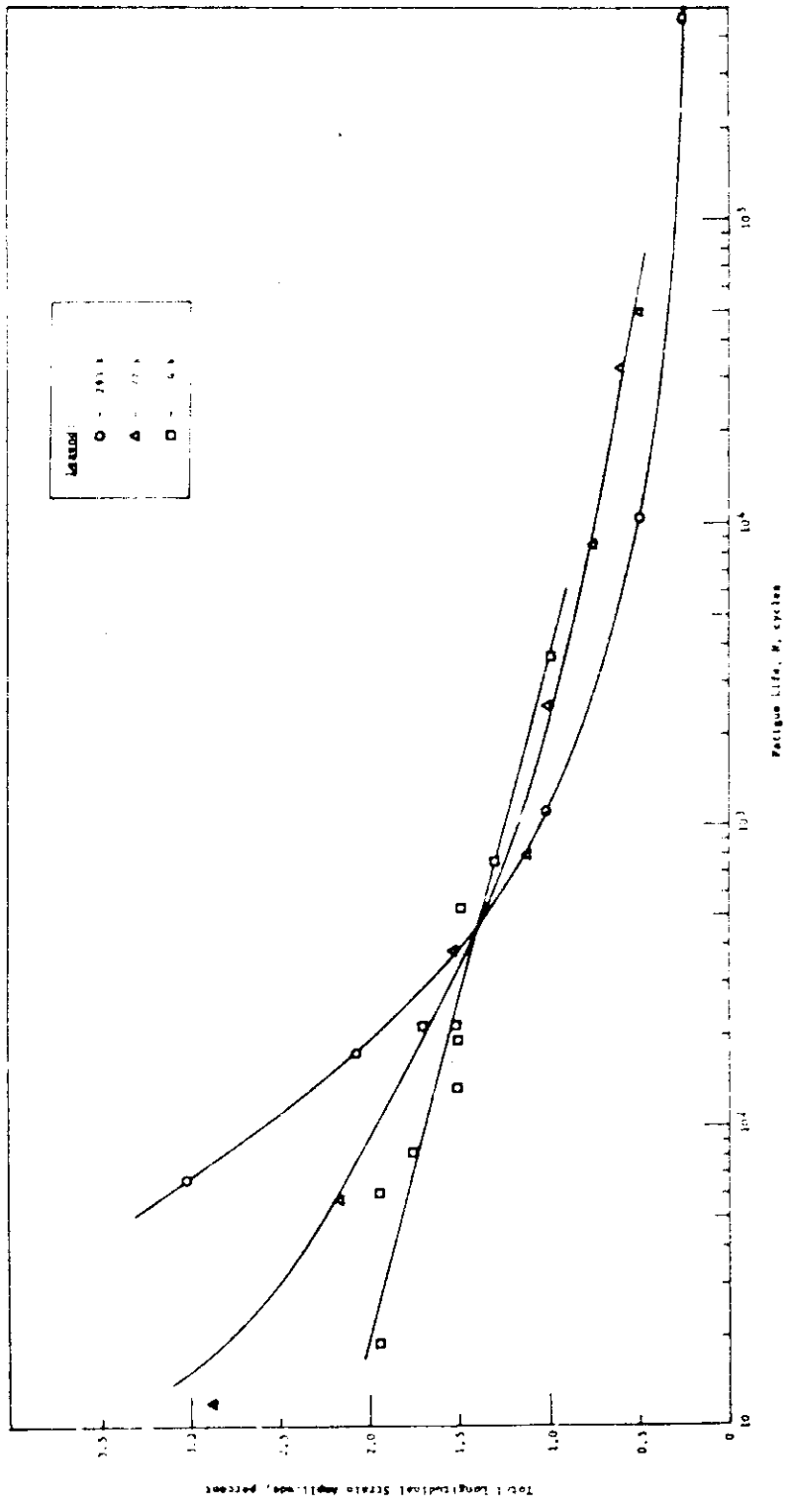

Fig. 18 *Fatigue Life Curves for 304*

Table 6 *Fatigue Data for 304 Stainless Steel*

Specimen Number	Temperature, K	Diametral Total Strain Amplitude, $\Delta\varepsilon_d$, Percent	Stress Amplitude at Half-Life, $\Delta\sigma$, MN/m^2 (ksi)	Longitudinal Elastic Strain Amplitude, $\Delta\varepsilon^e_1$, Percent	Longitudinal Plastic Strain Amplitude, $\Delta\varepsilon^p_1$, Percent	Longitudinal Total Strain Amplitude, $\Delta\varepsilon_1$, Percent	Cyclic Rate, Hz	Fatigue Life, N Cycles
304-1	293	0.96	655 (95)	0.35	1.72	2.07	0.10	176
-2		0.47	379 (55)	0.20	0.82	1.02	0.60	1,111
-3		1.42	758 (110)	0.41	2.61	3.02	0.10	67
-4		0.22	255 (37)	0.14	0.35	0.49	1.00	10,306
-6		0.10	200 (29)	0.11	0.14	0.25	3.00	457,430
304-7	77	0.94	1517 (220)	0.75	1.42	2.17	0.10	57
-8		0.46	1551 (225)	0.76	0.47	1.23	0.10	795
-9		0.21	814 (118)	0.40	0.19	0.59	1.10	32,077
-10		0.16	793 (115)	0.39	0.10	0.49	3.00	49,470
-11		0.61	1517 (220)	0.75	0.78	1.53	0.30	382
-12		0.28	965 (140)	0.47	0.28	0.75	0.60	8,480
-13		1.30	1517 (220)	0.75	2.12	2.87	0.10	12*
-14		0.37	1310 (190)	0.64	0.37	1.01	0.50	2,535
304-16	4	0.56	1793 (260)	0.88	0.61	1.49	0.30	531
-17		0.57	1793 (260)	0.88	0.63	1.51	0.10	216
-18		0.57	1793 (260)	0.88	0.62	1.50	0.05	134*
-19		0.57	1793 (260)	0.88	0.62	1.50	0.02	192
-20		0.80	1724 (250)	0.85	1.09	1.94	0.05	19
-21		0.67	1724 (250)	0.85	0.85	1.70	0.05	216
-22		0.49	1586 (230)	0.78	0.52	1.30	0.10	755
-23		0.79	1793 (260)	0.88	1.06	1.94	0.02	60
-24		0.36	1310 (190)	0.64	0.35	0.99	0.20	3,647

* Specimen Buckled

Temperature, K	293	77	4
Modulus, GN/m^2 (10^6 psi)	189 (27)	204 (29.5)	204 (29.5)
Poisson's Ratio	0.29	0.28	0.27

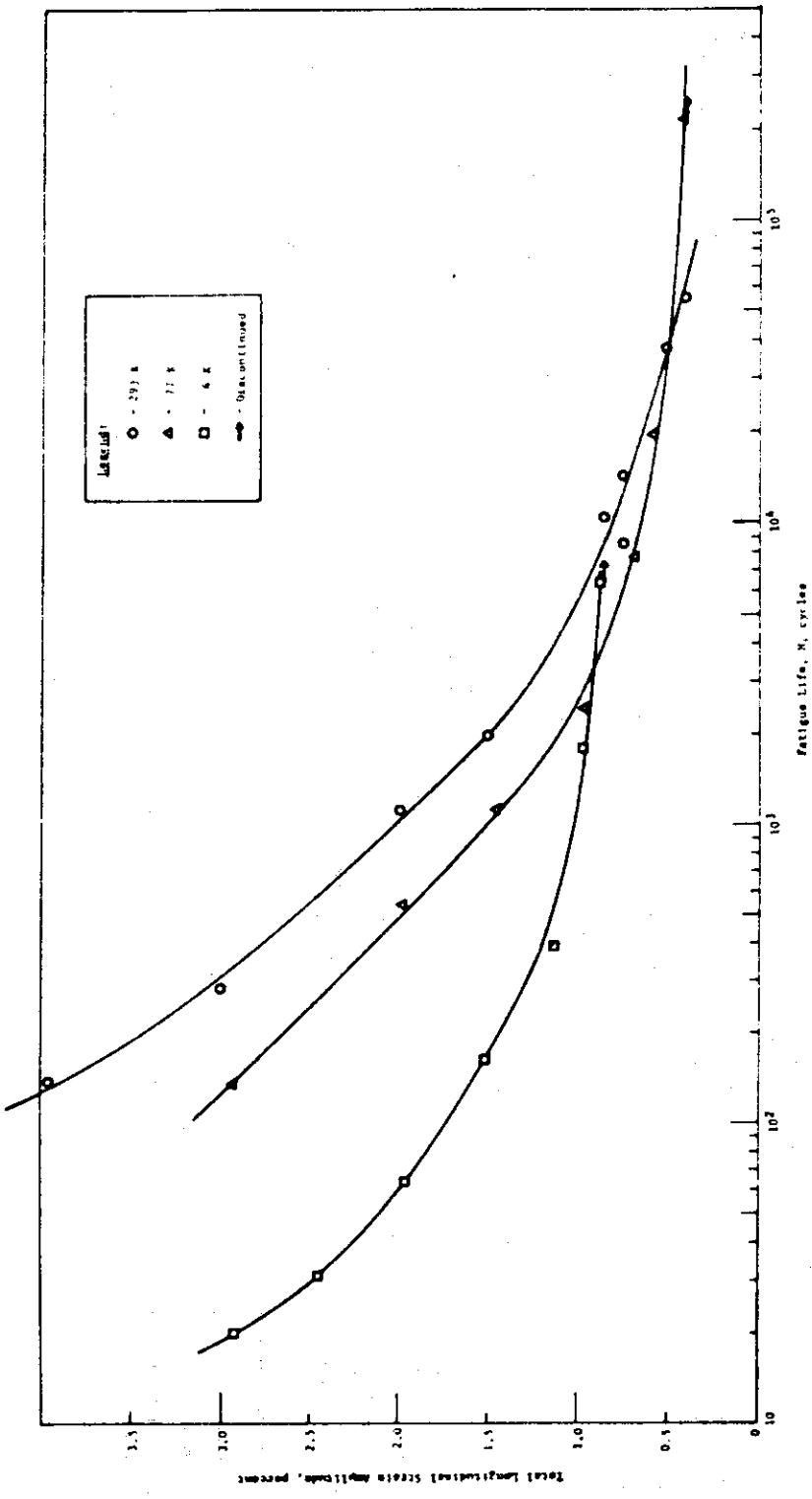

Fig. 19 *Fatigue Life Curves for 21-6-9*

Table 7 Fatigue Data for 21-6-9 Stainless Steel

Specimen Number	Temperature, K	Diametral Total Strain Amplitude, $\Delta\lambda_d$, Percent	Stress Amplitude at Half-Life, $\Delta\sigma$, MN/m^2 (ksi)	Longitudinal Elastic Strain Amplitude, $\Delta\varepsilon_l$, Percent	Longitudinal Plastic Strain Amplitude, $\Delta\varepsilon_l$, Percent	Longitudinal Total Strain Amplitude, $\Delta\lambda_l$, Percent	Cyclic Rate, Hz	Fatigue Life, N Cycles
2169-1	293	0.93	552 (80)	0.29	1.70	1.99	0.20	1,111
-2		0.39	345 (50)	0.18	0.67	0.85	0.90	10,236
-3		1.42	690 (100)	0.36	2.63	2.99	0.20	281
-4		0.70	448 (65)	0.23	1.27	1.50	0.70	1,995
-5		0.34	345 (50)	0.18	0.57	0.75	1.50	8,530
-6		0.34	345 (50)	0.18	0.57	0.75	1.50	14,160
-7a		0.22	310 (45)	0.16	0.35	0.51	1.50	37,640
-7b		0.17	310 (45)	0.16	0.26	0.42	3.00	56,430
-8		1.90	724 (105)	0.38	3.58	3.96	0.20	139
2169-9	77	0.89	1103 (160)	0.55	1.43	1.98	0.20	535
-10		0.39	896 (130)	0.45	0.51	0.96	1.00	2,443
-11		0.29	621 (90)	0.31	0.05	0.36	3.00	216,000
-12		0.63	965 (140)	0.48	0.96	1.44	1.00	1,117
-13		0.27	690 (100)	0.34	0.34	0.68	0.90	7,700
-14		1.36	1241 (180)	0.62	2.31	2.93	0.10	137
-15		0.23	655 (95)	0.33	0.26	0.59	2.00	19,470
2169-16	4	0.84	1448 (210)	0.72	1.23	1.95	0.10	64
-17		0.62	1379 (200)	0.69	0.81	1.50	0.10	163
-18		0.28	931 (135)	0.47	0.28	0.75	0.30	6,353*
-19		1.08	1586 (230)	0.79	1.65	2.44	0.05	31
-20		1.32	1586 (230)	0.79	2.13	2.92	0.02	20
-21		0.37	1103 (160)	0.55	0.42	0.97	0.10	1,786
-22		0.49	1310 (190)	0.66	0.59	1.25	0.10	389

* Test discontinued

Temperature, K	293	77	4
Modulus, GN/m^2 (10^6 psi)	195 (28)	203 (29)	203 (29)
Poisson's Ratio	0.29	0.28	0.28

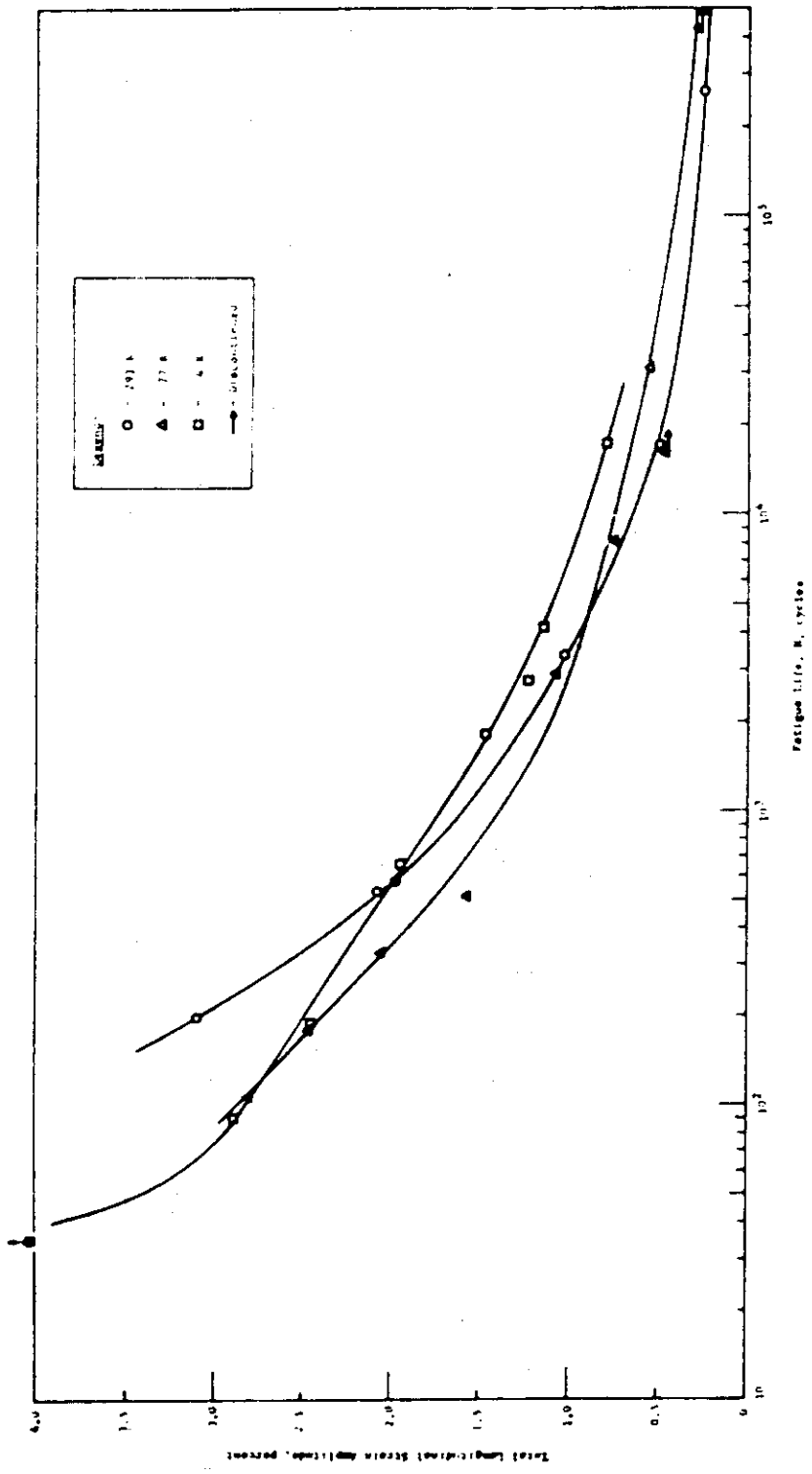

Figure 20 Fatigue Life Curves for 316

Table 8 Fatigue Data for 316 Stainless Steel

Specimen Number	Temperature, K	Diametral Total Strain Amplitude, $\Delta\varepsilon_d$, Percent	Stress Amplitude at Half-Life, $\Delta\sigma$, MN/m^2 (ksi)	Longitudinal Elastic Strain Amplitude, $\Delta\varepsilon_{e_l}$, Percent	Longitudinal Plastic Strain Amplitude, $\Delta\varepsilon_{p_l}$, Percent	Longitudinal Total Strain Amplitude, $\Delta\varepsilon_t$, Percent	Cyclic Rate, Hz	Fatigue Life, N Cycles
316-1	293	0.96	621 (90)	0.29	1.78	2.07	0.10	527
-2		0.47	379 (55)	0.18	0.84	1.02	0.80	3,328
-3		1.48	552 (80)	0.26	2.83	3.09	0.10	198
-4		0.93	517 (75)	0.24	1.73	1.97	0.40	579
-5		0.22	276 (40)	0.13	0.36	0.49	3.00	17,131
-6		0.10	193 (28)	0.09	0.16	0.25	3.00	259,459
-7		2.38	758 (110)	0.35	4.58	4.93	0.05	36
316-8	77	0.94	1000 (145)	0.43	1.62	2.05	0.40	329
-9		0.46	758 (110)	0.32	0.75	1.07	0.40	2,898
-10		0.21	586 (85)	0.25	0.30	0.55	1.10	31,300
-11		0.10	414 (60)	0.18	0.09	0.27	3.00	426,000*
-11a		1.36	828 (120)	0.35	2.45	2.80	0.10	107
-12		0.69	965 (140)	0.41	1.16	1.57	0.40	510
-13		1.86	965 (140)	0.41	3.45	3.86	0.10	30+
-14		1.14	1034 (150)	0.44	2.02	2.46	0.20	179
-16		0.18	483 (70)	0.21	0.25	0.46	3.00	164,567*
-17		0.31	621 (90)	0.26	0.49	0.75	1.10	8,157
316-18	4	0.64	965 (140)	0.41	1.06	1.47	0.05	1,815
-19		0.89	1123 (163)	0.48	1.46	1.94	0.07	661
-20		1.35	1337 (194)	0.41	2.47	2.88	0.05	90
-21		.55	882 (128)	0.38	0.85	1.23	0.05	2,751
-23		1.42	1468 (213)	0.63	2.60	2.45	0.05	188
-24		0.50	868 (126)	0.37	0.76	1.13	0.02	4,130
-25		0.33	785 (114)	0.34	0.44	0.78	0.03	17,100

* Discontinued
\+ Specimen buckled

Temperature, K	293	77	4
Modulus, GN/m^2 (10^6 psi)	216 (31)	234 (34)	234 (34)
Poisson's Ratio	0.30	0.28	0.28

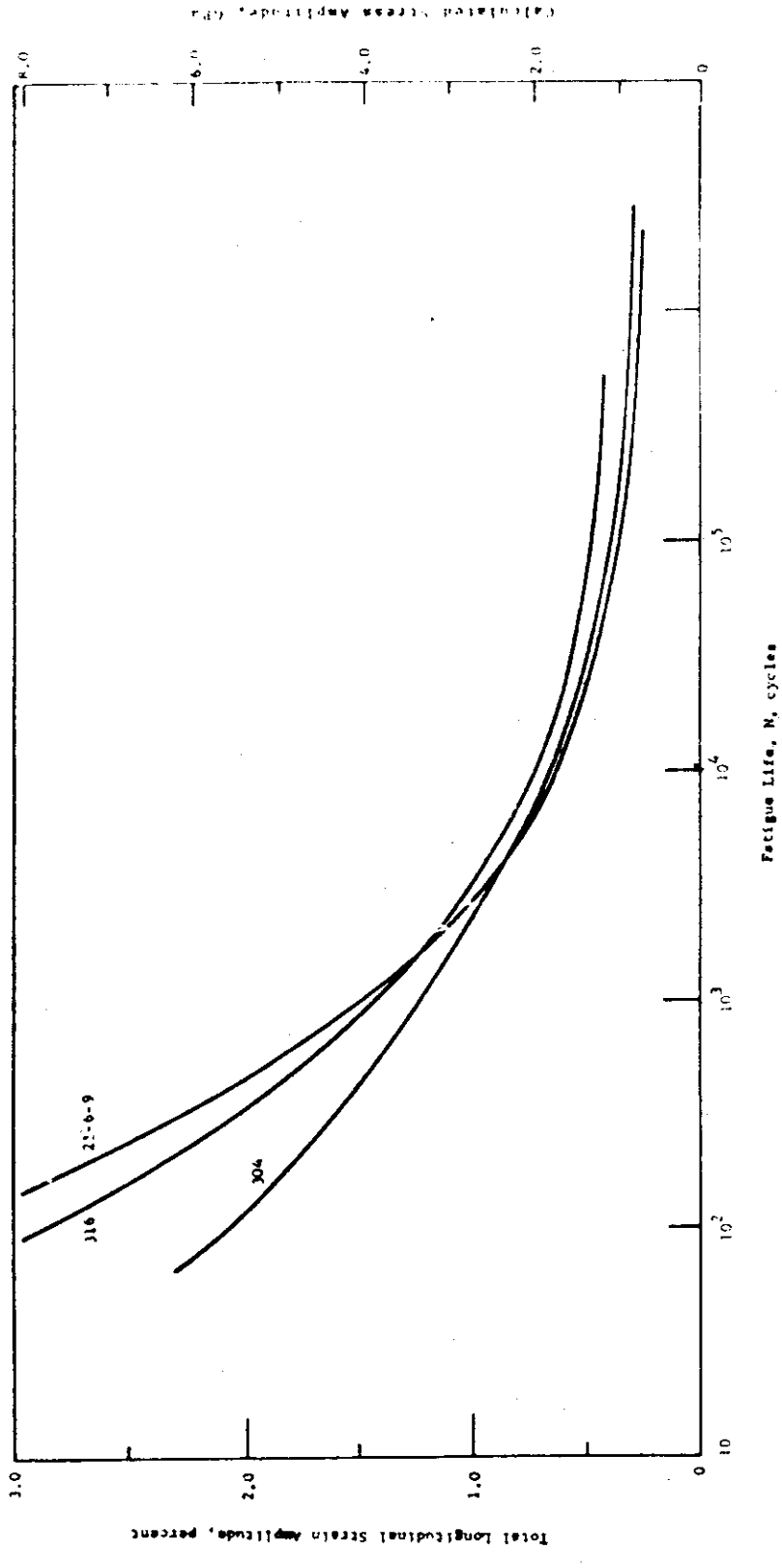

Figure 21 Comparison of Fatigue Behavior at 293 K

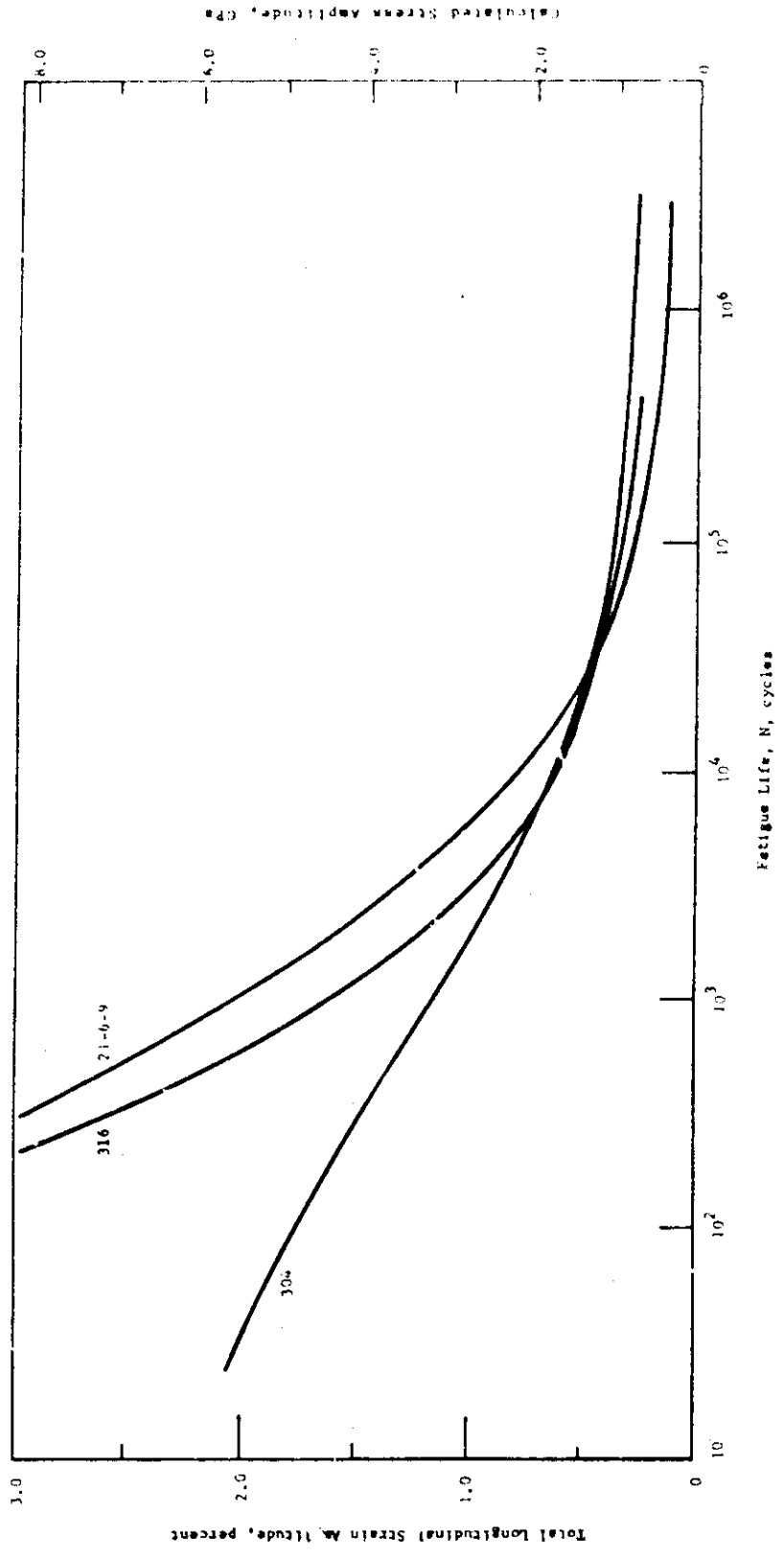

Figure 22 Comparison of Fatigue Behavior at 77 K

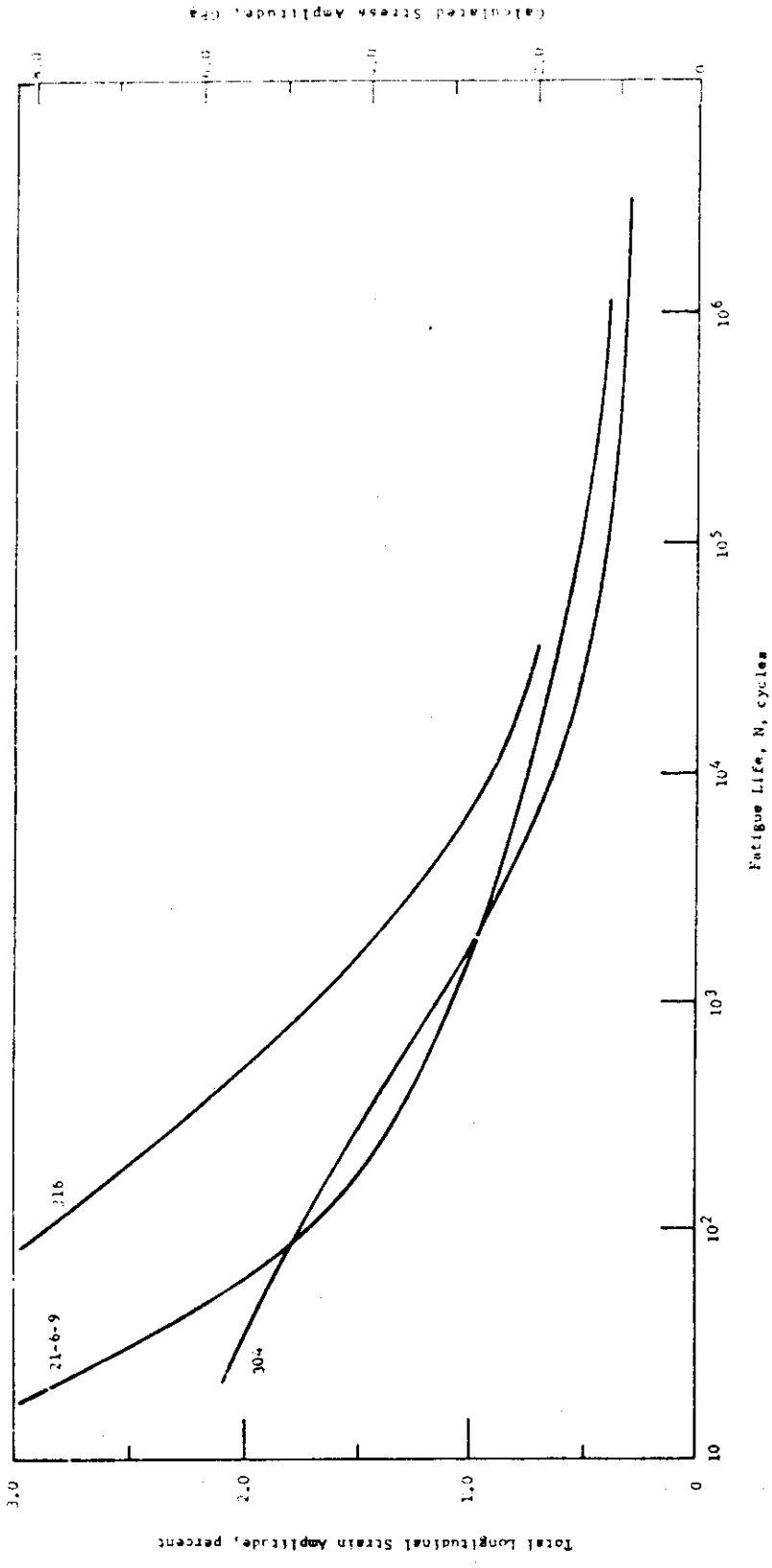

Figure 23 Comparison of Fatigue Behavior at 4 K

2.1.1.3 Fracture Mechanics

2.1.1.3.1 Fracture Toughness

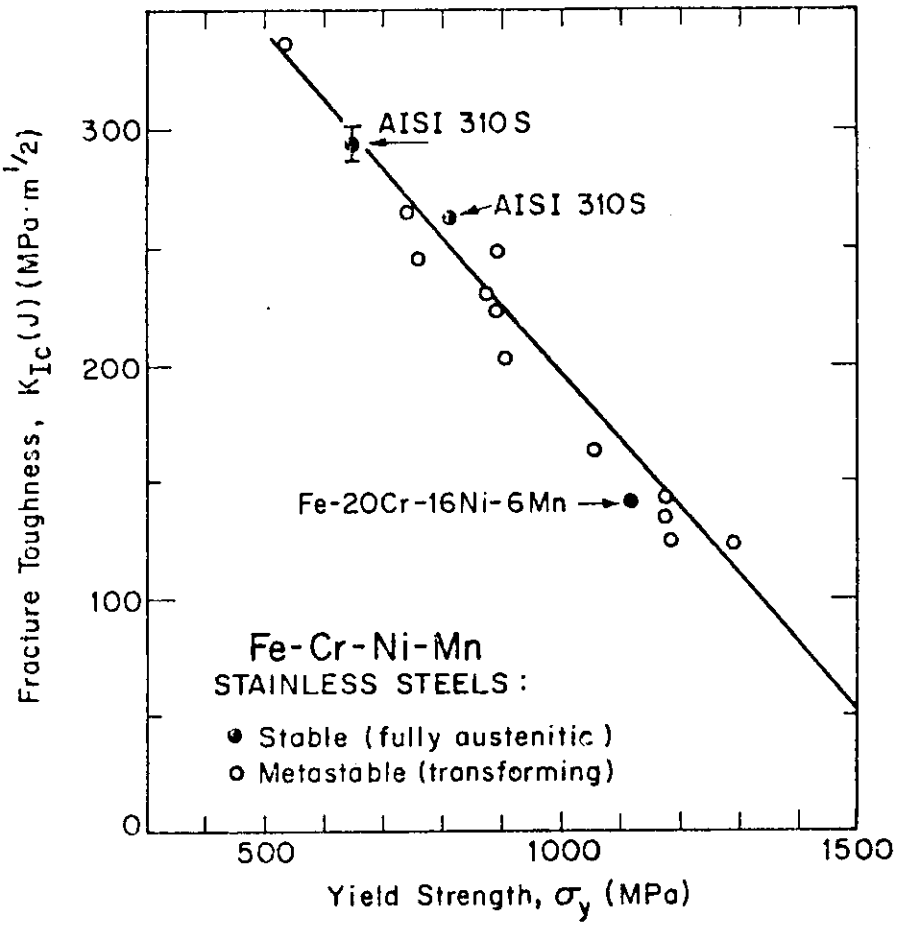

Figure 24 Fracture toughness versus tensile yield strength for many austenitic stainless steels, all measured at 4 K.

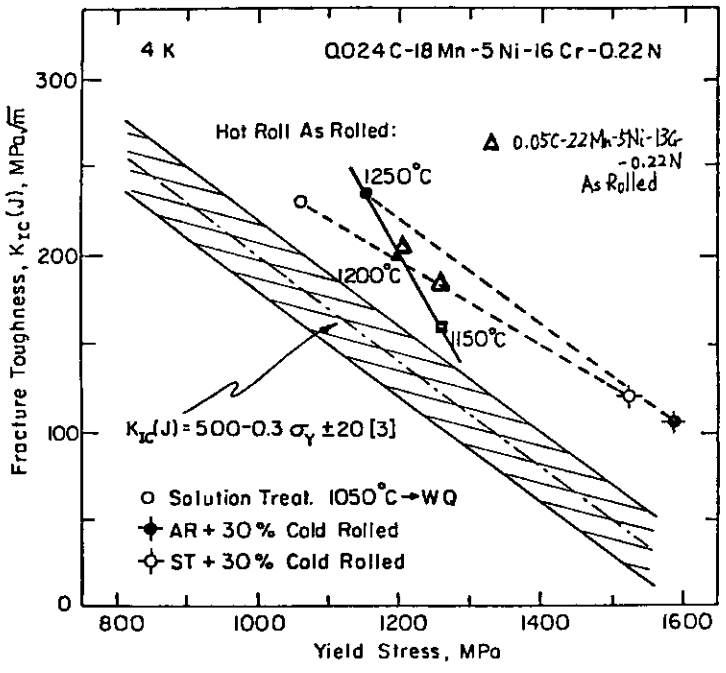

Fig. 25 Fracture toughness versus tensile yield strength

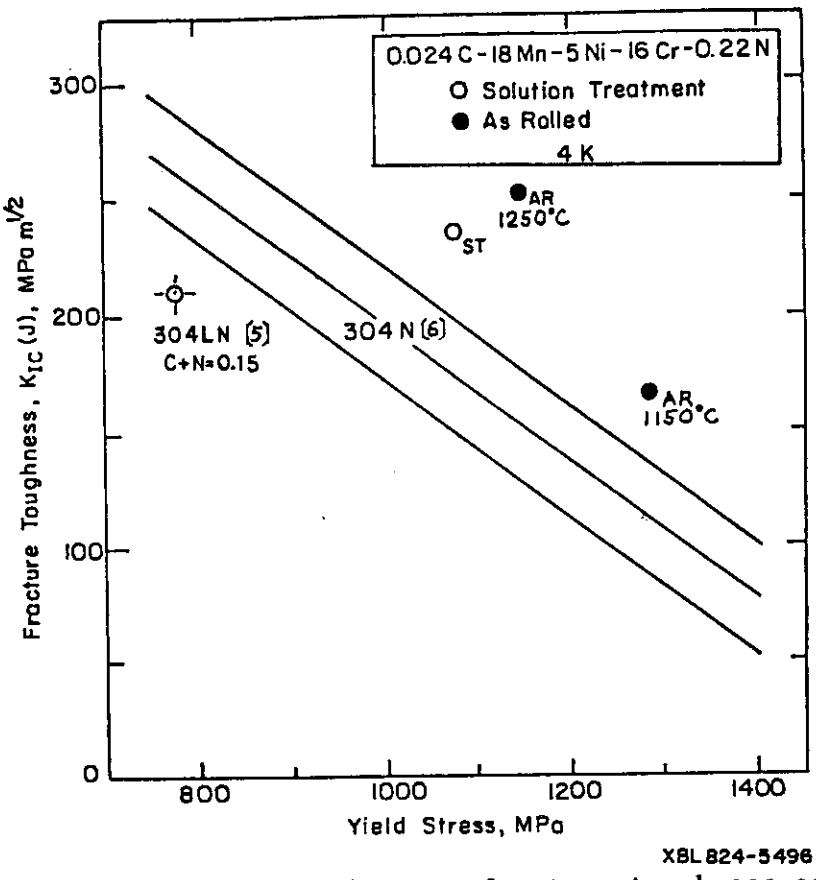

Figure 26 Relationship between fracture toughness and yield stress of the alloy at 4K.

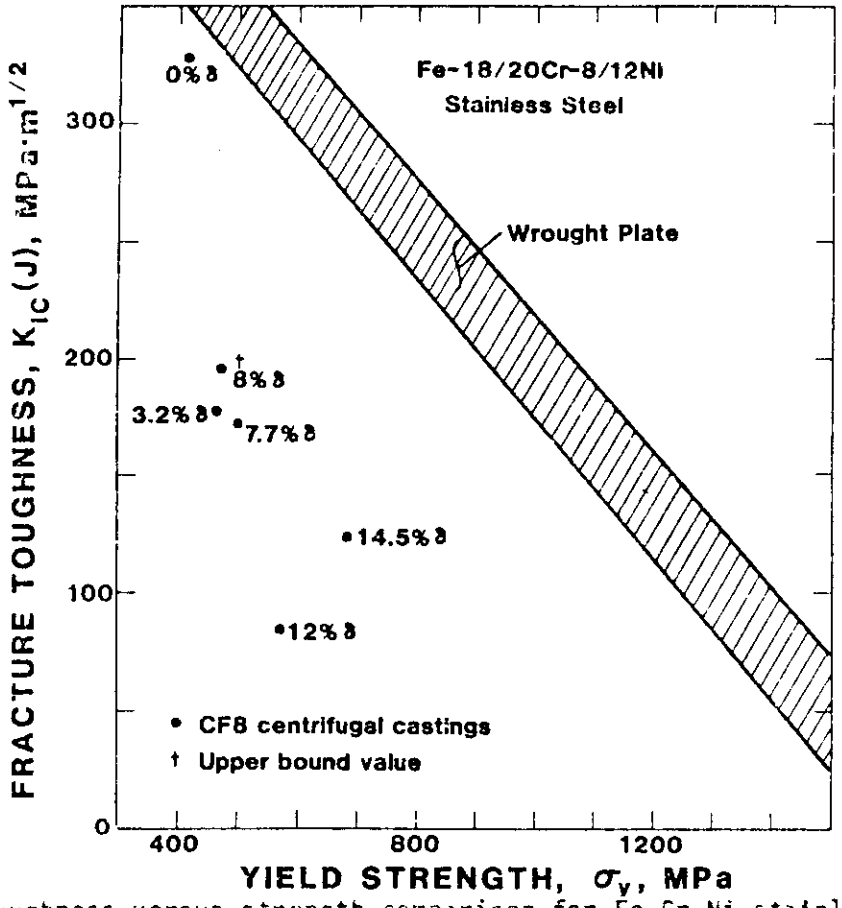

Figure 27 Toughness-versus-strength comparison for Fe-Cr-Ni stainless steels in wrought and cast forms at 4K.

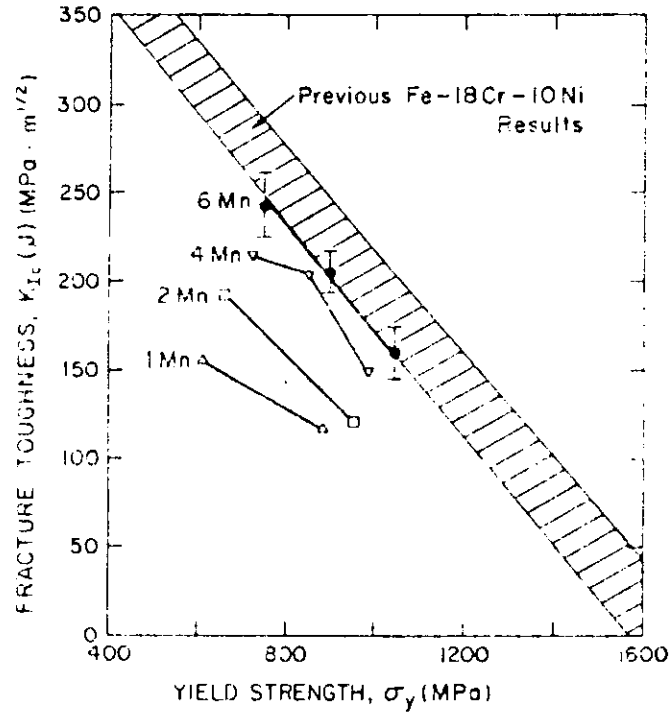

Fig.28 Fracture toughness-vs-yield strength results for Mn-N modified steels of the present study, as compared with previous results for AISI 304 type stainless steels.

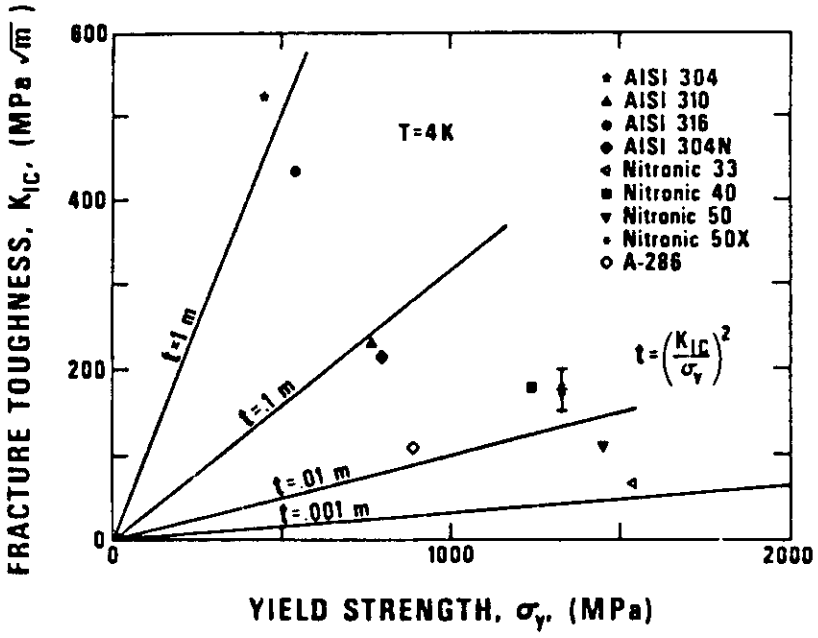

Figure 29 .Fracture toughness plotted against yielo strength at 4 K for conventional and nitrogen-strengthened austenitic stainless steels.

2.1.1.3.2 Curve of crack growth rate versus stress intensity factor (ΔK) including the ΔK threshold values

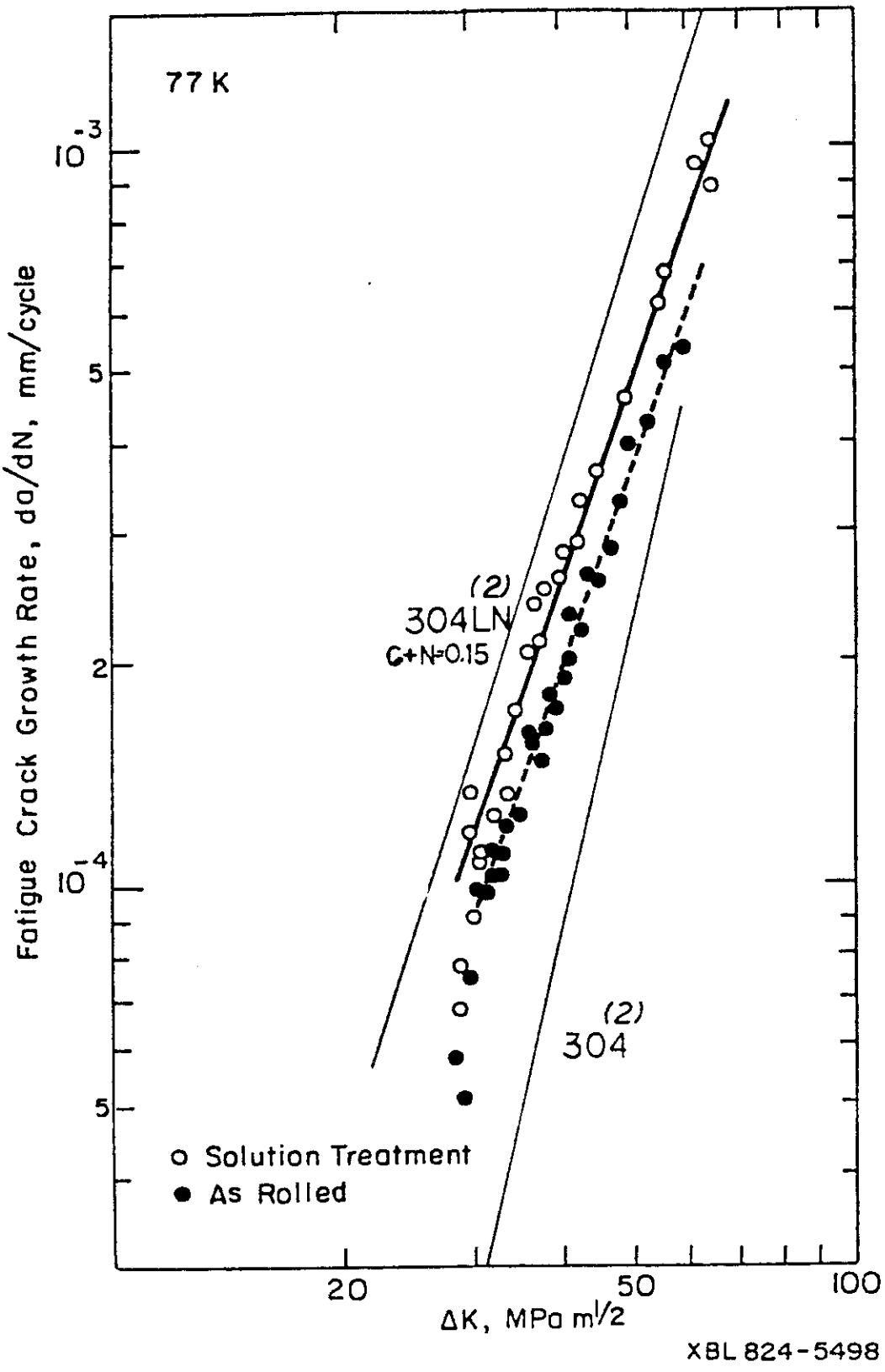

Figure 30 **Fatigue crack growth rates as a function of stress intensity range for 18Mn-5Ni-16Cr-0.01C-0.22N alloy at 77K.**

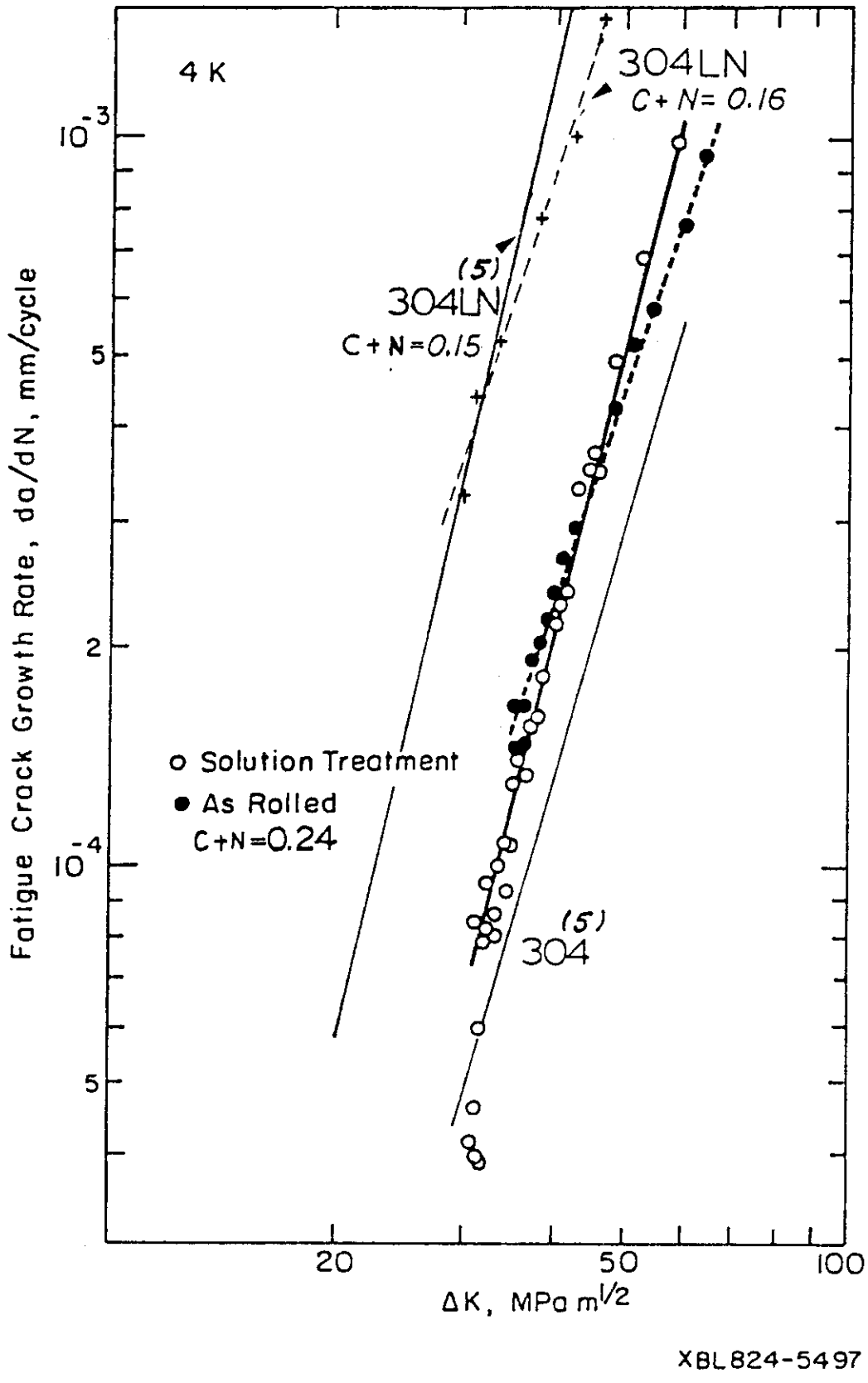

Figure 31 Fatigue crack growth rate of 0.024C-18Mn-5Ni-16Cr-0.22N alloy.

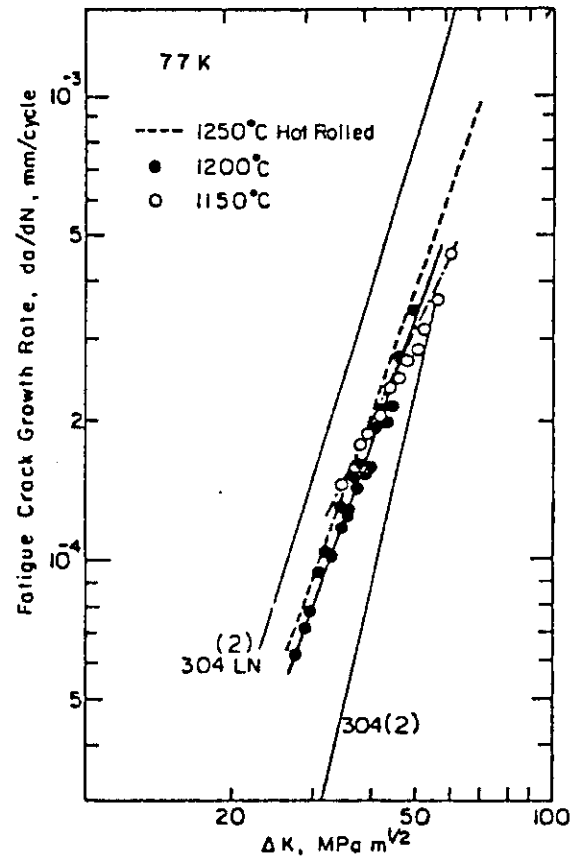

Fig. 32 The effect of hot-rolling conditions on the fatigue crack growth rates at 77k.

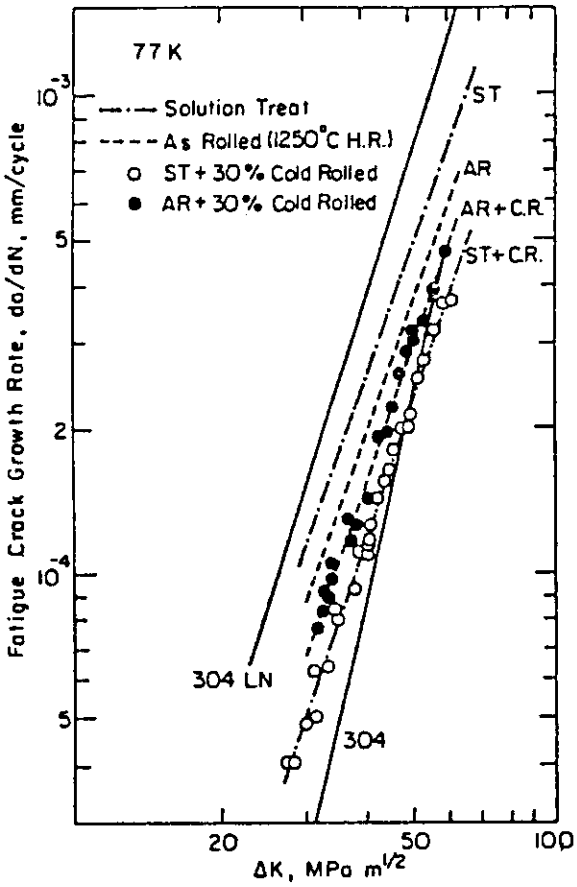

Fig. 33 The effect of cold rolling on the fatigue crack growth rates at 77K.

2.1.3 Radiation Effects

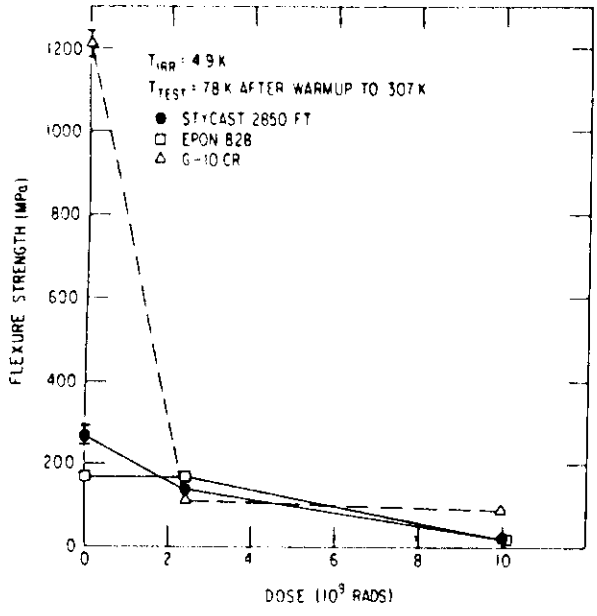

Fig. 34 Flexure strength in epoxies after irradiation at 4.9 K and warm-up to 307 K

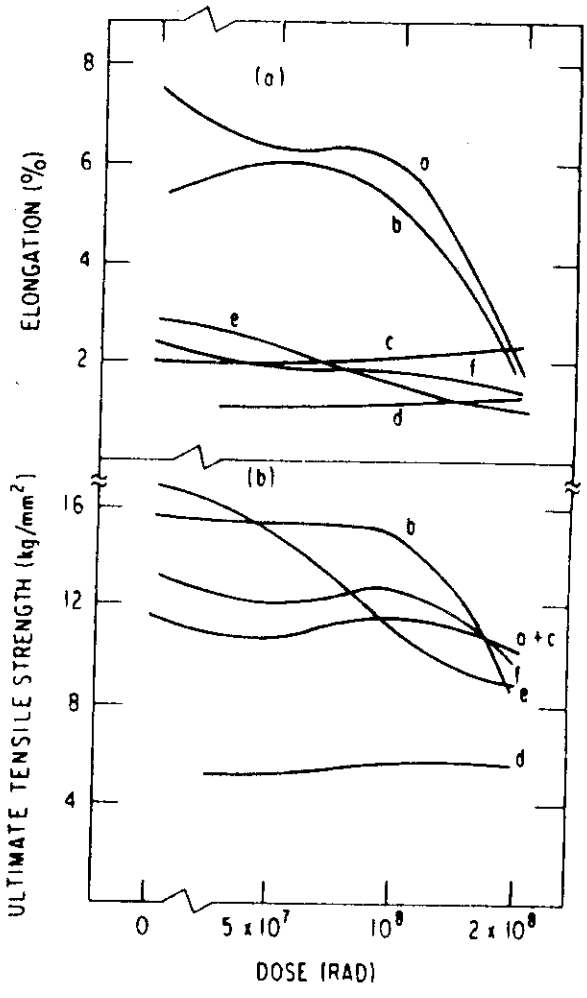

a PTFE
b POLYCARBONATE
c PVC (HARD)
d POLYSTYRENE
e POLYAMIDE
f POLYETHYLENE

Fig. 35 Mechanical properties of various insulators after irradiation at 77 K

Table 9 Structure of composites

No.	Composite forms	Component materials (Weight content in %) Reinforcements	Matrix resins
1	Epoxy pre-impregnated mica paper tape	Muscovite mica paper (54) E glass cloth (10)	Phenol novolac epoxy (36)
2	Epoxy pre-impregnated glass cloth tape	E glass cloth (53)	Phenol novolac epoxy (47)
3	Epoxy pre-impregnated polyamide paper sheet	Polyamide paper (45) E glass paper (10)	Phenol novolac epoxy (45)
4	Epoxy pre-coated polyimide film tape	Polyimide film (85)	Phenol novolac epoxy (15)
5	Epoxy coated & spread glass cloth tape	E glass cloth (48)	Phenol novolac epoxy (42) Bisphenol epoxy (10)
6	Epoxy glass cloth laminates	E glass cloth (68) Silica powder (5)	Bisphenol epoxy (27)
7	Epoxy glass cloth laminates	E glass cloth (70)	Cycloaliphatic epoxy (30)
8	ISOX resin glass cloth laminates	E glass cloth (60)	ISOX resin (40)
9	Unsaturated polyester glass cloth laminates	E glass cloth (46)	Unsaturated polyester (54)
10	Unsaturated polyester impregnated PET felt	Polyester felt (50)	Unsaturated polyester (50)

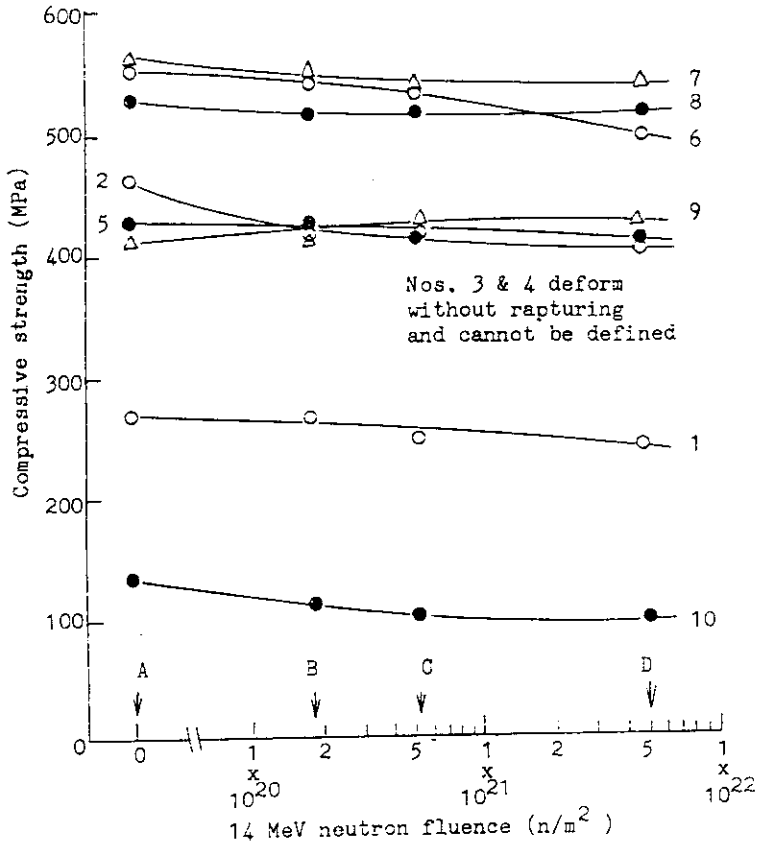

Fig. 36 Effects of 14 MeV neutron irradiation on compressive strength (edgewise)

Ref. T.Iida, et., al. EIM-83-128 Denki gakkai, 1983.

Table 10 Structure of composites (group T)

No.	Composite forms	Component materials (Weight content in %) Reinforcements		Matrix resins	
1	Epoxy glass cloth laminates (I)	E glass cloth	(59)	Aromatic-amine hardened bisphenol epoxy	(41)
2	Epoxy glass cloth laminates (II)	E glass cloth	(65)	Anhydride hardened bisphenol epoxy	(35)
3	Epoxy glass cloth laminates (III)	E glass cloth	(71)	Aromatic-amine hardened bisphenol epoxy	(29)
4	Unsaturated polyester glass cloth laminates	E glass cloth	(56)	Unsaturated polyester	(44)
5	Epoxy carbon cloth laminates	Carbon cloth	(68)	Aromatic-amine hardened phenol novolac epoxy	(32)

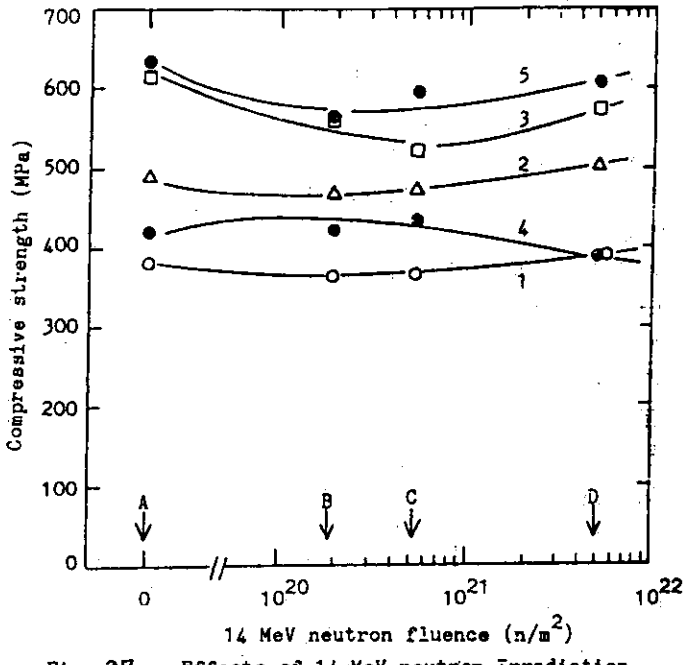

Fig. 37 Effects of 14 MeV neutron Irradiation on compressive strength (edgewise) (group T)

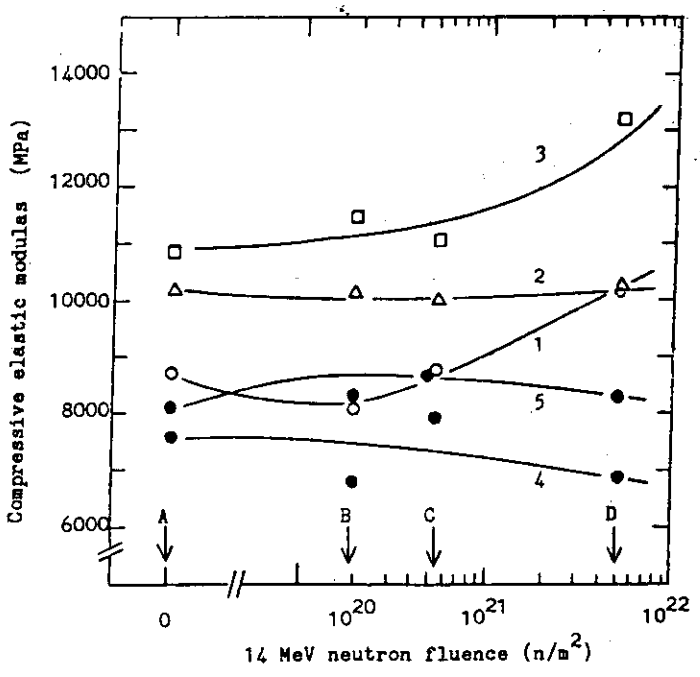

Fig. 38 Effects of 14 MeV neutron irradiation on compressive elastic modulas (edgewise) (group T)

2.2 Conductor

2.2.6 Radiation Effects

2.2.6.1 Effect on critical current characteristics

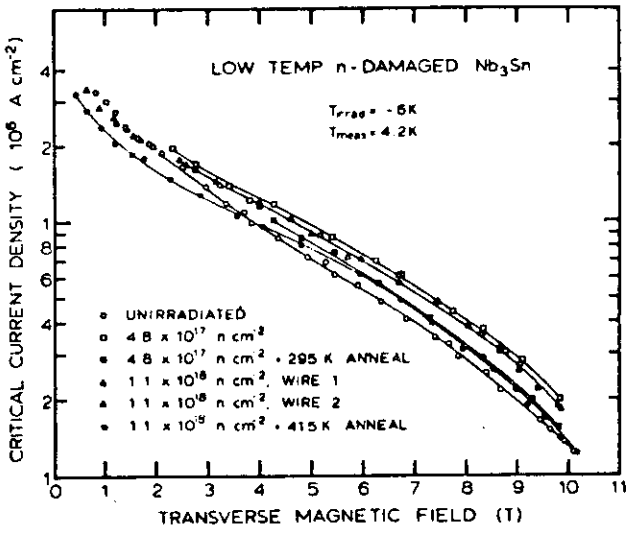

Fig.39 Relation between critical current density of Nb_3Sn and transverse magnetic field after fast-neutron irradiations at 6K. (Colucci et.,al)

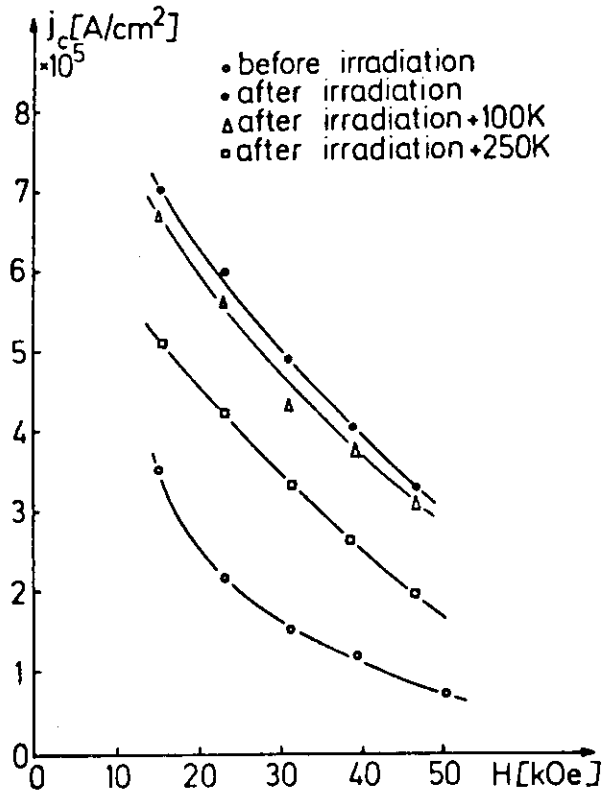

Fig.40 Relation between critical current density of Nb_3Sn and magnetic field after fast-neutron irradiation at 11° K. (Soell et.,al)

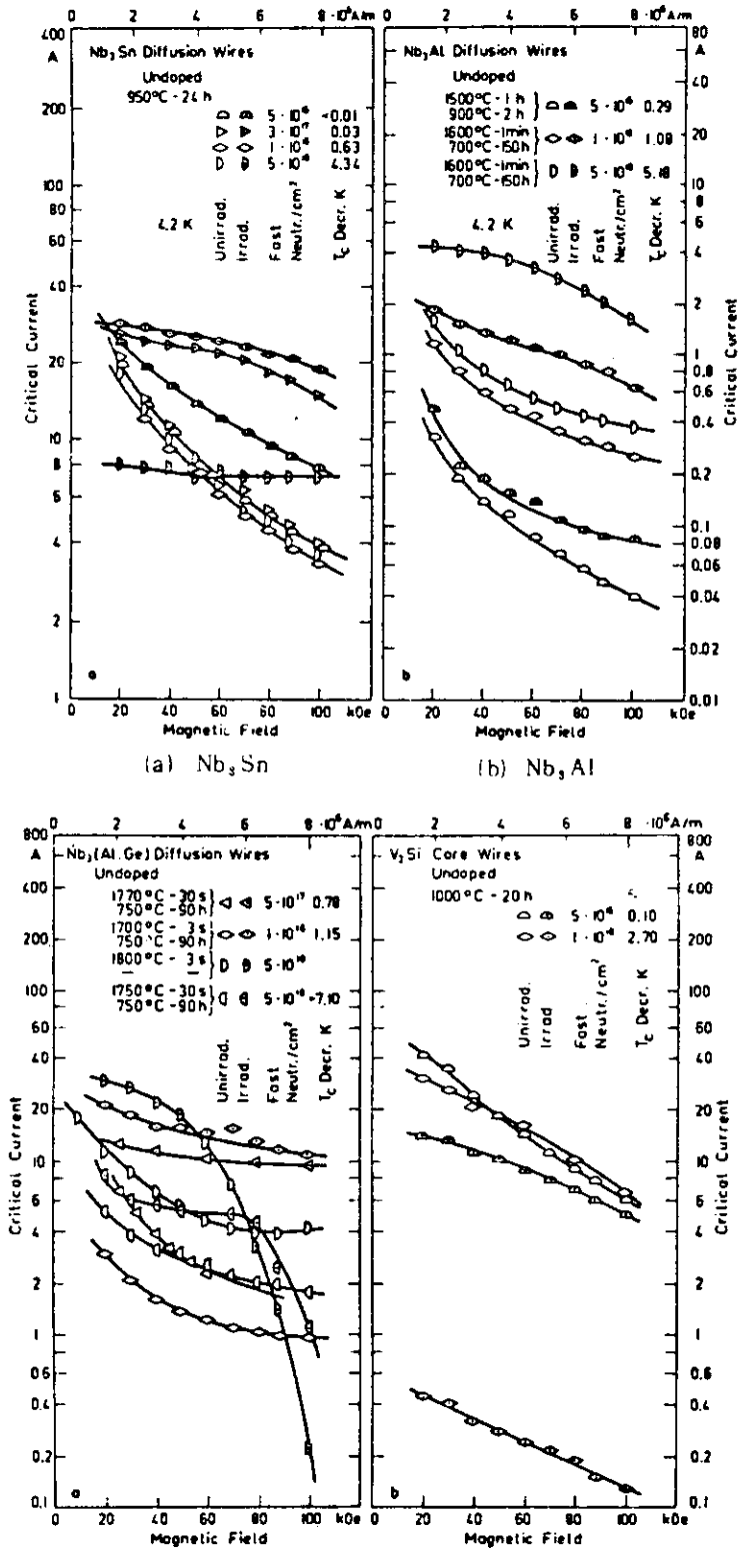

Fig.41 Relation between critical current and magnetic field after fast-neutron irradiation at 80°C. (Bauer et.al)

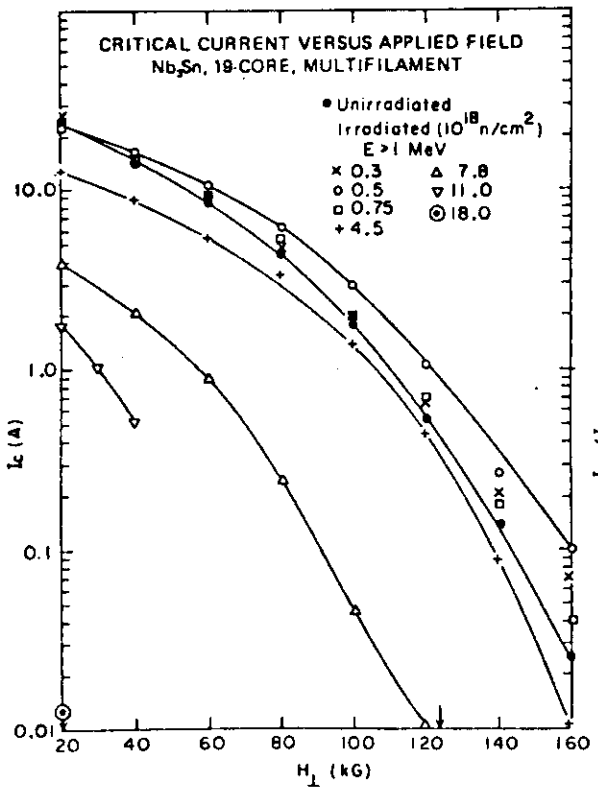

Fig.42 Critical current of multifilament Nb_3Sn versus magnetic field after fast-neutron irradiation. (Snead et.,al)

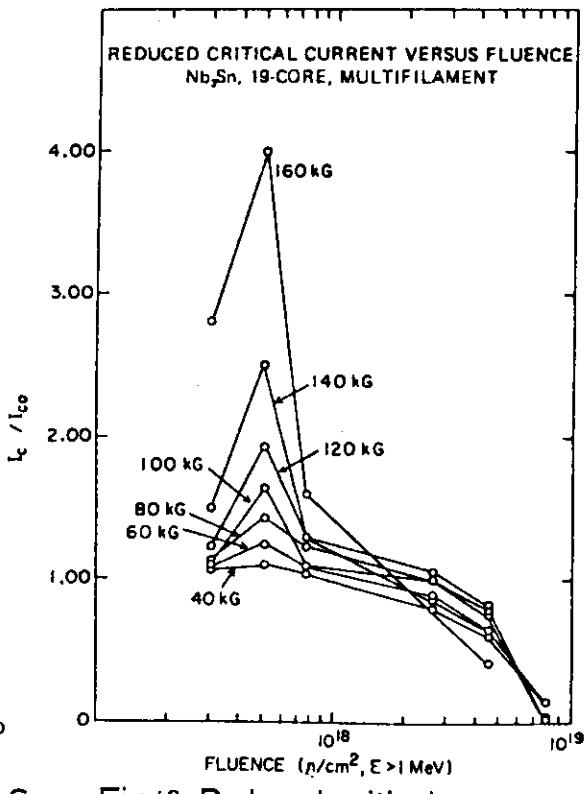

Fig.43 Reduced critical current versus Fluence (Snead et.,al)

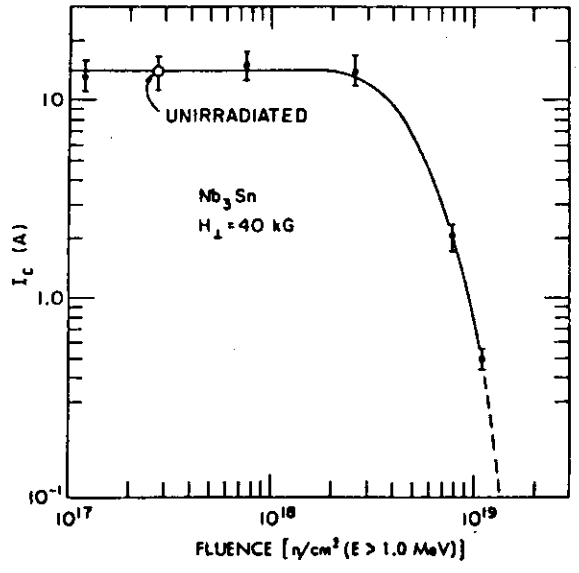

Fig.44 Critical current density of multifilament Nb_3Sn as a function of fast-neutron fluence (Parkin et.,al)

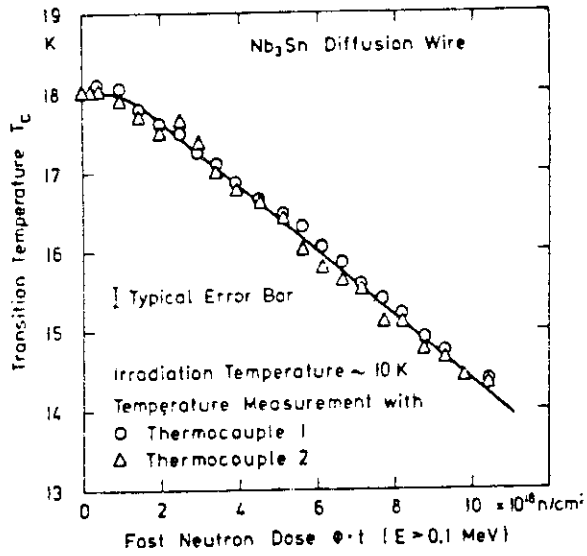

Fig.45 Transition temperature Tc change in Nb_3Sn during fast-neutron irradiation at 10K. (Soell et.,al)

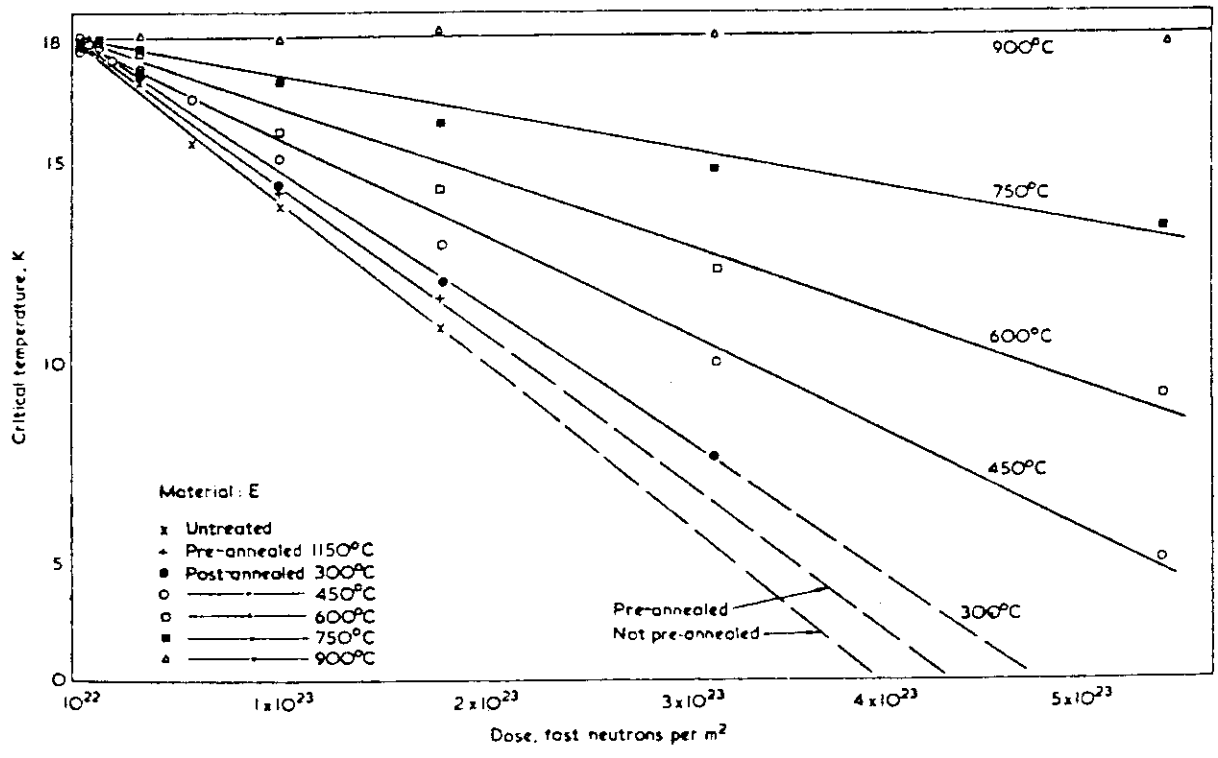

Fig 46 Relations between Tc in Nb_3Sn and fast-neutron dose, and Tc change after two hour annealing. (Bett et.,al)

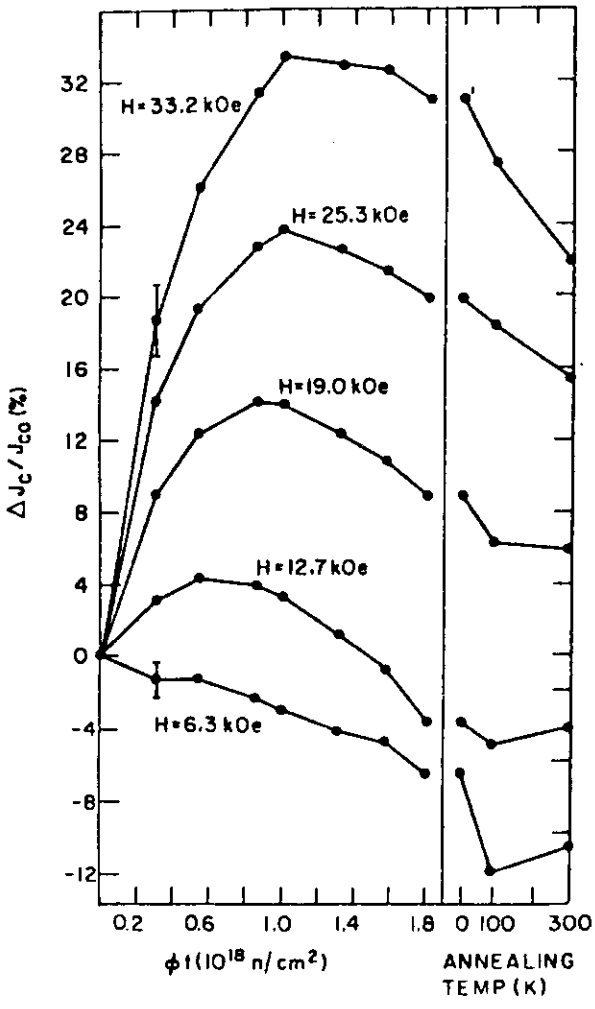

Fig.47 Relation between $\Delta Jc/Jco(\%)$ in Nb_3Sn and magnetic field after fast-neutron irradiation at 6K. (Brown et.,al)

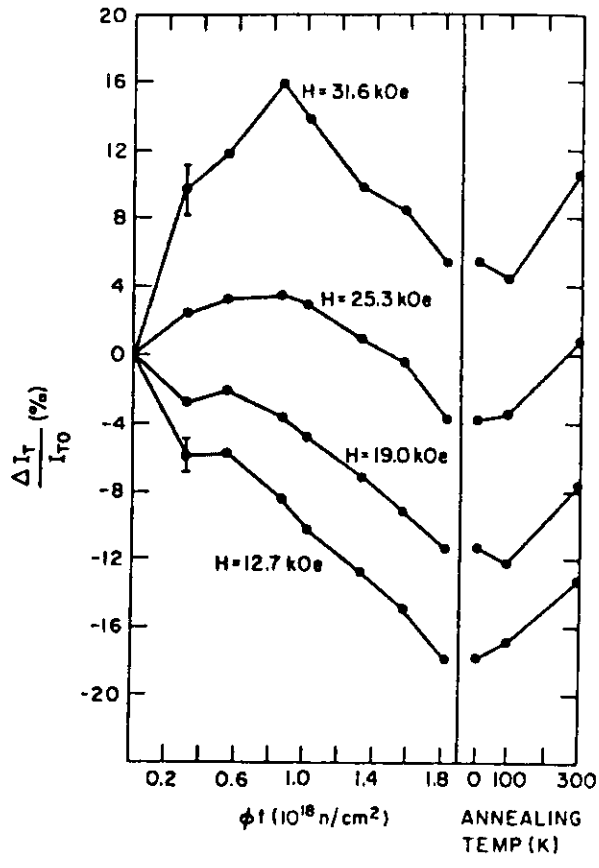

Fig.48 Relation between $\Delta I_T/I_{TO}$ in Nb_3Sn and magnetic field. (Brown et.,al)

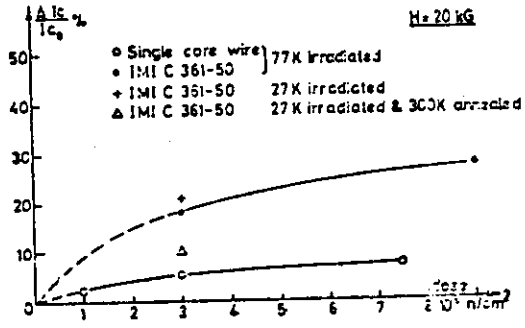

Fig.49 Relation between △Ic/Ico in NbTi and fast-newtron dose with 20KG magnetic field.
(Couach et.,al)

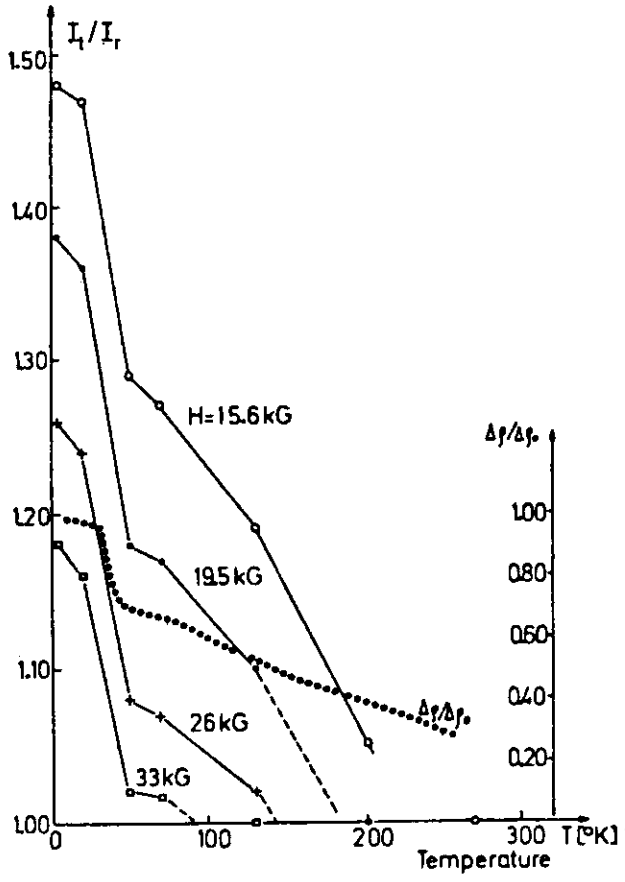

Fig.50 Annealing effect for It/Ir of copper coated NbTi multifilament.
(Soell et.,al)

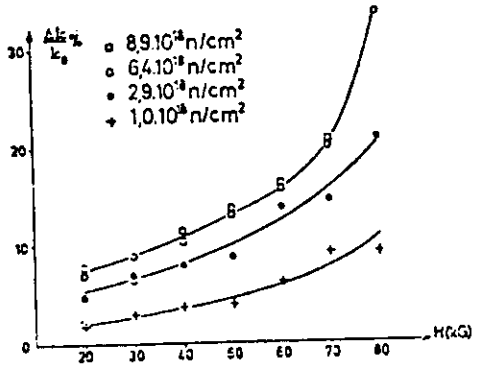

Fig.51 Relation between △Ic/Ico of single filament of NbTi and magnetic field after fast-neutron irradiation.
(Couach et.,al)

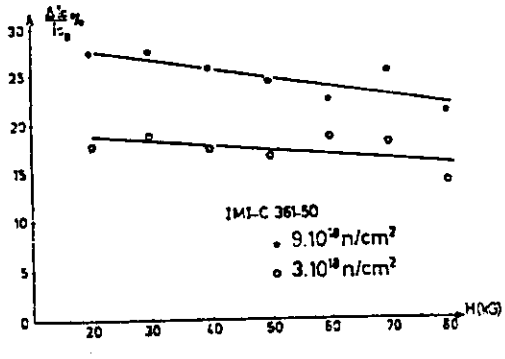

Fig.52 Relation between △Ic/Ico in NbTi after fast-neutron irradiation.
(Couach et.,al)

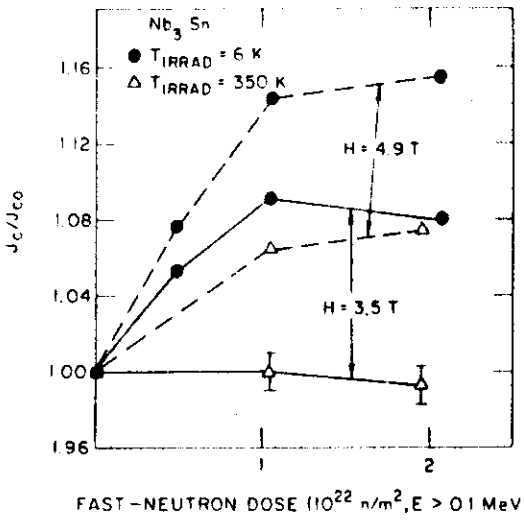

Fig.53 Fractional J_c change in Nb_3Sn with high J_{c0} during fast-neutron irradiation at 6 and 350 K (ref. [14]).

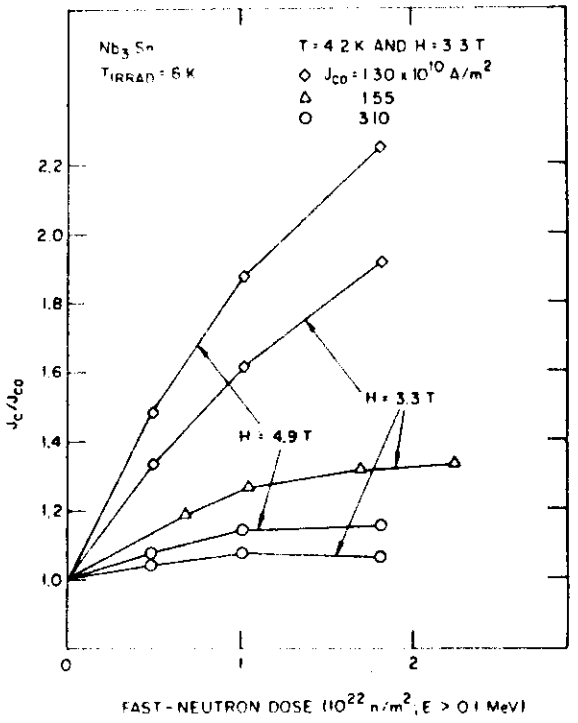

Fig.54 Fractional J_c change for materials with various J_{c0} values during fast-neutron irradiation at 6 K (ref. [14]).

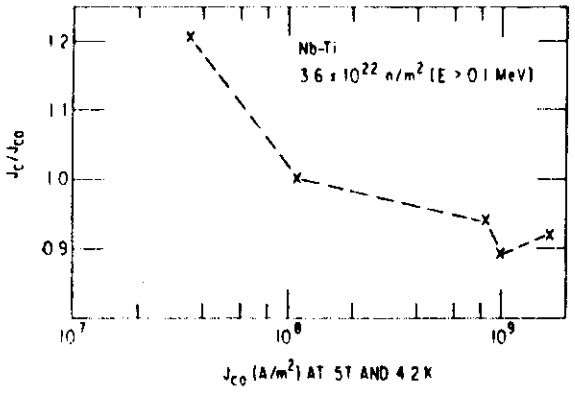

Fig.55 Fractional change in critical current density J_c in various samples of Nb Ti as a function of the preirradiation J_c value, J_{c0}, after fast-neutron irradiation at 5 K (ref. [8]).

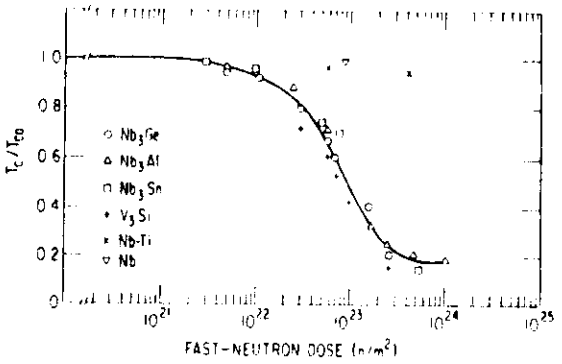

Fig.56 Fractional change in critical temperature for various superconductors after neutron irradiation at ~370 K (ref. [13]).

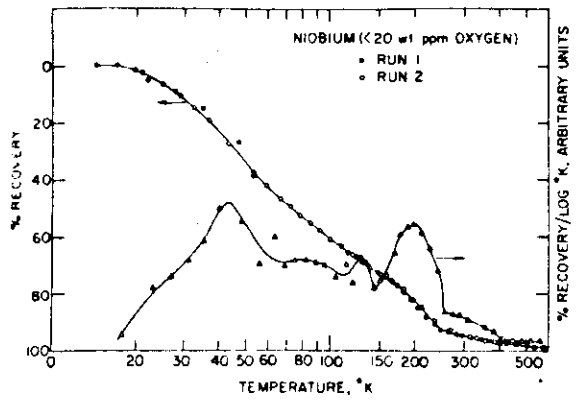

Fig. 57 Recovery and differential recovery versus logarithm of absolute temperature for niobium (< 20 wt ppm oxygen).

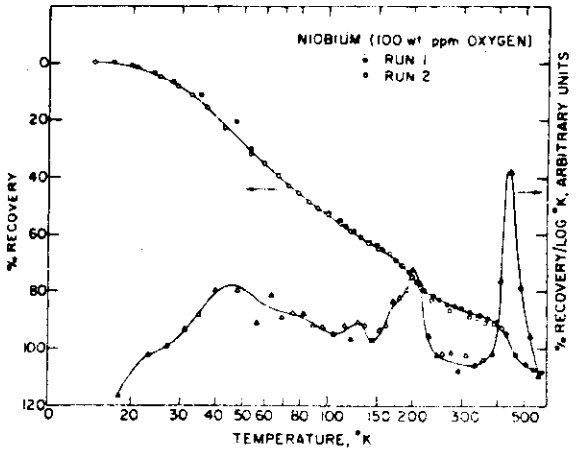

Fig. 58 Recovery and differential recovery versus logarithm of absolute temperature for niobium (100 wt ppm oxygen).

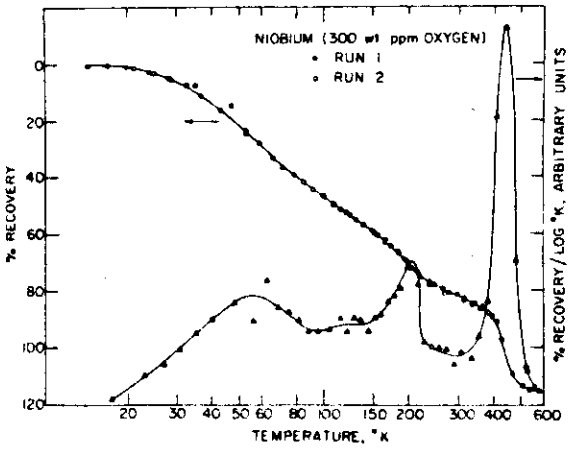

Fig. 59 Recovery and differential recovery versus logarithm of absolute temperature for niobium (300 wt ppm oxygen).

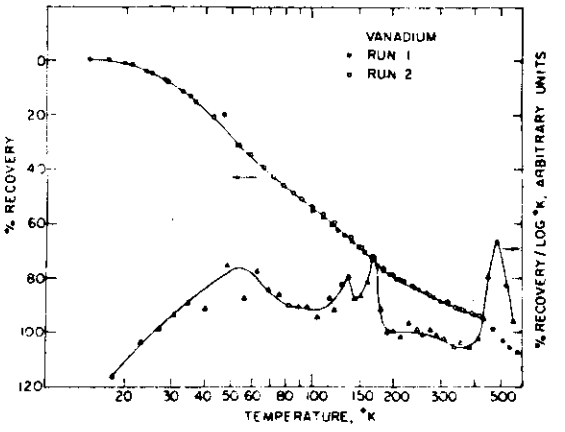

Fig. 60 Recovery and differential recovery versus logarithm of absolute temperature for vanadium.

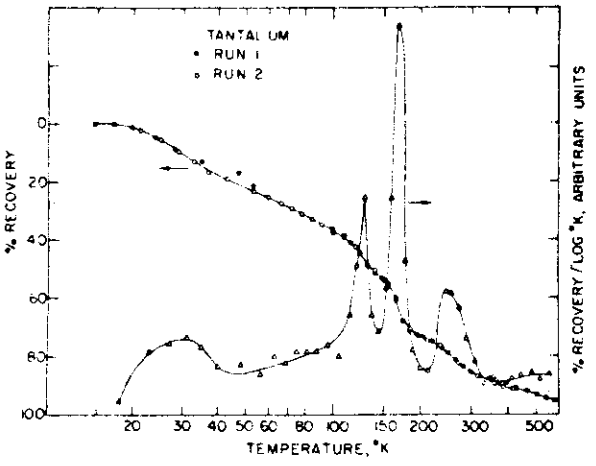

Fig 61 Recovery and differential recovery versus logarithm of absolute temperature for tantalum.

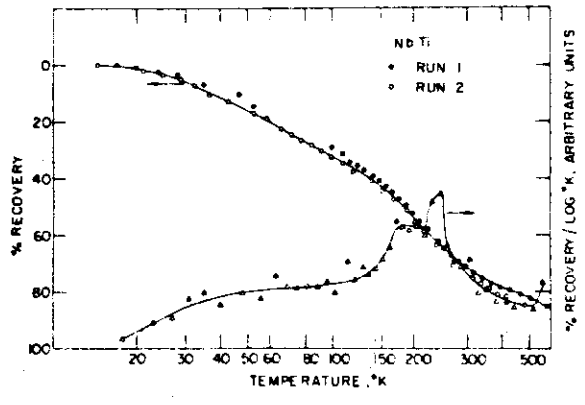

Fig. 62 Recovery and differential recovery versus logarithm of absolute temperature for Nb–48 wt % Ti.

2.2.6.2 Effects on electrical properties of Cu and Al

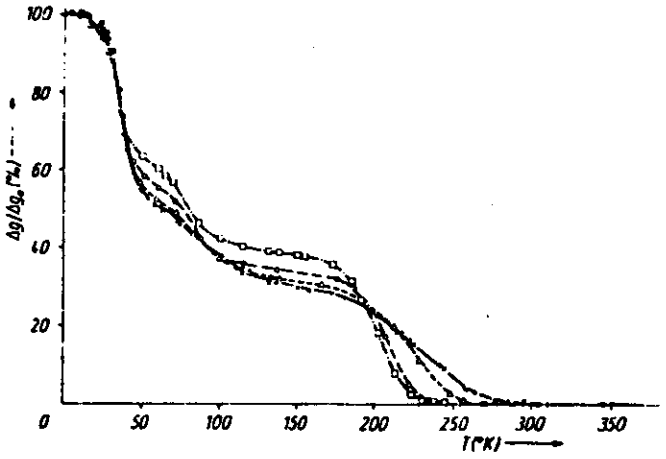

aluminium				
	irradiation dose	annealing time 1 min	3 min	$\Delta\rho_0$
+	1.017 MWh	< 120 °K	> 120 °K	0.00745 μΩcm
×	1.00 MWh	< 100 °K	> 100 °K	0.00750 μΩcm
△	18.00 MWh	all values	—	0.0806 μΩcm
○	49.70 MWh	< 130 °K	> 130 °K	0.305 μΩcm
□	110.80 MWh	—	all values	0.524 μΩcm

Fig.63 Recovery of electrical resistivity in Alminum after fast-neutron irradiation at 4.5K. (Burger t., l)

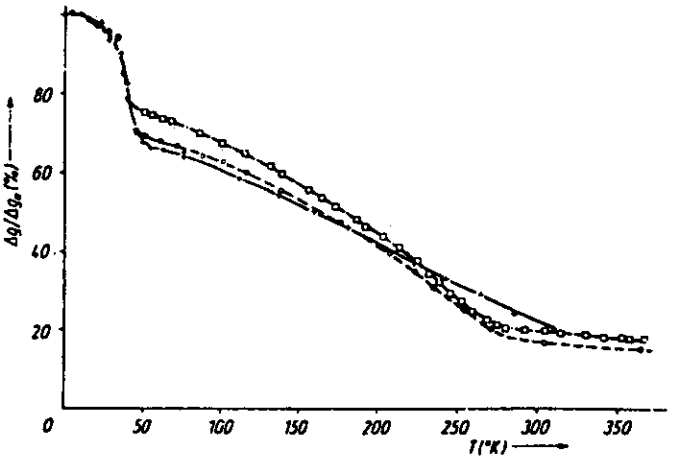

copper				
	irradiation dose	annealing time 1 min	3 min	$\Delta\rho_0$
+	1.017 MWh	< 140 °K	> 140 °K	0.00238 μΩcm
○	49.7 MWh	< 130 °K	> 130 °K	0.09433 μΩcm
□	110.8 MWh	—	all values	0.17083 μΩcm

Fig.64 Recovery of electrical resistivity in copper after fast-neutron irradiation at 4.5°K (Burger et.,al)

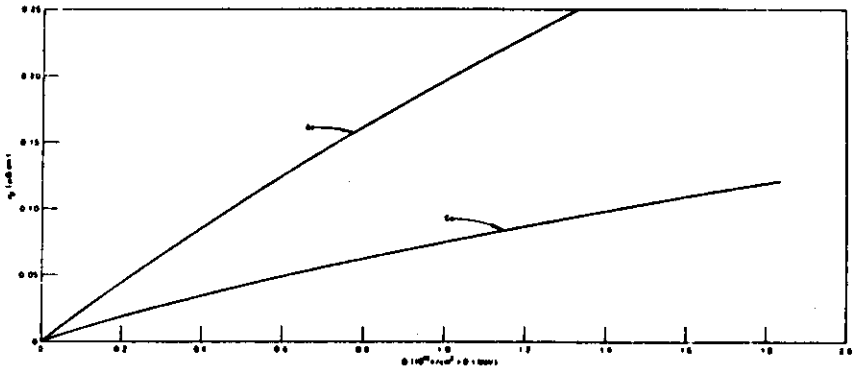

Fig.65 Relation between the resistivity in Al and Cu and fast-neutron irradiation at 4.9K. (Blewitt)

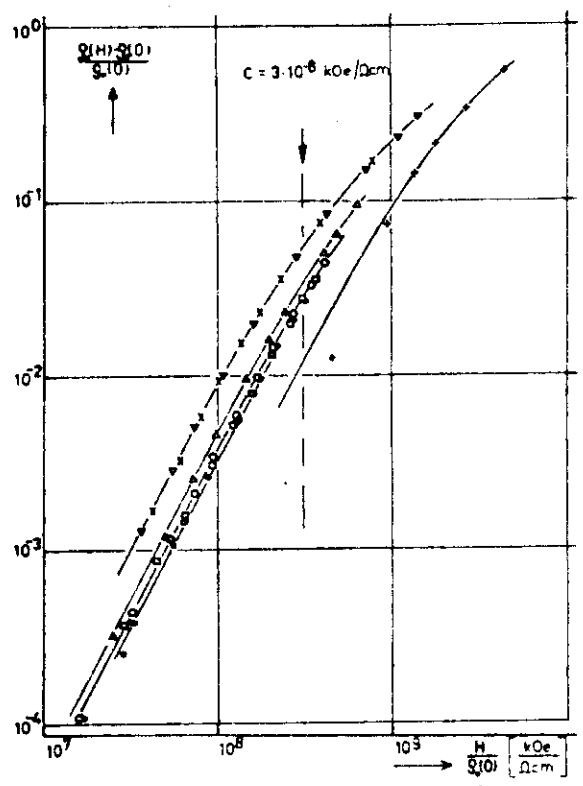

Fig. 66 Relation between magnetoresist in copper and magnetic field.
× before irradiation
● after irradiation
Another is after annealing. (Boning et., al)

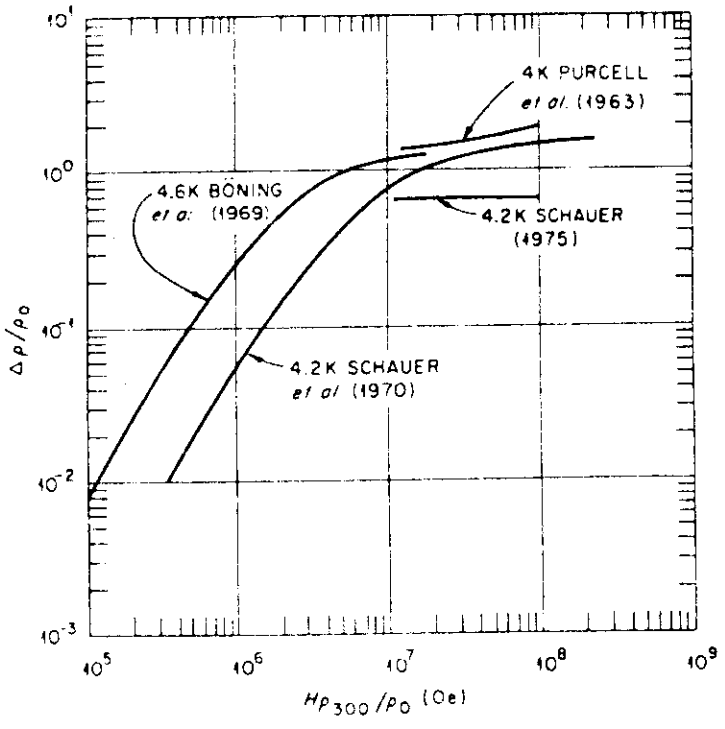

Fig 67 Relation between magnetoresist in Al and magnetic field.
$\Delta\rho = \rho_0(H) - \rho_0(0)$ (Guess et., al)

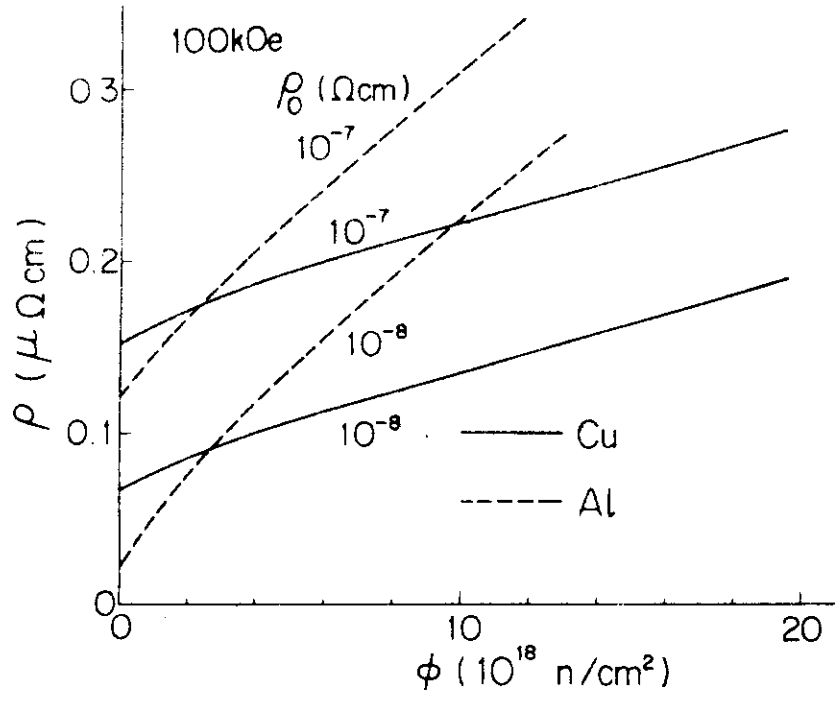

Fig.68 Resistivity change with fast-neutron irradiation at 4.2 K under 100KG magnetic field.

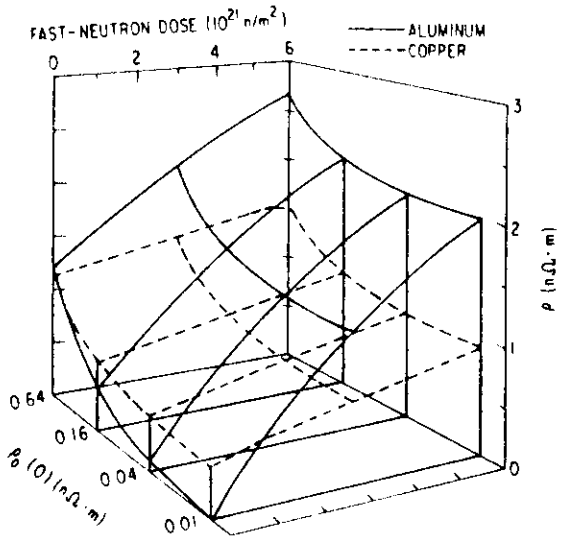

Fig. 69 Typical change in total resistivity ρ in Al and Cu at H = 10T for different initial values of resistivity ρ_0 under various irradiation conditions. (ref. [22]).

2. Impact of Short Channel Divertor

Task 1. Determine the impact on the design of incorporating a divertor channel configuration with less vertical build.

K. Kitamura

T. Uchida

K. Shinya

1. Short channel divertor reactor concept

1.1. Introduction

The impact of the reactor concept with short channel divertor on engineering design features is studied to realize the compact reactor system. The structure of this reactor system is illustrated in Fig. 1.1.1. This reactor system has the following features. Figure 1.1.2 shows the radial build of short channel divertor concept.

(1) The bore of the toroidal filed (TF) coil is 6.6 m width × 0.9 m in height. Number of TF coils amounts to 12. The cross section of the TF coil helium vessel is 0.9 m × 1.25 m.

(2) All superconducting poloidal field (PF) coils are located outside of the TF coils. The distance between the plasma center and the TF coil center is 500 mm. Location and ampere turns of the PF coils for short channel divertor concept are employed according to the reduction of the TF coil height.

1.2 Design conditions

The design study of short channel divertor concept is performed with the following conditions.

(1) As vacuum boundary, combined typs is adopted.

(2) Vacuum boundary wall is installed in shielding structure.

(3) Weight of torus structures is supported by exhaust duct located the bottom of reactor structure.

(4) Both divertor plates and blanket structure are radially retracted with single straight motion.

(5) As divertor plates, the structure for short channel studied in group A is employed.

(6) The coil has the same cross sectional dimension as that studied in Phase IIa Part I.

1.3 Torus segmentation

The reduction of TF coil vertical size does not permit the blanket replacement by 1 segment/TF coil. The blank should be segmented as 2 ∿ 3 sectors/ TF coil. In order to avoid problems for the vertical plasma stability due to the excessive segmentation, the concept of 2 sectors/TF coils is adopted here.
The TF coil bore is 6.6m × 9.0m which is reduced by 0.3m in vertical direction in comparison with that of Phase IIa Part I (6.6m × 9.3m).
The blanket structure between TF coils are of equal toroidal span. Each blanket sector which is supported with outer shield structure is connected by flange with semi-permanent shield-post in order to form the torus configuration.
In this concept, each access port serves two blanket sectors which can be removed one after another.
The retraction of the first blanket sector is carried out by single straight line motion, the retraction of the second one is carried by two straight line motions.

1.4 Divertor segmentation

Short channel divertor as shown in Fig. 1.4.1 is installed at considerably inboard and upper position in comparison with that in INTOR universal concept.

Divertor configuration and segmentation should be considered from the view points of both the strength of shielding structure in which the divertor sectors are supported and the coverage of the divertor plate.

The studies for the segmentation and sector retraction of the divertor plate is conducted as follows.

(1) Segmentation as one sector per TF coil

The segmentation of divertor structure is shown in Fig. 1.4.1. In this case, blanket structure, in particular, outboard supporting structure of the blanket indicated with hatching lines in the figure, does not have enough strength for reduction of supporting space. Therefore, adoption of segmentation as one sector per TF coil is unsuitable.

(2) Segmentation as 2 sectors per TF coil

The segmentation of divertor structure is shown in Fig. 1.4.3. The divertor is segmented as 2 sectors/TF coil and each sector is retracted one after another by single straight line motion.

Table 1.4.1 summarizes the characteristics of reactor structure for short channel divertor concept.

1.5 Toroidal field coil and poloidal field coil

The examinations on several impacts to the magnet design of the short channel divertor reactor concept are carried out.

The discussion is mainly forcused on the following five principle points.

(a) PF coil location and ampere turn

(b) Out-of-plane force of TF coil

(c) AC loss in TF coil

(d) AC loss in PF coil

(e) Capacity of PF power supply

The bore size of TF coil, of which number is 12, is set to be 6.6m × 9.0m. The dimension and the major characteristics of TF coil are shown in Fig. 1.5.1 and Table 1.5.1, respectively. TF coil provides the maximum field of 11.7T on the inner surface of the coil and the magnetic ripple of 1.07% at the plasma outer edge.

The toroidal field distribution on a mid-plane is indicated in Fig. 1.5.2.

(1) PF coil location and ampere turn

The location and ampere turn of the PF coil are arranged according to the reduction of the TF coil height. The PF coils are located at the outside of the TF coils, and their total number is 18 (8 inner solenoid coils and 10 outer ring coils).

The location of PF coils is illustrated in Fig. 1.5.3, and Table 1.5.7 shows the ampere turns of the coils.

(2) Out-of-plane force of TF coil

The out-of-plane force acting on TF coil are calculated in corresponding to these location and ampere turn of the PF coil, and the in-plane force of the TF coil also obtained because of the reduction of the TF coil bore. Figures 1.5.4 and 1.5.5 shows these electromagnetic force distributions along the TF coil perimeter.

The maximum local out-of-plane pressures, f_{max}, act on the TF coil side plate at the lower nose region. And these pressures occur the local bending stress in the side plate. The moment around vertical axis, M_Z, is supported mainly by the bending stiffness of the outer TF coil legs.

These values, f_{max} and M_Z, are estimated to be 29.8 MN/m and ±242 MN·m, respectively.

(3) AC losses in TF coils

AC losses in TF coils during normal operation

The AC loss is caused by the changing poloidal field mainly at the superconductor, the helium vessel and the coil support in the TF coils.

(i) AC loss in the superconductors

The configuration of the superconductor in the TF coil of the all-remote operation concept is same as that of the personel access concept.

Figure 1.5.6 shows the conductor structures and Table 1.5.3 indicates their characteristics.

In the superconductor the AC losses are composed of the hysteresis loss, the eddy current loss and the coupling loss, as listed in Table 1.5.4. The coupling loss is the largest for the adopted conductor configuration such as the large matrix area. The CuNi fins are inserted in the matrix to cut the coupling current. The time averaged loss can be calculated from Table 1.5.4 as follows,

Pav = 40.1 kW

(ii) AC loss in TF coil helim vessels

Since the helium vessel is required to withstand against the electromagnetic force, th; material should be thick stainless steel. The changing poloidal field generates the eddy current loss in the vessel. The models for the estimation of the loss are shown in Fig. 1.5.7. The time averaged loss is

Pav = 41.8 kW

(iii) AC loss in TF coil supports

The TF coil support is placed between TF coils to withstand the electromagnetic out-of-plane forces, and the contact face with the TF coil is covered with insulator to cut the one-turn loop. The eddy current induced by the changing poloidal field generates the loss. The model for the loss calculation is shown in Fig. 1.5.7.

The time averaged loss is

Pav = 36.5 kW

The loss in the supports is dominant compared with other AC losses, since the high field is applied to the support region. Therefore, it is needed that the more insulators should be inserted into the support to reduce the loss. The sum of the AC loss in TF coil is shown in Table 1.5.5.

(4) AC loss in PF coil

AC loss in PF coils during normal operation

The same superconductor structure as the personel access concept is employed, similarly to TF coil.
Figure 1.5.8 shows the conductor configuration and Table 1.5.6 depicts the parameters of the superconductor.
The coil is the source of changing field which holds the plasma in equilibrium, and is subject to the AC loss due to the changing field. The loss occurs in the superconductors, the coil supports and the helium leak shield if unsed, for PF coils.
The loss can be estimated for above components, as follows.

(i) AC loss of PF coil superconductor

The superconductor has been intensively developed to reduce the AC loss. Therefore, the conductors are stranded several times and consist of mixed matrices. The superconductor AC loss is conveniently divided into

three contributions, i.e. the hysteresis loss, the eddy current loss and the coupling loss. The formulae are listed in Table 1.5.7. The losses for each coil are summed up taking account of the field patterns from each coil, and then, they are averaged over the duration.

$$Pav = 2.68 \text{ kW}$$

The coupling loss between bundles is the most dominant for the adopted conductor configuration.

(ii) AC loss of PF coil supports

It is required for PF coil supports that the AC loss should be reduced as small as possible and the supports should endure the electromagnetic forces. First of all, the supports should not electrically close to make a circle around the torus axis, otherwise the loss is vast.

The AC Loss can be estimated from the following equation.

$$p = \frac{t_w}{12\rho} \int \dot{B}^2 d\ell \qquad (W)$$

where, ρ is the resistivity of the support material, and the other nomenclatures are shown in Fig. 1.5.9. The thickness 50 mm needed from the stress analysis, and the magnetic field corresponding to the PF coil current waveforms are inserted into above equation. The losses of each coil are summed up and then,

they are averaged over the duration.

Pav = 9.0 kW

(iii) AC loss in PF coil helium leak shields

The helium leak shield may be needed at the present time, since the helium leakage from the vessel is inevitable as long as the large FRP's are adopted to the vessels. It can consist of metal such as stainless steel to be sealed tightly, and therefore it is expected that the AC loss might be vast due to one turn loop, even though the thickness is as thin as possible. The SS thickness of 0.5 mm is assumed in the following analysis.

The dominant loss may be the induced current loss due to the linkage flux, and obtained as follows,

$$p = \frac{\dot{\phi}^2}{R} \qquad (W)$$

where, ϕ is the linkage flux in the shield, R the resistance. The losses for each leak shield are summed up taking account of the field patterns, and they are averaged over the duration.

Pav = 40.1 kW

The shield loss is inacceptably large comparing with the other AC losses in superconductors and coil supports. Therefore, it is necessary to develop the way to seal the FRP vessel through non-metalic materic. The sum of the AC loss in PF coil is shown in Table 1.5.8.

(5) Power supply

The power supply capacity for the PF coils is approximately in proporation to the MG peak power for the PF coils.
The MG peak power for the PF coils of the short channel divertor concept is estimated to be 1.8GW.

Table 1.5.9 summarizes the other studied results concerning magnet system of the short channel divertor concept.

Table 1.4.1 Characteristics of reactors structure for short channel divertor concept

	Short channel divertor
TF coil bore	6.6mW × 9.0mH
*	(28.74m)
Ripple of TFC	1.07
Height of replacement structure	6.45m
Segmentation of blanket	2 sectors/TFC
Segmentation of divertor	2 sectors/TFC
Blanket retraction	Single straight motion for first sector 2 straight motions for second sector
Divertor retraction	Single straight motion
Size of cryostat	ϕ25m × 20 mH

Note: * ( ) showes length of toroidal coil along a center of conductor.

Table 1.5.1 Major characteristics of the TF magnet system

1.	Total ampere-turns	143 MAT
2.	No. of coils	12
3.	Ampere-turns per coil	11.9 MAT
4.	Plasma major radius	5.2 m
5.	Field at plasma axis	5.5 T
6.	Helium condition	Pool boiling
7.	Grading concept	3 grades (12, 10, 5^T)
8.	Winding configuration	Flat wound in pancakes
9.	Superconductor	Copper stabilized Nb$_3$Sn and NbTi
10.	No. of turns per coil	540
11.	No. of pies per coil	22
12.	Operation current	22.07 kA
13.	Critical current	33 kA
14.	Avg. winding current density	19.4 A/mm^2
15.	Maximum field	11.7 T
16.	Cooling spacer thickness	3.0 mm
17.	Cooling surface	Rough surface (mechanical and chemical treatment)
18.	Inductance	∿120 H
19.	Magnetic field energy	∿28.7 GJ

Table 1.5.2 Coordinate and ampere-turns of PF coils for short channel divertor concept

Coil No.	Black No.	Coil Location		Time (sec)						
		R(m)	Z(m)	0	0.2	5	11	211	226	246
1	1	1.35	0.50	5.430	4.325	-3,424	-4.636	-5.993	0	5.430
2	2	1.35	1.50	5.495	4.384	-3.408	-4.661	-6.034	0	5.495
3	3	1.35	2.50	5.283	4.184	-3.467	-4.587	-5.908	0	5.283
4	4	1.35	3.50	6.525	5.698	1.302	-2.768	-4.400	0	6.525
5	5	1.70	4.80	5.578	5.003	1.245	-2.234	-3.629	0	5.578
6	6	3.00	6.00	2.031	2.203	4.475	0.681	0.173	0	2.031
7	7	4.50	6.20	0.509	0.872	3.685	2.717	2.590	0	0.509
8	8	7.40	6.00	0.378	-0.125	-3.992	1.068	0.974	0	0.378
9	9	11.00	4.20	0.309	0.410	1.314	-4.597	-4.675	0	0.309
10	10	1.35	-0.50	5.430	4.325	-3.424	-4.636	-5.993	0	5.430
11	11	1.35	-1.50	5.495	4.385	-3.407	-4.660	-6.033	0	5.495
12	12	1.35	-2.50	5.283	4.185	-3.466	-4.586	-5.907	0	5.283
13	13	1.35	-3.50	6.527	5.831	1.433	-2.638	-4.270	0	6.527
14	14	1.70	-4.80	5.580	4.988	1.229	-2.251	-3.646	0	5.580
15	15	3.00	-6.00	2.031	3.221	13.153	12.428	11.921	0	2.031
16	16	4.50	-6.20	0.508	2.104	14.852	14.788	14.661	0	0.508
17	17	7.40	-6.00	0.353	-0.468	-6.973	-3.278	-3.366	0	0.553
18	18	11.10	-4.70	0.370	-0.609	-8.246	-12.570	-12.662	0	0.370
Plasma		5.30	0.50	0.000	0.600	5.400	6.400	6.400	0	0.000

Unit: MAT

Table 1.5.3 Characteristics of the superconductor

		12^T conductor	10^T conductor	5^T conductor
1.	Superconducting wire	Copper stabilized Nb_3Sn	Copper stabilizee Nb_3Sn	Copper stabilized NbTi
2.	Maximum field	11^T	10.2^T	4.9^T
3.	Conductor current	22.07 kA	22.07 kA	22.07 kA
4.	Ic at 4.2 k	33 kA	33 kA	33 kA
5.	Conductor size	30×39 mm^2	21×39 mm^2	16×39 mm^2
6.	Element size	35×42 mm^2	26×42 mm^2	21×42 mm^2
7.	Cable size	8×18.4 mm^2	8×10.2 mm^2	3.6×9.3 mm^2
8.	Conductor current density	18.8 A/mm^2	26.9 A/mm^2	35.4 A/mm^2
9.	Element current density	15.0 A/mm^2	20.2 A/mm^2	25.0 A/mm^2
10.	Conductor copper ratio	15.5	18.2	42.5
11.	Interturn reinforcement	5 mm	5 mm	5 mm
12.	$\rho 0$	6.2×10^{-8} Ωcm	5.6×10^{-8} Ωcm	3.4×10^{-8} Ωcm
13.	$\Delta\rho$ (1.1×10^{18} n/cm^2)	9×10^{-8} Ωcm	5.3×10^{-8} Ωcm	0.6×10^{-8} Ωcm
14.	ρt	15.2×10^{-8} Ωcm	10.9×10^{-8} Ωcm	3.9×10^{-8} Ωcm
15.	Heat flux	0.39 w/cm^2	0.47 w/cm^2	0.24 w/cm^2
16.	No. of strands	9	5	11
17.	Cooling surface	Rough surface (mechanical and chemical treatment)		
18.	Minimum winding radius	2.21 m	2.32 m	2.63 m
19.	Maximum winding strain	0.18%	0.17%	0.06%

Table 1.5.4 AC loss formulae in TF coil superconductor

1. Hysteresis loss

$$Ph_{\perp} = \frac{2}{3\pi} Jc(B)\dot{dB}_{\perp} \qquad (w/m^3)$$

$$Ph_{\parallel} = \frac{1}{6} Jc(B)\dot{dB}_{\parallel} \qquad (w/m^3)$$

2. Eddy current loss

$$Pe_{\perp} = \frac{1}{12\rho} a^3 b \dot{B}_{\perp}^2 \qquad (w/m)$$

$$Pe_{\parallel} = \frac{1}{2\pi^2\rho} \frac{a^3b^3}{a^2+b^2} \dot{B}_{\parallel}^2 \qquad (w/m)$$

3. Coupling loss

$$Pc_{\perp} = \frac{1}{\rho_{\perp}} \left(\frac{\ell P}{2\pi}\right)^2 \dot{B}_{\perp}^2 \qquad (w/m^3)$$

where,

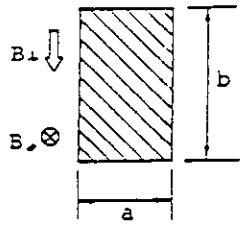

Cross section and field direction

Jc(B): critical current density

d : filament diameter

ρ : matrix resistivity

ρ : transverse resistivity

ℓP: twist pitch

Table 1.5.5 AC losses in TF coil with short channel divertor

Superconductors	40.1 kW
Helium Vessel	41.8 kW
Coil Supports	36.5 kW
Sum	118.4 kW

Table 1.5.6 Parameters of superconductor

1.	Final Level	
	(1) Operating current	53.8 kA
	(2) Critical current	85 kA
	(3) Cable size	130mm × 18mm
	(4) Number of subcables	31
	(5) Mandrel core size	115mm × 4mm
	(6) Cable twist pitch	1300 mm
	(7) Effective perimeter	520 mm
	(8) Conductor current density	23 A/mm^2
	(9) Winding current density	14 A/mm^2
	(10) Maximum field	7.1^T
2.	Subcable	
	(1) Subcable diameter	8 mm
	(2) Number of strands	6
	(3) Core strand material	Stainless steel
	(4) Twist pitch	50 mm
3.	Strand	
	(1) Strand diameter	2.67 mm
	(2) Number of NbTi filaments	6156
	(3) Twist pitch	40 mm
	(4) Surface treatment	Formval
	(5) Number of bundless	18
	(6) NbTi : Cu : CuNi	1 : 9.58 : 1.04

Table 1.5.6 Parameters of superconductor (continued)

4. Bundle		
	(1) Bundle diameter	0.338 mm
	(2) Number of filaments	342
	(3) Surface CuNi thickness	11.7μm
	(4) NbTi:Cu:CuNi	1:1.33:1.04
5. Filament		
	(1) NbTi filament diamter	10μm
	(2) OFHC thickness	2.1μm
	(3) Surface CuNi thickness	1μm
	(4) NbTi:Cu:CuNi	1:1.02:0.59

Table 1.5.7 AC loss formulae in PF coil superconductor

1. Hysteresis loss

$$Ph_{\perp} = \frac{2}{3\pi} Jc(B)\dot{dB}_{\perp} \qquad (w/m^3)$$

$$Ph_{\parallel} = \frac{1}{6} Jc(B)\dot{dB}_{\parallel} \qquad (w/m^3)$$

2. Eddy current loss

$$Pe_{\perp} = \frac{1}{4\rho} \dot{B}_{\perp} r_0^2 \qquad (w/m^3)$$

3. Coupling loss

$$Pc_{\perp} = \frac{1}{\rho_{\perp}} \left(\frac{\ell P}{2\pi}\right)^2 \dot{B}_{\perp}^2 \qquad (w/m^3)$$

where,

$Jc(B)$: critical current density

d : filament diameter

$\rho_{\perp}$: matrix resistivity

ρ : transverse resistivity

ℓP: twist pitch

γ_0: strand radius

Table 1.5.8 AC losses in PF coil with short channel divertor

Superconductors	2.7 kW
Coil supports	9.0 kW
(Helium leak shield)	(40.1 kW)
Sum	11.7 kW (51.8 kW)

Table 1.5.9 Summary of studied results for short channel divertor concept

		Short channel divertor
Plasma	Major radius	5.3m
	Minor radius	1.2m
	Plasma elongation	1.5
	Plasma start-up	by RFCD and OH coils
Main characteristics	No. of TFC	12
	Start-up voltage	35V
	Max. ring-coil radius	11.1m
	TFC Perimeter	28.7m
	TF coil bore	6.6 × 9.0m
	Magnetic ripple	1.066%
TF coil	Max. Bt	11.7 T
	Hoop force	1149 MN
	Centering force	-377 MN
	f_{max}	29.8 MN/m
	M_R	145 MN·m
	M_Z	242 MN·m
	AC loss	118 kW
	$\langle \int \dot{B}_{//}^2 d\ell \rangle$	2.96×10^{-2} T^2m/S^2
	$\langle \int \dot{B}L^2 d\ell \rangle$	2.76×10^{-2} T^2m/S^2
	Stored energy	29.2 GT
PF coil	Ampere turn	102 MAT
	Max. field B_{pmax}	7.26 T
	Field change, $\dot{B}_{pmax}$	6.34 T/S
	One-turn voltage	228 V
	AC loss	12 (52) kW
	Energy	6.90 GJ
	MG peak power	1.77 GW

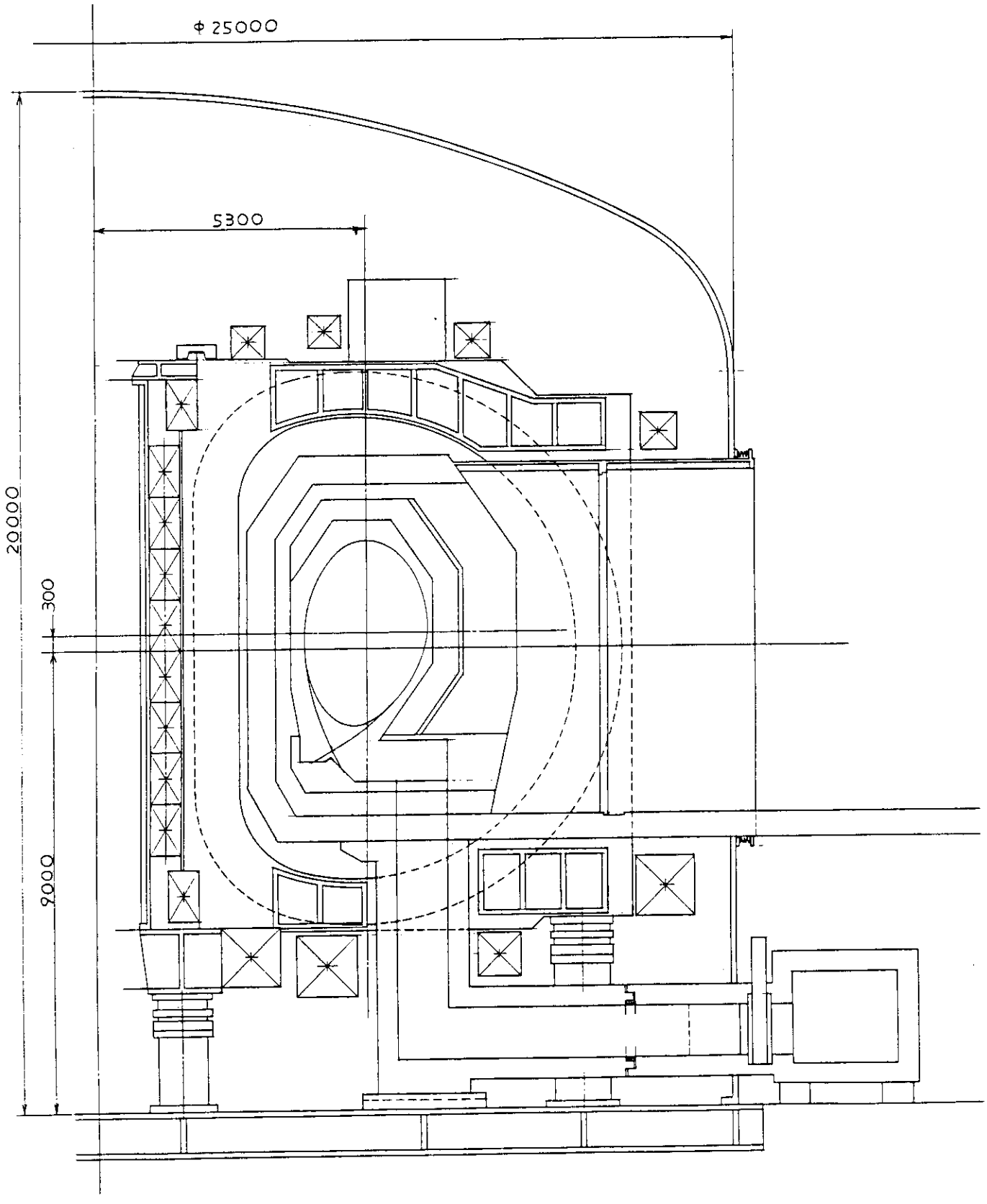

Fig. 1.1.1 Vertical view of short channel divertor concept reactor

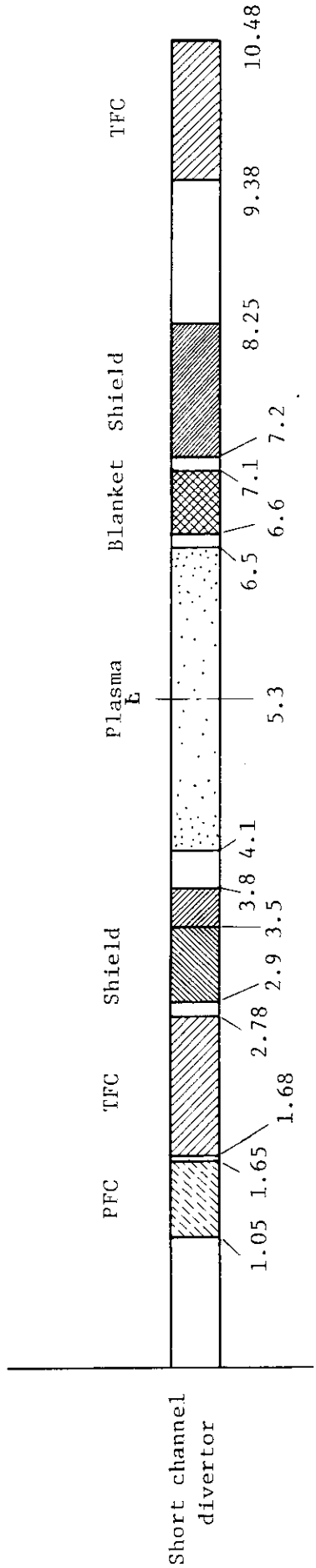

Fig. 1.1.2 Radial build of short channel divertor concept

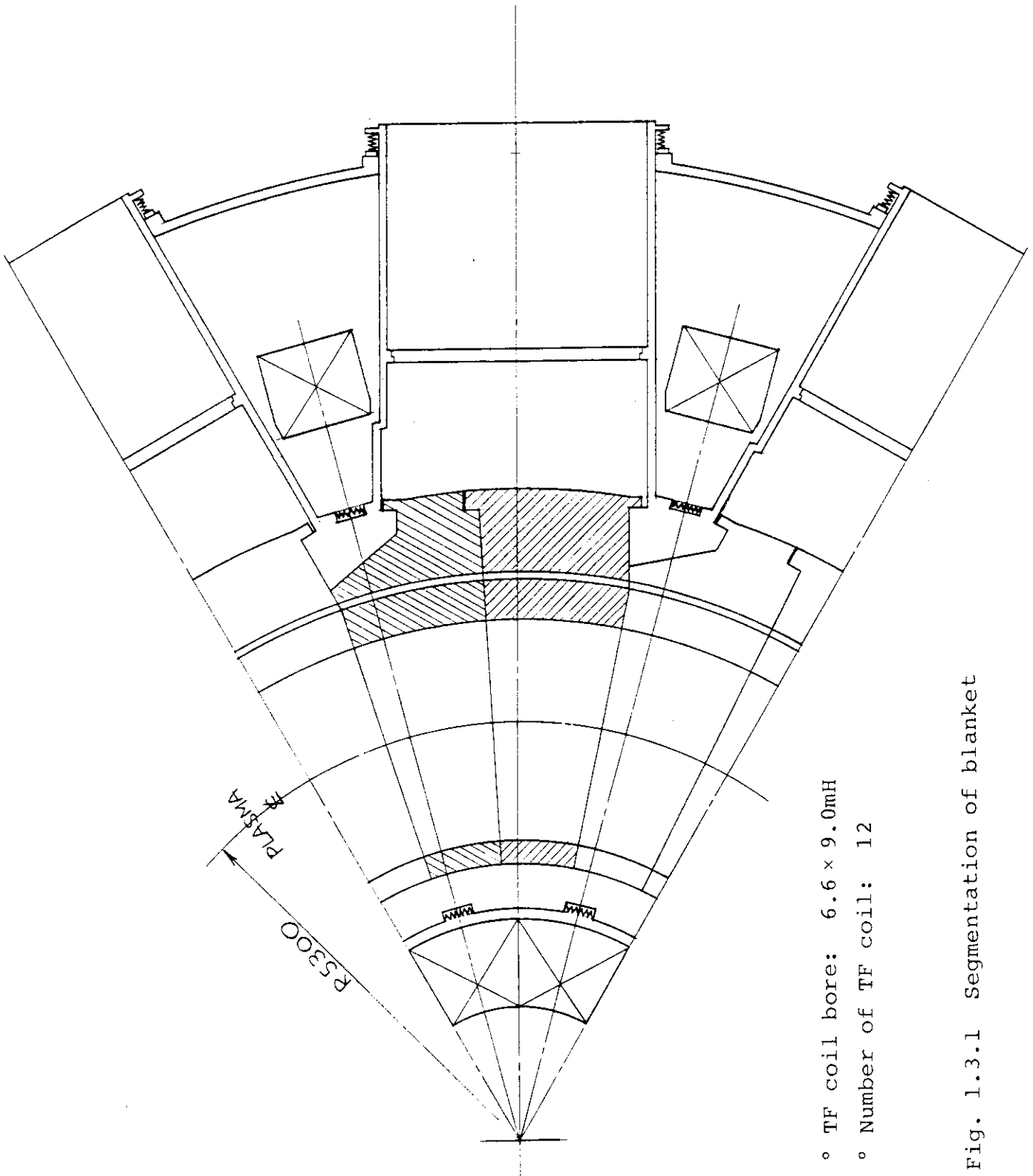

° TF coil bore: 6.6 × 9.0mH
° Number of TF coil: 12

Fig. 1.3.1 Segmentation of blanket

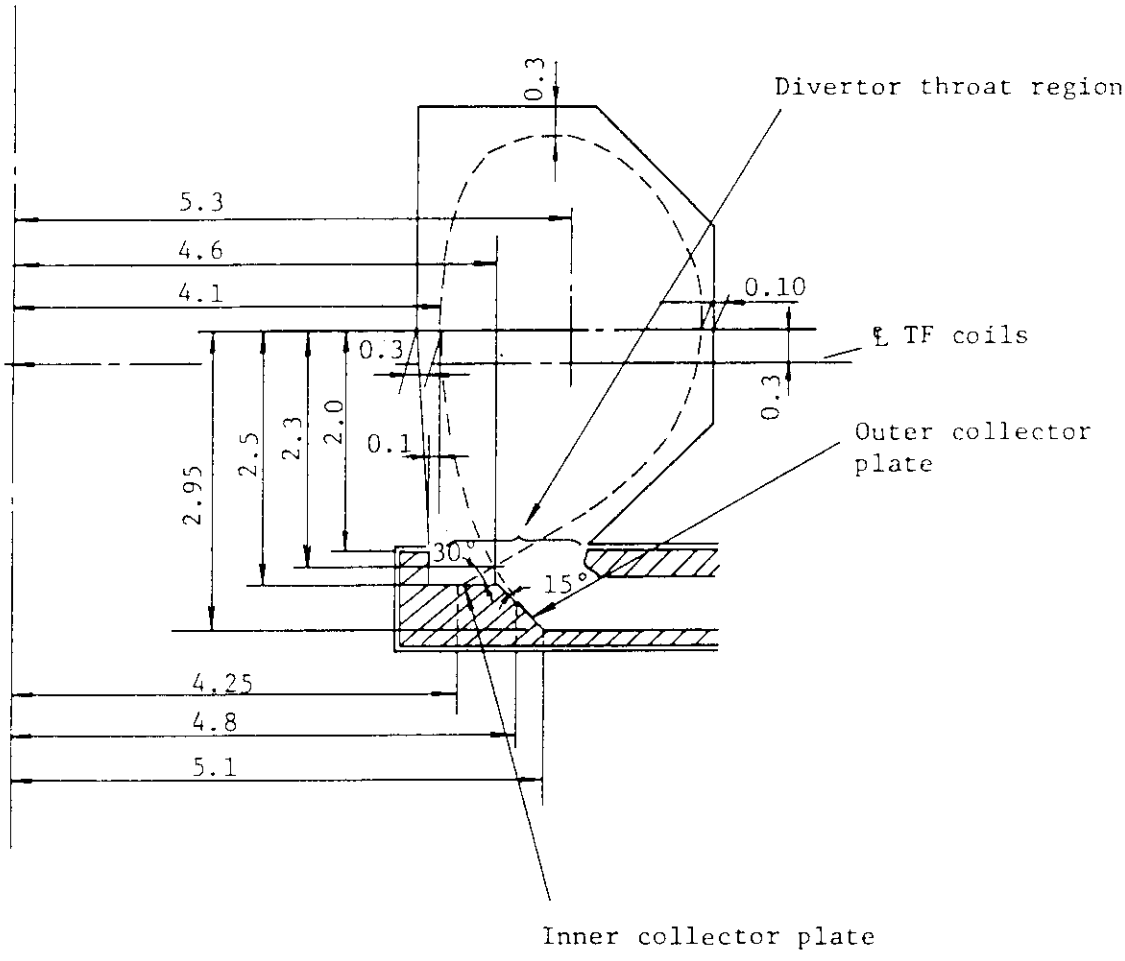

Fig. 1.4.1 Profile of the divertor region for the reduced channel length divertor

The plasma configuration is based upon the Japanese prediction.

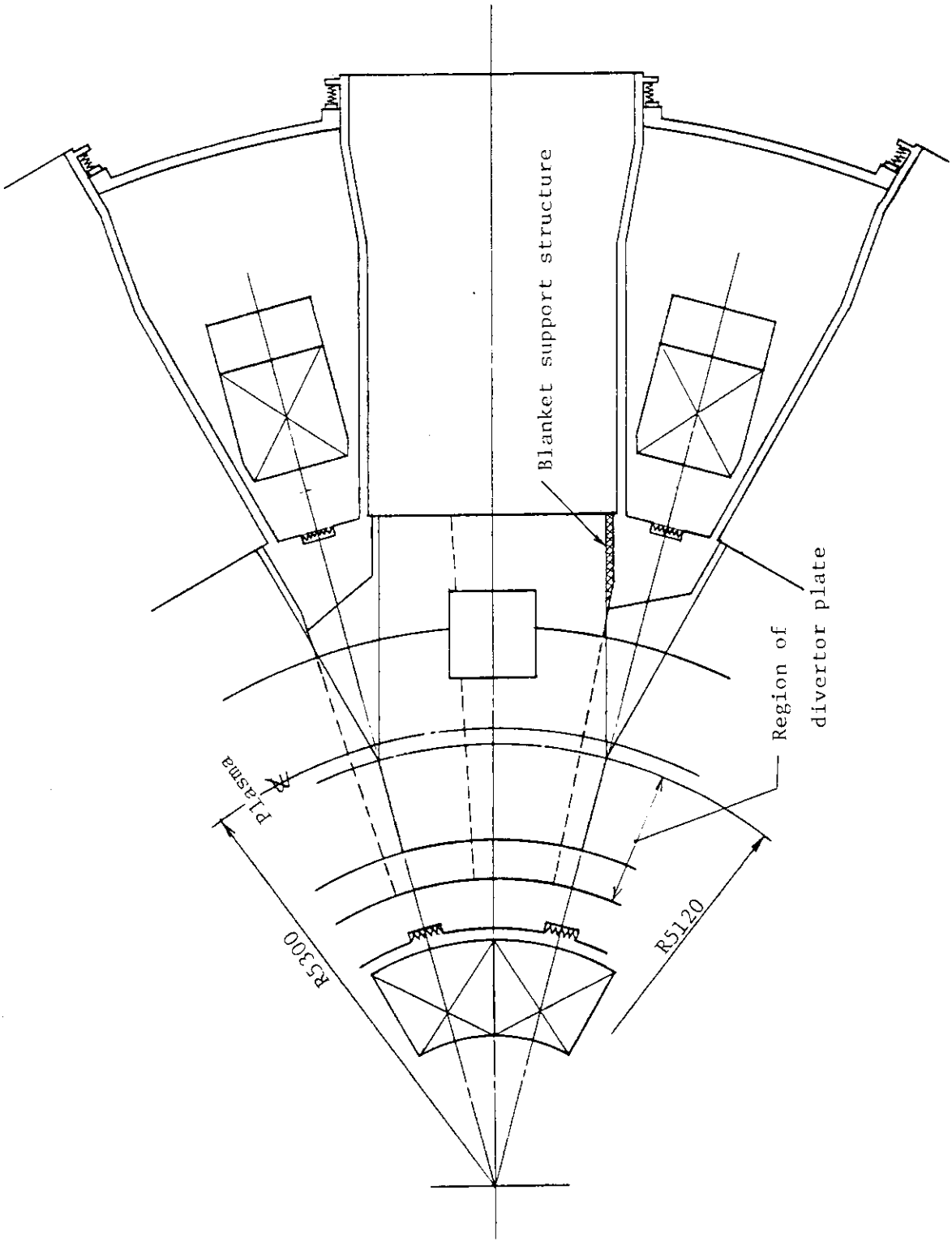

Fig. 1.4.2 Segmentation of divertor as one sector per TF coil

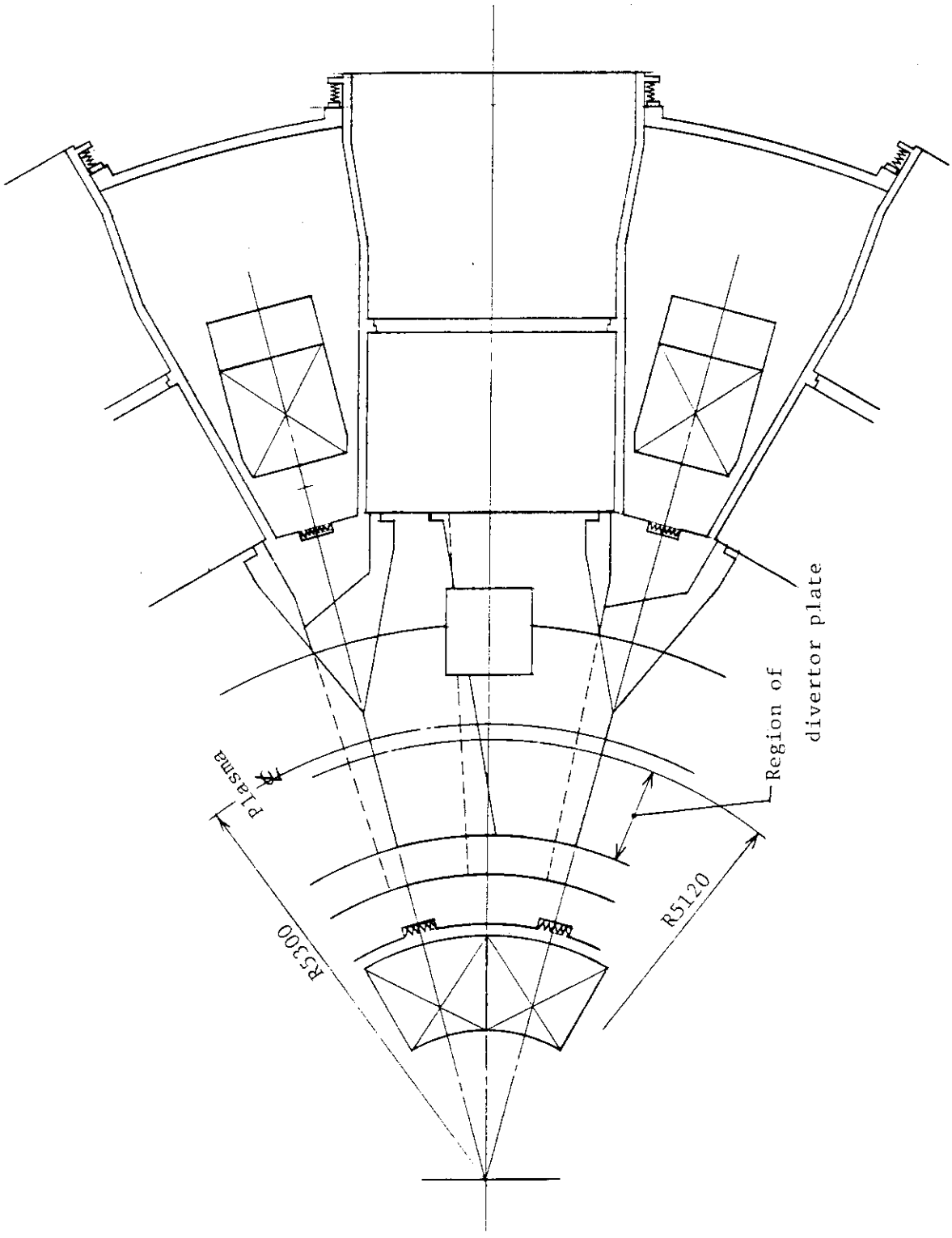

Fig. 1.4.3 Segmentation of divertor as 2 sectors per TF coil

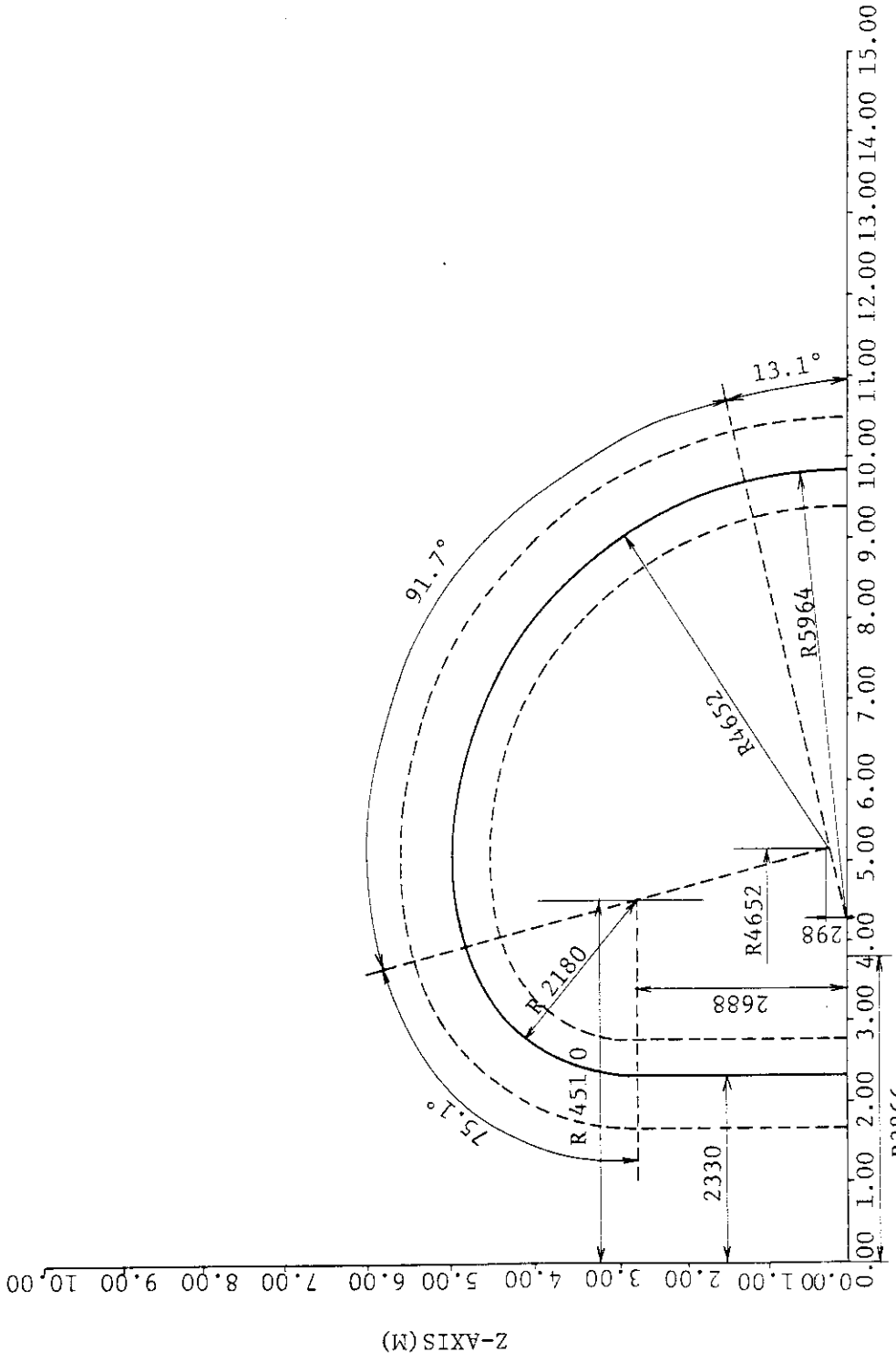

Fig. 1.5.1 TF coil dimension for short channel divertor concept

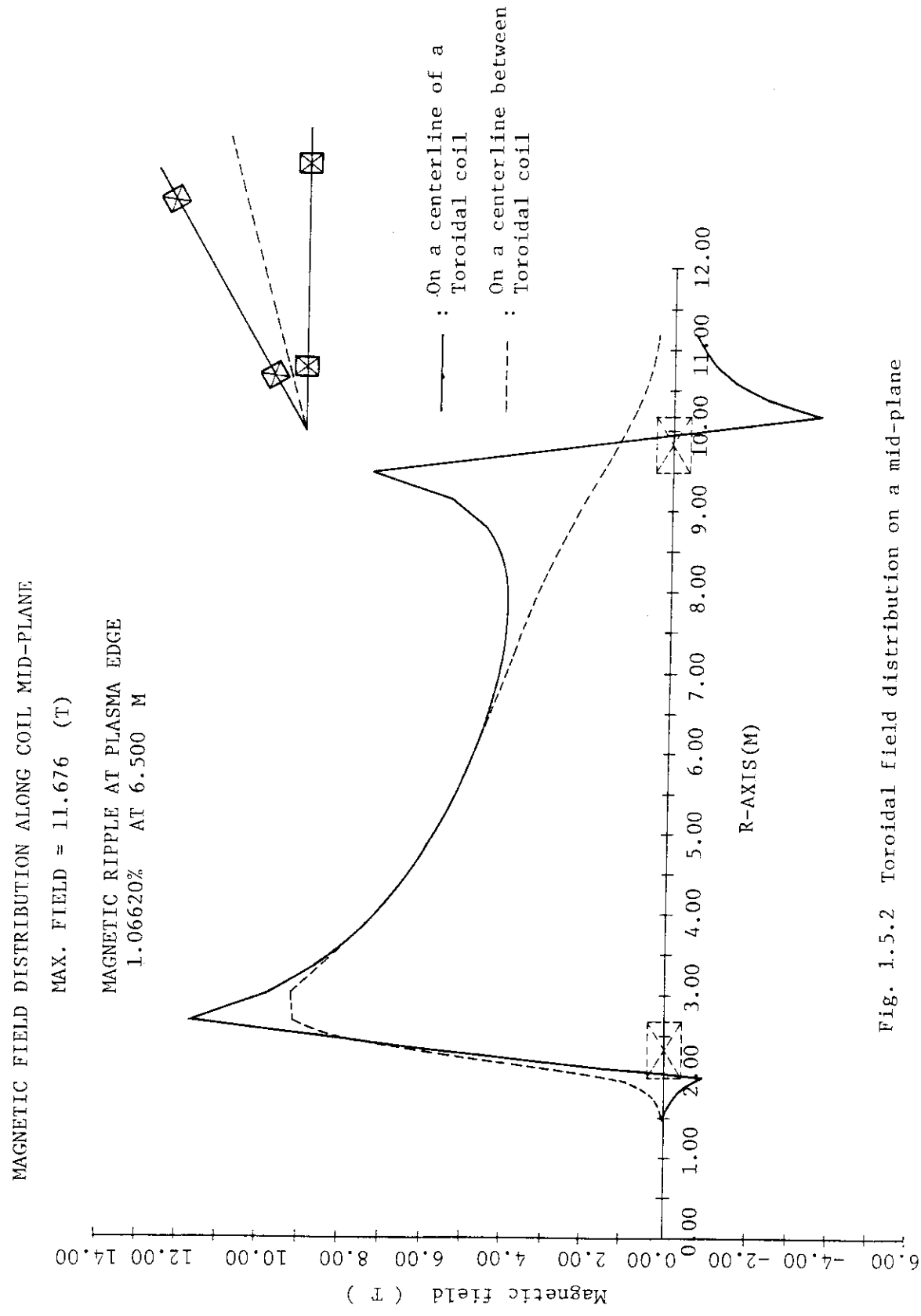

Fig. 1.5.2 Toroidal field distribution on a mid-plane

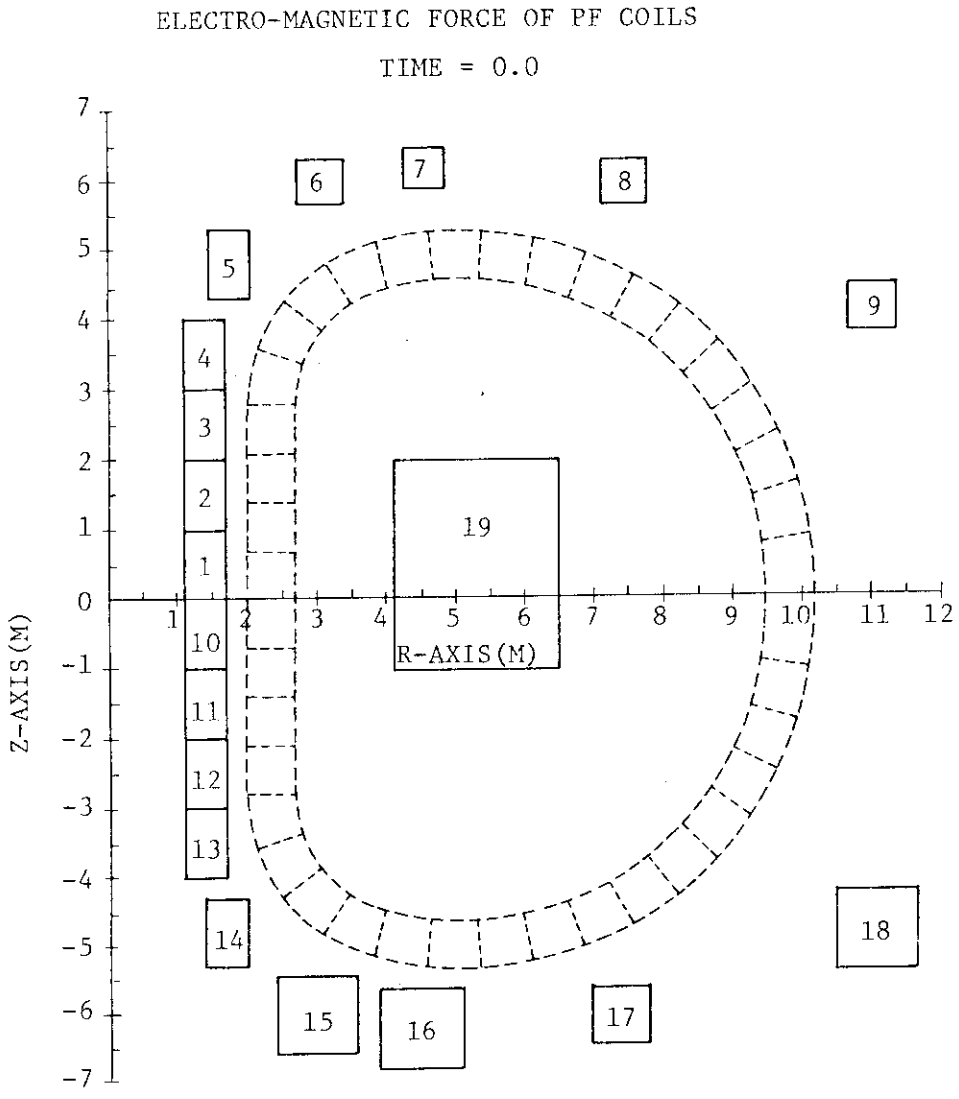

Fig. 1.5.3 Poloidal coil location for short channe divertor reactor concept

Note : TF coil configuration indicates coil winding area

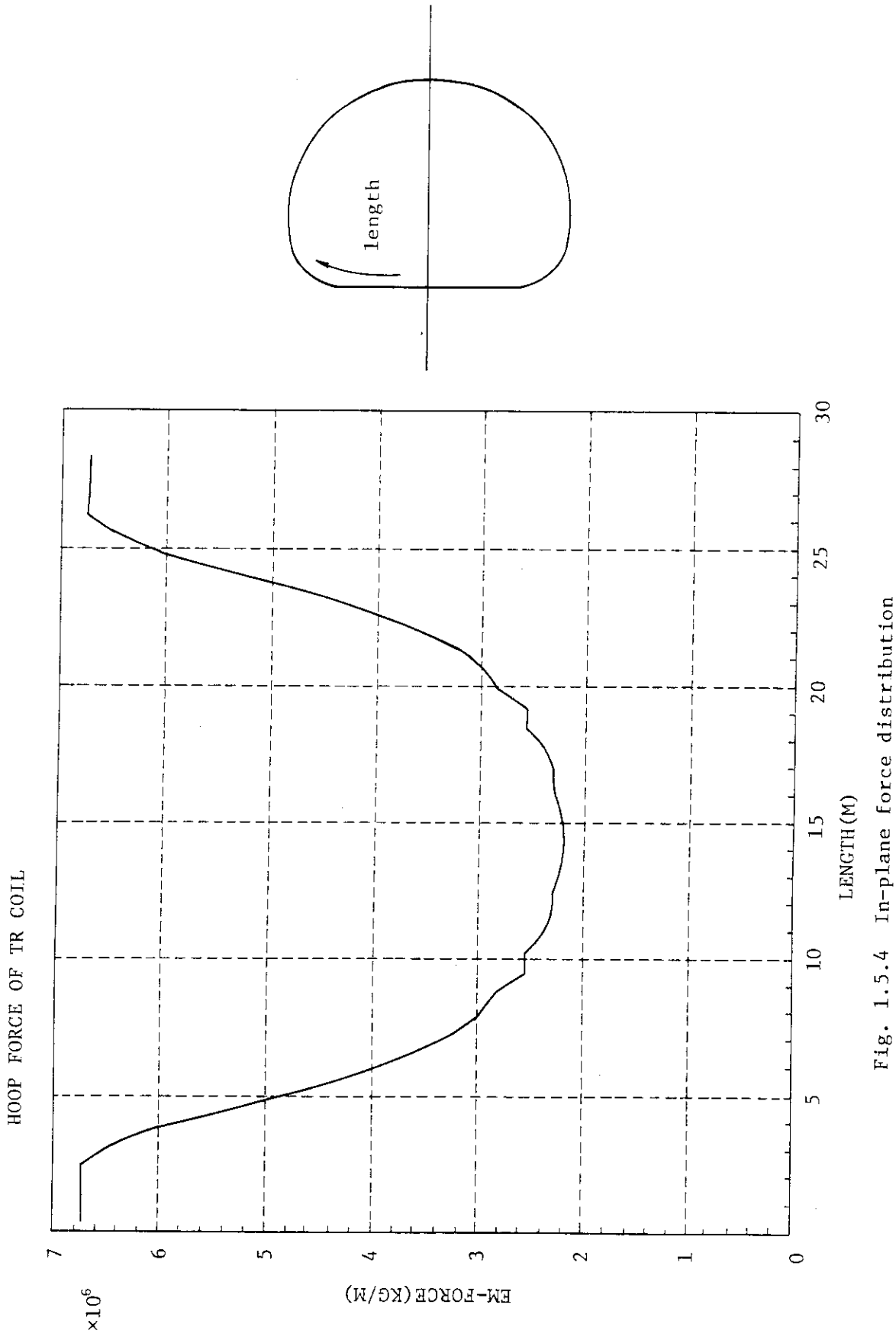

Fig. 1.5.4 In-plane force distribution

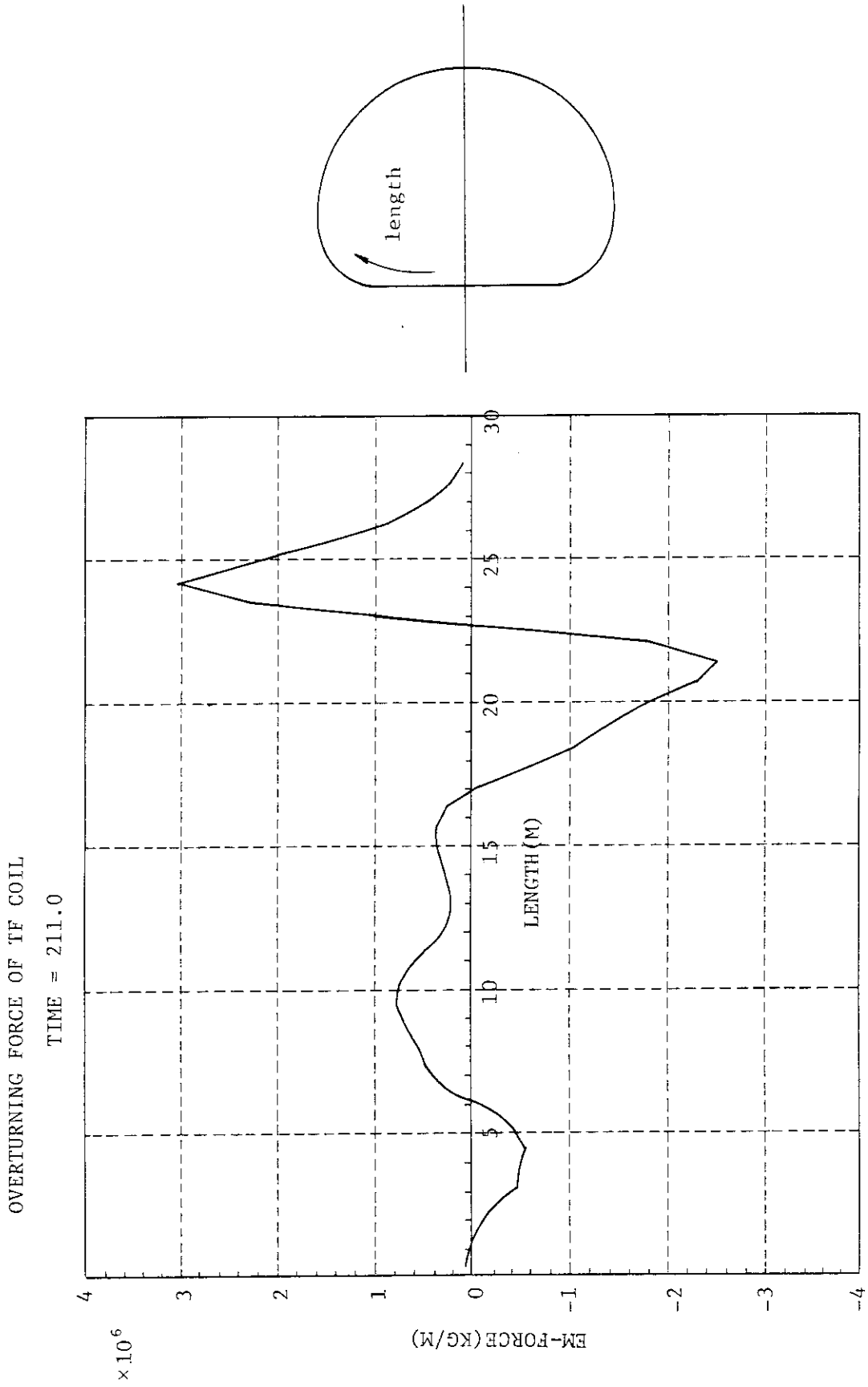

Fig. 1.5.5 Out-of-plane force distribution

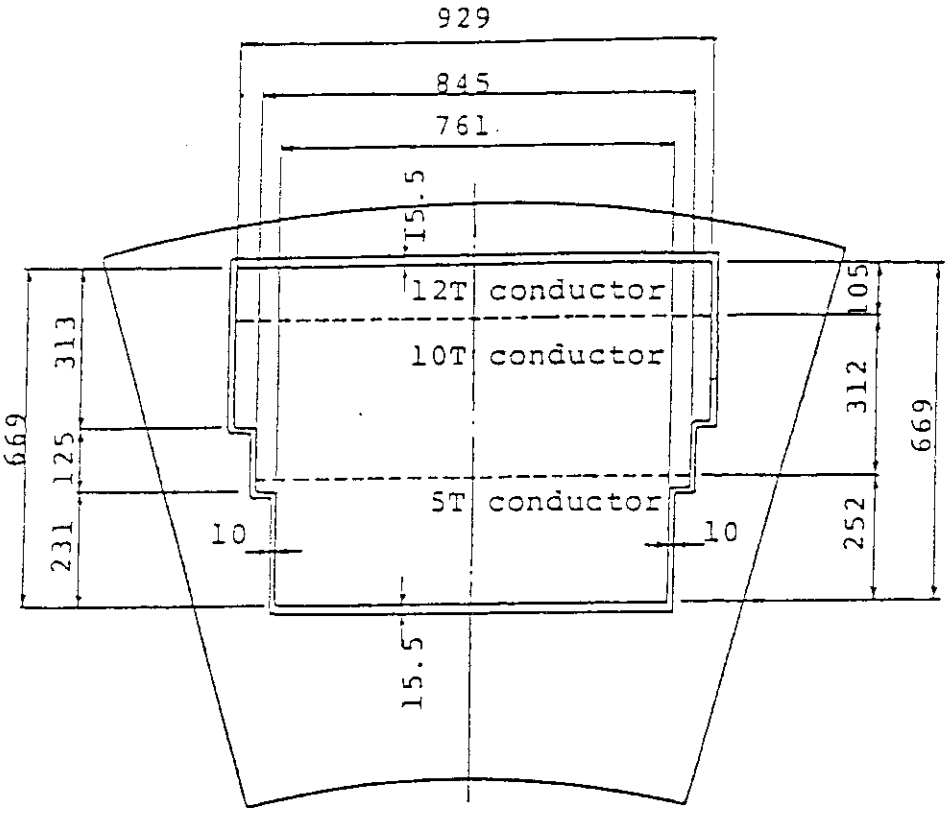

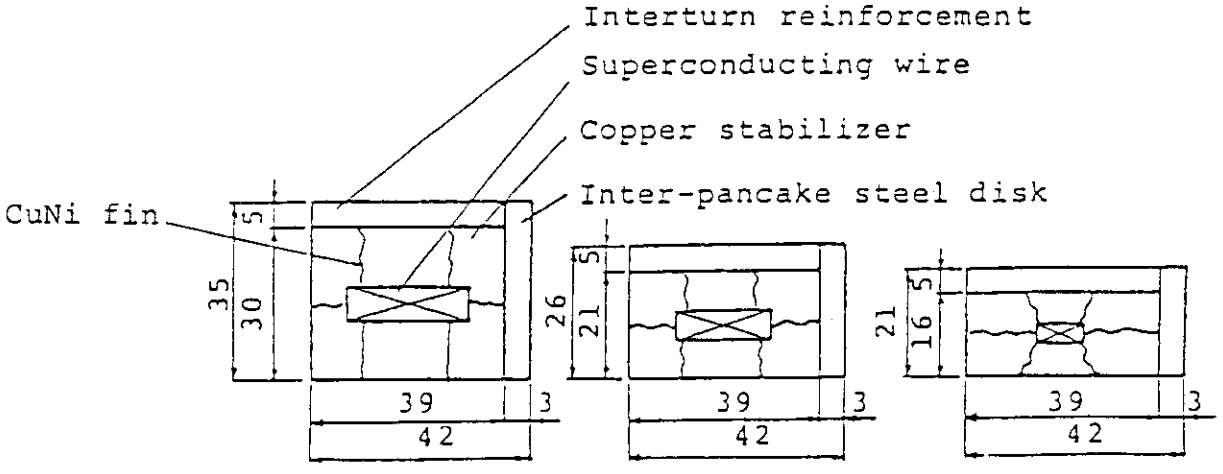

(1) 12T conductof (2) 10T conductor (3) 5T conductor

Fig. 1.5.6 TF coil winding concept and its conductors

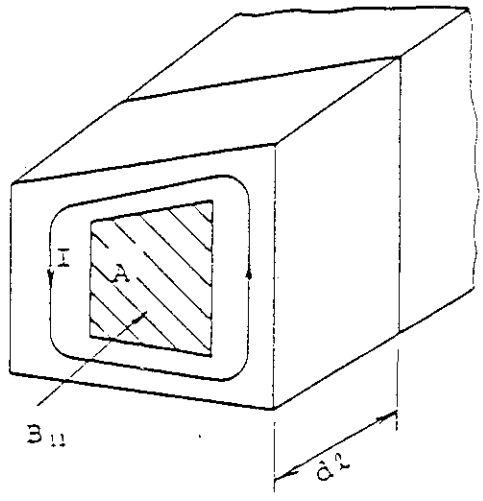

$$P_{\parallel} = \frac{A^2}{\langle R \rangle} \int_{\ell} \dot{B}_{\parallel}^2 \, d\ell$$

A : Crosssectional area

$\langle R \rangle$: Averaged resistance per unit length

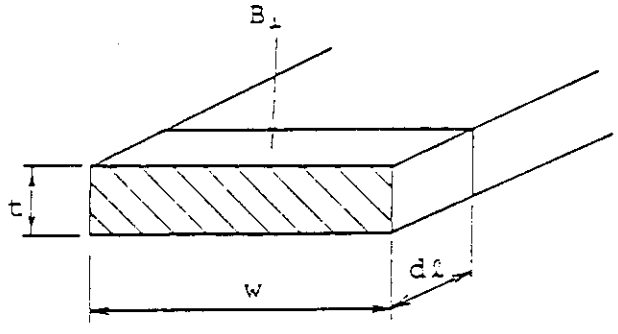

$$P_{\perp} = \frac{tw^3}{12\rho} \int_{\ell} \dot{B}_{\perp}^2 \, d\ell$$

t : Thickness

w : Width

ρ : Resistivity

Fig. 1.5.7 The models for calculation of AC loss in TF vessel

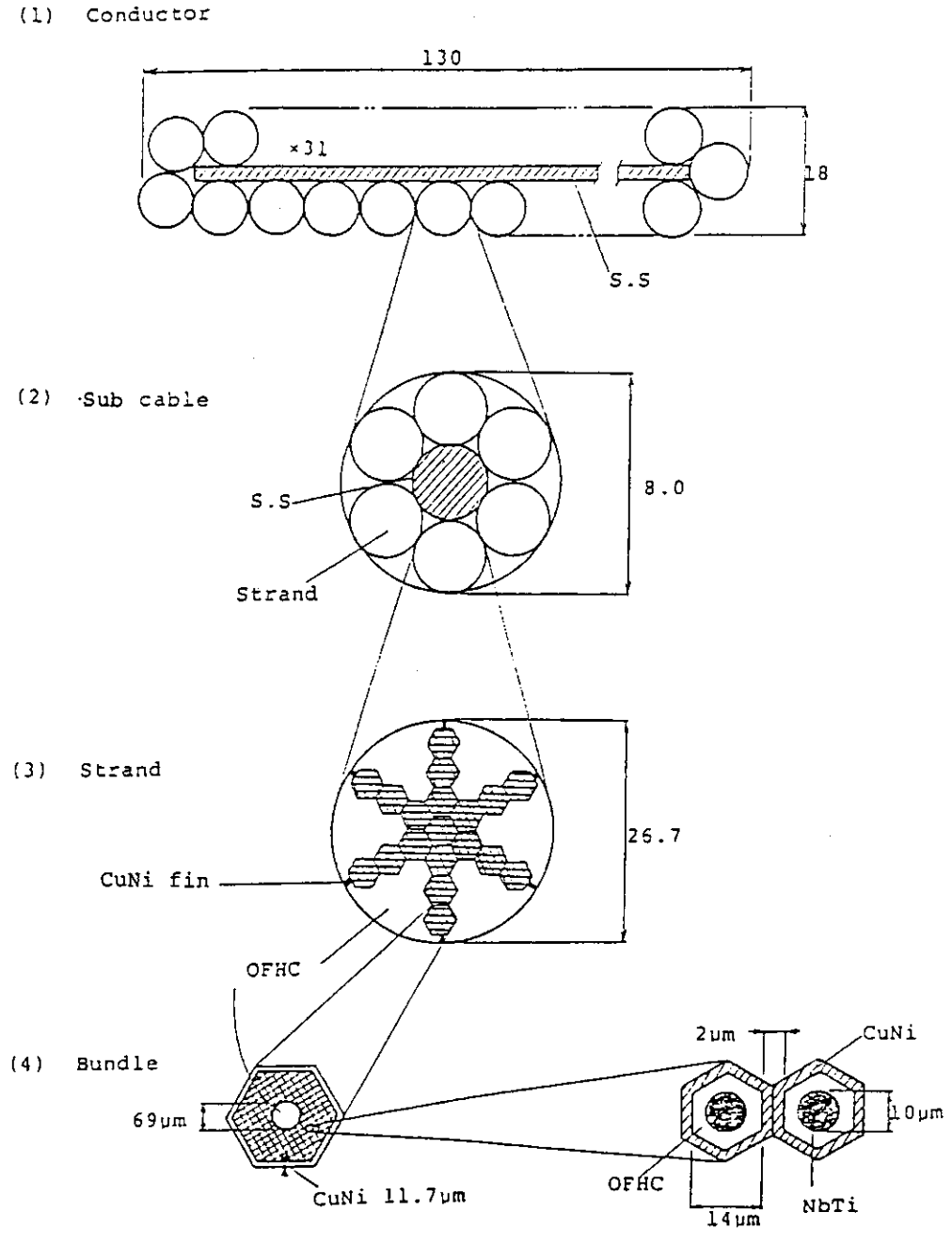

Unit: mm except noted above

Fig. 1.5.8 PF coil conductor

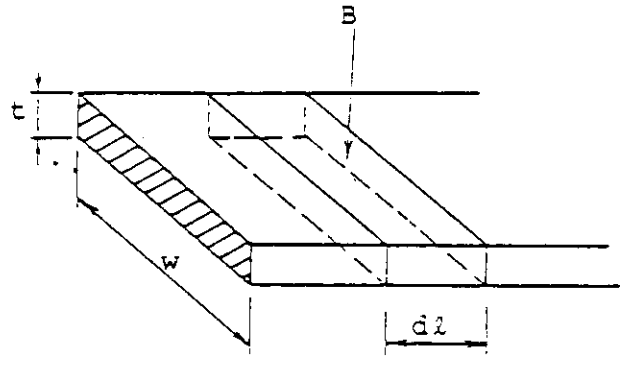

Fig. 1.5.9 AC loss model

3. Advantage of RF Current Ramp-up

Task 2. Determine how to take advantage of the RF current drive to ramp-up the current and/or transformer recharge. Quantity the engineering benefit to the design of extending the burn pulse from 200 s to 1000 s.

R. SAITO

S. ITOH

A. HATAYAMA

M. KASAI

H. IIDA

Task 2. Determine how to take advantage of the use of RF current drive to ramp-up the current and/or transformer recharge. Quantity the engineering benefit to the design of extending the burn pulse from 200s to 1000s.

Simplified operation scenario using of RF current ramp-up and inductive current drive is shown illustratively in Fig. 1.

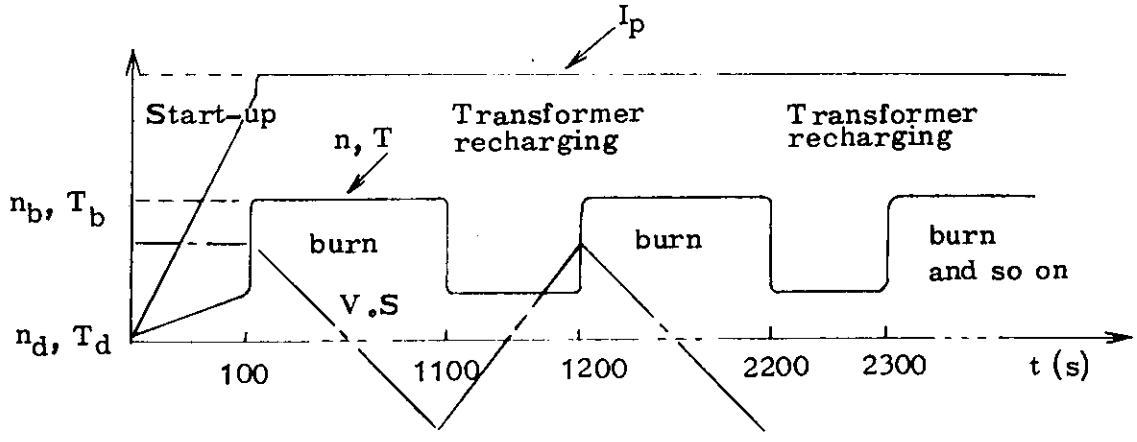

Fig. 1 Simplified operation scenario

(1) Reactor size

In the RF ramp-up operation scenario specified in Fig. 1, the required volt-second is reduced to be about 50 VS from 85 VS which is necessary for the reference operation scenario. By virtue of this reduction, the bore of selenoid coils, then plasma major radius, become smaller. Figure 2 showes the plasma major and minor radiuses in the case of RF ramp-up operation. The major radius become smaller by about 35 cm than that of reference INTOR while the minor radius become slightly larger (~3 cm). When we assume same burn time as reference value (~200 sec), the reduction of plasma major radius is found to be smaller by about 80 cm than reference. However it should be noted that too small solenoid coil bore might cause some engineering problems such as power leads

arrangements. When we assume the same reactor size as that of reference INTOR, the burn time can be about 2000 second. We can conclude that the use of RF ramp-up gives us engineering advantages which is longer burn time and/or smaller reactor size.

(2) Bucking post

Electrical one turn breaks of a bucking post can be eliminated since the refrigerating load of liguid helium of the post, i.e. AC loss, is allowable level[*1, *2]. This fact is considered to be favorable to mechanical structure designs of the bucking post.

*1. AC loss of the bucking post without electrical one turn breaks

$$\bar{P}_{ac} = \Sigma \frac{V^2}{R} \cdot t / T$$

where $\bar{P}_{ac}$: average AC loss

V : inductive loop voltage

R : one turn registance of bucking post for SS

$= 50 \times 10^{-8} (\Omega \cdot m) \times 2\pi \times 1.5(m) / 0.2(m) \times 7(m)$

$= 3.4 \times 10^{-6} (\Omega)$

t : time during loop voltage V

T : time between burn phases

= 1100 sec

at recharging phase V = 0.5 volt, t = 100 sec

at burn phase V = 0.05 volt, t = 1000 sec

therefore

$\bar{P}_{ac}$ = 6.7 kw + 0.7 kw = 7.4 kw

*2. AC losses of other structures, i.e. TF coil vessel and intercoil supports etc., can be reduced to 5 ~ 10 kw while about 100 kw level in case of reference design.

rough estimation

- Total heating energy at ignition approach phase is reduced to about 1/4
- Time from burn to burn becomes from 300 sec to 1100 sec.
- So, AC Losses are reduced to one fifteenth.

(3) Mechanical design

By means of extending the burn time and the periods of sustaining plasma current, the number of reactor operations during a life time is estimated to be about 1/10 ~ 1/100 in comparison with the reference reactor (burn pulse 200 sec). The reduction of electromagnetic and thermal fatigue cycles leads to the increment of allowable stress intensity for mechanical structure materials (ex. first wall, blanket, shield, magnets etc.) and so, the simplification of mechanical structures and large design margins in mechanical stress analysis are sufficiently expected, especialy for electromagnetic fatigue cycles. For example, in the case of 1/100 fatigue cycles allowable stress intensity is twice as shown in Fig. 3 and for thermal fatigue cycles, the effect is obtained slightly. (Fig. 4)

(4) Power supply capacity

Comparison of typical load pattern of PF-coil power supply between conventional pulse-reactor and current-drive reactor is made and shown in Fig. (a) and (b) (these load patterns are obtained for FER).

For the conventional reactor, peak power load appears at the end of plasma current ramp-up phase (t = 5 s), shown in Fig. (a). At this time, apparent power for PF-coil power supply becomes as ~ 2000 MVA.

On the other hand, in the case of current drive reactor, apparent power is reduced to be ~ 600 MVA at the end of current ramp-up phase (t = 100 s). This is mainly due to the docrease of current ramp-up rate, which is about 1/20 compared with conventional pulsed reactor. The maximum apparent power in RF ramp-up scenario appears to be ~ 1400 MVA at beginning of additional heating phase.

In the above example, plasma current was ramped-up at its full value (= 5.3 MA) at the end of the current ramp-up phase and maintained at constant value through out the additional heating phase inductively by OH-coil. Low-β plasma with full current requires fairly large MVA for EF-coils. This causes an apparent power peak at beginning of additional heating phase. If we adopt such a current ramp-up scenario that the plasma current is slightly reduced (about 4 ~ 5 MA) from the full value at the end of current ramp-up phase and ramped-up at its value at the end of additinal heating phase, further reduction of peak apparent power will be expected.

(5) Bellows

Detailed studies is shown in Appedix. The toroidal one turn resistance of the order of 0.2 mΩ will be needed to avoid the difficulties to make the concept of active coils inside the shield for vertical position control.

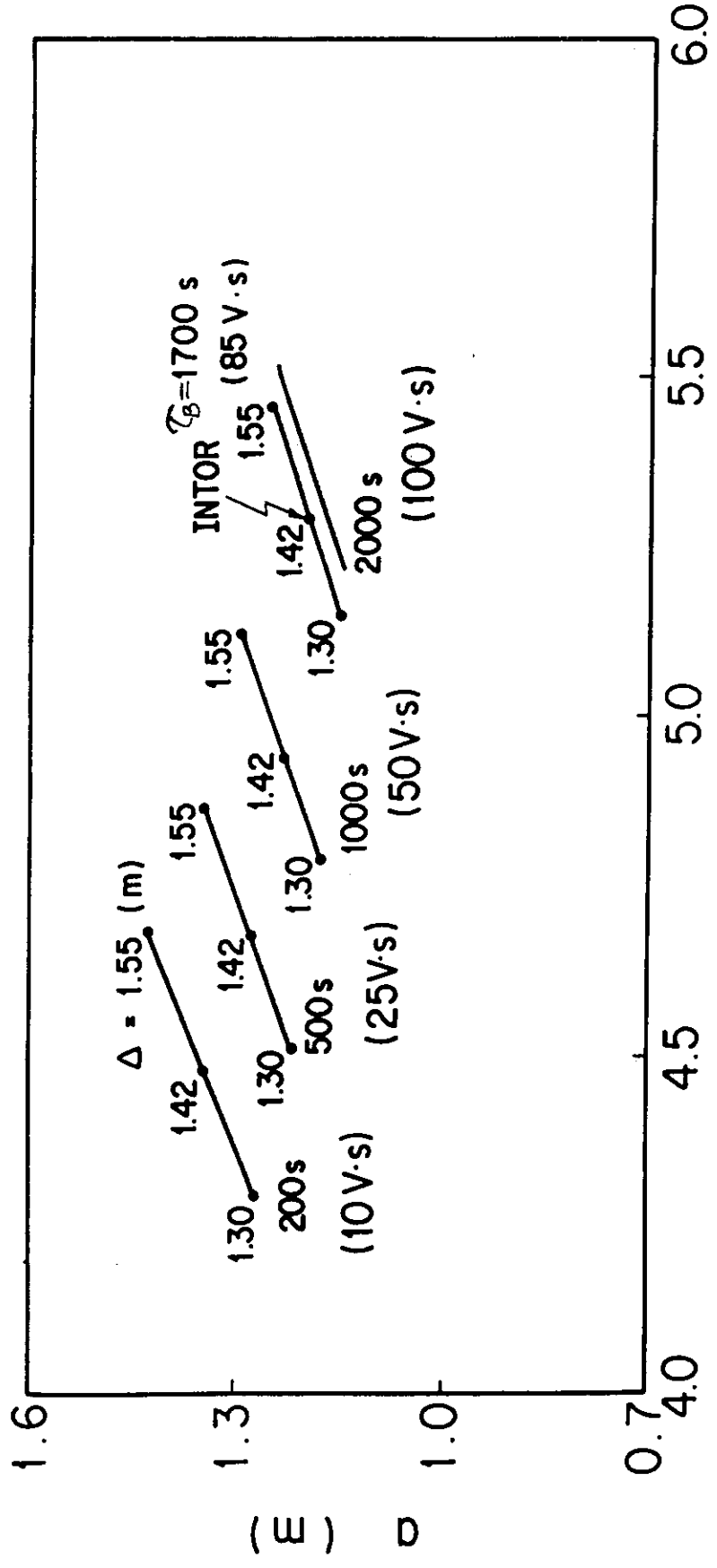

Fig.2 Reactor size ; plasma major radius R vs. minor radius a

Δ : distance bt. plasma surface and inboad TF coil vessel

τ_β: burn time

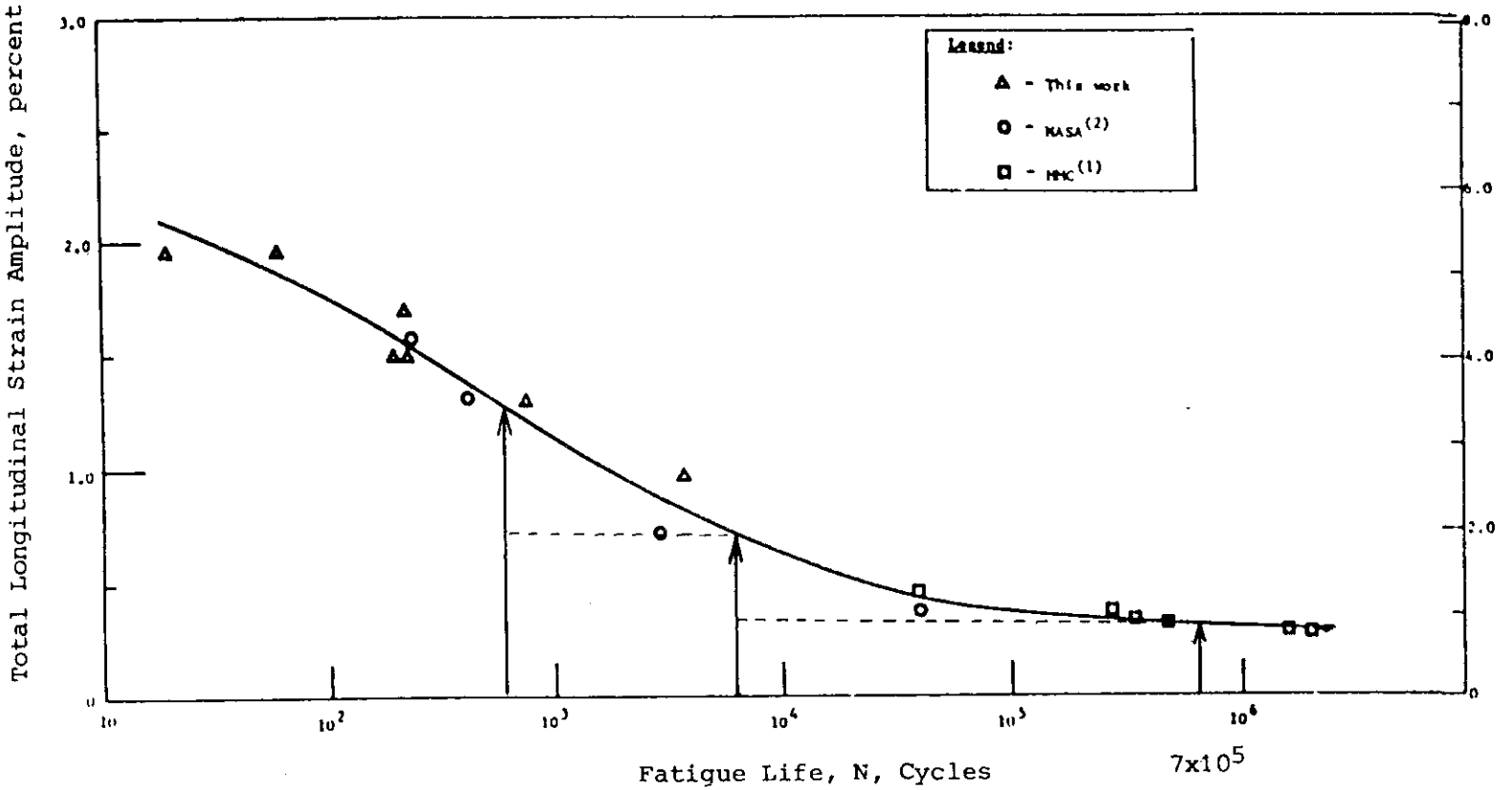

Fig. 3 Fatigue Life Curve for 304 at 4 K

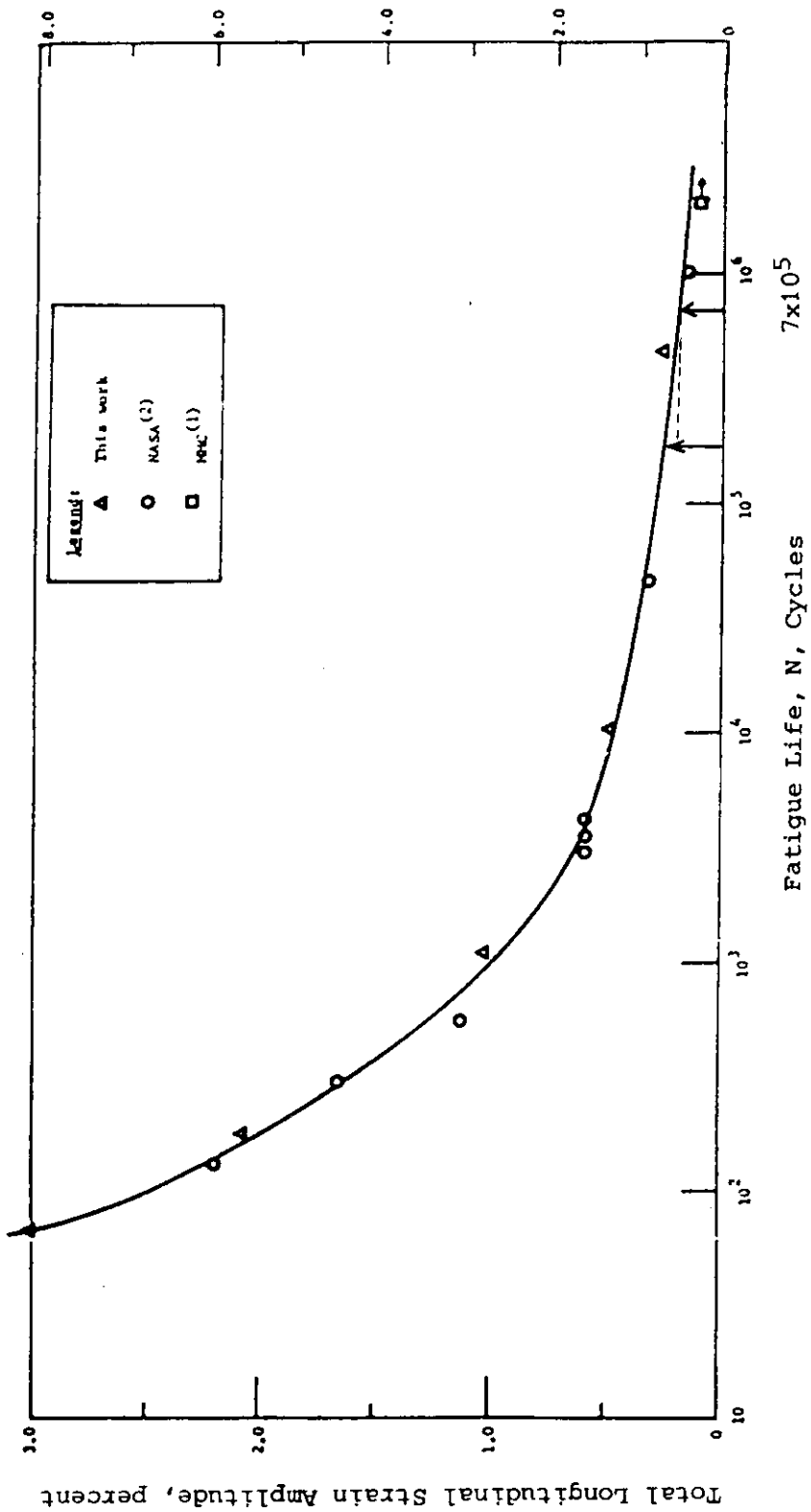

Fig. 4 Fatigue Life Curve for 304 at 293 K

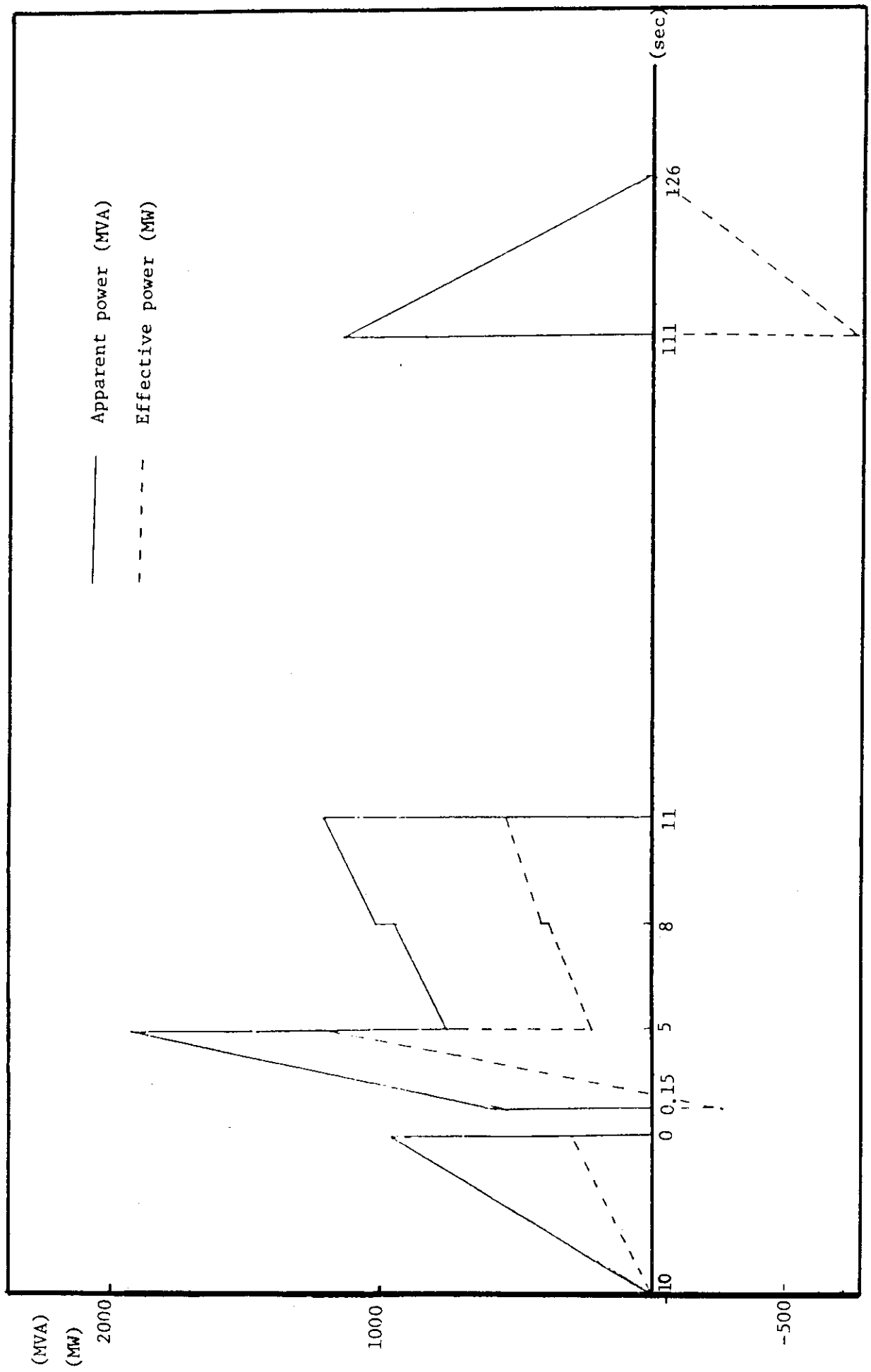

Fig.5 (a) Load pattern of PF-coil power supply for conventional pulsed reactor

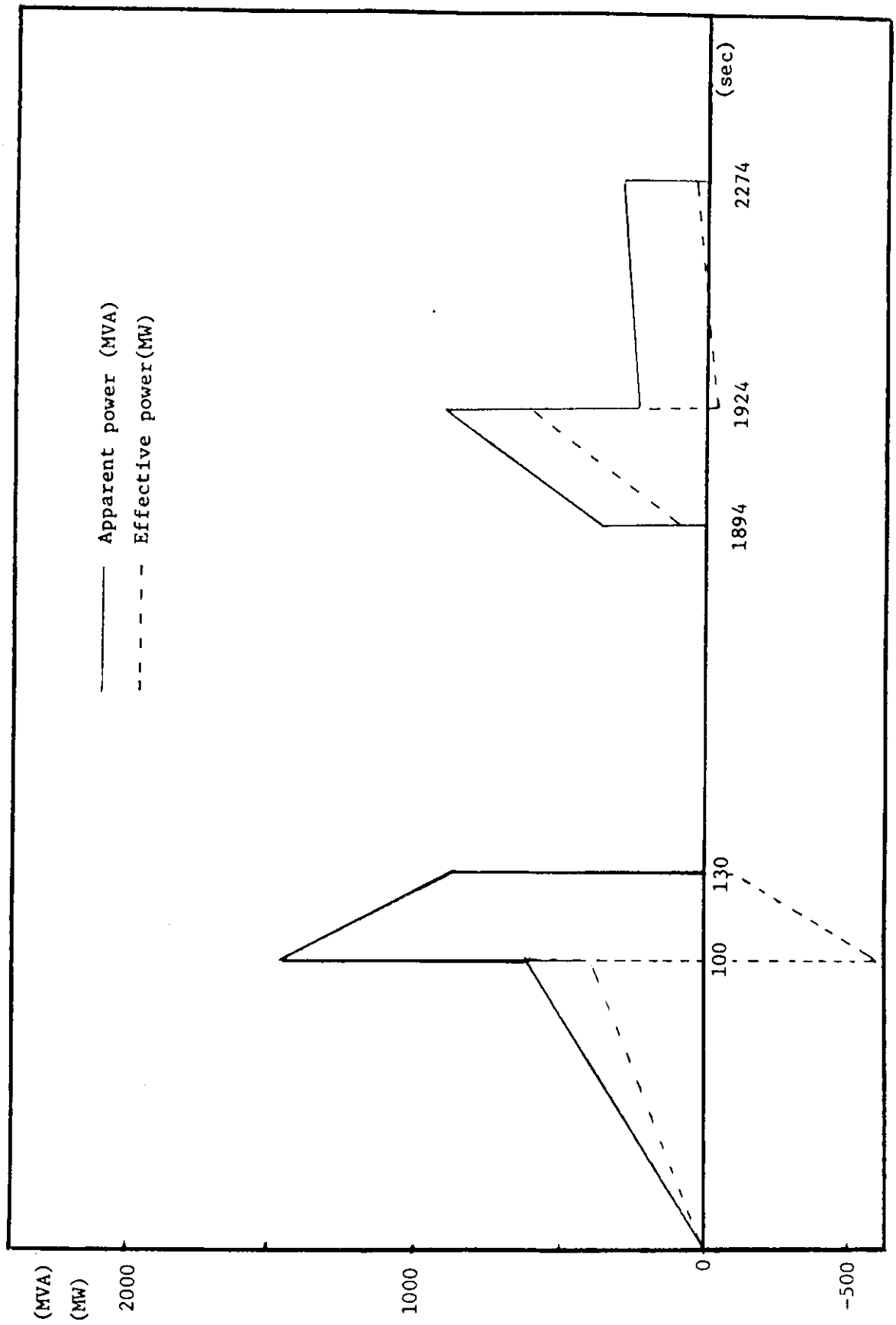

Fig.5 (b) Load pattern of PF-coil power supply for current drive reactor

APPENDIX Magnetic and Electrical Field Penetration

In future tokamak reactors, plasmas are surrounded by mutiple layers such as first wall, blanket, shield, coil vacuum chamber and toroidal field magent including shear panels. This multilayer structure will prevent fast penetration of magnetic and electrical field at start-up phase.

The magnetic field and loop voltage applied to plasma are reduced by eddy currents and represented by eqs (A-]) and (A- 2) respectively, using Laplace transform as described in sec. 2.3.[NL.Rept.].

$$B_v(s) = \frac{M_{pc} I_c}{2\pi R_p} \{1 - M(s)\} \qquad (A-1)$$

$$V_p(s) = -M_{pOHs} I_{OH} \{1 - V(s)\} \qquad (A-2)$$

$$M(s) = \sum_k \frac{s\tau_k}{1+s\tau_k} m_k, \quad m_k = \frac{M_{pk} M_{ck}}{M_{pc} \tau_k}$$

$$V(s) = \sum_k \frac{s\tau_k}{1+s\tau_k} v_k, \quad v_k = \frac{M_{pk} M_{OHk}}{M_{pOH} \tau_k}$$

where, M_{pk} : mutual inductance between plasma and k-th eddy current mode

M_{ck} : mutual inductance between magnetic field coil and k-th eddy current mode

M_{pOH}: mutual inductance between plasma and OH coil

M_{OHk}: mutual inductance between OH coil and k-th eddy current mode

τ_k : time constant of k th eddy current mode

M' : derivative of mutual inductance

I_c : Laplace transform of magnetic field coil current

$\dot{I}_{OH}$: Laplace transform of ohmic coil current decay rate

When plasma is perfectly surrounded by conductive structures and coils are located outside the structures, $M(s\to\infty)$ and $V(s\to\infty)$ are equal to one. So the fields are completely shielded at $t = 0$.

Magnetic field penetration

Figures A- 1 and A-2 show M(s) of JAERI FER system. The comparison between the cases with and without high conductive shells is represented in Fig. A- 1 , and the effect of one turn resistance is shown in Fig. A- 2 . The configuration of passive elements is shown in Fig. A- 3. The presence of high conductive shells does not largely affect the shielding effect, M(s), since the high conductive shells does not perfectly enclose the plasma. On the other hand, the M(s) depends strongly on one turn resistance of radiation shield/coil vacuum chamber. This result suggests that the radial magnetic field for plasma vertical position control will be shielded by radiation shield/coil vacuum chamber, and the control property will be deteriorated, if the active coils are located outside the toroidal field coils, and toroidal one turn resistance will not be required because of plasma current ramp up by LHRF current drive. On the other hand, low one turn resistance of radiation shield/coil vacuum chamber will improve the property of stabilizing plasma vertical position instability, whether the control property of feedback system will be improved or not depends on which property (shielding property or stabilizing property) is effective to the overall control

property. Figure A- 4 shows the gain-phase diagrams of the feedback control system of the JAERI FER. The curve (a) is the diagram for the standard case that one turn toroidal resistance is 0.2 mΩ. In curves (b) and (c), the shield/coil chamber has no bellows and toroidal high electric conductance. The effective thickness of the shield/coil chamber is 35 ∿ 40 cm in curves (a) and (b). In order to analyze the case that the active coils are located between shield/coil chamber and toroidal field coils, the effective thickness is set at 10 cm. A large gain value is required for feedback control when the shield/coil chamber has high electric conductance in the toroidal direction, though low one turn resistance expands the stable range of feedback controller where the phase is larger than -180 degrees when the gain in diagram is equal to one. This result suggests that the required power supply capacity of the active coils will be too large unless the active coils are located inside the shield/coil chamber. The toroidal one turn resistance of the order of 0.2 mΩ will be needed to avoid the difficulties to make the concept of active coils inside the shield compatible with other engineering problems such as remote maintenance, coil insulations, installations, space arrangements, etc.

Electrical field penetration

Assuming that plasma current is absent and ohmic heating coil current is linearly decreased, the loop voltage can be derived from eq.(A- 2) as

$$V_p = -M_{pOH} I_{OH} \left\{1 - \sum_k \frac{M_{pk} M_{OHk}}{M_{pOH} \tau_k} e^{-\frac{t}{\tau_k}}\right\} \qquad (A-3)$$

$$V_p^{Norm} = 1 - \sum_k \frac{M_{pk} M_{OHk}}{M_{pOH} \tau_k} e^{-\frac{t}{\tau_k}}$$

Figure A- 5 shows the normalized loop voltage, V_p^{Norm}, as a parameter of one turn resistance. The property of shielding loop voltage tends to saturate, when one turn resistance is higher than approximately 0.2 mΩ, since the shielding property due to saddle type currents is more dominant rather than that due to one turn type currents in the region of high one turn resistance.

Summarizing the magnetic and electrical field penetration, one turn resistance of approximately 0.2 mΩ is reasonable, when active coils are located outside the shield or plasma current is inductively ramped up.

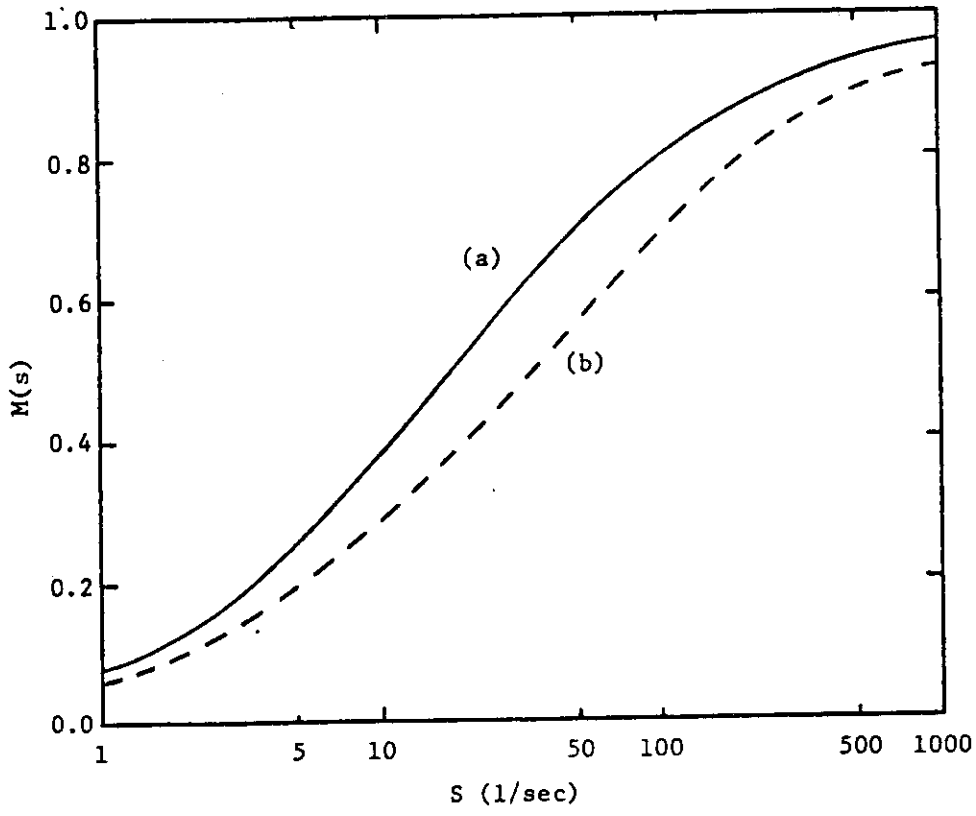

Fig. A- 1 Effects of magnetic field shielding as a function of conductive shell thickness.
(a) Standard shells, (b) Half of standard shell thickness.

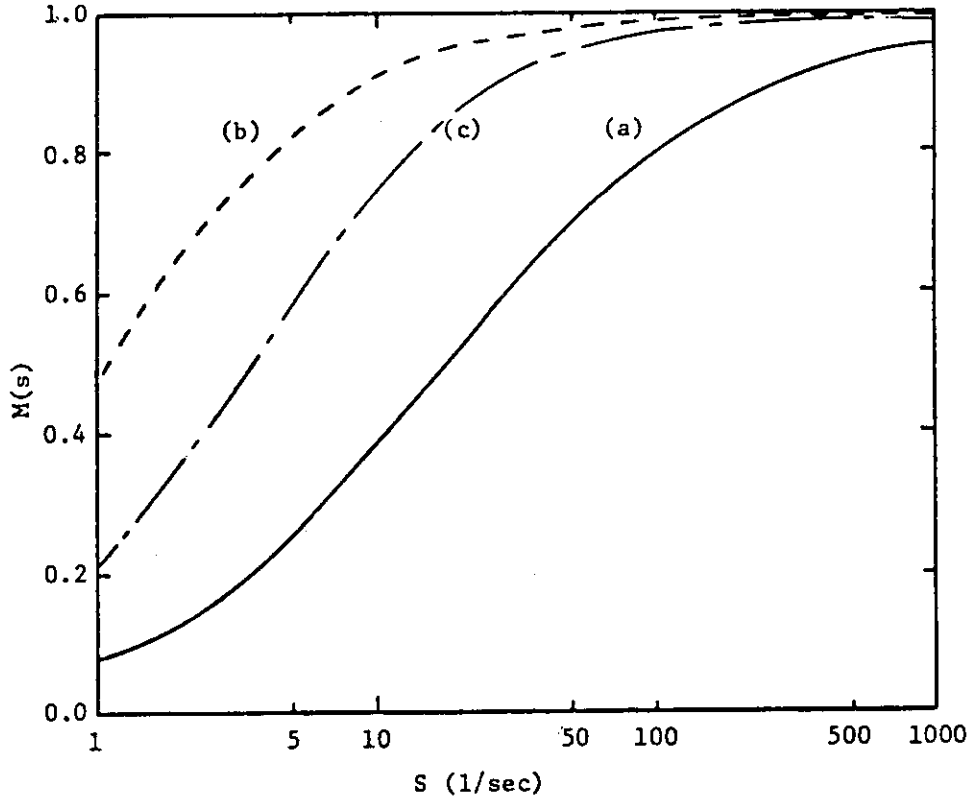

Fig. A- 2 Effects of magnetic field shielding as a function of toroidal one turn resistance and effective electrical thickness of shield.
(a) 0.2 mΩ of bellows resistance and 35-40 cm of effective shield thickness.
(b) 0 mΩ of bellows resistance and 35-40 cm of effective shield thickness.
(c) 0 mΩ of bellows resistance and 10 cm of effective shield thickness.

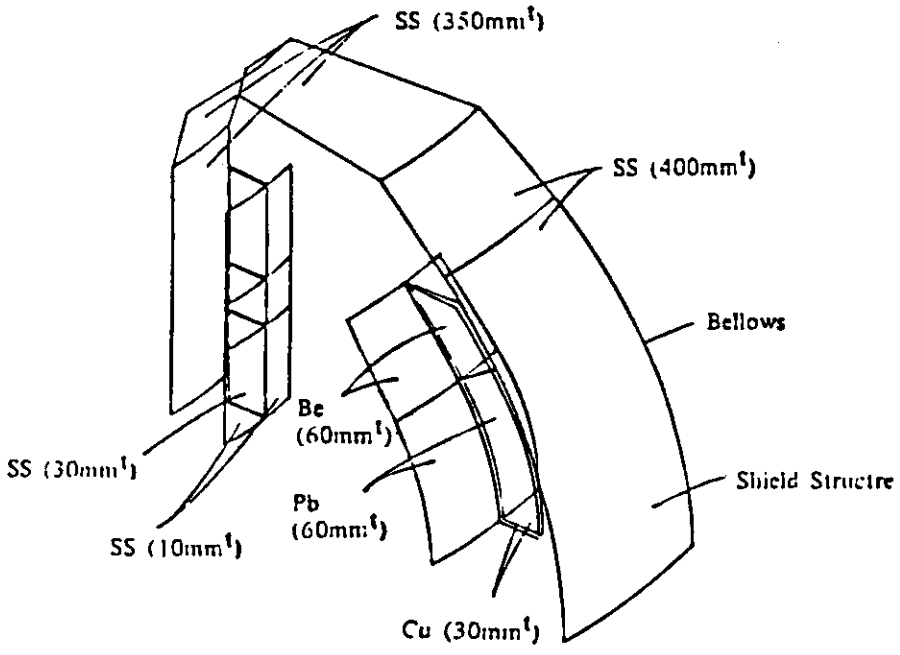

Fig. A- 3 Analysis model of passive elements

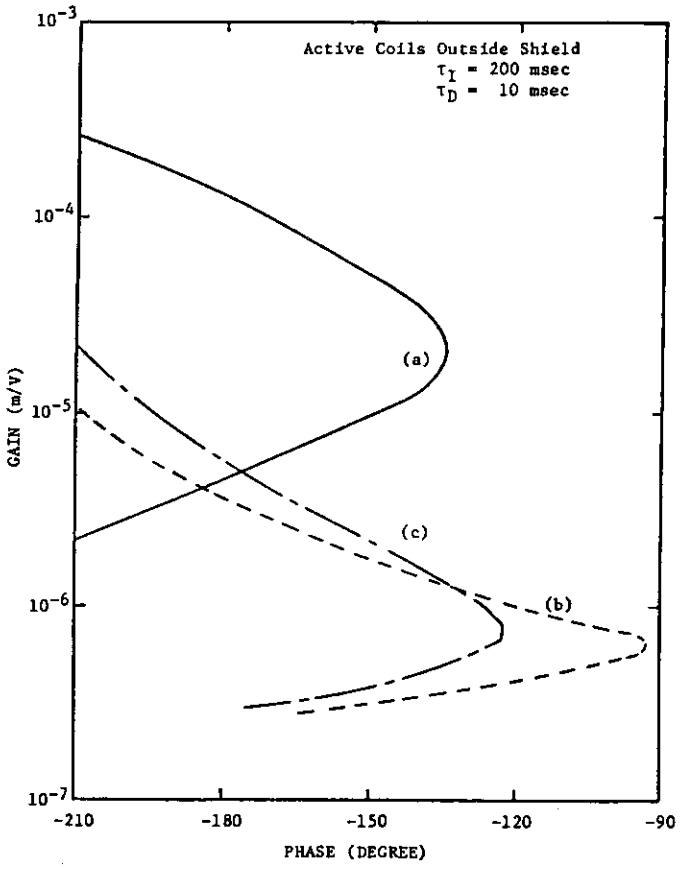

Fig. A- 4 Gain-phase diagrams of open loop transfer functions for PID control systems.
(a) 0.2 mΩ of bellows resistance, 35-40 cm of effective shield thickness.
(b) 0 mΩ of bellows resistance, 35-40 cm of effective shield thickness.
(c) 0 mΩ of bellows resistance, 10 cm of effective shield thickness.

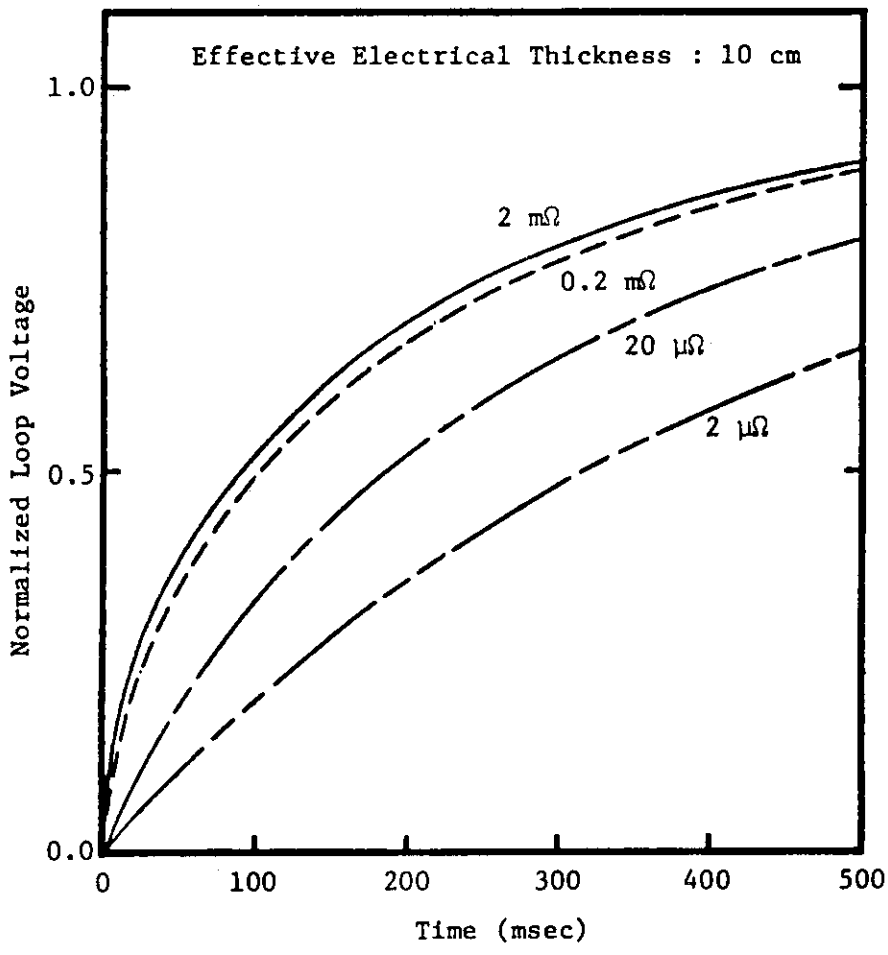

Fig. A- 5 Time evolution of normalized plasma loop voltage as a function of bellows resistance.

4. Advantage of RF assisted Start-up

Task 3 Determine the engineering advatage of using RF start-up assist to reduce the loop voltage requirements (to 5 ~ 7 V). Determine how the design would change. This study should use input from Group B as guidance for the study.

S. Itoh

The reduction of the loop voltage may be obtained, by means of using RF start-up assist in the initial plasma build-up, and so, a little saving of V.S may be expected to extend slightly the burn time (ex。~ 30 sec。in the loop voltage of 5 ~ 7 V)。 As result of such the low loop voltage the following results are obtained;

(1) Bellows of vacuum vessel are simplified。

(2) Electrical condition of insulaters of PF coils become easy.

(3) Plasma build-up may be made without high voltage power supply circuits of transformer power supplies。

5. Consideration on Active Control Coil Location

Task 4 Impacts of Active Control Coil Installtion on the Reactor Design

M. Yamada

M. Kasai

Y. Imamura

H. Iida

Y. Itou

IMPACTS OF ACTIVE CONTROL COIL INSTALLATION ON THE REACTOR DESIGN

1. Candidate Positions for Active Control Coil Installation

Fig. 1 shows seven candidate positions, ranging from the outside part of the blanket to the neighborhood of the shaping coils, for installation of active control coils for plasma vertical position control.

Table 1 indicates environmental conditions and requirements for the active control coil at each position.

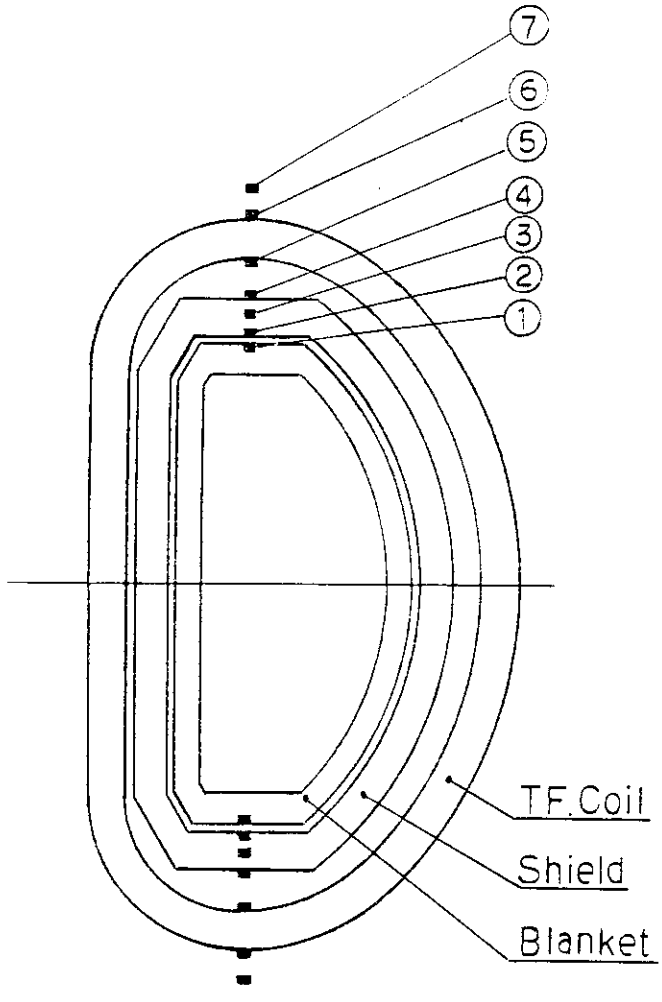

Fig. 1 Candidate Positions of Active Control Coil

2. Active Control Coil Concepts

Concepts and structures of the active control coil have been examined for each candidate position described in the previous section, assuming that blanket and shield modules be removed radially from the torus for maintenance. The results are summarized as follows;

Concept(1): Installed on the outside surface of the blanket

For maintenance the blanket is devided toroidally into sectors and each sector is to be removed radially from the torus. Since the active control coil is supported by the blanket, the coil system, being unable to form one-turn toroidally, has to consist of modular (partial) coils. Due to the temperature and nuclear heating conditions, normal conducting material (copper) should be selected for the conductor. It is inappropriate to use organic materials for the electrical insulator since the expected dose is approximately $\sim 10^{11}$ rad. Then, for electrical insulation, the coil system should use sintered ceramics or MI cable. The former is to be installed on the conductor surface with a distance enough to prevent surface creepage. The MI cable is a component in which powder of an inorganic material is filled up in the space between the conductor and metal casing. Physical properties of irradiated ceramics will be shown in Group H Blanket Data Base Assessment 2.5. Joule and nuclear heatings in the coil require use of hollow conductor cooled by water. In addition, consideration should be given to cooling of the insulator. Since the required total Ampere-turn is $\sim$25 kA, the active control coil need not be made of plural turns. However, when MI cables are

to be used, slender ones are preferred because of flexibility for bending, and the selection might result in a design with eight cables running in parallel. The active control coil modules can be disassembled and removed from the torus along with the blanket modules for maintenance.

Concept (2): Installed on the plasma-side surface of the shield

The conditions of temperature, dose rate and nuclear heating at this position are similar to those on the outside surface of the blanket. Then the considerations given to the conductor and electrical insulator of Concept(1) are applicable also to the active control coil system to be installed on the plasma-side surface of the shield. When the coil is to be supported by the removable shield modules, the coil system should be made of modular (partial) coils. On the other hand, a toroidal one-turn coil can be used when it is to be supported by the semi-permanent shield, though high reliability is required for the coil due to difficulty in remote maintenance.

Concept(3): Installed in the mid-section of the shield

The dose to the insulator and the nuclear heating rate in the coil are expected to be $\sim 10^{9}$ rad and $\sim 10^{-2}$ W/cc, respectively. Thus the environmental conditions in the mide-section of the shield are largely relaxed compared to those on the outside surface of the blanket, providing possibility of using an organic material for the insulator. The other structural features of this coil system should be similar to that of Concept(2).

Concept(4): Installed on the outside surface of the shield

When the coil system is assumed to be supported by the semi-permanent shield, it should use normal conducting coils forming one-turn toroidally. Under the expected dose condition of $\sim 10^8$ rad, an epoxy material can not be used for the coil insulator due to its poor reliability under irradiation. Then, a coil using a polyimid material for electrical insulation should be developed.

In the lower region of the torus, the active control coil has to be located so as to avoid an interference with the support structure of the shield. When the coil is to be located in the inner-side (torus axis-side) region of the shield support structure, space available for installation is very limited, and careful arrangement should be provided for the installation procedures, such that the active control coil installation precede construction of part of the TFC intercoil structures. It is impossible to make an access to the coil for maintenance because of high activation of the surrounding structures.

Concept(5): Installed on the plasma-side surface of the TFC

In this case, the active control coil should be superconducting since it is to be supported by the toroidal field coils. In general, poloidal field coils have thinner coil/helium vessels than those of toroidal field coils. Accordingly the nuclear heating rate and dose rate in the active control coil are anticipated to be larger than those of the toroidal field coils, and then particular provisions should be given to the design for electrical insulation and cooling. When the thickness of the active control coil helium vessel is increased to one similar to that of the

toroidal field coils, some attention should be paid so as to secure a certain toroidal one-turn resistance in the helium vessel. The construction of the active control coil is expected to face large difficulties since it is preceded by the installation of all of the toroidal field coils. Access to the active control coil for maintenance is almost impossible due to the same reason as given for Concept(4).

Concept(6): Installed on the outside surface of the TFC

The active control coil, being supported by the toroidal field coils, should be super-conducting. Since the coil is located outside the toroidal field coils, its fabrication can be completed in a factory (on-site shop) and installed as a whole onto the torus in the same way as the plasma shaping coils are constructed.

The expected nuclear heating rate and dose to the insulator are considerably small, i.e., $\sim 10^{-6}$ W/cc and $\sim 10^{5}$ rad, respectively, due to shielding effects of the intercoil structures between the toroidal field coils. Similarly the requirements to the helium vessel are not so severe, and it might be feasible to use FRP for the helium vessel.

Concept(7): Installed in the coil vacuum chamber

Both super-conducting coil and normal conducting coil are feasible for this case.

When super-conducting type is selected, the coil system should be similar to that of Concept(6). The coil can be supported by either the shaping coils or the toroidal field coils. It might

be impossible to incorporate the active control coil into the helium vessel of the plasma shaping coil, since large voltages induced in and coupling loss with the shaping coil would pose a problem.

When normal conductor is used, the coil can be fabricated completely in a factory. Unlike the coil for Concept(4), epoxy materials are applicable for electrical insulation. From the viewpoint of thermal insulation, the coil should be supported by the coil vacuum chamber.

3. Evaluation and Impacts on the Reactor Design

Table 2 summarizes the features of the active control coils identified for the candidate positions.

Generally active control coils should be located symmetrically with respect to the midplane, avoiding special interferences with the shaping coils, support structures and exhaust ducts.

In the following section, the active control coils examined are evaluated for the different levels of shell effects required.

3-1 Concepts require less shell effects (Concepts(1),(2) and (3))

Concepts(1), (2) and (3) should not be selected due to the following reasons;

1) Data and practices are insufficient for coils using ceramics for electrical insulation to be located in the plasma vacuum region.
2) Modular (partial) coils have many feeders on which large electromagnetic forces ($\sim$10 t/m) will be exerted. In addition, connection/disconnection operations (including

insulation work) of the feeders, along with those of cooling water tubes, are required on assembling/disassembling of the modules for maintenance.

3) The concepts with one-turn coils can not be reliable systems since the coils, to be located in the plasma vacuum region, are to undergo final fabrication on site, and furthermore access to the coils for maintenance is impracticable after DT operation.

3-2 Concepts require medium shell effects (Concepts(4) and (5))

In these concepts, the active control coils are to be installed on the specified locations after the toroidal coil installation, which means that use of super-conducting is not encouraging.

The active control coil, being normal conducting, should be supported by the outside surface of the shield, and their installation has to wait for completion of the semi-permanent shield construction inside the toroidal field coils. This procedure makes it very difficult to install the active control coil in the lower region of the torus and to make an access to it for maintenance.

Therefore it is highly requested to locate the active control coils outside the toroidal field coils based on the reactor design with large shell effects.

3-3 Concepts require large shell effects (Concepts(6) and (7))

The active control coils for Concepts(6) and (7) can be of high reliability since they are to be fabricated completely in a factory (on-site shop).

For Concepts(6) and (7) the shell effects are required to in-

crease the time scale of plasma vertical movement, γ^{-1}, to approximately 35 msec. Even when the shell offects can not enhance the time scale, γ^{-1}, to more than 20 msec, it is still practical to locate the active control coils outside the toroidal field coils by raising the voltage limit to 500 V and allowing large control power ($\sim$60 MVA).

In order to apply super-conducting coils to the concepts, it is necessary to develop a super-conducting coil endurable against rapid magnetic flux changes, and the efforts seem to yield promising results.

As for normal conducting coils, they can be constructed based on the conventional technologies, and there are no needs for further development.

Impacts on reactor designs are briefly summarized in Table 3.

Table 1 Requirement and Representative Characteristics of Active Coil at Candidate Positions

Position		Vacuum condition	Temperature condition (°K)	Radiation condition (rad) *1	Nuclear heating (w/cc)	One-turn voltage (V) *2,3	Total AT (kAT) *2,3	Power capacity (MVA) *2,3	Plasma instability growth time (msec)
①	Outside blanket	high vacuum for plasma	300 ∿ 420	∿ 10^{11}	∿ 1	200 / 500	∿25 / ∿23	∿5 / ∿11	∿ 5
②	Inside shield	"	"	∿0.3 x 10^{11}	∿0.3	"	"	"	"
③	Within shield	"	"	∿ 10^{9}	∿ 10^{-2}	"	-	-	-
④	Outside shield	Vacuum for cryogenic	"	∿ 10^{8}	∿ 10^{-3}	"	∿75 / ∿70	∿15 / ∿35	∿ 20
⑤	Inside TF/C	"	∿ 4	∿ 10^{8}	∿ 10^{-3}	"	"	"	"
⑥	Outside TF/C	"	∿ 4	∿ 10^{5}	∿ 10^{-6}	"	"	"	∿ 35
⑥	" *4	"	"	"	"	500	∿120	∿60	∿ 20
⑦	Inside cryostat	"	∿ 4 or ∿ 300	∿ 10^{5}	∿ 10^{-6}	200 / 500	∿75 / ∿70	∿15 / ∿35	∿ 35
⑦	" *4	"	"	"	"	500	∿120	∿60	∿ 20

*1 Radiation condition is expressed as a total dose (6.5 MWY/m^2 of fluence at the first wall).

*2 Upper and lower values correspond to the conditions of voltage limiter of 200 and 500 V, respectively.

*3 Electrical resistance along the torus is assumed as 0.2 mΩ.

*4 In case of these coil positions, plasma is unstable when coil voltage limiter = 200 V and plasma instability growth time = 20 msec. Therefore, values for voltage limiter = 500 V are shown.

Table 2 Considerations for Active Control Coilsat Candidate Positions

Position		Conductor	Coolant	Coil type	Insulation	Maintenability	Component to be supported	Note
①	Outside blanket	Normal conducting	H_2O	Partial	Inorganic	Possible	Blanket	① Experience of inorganic insulation in high vacuum is poor. ② Partial coil requires much assemble and disassemble process. ③ Maintenance of full-turn coil is impossible.
②	Inside shield	"	"	Partial / Full turn	"	Possible / Impossible	Movable shield / Semi-permanent shield	
③	Within shield	"	"	Full turn	"	Possible	"	
④	Outside shield	"	"	"	Poly-inside	Impossible	Semi-permanent shield	① Super conduction coil is hard to winding for these positions. ② Maintenance of lower coil is impossible.
⑤	Inside TF/C	Super conducting	Liq. He	"	Epoxy	"	TF-coil	
⑥	Outside TF/C	"	Liq. He	"	"	Possible	"	① Shell structure with higher shell effect is required.
⑦	Inside cryostat	Super conducting / Normal conducting	Liq.He / H_2O	"	"	"	Coil vacuum chamber	

Table 3 Impacts on the Reactor Design

Coil Position	Impacts
①, ②, ③	1. Complicated design of torus module is required in order to provide enough support structure and cooling for active control coils. 2. Lower availability is expected due to less reliability of torus modules on active coil systems. 3. Torus structure without bellows or electric insulation is applicable if RF system is used for plasma current ramp up.
④, ⑤	1. Highly complicated reactor assembling process is required.
⑥, ⑦	1. Rather high shell effects are required for blanket modules.

6. Impact of Blanket Tritium Producing Capability

Task 5

a) Determine the engineering impact of eliminating the T-producing blanket.

b) Determine the engineering impact of incorporating a full T-producing blanket that provides a TBR ≅ 1.

K. Kitamura

T. Uchida

K. Shinya

T. Inoue

5.1. Evaluation of neutronic performance for substitutional blanket concept

5.1.1. Shield blanket concept in the outboard system

Shield thickness in the outboard system is evaluated in case that the outboard tritium breeding blanket is replaced by a shield blanket that has the same material composition with the outboard shield. The thickness of the tritium breeding blanket is 44.35 cm excluding the first wall and the end wall, so the thickness of the shield blanket to be considered here is limited within 44.35 cm. Since the dominant shielding parameter that determines shield thickness in the outboard system is the spatial dose rate in the reactor room, spatial dose rate behind the shield one day after reactor shutdown after two years operation are calculated for variable shield blanket thickness. Calculational model for outboard system is shown in Fig. 5.1.1. One dimensional 42-group neutron transport calculations are performed with ANISN in S_8, P_3 approximations. Using these calculated neutron flux distributions, 54-group gamma sources for gamma transport calculation are calculated with induced activity calculational code ACT4.

Fig. 5.1.2 shows relationship between shield blanket thickness and spatial dose rate behind the outboard shield one day after reactor shutdown. As shown in Fig. 5.1.2, in case of blanket shield thickness of 44.35 cm which is the same thickness with the tritium breeding blanket dose rate behind the outboard shield is 0.19 m rem/hr. This is an order of magnitude lower than not only the design criterion (<2.5 m rem/hr) but also the dose rate in case of tritium breeding blanket (=2.1 m rem/hr).

Since the shield blanket is much better than the tritum breeding blanket in regard to shielding performance, some reduction in shield thickness in case of shield blanket concept can be expected. Fig. 5.1.2 shows that shield blanket of only 27.4 cm thick is equivalent to 44.35 cm thick of the tritium breeding blanket in regard to shielding performance. Then, in case of shield blanket concept, blanket thickness or outboard shield thickness can be approximately 17 cm thinner than that of the tritium breeding blanket, which allows flexibility in TF coil design.

Shielding performance for TF-coils in the outboard system in this shield blanket is summarized in Table 5.1.1. As shown in Table 5.1.1, radiation response parameters in the TF coils in the outboard system are well blow the shielding criteria.

5.1.2 Tritium breeding blanket concept in the inboard system

Shield performance for the TF coils and tritium breeding ratio in the inboard system is evaluated in case that the inboard shield blanket (40 cm thick) is replaced by a tritium breeding blanket. Thickness of the tritium breeding blanket is 40 cm including the first wall, and it material composition is almost same as the outboard blanket, and is shown in Fig. 5.1.3.

One dimensional 42-group neutron and 21-group gamma transport calculation is performed with ANISN in S_8P_3 approximation, and 54-group gamma source is calculated with induced activity calculational code ACT4. One dimensional cylindrical calculational model is shown in Fig. 5.1.3.

(1) Shield performance for the TF coils

Calculated radiation response parameters in the TF coils are summarized in Table 5.1.2.

As shown in Table 5.1.2 none of them except maximum dose in the insulator meet the shielding criteria for TF-coils. The most severe radiation response parameter is the neutron fluence ($E > 0.1MeV$) in the superconductor which is more than five times higher than the criterion. Therefore, additional shield is necessary to meet the shielding criteria, and the thickness of the additional shield is estimated to be 13.0 cm.

(2) Tritium breeding ratio

The tritium breeding zone in the inboard system is 27.85 cm, and its material compositions are SS(12%)+H_2O(6%)+Li_2O(5%) +Li_2O(35.4%) for the blanket (2), where 85% theoretical density and packing fraction 0.7 are taken into account for Li_2O pebbles. In order to breed tritium effectively Li is enriched with 30% ^6Li, and neutron multiplying zone of the 100% Pb proceeded the tritium breeding zone.

The obtained results of tritium breeding ratio by one-dimensional calculation is 0.794. Estimated coverage of the inboard tritium breeding blanket is 20%. Therefore, the tritium breeding ratio in the inboard tritium breeding blanket is estimated 0.159 (0.794×0.2).

5.2. Plasma Parameters

Concerning the shield blanket concept in the outboard system, there is no change in plasma parameters. However, for the tritium breeding banket concept in the inboard system, additional shield is necessary to meet the shielding criteria, and the thickness of the additional shield is estimated to be 13.0 cm. Therefore, the distance between TF coil conductor and plasma surface (Δ=1.42m for INTOR Reference design) should be increased to be Δ=1.55m.

Plasma parameters of full blanket concept are determined by maintaining the ignition with the same risk on plasma confinement performance (confinement time and plasma β). Fig. 5.2.1 shows the relation between plasma main radius and minor radius with variation of the value of Δ.

From this figure, the main plasma radius and minor plasma radius are determined to be R_p=5.47 and a=1.25 respectively.

5.3. Reactor structure

(1) Non-breeding blanket concept

Same structures of vacuum boundary and torus support etc. as long channel diverter concept are basically employed for non-breeding blanket concept.

Figure 5.3.1 illustrates the reactor structure of non-breeding blanket concept.

The bore size of TF coil, of which number is 12, is set to be 6.42 × 9.0m, and the height of the removable core structure is 6.55m.

Though the width region required for retraction becomes narrow for nothing of blanket as shown in Fig. 5.3.1a, adoption of segmentation as one sector per TF coil is impossible. Then the torus structure is segmented as 2 sectors per TF coil, as well as short channel divertor concept.

The divertor structure is also segmented as 2 sectors per TF coil.

(2) Full-breeding blanket concept

Same structures of vacuum boundary and torus support etc. as long channel divertor concept are basically used for full-breeding blanket concept.

The reactor structure of the full-blanket concept is shown in Fig. 5.3.2.

The bore size of TF coil, of which number is 12, is set to be 6.83 × 9.4m, and the height of removable torus structure is 6.7m.

The segmentation of both torus structure and divertor plate is as 2 sectors per TF coil.

The drawings of radial builder for non-breeding blanket and full-breeding blanket concept is illustrated in Fig. 5.3.3.

5.4. Toroidal field coil and poloidal field coil

The esaminations of several impacts on the magnet design of the non-breeding blanket and full-breeding concepts are carried out to compare with the partial breeding blanket concept, which has been designed for INTOR.

The discussion is mainly forcused on the following five principle points.

(a) PF coil location and ampere turn

(b) Out-of-plane force of TF coil

(c) AC loss in TF coil

(d) AC loss in PF coil

(e) Capacity of PF power supply

The bore size of TF coil, of which number is 12, is set to be 6.42 × 9.3m in non-breeding blanket concept and 6.83 × 9.4m in full-breeding blanket concept, respectively. The dimension and the major characteristics of TF coil are shown in Fig. 5.4.1 and Table 5.4.2. TF coil provides the maximum field of 11.7T on the inner surface of the coil and the magnetic ripple of 1.27% in non-breeding blanket concept and 1.19% in full-breeding blanket concept at the plasma outer edge.

The toroidal field distribution on a mid-plane is indicated in Fig. 5.4.2 and Fig. 5.4.3.

(1) PF coil location and ampere turn

Same location and ampere turn of PF coil as the short channel divertor concept are employed for non-breeding blanket concept because of approximate equality of TF coil sizes.

The location and ampere turn of the PF coil for full-breeding blanket concept are arranged according to the increase of the TF coil bore. The PF coils are located at the outside of the TF coils, and their total number is 18 (8 inner solenoid coils and 10 outer ring coils). The location of PF coils for non-breeding blanket concept is illustrated in Fig. 5.4.4 and Table 5.4.3 shows the ampere turns of the coils. Those of full-breeding blanket concept are indicated in Fig. 5.4.5 and Table 5.4.4.

(2) Out-of-plane force of TF coil

The out-of-plane force acting on TF coil are calculated in corresponding to these location and ampere turn of the PF coil, and the in-plane force of the TF coil also obtained because of the difference of the TF coil bore. Figures 5.4.6 to 5.4.9 show these electromagnetic force distributions along the TF coil perimeter.

The maximum local out-of-plane pressures, f_{max}, act on the TF coil side plate at the lower nose region. And these pressures occur the local bending stress in the side plate. The moment around vertical axis, M_Z, issupported mainly by the bending stiffness of the outer TF coil legs.

These values, f_{max} and M_z, are estimated to be 31.9 MN/m and ±230 MN·m for non-breeding blanket concept, and to be 36.1 MN/m and ±257 MN·m for full-breeding blanket concept.

(3) AC losses in TF coils

AC losses in TF coils during normal operation

The AC loss is caused by the changing poloidal field mainly at the superconductor, the helium vessel and the coil support in the TF coils.

(i) AC loss in the superconductors

The configuration of the superconductor in the TF coil of the non-breeding blanket and full-breeding blanket concepts is same as that of the short channel divertor concept.

Figure 5.4.10 shows the conductor structures and Table 5.4.5 indicates their characteristics.

In the superconductor the AC losses are composed of the hysteresis loss, the eddy current loss and the coupling loss, as listed in Table 5.4.6. The coupling loss is the largest for the adopted conductor configuration such as the large matrix area. The CuNi fins are inserted in the matrix to cut the coupling current. The time averaged loss can be calculated from Table 5.4.6 as follows,

Pav=45.5 kW (for non-breeding blanket concept)

Pav=47.5 kW (for full-breeding blanket concept)

(ii) AC loss in TF coil helium vessels

Since the helium vessel is required to withstand against the electromagnetic force, the material should be thick stainless steel. The changing

poloidal field generates the eddy current loss in the vessel. The models for the estimation of the loss are shown in Fig. 5.4.11. The time averaged loss is

Pav = 47.5 kW (for non-breeding blanket)

Pav = 46.0 kW (for full-breeding blanket)

(iii) AC loss in TF coil supports

The TF coil support is placed between TF coils to withstand the electromagnetic out-of-plane forces, and the contact face with the TF coil is covered with insulator to cut the one-turn loop. The eddy current induced by the changing poloidal field generates the loss. The model for the loss calculation is shown in Fig. 5.4.11.

The time averaged loss is

Pav=44.4 kW (for non-breeding blanket concept)

Pav=49.3 kW (for full-breeding blanket concept)

The loss in the supports is dominant compared with other AC losses, since the high field is applied to the support region. Therefore, it is needed that the more insulators should be inserted into the support to reduce the loss. The sum of the AC loss in TF coil is shown in Table 5.4.7.

(4) AC loss in PF coil

AC loss in PF coils during normal operation

The same superconductor structure as the personel access concept is employed, similarly to TF coil.

Figure 5.4.12 shows the conductor configuration and Table 5.4.8 depicts the parameters of the superconductor.
The coil is the source of changing field which holds the plasma in equilibrium, and is subject to the AC loss due to the changing field. The loss occurs in the superconductors, the coil supports and the helium leak shield if used, for PF coils. The loss can be estimated for above components, as follows.

(i) AC loss of PF coil superconductor

The superconductor has been intensively developed to reduce the AC loss. Therefore, the conductors are stranded several times and consist of mixed matrices. The superconductor AC loss is conveniently divided into three contributions, i.e. the hysteresis loss, the eddy current loss and the coupling loss. The formulae are listed in Table 5.4.9. The losses for each coil are summed up taking account of the field patterns from each coil, and then, they are averaged over the duration.

Pav=2.7 kW (for non-breeding blanket concept)

Pav=3.1 kW (for full-breeding blanket concept)

(ii) AC loss of PF coil supports

It is required for PF coil supports that the AC loss should be reduced as small as possible and the supports should endure the electromagnetic forces.

First of all, the supports should not electrically close to make a circle around the torus axis, otherwise the loss is vast.

The AC Loss can be estimated from the following equation.

$$P = \frac{t_w}{12\rho} \int \dot{B}^2 d \quad (W)$$

where, ρ is the resistivity of the support material, and the other nomenclatures are shown in Fig. 5.4.13. The thickness 50 mm needed from the stress analysis, and the magnetic field corresponding to the PF coil current waveforms are inserted into above equation. The losses of each coil are summed up and them, they are averaged over the duration.

Pav = 9.0 kW (for non-breeding blanket concept)

Pav = 10.0kW (for full-breeding blanket concept)

(iii) AC loss in PF coil helium leak shields

The helium leak shield may be needed at the present time, since the helium leakage from the vessel is inevitable as long as the large FRP's are adopted to the vessels. It can consist of metal such as stainless steel to be sealed tightly, and therefore it is expected that the AC loss might be vast due to one turn loop, even though the thickness is as thin as possible. The SS thickness of 0.5 mm is assumed in the following analysis.

The dominant loss may be the induced current loss due to the linkage flux, and obtained as follows,

$$p = \frac{\dot{\phi}^2}{R} \quad (W)$$

where, ϕ is the linkage flux in the shield, R the resistance. The losses for each leak shield are summed up taking account of the field patterns, and they are averaged over the duration.

Pav = 40.1 kW (for non-breeding blanket concept)

Pav = 46.6 kW (for full-breeding blanket concept)

The shield loss is inacceptably large comparing with the other AC losses in superconductors and coil supports. Therefore, it is necessary to develop the way to seal the FRP vessel through non-metalic material.
The sum of the AC loss in PF coil is shown in Table 5.4.10.

(5) Power supply

The power supply capacity for the PF coils is approximately in proporation to the MG peak power for the PF coils. The MG peak power for the PF coils of the non-breeding and full-breeding blanket concept is estimated to be 1.77 GW and to be 2.17 GW, respectively.
Table 5.4.11 summarizes the other studied results concerning the magnet system of the non-breeding blanket and full-breeding blanket concepts.

Table 5.1.1 Radiation response parameters in the TF coils in the outboard system in case of 27.4 cm shield blanket thickness

Parameters	Criteria	Calculated
(1) Total nuclear heating in the TF-coils (kW)	<5.0	0.6×10^{-3}
(2) Maximum neutron fluence in the superconductor (ncm^2) (E>0.1 MeV)	$<10^{18}$	6.9×10^{13}
(3) Maximum induced resistivity in the copper stabilizer (Ω-cm)	$<9\times10^{-8}$	6.2×10^{-12}
(4) Maximum dose in the insulator (rads)	$<10^{10}$	1.1×10^{4}

Table 5.1.2 Radiation response parameters in the TF coils in the inboard system in case of shield blanket and the tritium breeding blanket

Parameters	Criteria	Shield blanket	T-breeding blanket
(1) Total nuclear heating in the TF coils (kW)	<5	2.05	10.7
(2) Maximum neutron fluence in the superconductor (n/cm^2) (E>0.1 MeV)	$<10^{18}$	1.0×10^{18}	5.3×10^{18}
(3) Maximum induced resistivity in the copper stabilizer (Ω-cm)	$<9 \times 10^{-8}$	8.3×10^{-8}	4.7×10^{-7}
(4) Maximum dose in the insulator (rads)	$<10^{10}$	7.4×10^{8}	5.8×10^{9}

Table 5.4.1 Characteristics of reactor structure for non-breeding blanket and full-breeding blanket concepts.

	Non breeding blanket	Full blanket
TF coil bore	6.42mW × 9mH	6.83mW × 9.4mH
*	(28.96m)	(29.79m)
Ripple of TFC	1.27	1.19
Height of replacement structure	6.55m	6.7m
Segmentation of blanket	2 Sectors/TFC	2 Sectors/TFC
Segmentation of divertor	2 Sectors/TFC	2 Sectors/TFC
Blanket retraction	Single straight motion for first sector 2 straight motions for second sector	Single straight motion for first sector 2 stragiht motions for second sector
Divertor retraction	Single straight motion	Single straight motion
Size of cryostat	ϕ25m × 20mH	ϕ25m × 20.5m

Note: * ( ) shows length of toroidal coil along a center of conductor.

Table 5.4.2 Major characteristics of TF magnet system for non-breeding blanket and full-breeding blanket concepts.

1.	Total ampere-turns	143 MAT	143 MAT
2.	No. of coils	12	12
3.	Ampere-turns per coil	11.9 MAT	11.9 MAT
4.	Plasma major radius	5.2 m	5.2 m
5.	Field at plasma axis	5.5 T	5.5 T
6.	Helium condition	Pool boiling	Pool boiling
7.	Grading concept	3 grades (12, 10, 5T)	3 grades (12, 10, 5T)
8.	Winding configuration	Flat wound in pancakes	Flat wound in pancakes
9.	Superconductor	Copper stabilized Nb_3Sn and NbTi	Copper stabilized Nb_3Sn and NbTi
10.	No. of turns per coil	540	540
11.	No. of pies per coil	22	22
12.	Operation current	22.07 kA	22.07 kA
13.	Critical current	33 kA	33 kA
14.	Avg. winding current density	19.4 A/mm^2	19.4 A/mm^2
15.	Maximum field	11.7 T	11.7 T
16.	Cooling spacer thickness	3.0 mm	3.0 mm
17.	Cooling surface	Rough surface (mechanical and chemical treatment)	Rough surface (mechanical and chemical treatment)
18.	Inductance	∿122 H	∿127 H
19.	Magnetic field energy	∿29.7 GJ	∿30.9 GJ

Table 5.4.3 Coordinate and ampere-turns of PP coils for non-breeding blanket concept

Coil No.	Black No.	Coil Location R(m)	Coil Location Z(m)	Time (sec) 0	0.2	5	11	211	226	246
1	1	1.35	0.50	5.430	4.325	-3.424	-4.636	-5.993	0	5.430
2	2	1.35	1.50	5.495	4.384	-3.408	-4.661	-6.034		5.495
3	3	1.35	2.50	5.283	4.184	-3.467	-4.587	-5.908		5.283
4	4	1.35	3.50	6.525	5.698	1.302	-2.768	-4.400		6.525
5	5	1.70	4.80	5.578	5.003	1.245	-2.234	-3.629		5.578
6	6	3.00	6.00	2.031	2.203	4.475	0.681	0.173		2.031
7	7	4.50	6.20	0.509	0.872	3.685	2.717	2.590		0.509
8	8	7.40	6.00	0.378	-0.125	-3.992	1.068	0.974		0.378
9	9	11.00	4.20	0.309	0.410	1.314	-4.597	-4.675		0.309
10	10	1.35	-0.50	5.430	4.325	-3.424	-4.636	-5.993		5.430
11	11	1.35	-1.50	5.495	4.385	-3.407	-4.660	-6.033		5.495
12	12	1.35	-2.50	5.283	4.185	-3.446	-4.586	-5.907		5.283
13	13	1.35	-3.50	6.527	5.831	1.433	-2.638	-4.270		6.527
14	14	1.70	-4.80	5.580	4.988	1.229	-2.251	-3.646		5.580
15	15	3.00	-6.00	2.031	3.221	13.153	12.428	11.921		2.031
16	16	4.50	-6.20	0.508	2.104	14.852	24.788	24.641		0.508
17	17	7.40	-6.00	0.353	-0.468	-6.973	-3.278	-3.366		0.353
18	18	11.10	-4.70	0.370	-0.609	-8.246	12.570	-12.662		0.370
Plasma		5.30	0.50	0.000	0.600	5.400	6.400	6.400	0	0.000

Unit : MAT

Table 5.4.4 Coordinate and ampere-turns of PF coils for full-breeding blanket concept

Coil No.	Black No.	Coil Location		Time (sec)						
		R(m)	Z(m)	0	0.2	5	11	211	226	246
1	1	1.350	0.500	5.001	3.692	-4.816	-4.901	-6.013	0	5.001
2	2	1.350	1.500	5.027	3.714	-4.817	-4.916	-6.033	↓	5.027
3	3	1.350	2.500	4.946	3.646	-4.814	-4.872	-5.971		4.946
4	4	1.350	3.500	5.558	4.662	-0.235	-3.020	-4.255		5.558
5	5	1.700	4.800	7.237	6.069	-0.306	-3.932	-5.540		7.237
6	6	3.000	6.000	1.941	1.786	1.879	-0.541	-0.992		1.941
7	7	4.500	6.400	0.817	1.023	3.067	1.825	1.643		0.817
8	8	7.400	6.200	0.422	-0.003	-3.363	1.262	1.148		0.422
9	9	11.000	4.200	0.283	0.395	1.436	-4.250	-4.312		0.283
10	10	1.350	-0.500	5.003	3.694	-4.816	-4.902	-6.014		5.003
11	11	1.350	-1.500	5.025	3.712	-4.817	-4.914	-6.031		5.025
12	12	1.350	-2.500	4.953	3.652	-4.814	-4.875	-5.976		4.953
13	13	1.350	-3.500	5.545	4.650	-0.234	-3.013	-4.245		5.545
14	14	1.700	-4.800	7.261	6.090	-0.307	-3.945	-5.559		7.261
15	15	3.000	-6.000	1.923	3.030	12.908	13.216	12.789		1.923
16	16	4.500	-6.400	0.824	2.381	15.459	25.827	25.644		0.824
17	17	7.400	-6.200	0.396	0.115	-2.005	0.235	0.147		0.396
18	18	11.000	-4.600	0.310	-1.047	-11.991	-14.646	-14.715	↓	0.310
Plasma		5.470	0.400	0.000	0.600	5.500	6.520	6.520	0	0.000

Table 5.4.5 Characteristics of the superconductor

		12^T conductor	10^T conductor	5^T conductor
1.	Superconducting wire	Copper stabilized Nb_3Sn	Copper stabilizee Nb_3Sn	Copper stabilized NbTi
2.	Maximum field	11.7^T	10.2^T	4.9^T
3.	Conductor current	22.07 kA	22.07 kA	22.07 kA
4.	Ic at 4.2 k	33 kA	33 kA	33 kA
5.	Conductor size	30×39 mm^2	21×39 mm^2	16×39 mm^2
6.	Element size	35×42 mm^2	26×42 mm^2	21×42 mm^2
7.	Cable size	8×18.4 mm^2	8×10.2 mm^2	3.6×9.3 mm^2
8.	Conductor current density	18.8 A/mm^2	26.9 A/mm^2	35.4 A/mm^2
9.	Element current density	15.0 A/mm^2	20.2 A/mm^2	25.0 A/mm^2
10.	Conductor copper ratio	15.5	18.2	42.5
11.	Interturn reinforcement	5 mm	5 mm	5 mm
12.	$\rho 0$	6.2×10^{-8} Ωcm	5.6×10^{-8} Ωcm	3.4×10^{-8} Ωcm
13.	$\Delta\rho$ (1.1×10^{18} n/cm^2)	9×10^{-8} Ωcm	5.3×10^{-8} Ωcm	0.6×10^{-8} Ωcm
14.	ρt	15.2×10^{-8} Ωcm	10.9×10^{-8} Ωcm	3.9×10^{-8} Ωcm
15.	Heat flux	0.39 w/cm^2	0.47 w/cm^2	0.24 w/cm^2
16.	No. of strands	9	5	11
17.	Cooling surface	Rough surface (mechanical and chemical treatment)		
18.	Minimum winding radius	2.21 m	2.32 m	2.63 m
19.	Maximum winding strain	0.18%	0.17%	0.06%

Table 5.4.6 AC loss formulae in TF coil superconductor

1. Hysteresis loss

$$Ph_{\perp} = \frac{2}{3\pi} Jc(B)\dot{B}_{\perp} \quad (w/m^3)$$

$$Ph_{\parallel} = \frac{1}{6} Jc(B)\dot{B}_{\parallel} \quad (w/m^3)$$

2. Eddy current loss

$$Pe_{\perp} = \frac{1}{12\rho} a^3 b \dot{B}_{\perp}^2 \quad (w/m)$$

$$Pe_{\parallel} = \frac{1}{2\pi^2\rho} \frac{a^3b^3}{a^2+b^2} \dot{B}_{\parallel}^2 \quad (w/m)$$

3. Coupling loss

$$Pc_{\perp} = \frac{1}{\rho_{\perp}} \left(\frac{\ell P}{2\pi}\right)^2 \dot{B}_{\perp}^2 \quad (w/m^3)$$

where,

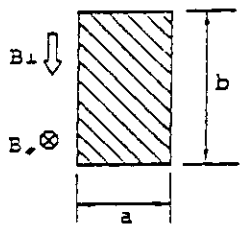

Cross section and field direction

Jc(B): critical current density

d : filament diameter

ρ : matrix resistivity

ρ : transverse resistivity

ℓP: twist pitch

Table 5.4.7 AC losses in TF coil with operation

	Non-breeding blanket concept	Full-breeding blanket concept
Superconductors	45.5 kW	46.5 kW
Helium Vessel	47.5 kW	46.0 kW
Coil Supports	44.4 kW	49.3 kW
Sum	137.4 kW	141.9 kW

Table 5.4.8 Parameters of superconductor

1.	Final Level	
(1)	Operating current	53.8 kA
(2)	Critical current	85 kA
(3)	Cable size	130mm × 18mm
(4)	Number of subcables	31
(5)	Mandrel core size	115mm × 4mm
(6)	Cable twist pitch	1300 mm
(7)	Effective perimeter	520 mm
(8)	Conductor current density	23 A/mm²
(9)	Winding current density	14 A/mm²
(10)	Maximum field	7.1T
2.	Subcable	
(1)	Subcable diameter	8 mm
(2)	Number of strands	6
(3)	Core strand material	Stainless steel
(4)	Twist pitch	50 mm
3.	Strand	
(1)	Strand diameter	2.67 mm
(2)	Number of NbTi filaments	6156
(3)	Twist pitch	40 mm
(4)	Surface treatment	Formval
(5)	Number of bundless	18
(6)	NbTi : Cu : CuNi	1 : 9.58 : 1.04

Table 5.4.8 Parameters of superconductor (continued)

4. Bundle		
	(1) Bundle diameter	0.338 mm
	(2) Number of filaments	342
	(3) Surface CuNi thickness	11.7μm
	(4) NbTi:Cu:CuNi	1:1.33:1.04
5. Filament		
	(1) NbTi filament diamter	10μm
	(2) OFHC thickness	2.1μm
	(3) Surface CuNi thickness	1μm
	(4) NbTi:Cu:CuNi	1:1.02:0.59

Table 5.4.9 AC loss formulae in PF coil superconductor

1. Hysteresis loss

$$Ph_{\perp} = \frac{2}{3\pi} Jc(B)\dot{dB}_{\perp} \qquad (w/m^3)$$

$$Ph_{\parallel} = \frac{1}{6} Jc(B)\dot{dB}_{\parallel} \qquad (w/m^3)$$

2. Eddy current loss

$$Pe_{\perp} = \frac{1}{4\rho} \dot{B}_{\perp} r_0^2 \qquad (w/m^3)$$

3. Coupling loss

$$Pc_{\perp} = \frac{1}{\rho_{\perp}} \left(\frac{\ell P}{2\pi}\right)^2 \dot{B}_{\perp}^2 \qquad (w/m^3)$$

where,

$Jc(B)$: critical current density

d : filament diameter

$\rho_{\perp}$: matrix resistivity

ρ : transverse resistivity

ℓP: twist pitch

γ_0: strand radius

Table 5.4.10 AC losses in PF coil with operation

	Non-breeding blanket concept	Full-breeding blanket concept
Superconductors	2.7 kW	3.0 kW
Coil supports	9.0 kW	10.0 kW
(Helium leak shield)	(40.1 kW)	46.6 kW
Sum	11.7 kW (51.7 kW)	13.1 kW (59.7 kW)

Table 5.4.11 Summary of studied results for non-breeding blanket and full-breeding blanket concepts

		Non-breeding blanket	Full breeding blanket
Plasma	Major radius (m)	5.3	5.47
	Minor radius (m)	1.2	1.25
	Plasma elongation	1.5	1.5
	Plasma start-up	by RFCD and OH coils	by RFCD and OH coils
Main characte-ristics	No. of TFC	12	12
	Start-up voltage (V)	35	35
	Max. ring-coil radius (m)	11.1	11.0
	TFC perimeter (m)	29.0	29.8
	TF coil bore (m)	6.42 × 9.3	6.83 × 9.4
	Magnetic ripple (%)	1.266	1.192
TF coil	Max. Bt (T)	11.7	11.7
	Hoop force (MN)	1164	1181
	Centering force (MN)	-386	-397
	f_{max} (MN/m)	31.9	36.1
	M_R (MN.m)	127	138
	Mz (MN.m)	230	257
	AC loss (kW)	137	142
	$<\int \dot{B}^2_{\perp} d\ell>$ (T^2m/s^2)	3.364×10^{-2}	3.22×10^{-2}
	$<\int \dot{B}_{L\perp} d\ell>$ (T^2m/s^2)	3.13×10^{-2}	3.07×10^{-2}
	Stored energy (GJ)	29.7	30.9
PF coil	Ampere turn (MAT)	103	107
	Max field, B_{pmax} (T)	7.26	7.58
	Field change, B_{pmax} (T/S)	6.34	7.67
	One-turn voltage (V)	228	276
	AC loss (kW)	12(52)	13(60)
	Energy (GJ)	6.90	7.81
	MG peak power (GW)	1.77	2.17

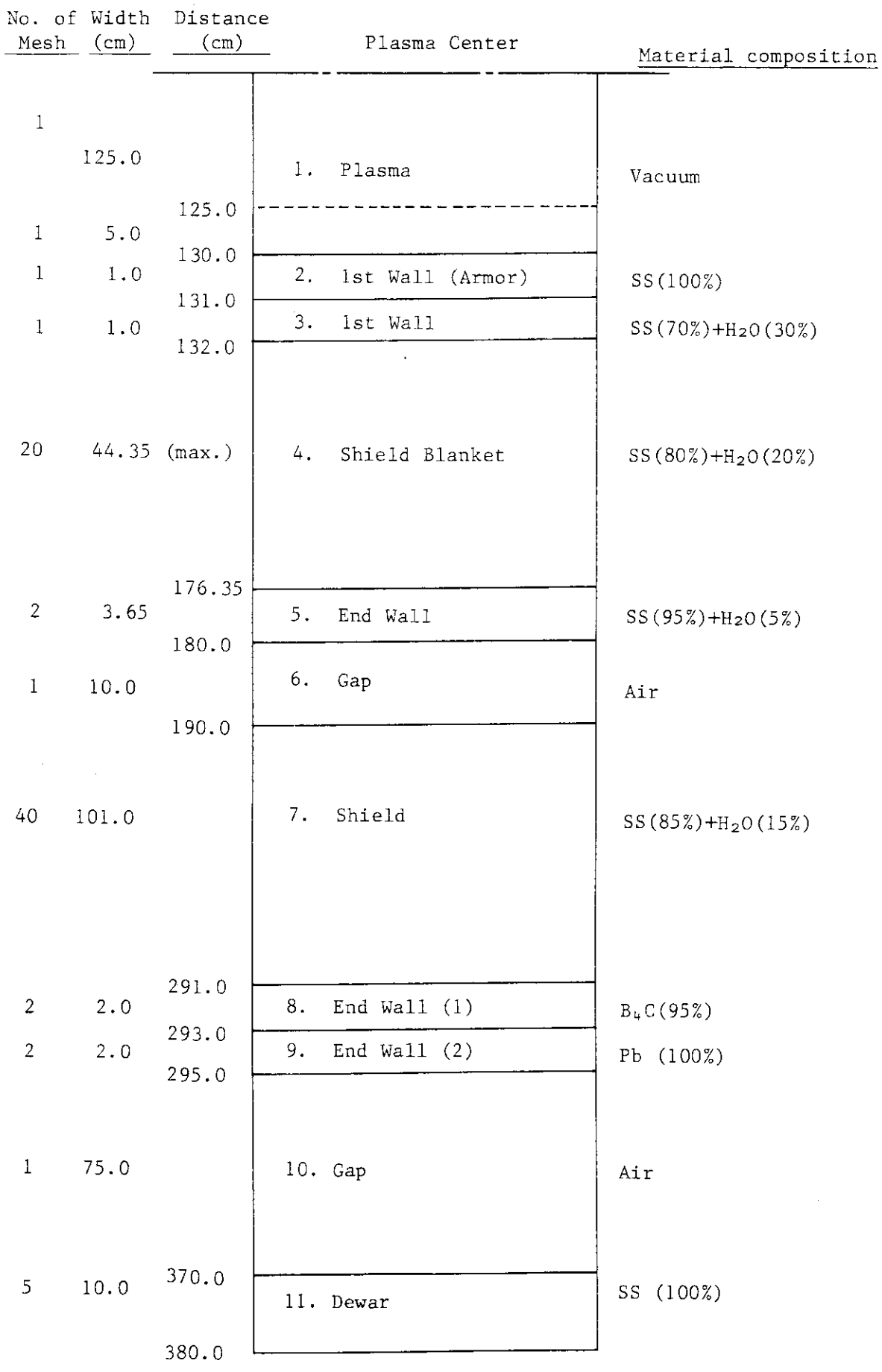

Fig. 5.1.1 Calculation model for outboard system in case of shield blanket concept

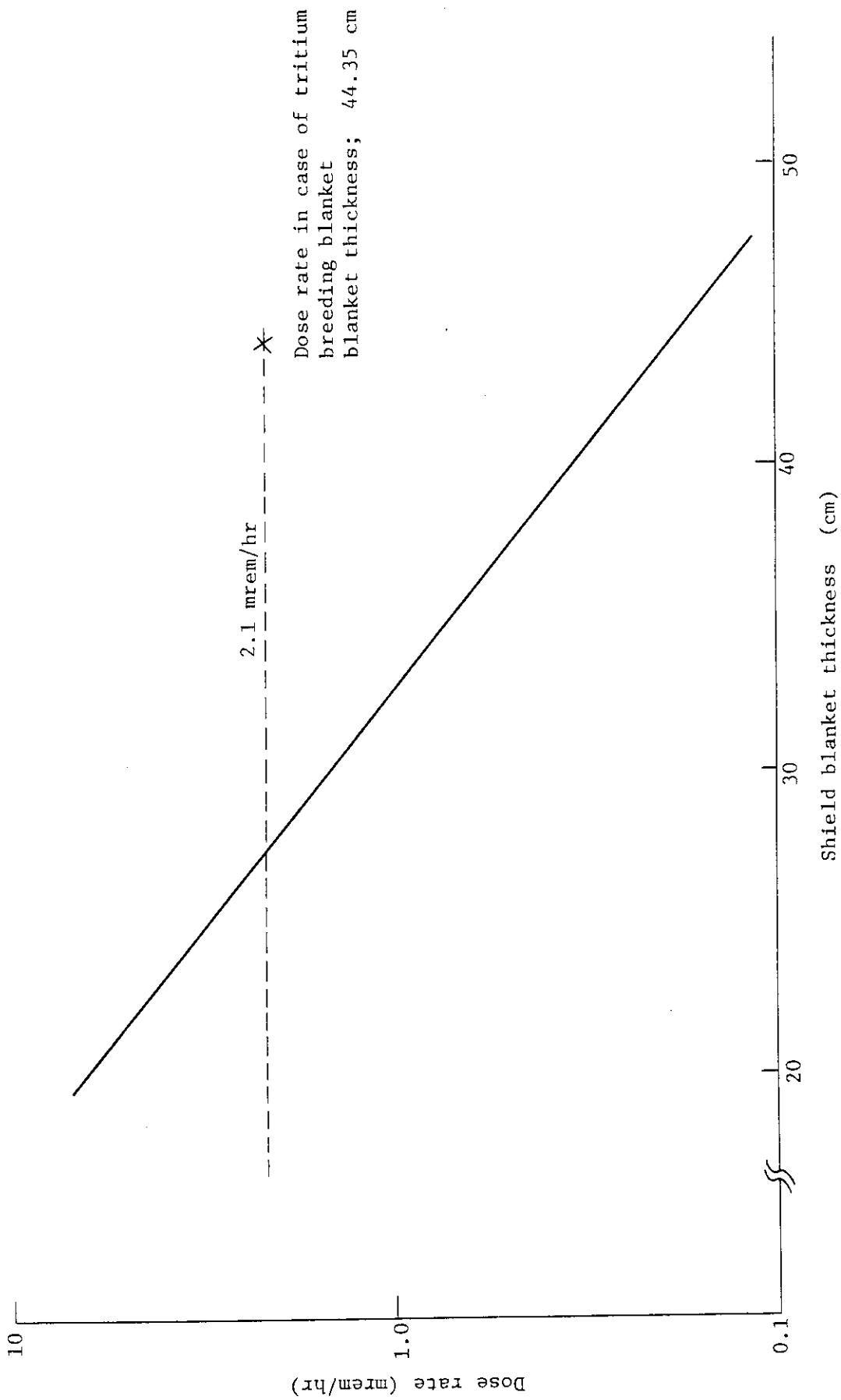

Fig. 5.1.2 Relationship between shield blanket thickness and dose rate behind the outboard shield one day after reactor shutdown after two years full power operation

No. of Mesh	Width (cm)	Distance (cm)	Plasma Center	Material composition
			1. Plasma	Vacuum
1	145	145		
1	5	150	2. 1st Wall (Armor)	SS(100%)
1	1.5	151.5 152.5	3. 1st Wall	SS(50%)+H_2O(50%)
3	5		4. Pb Multiplier	Pb(100%)
1	1	157.5	5. 2nd Wall	SS(70%)+H_2O(30%)
3	6	158.5	6. Blanket (1)	SS(12%)+H_2O(6%)+Li_2O(34.2%)
11	21.85	164.5	7. Blanket (2)	SS(11%)+H_2O(5%)+Li_2O(35.4%)
2	3.65	186.35	8. Blanket End Wall	SS(21%)+H_2O(30%)
19	38	190	9. Semi-Permanent Shield	SS(80%)+H_2O(20%)
1	4	228 232	10. Gap	Air
6	12		11. Dewar	SS(100%)
1	16.5	244 260.5	12. Gap	Air
5	10		13. TF-coil Support	SS(100%)
1	1.35	270.5 271.85	14. Gap	Air
18	67.3		15. TF Coil Conductor	Cu(76%)+SS(12%)+LiqHe(12%)
1	1.35	339.15 340.5	16. Gap	Air
11	34		17. TF Coil Support	SS(100%)
		374.5		

Fig. 5.1.3 Calculation model for inboard system in case of tritium breeding blanket.

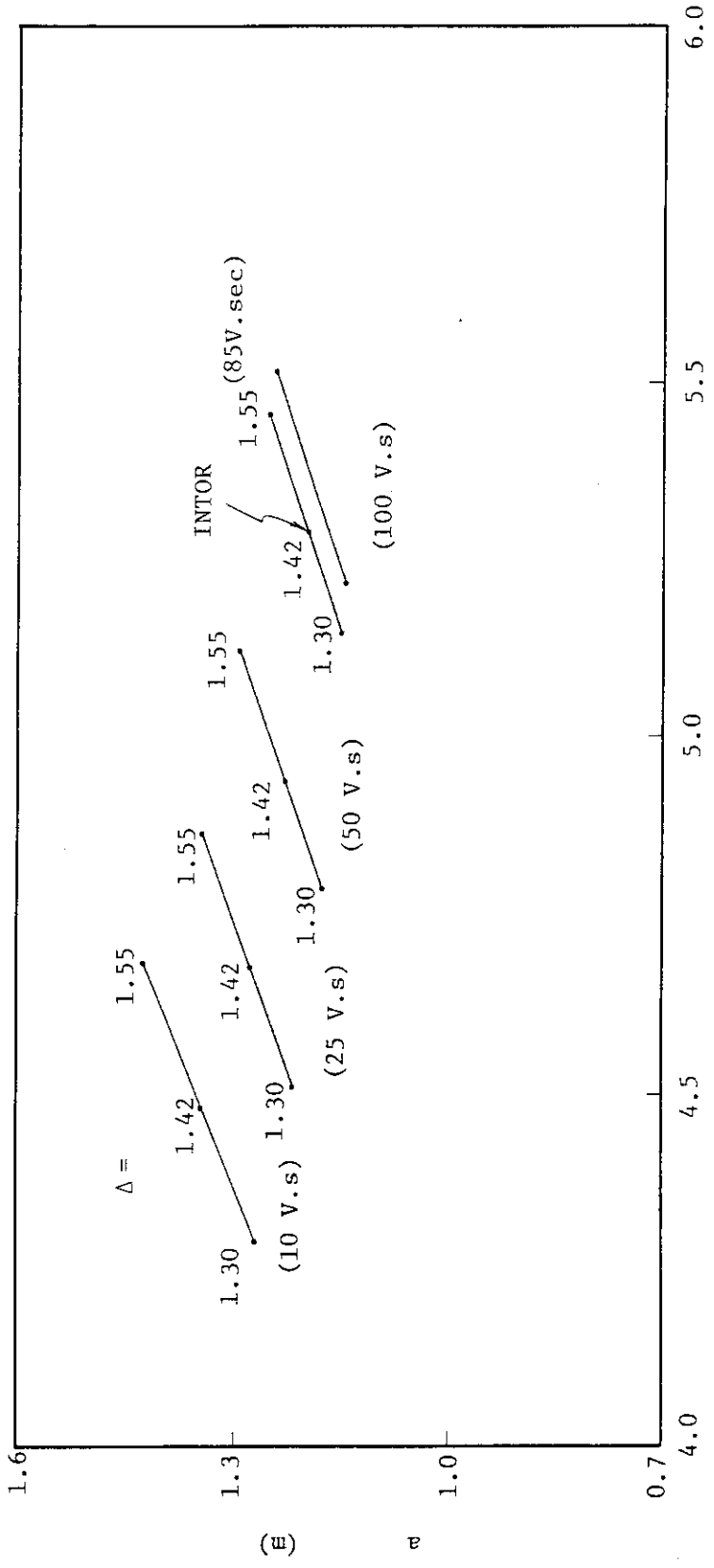

Fig. 5.2.1 Relation between R and a

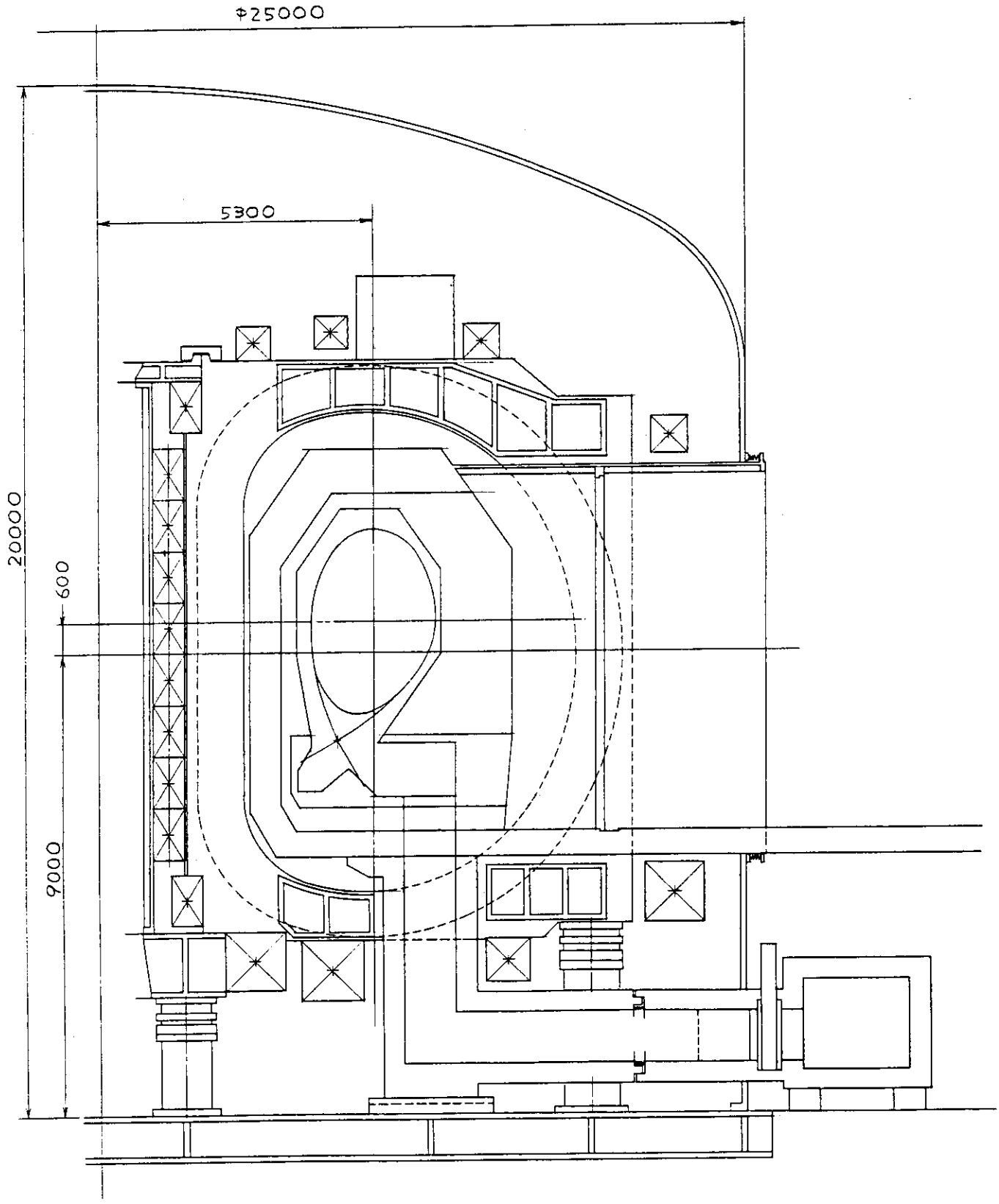

Fig. 5.3.1 Vertical view of non breeding reactor concept

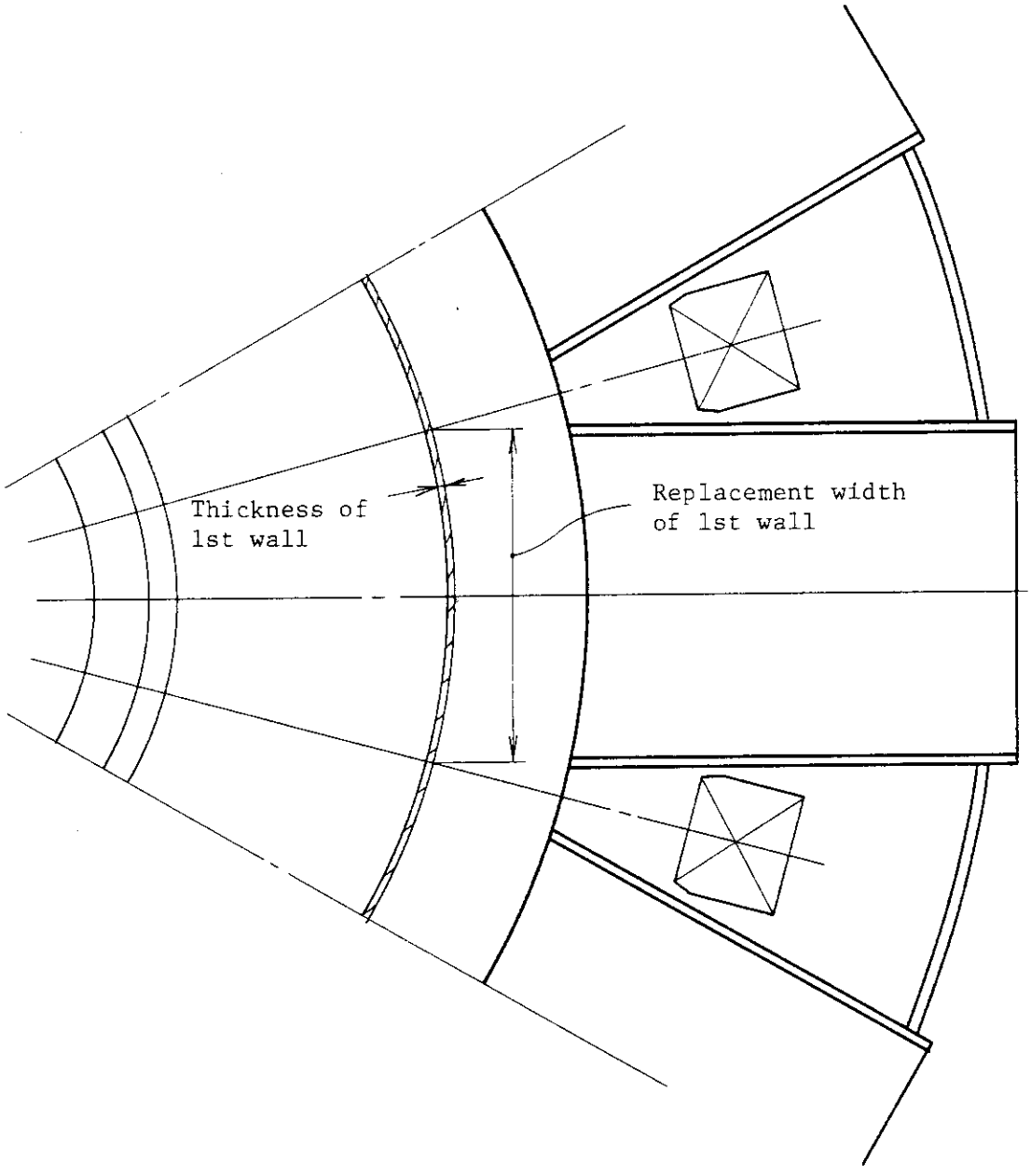

Fig. 5.3.1a Retraction of torus structure with segmentation as one sector per TF coil

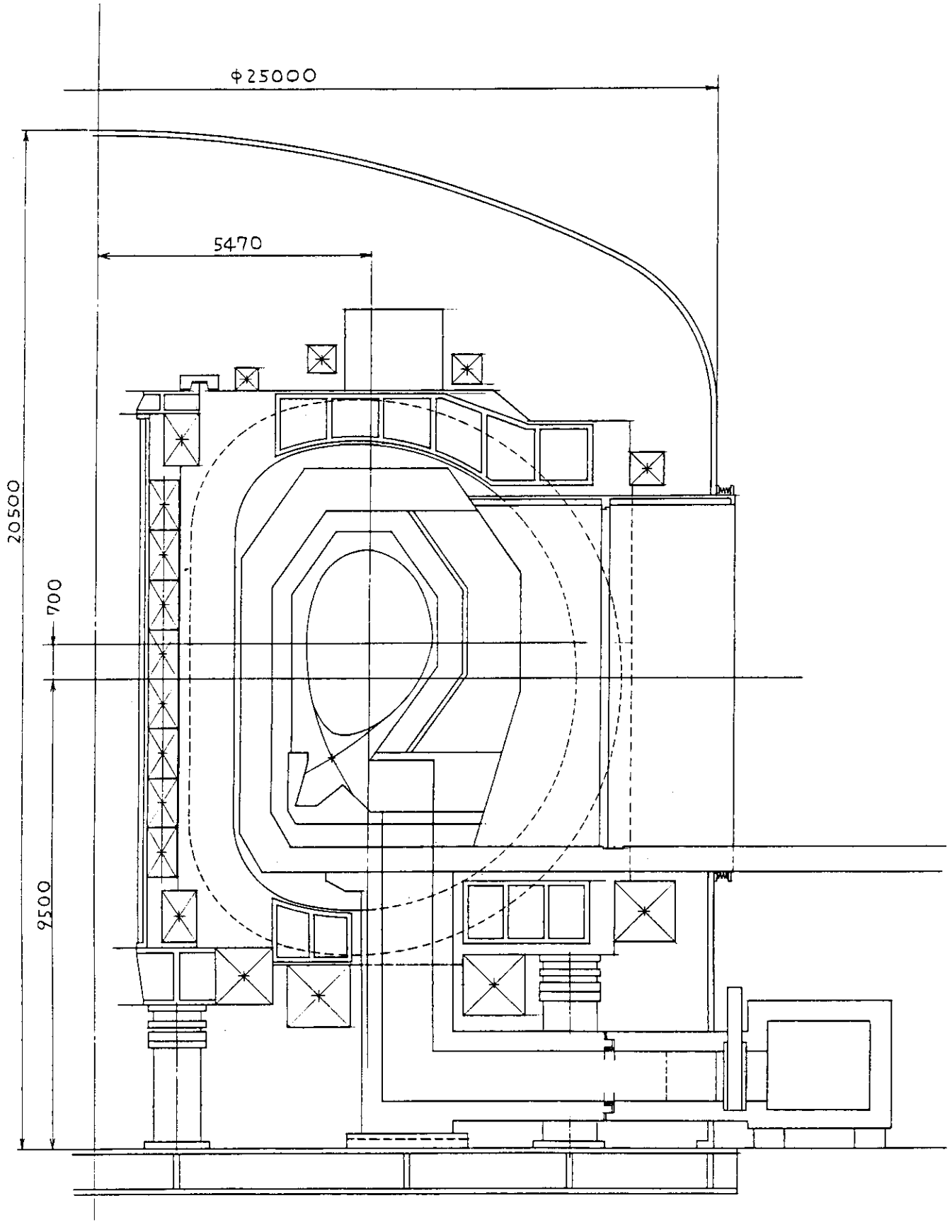

Fig. 5.3.2 Vertical view of full-breeding reactor concept

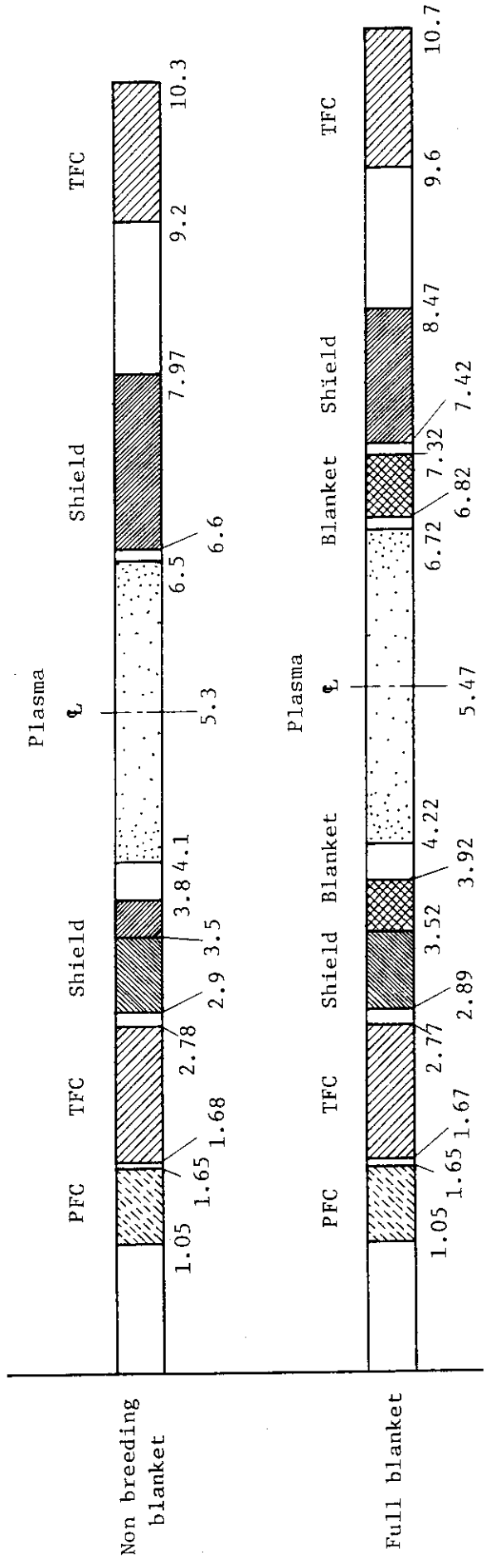

Fig. 5.3.3 Radial builds of non-breeding blanket and full-breeding blanket concepts

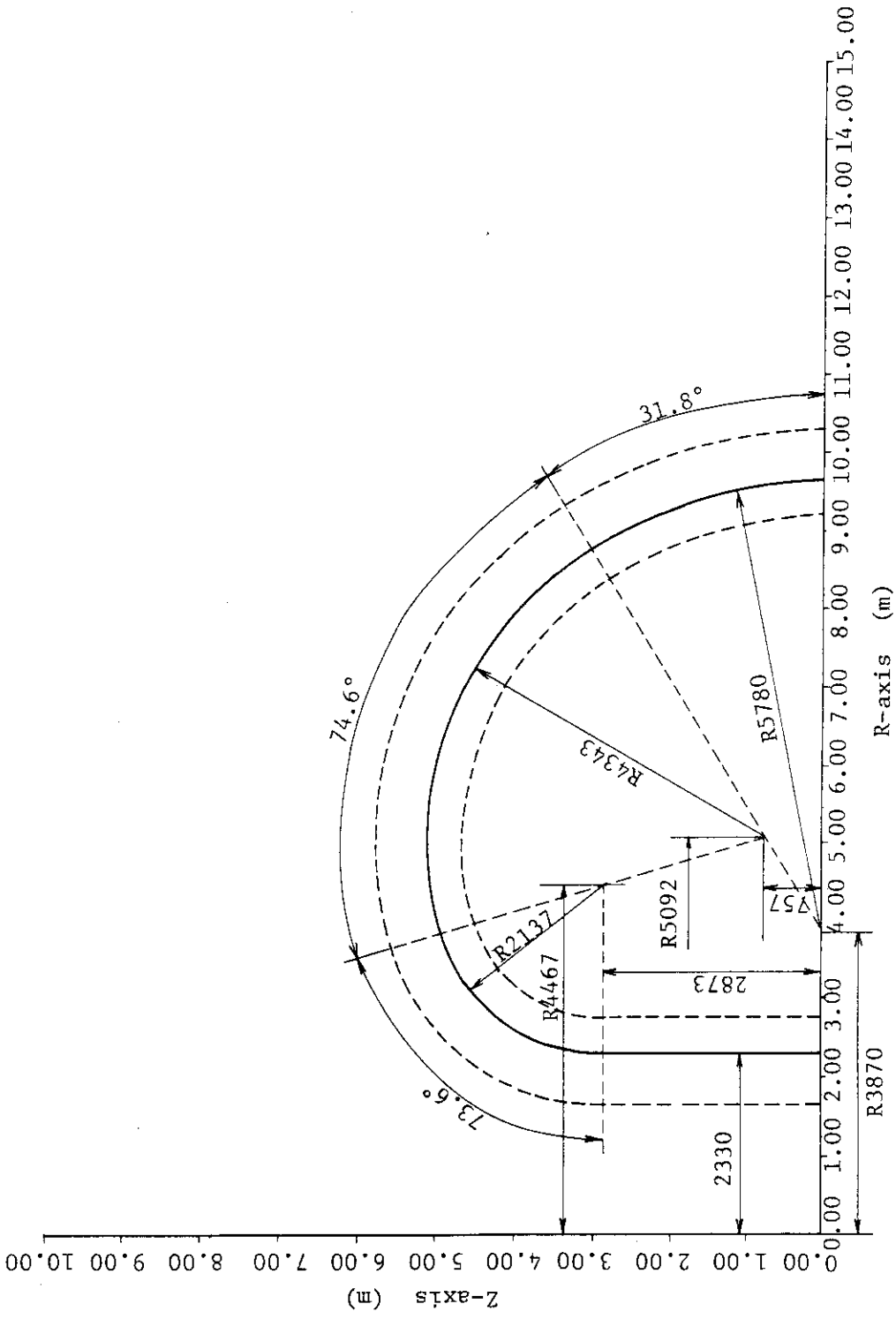

Fig. 5.4.1a TF coil dimension for non-breeding blanket concept

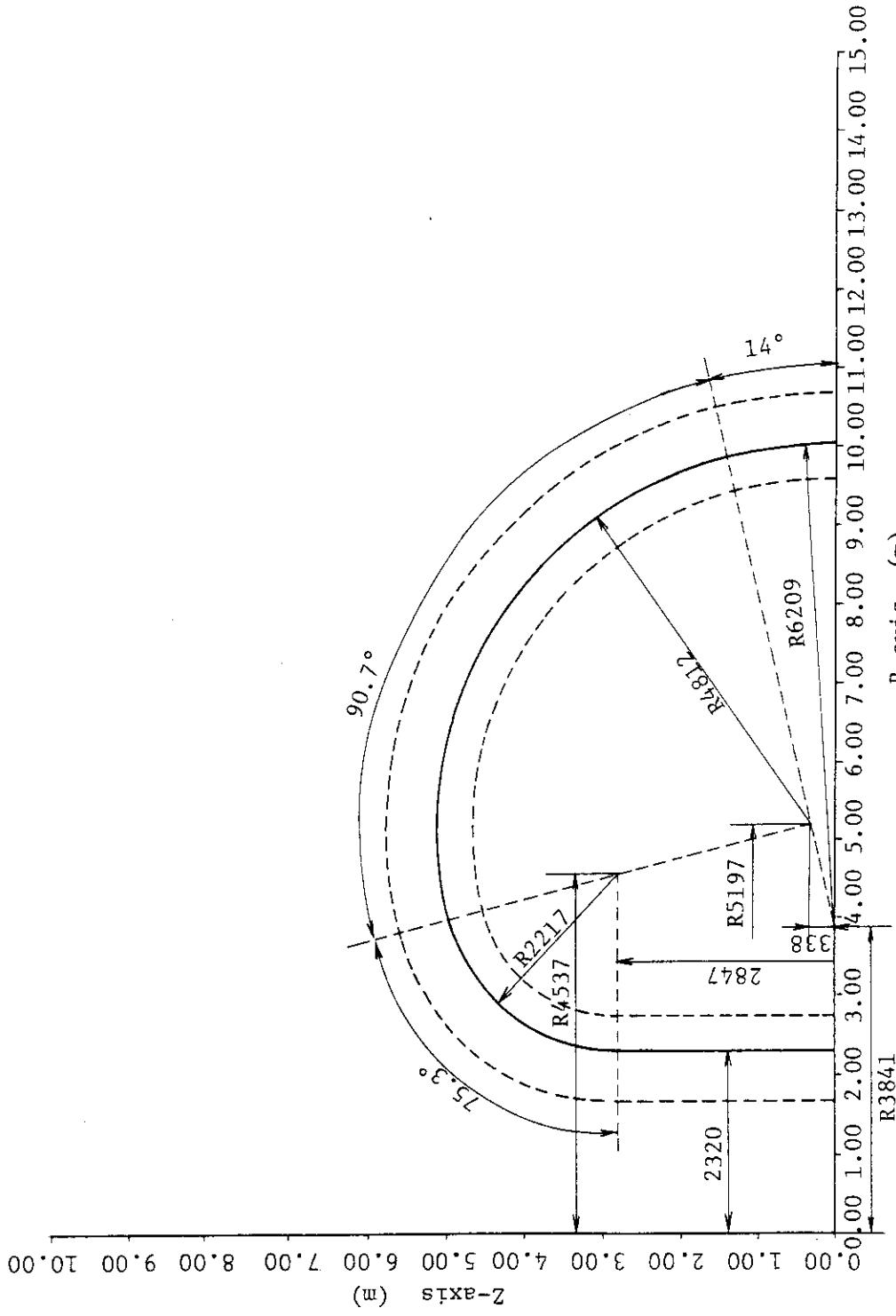

Fig. 5.4.1b TF coil dimension for full-breeding blanket concept

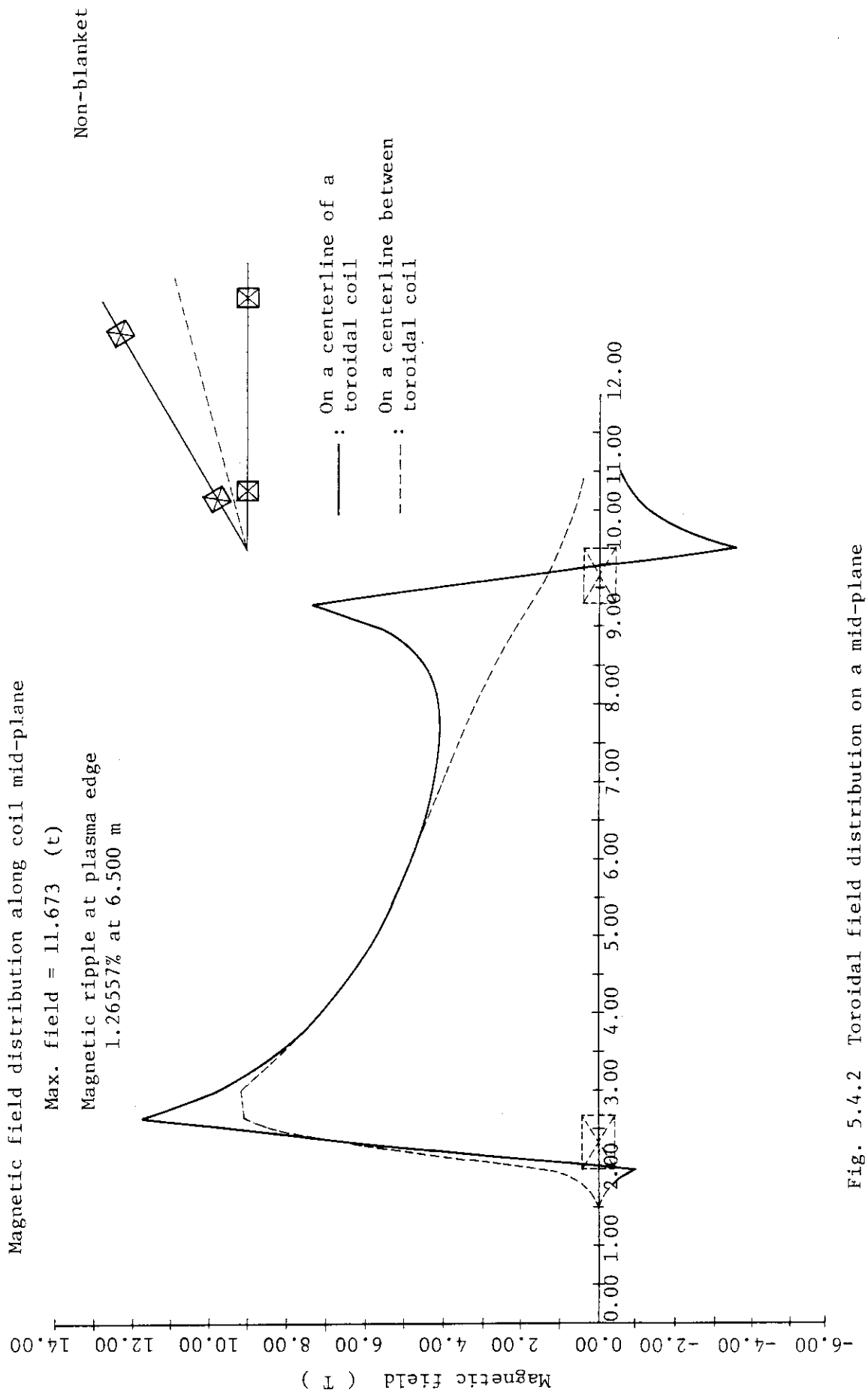

Fig. 5.4.2 Toroidal field distribution on a mid-plane
(for non-breeding blanket concept)

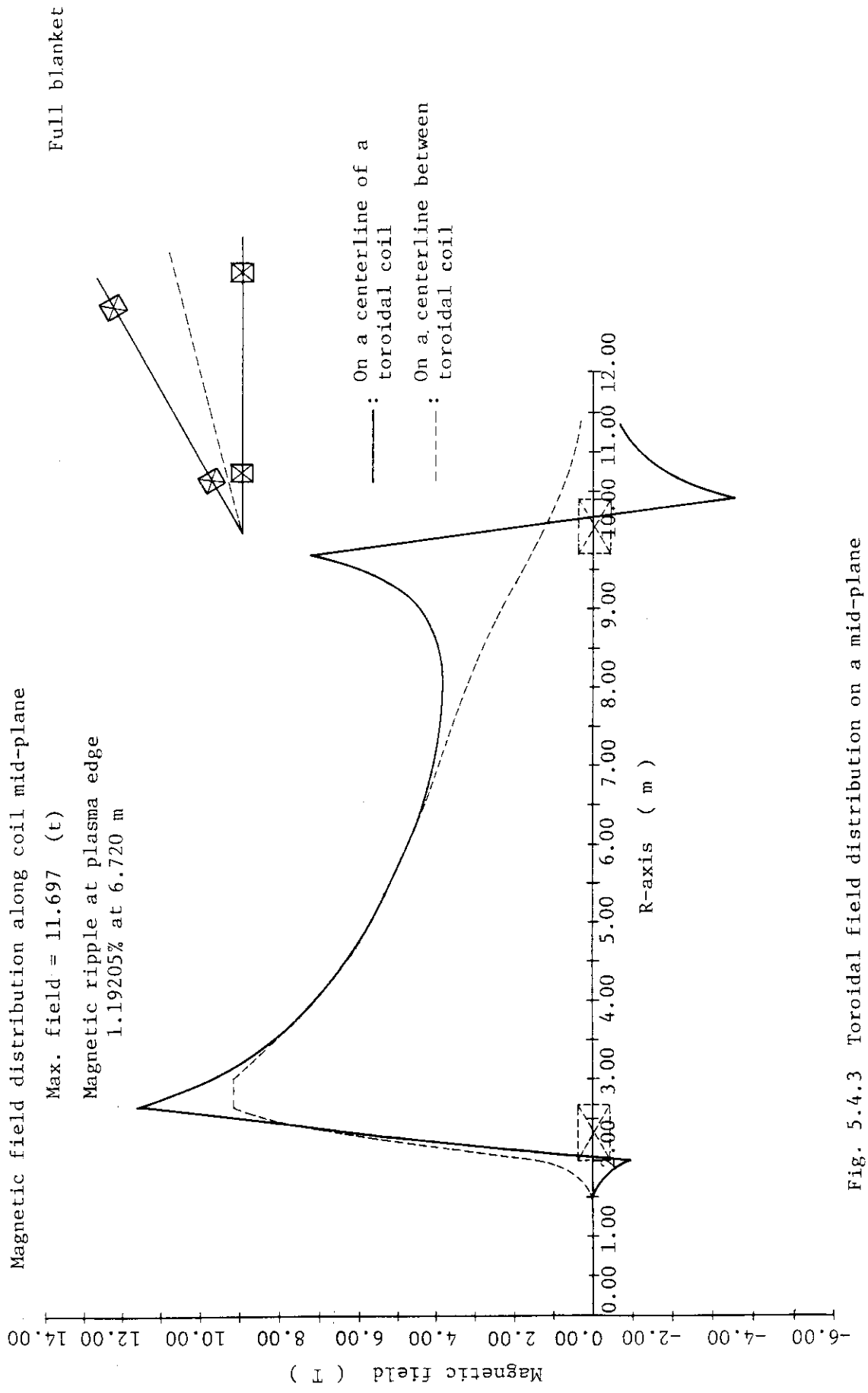

Fig. 5.4.3 Toroidal field distribution on a mid-plane
(for full-breeding blanket concept)

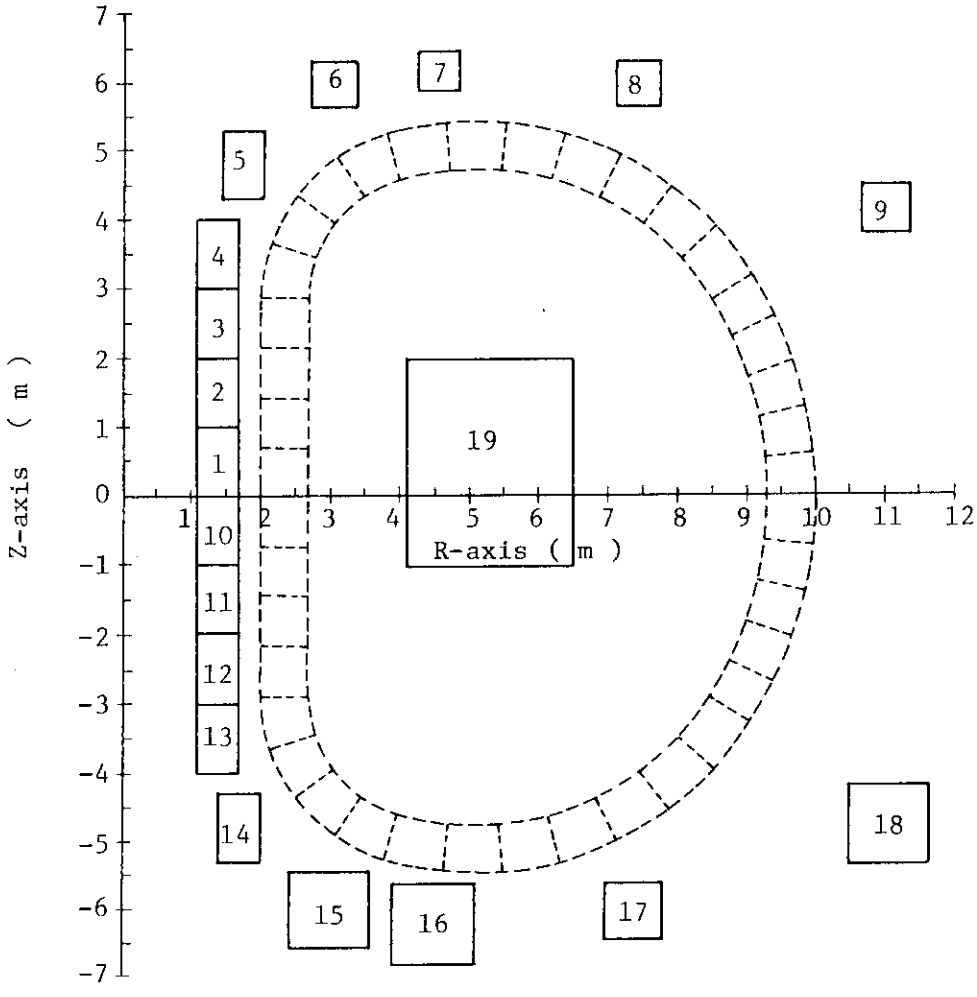

Fig. 5.4.4 Poloidal coil location for non-breeding blanket concept

Note: TF coil configuration indicates coil winding area

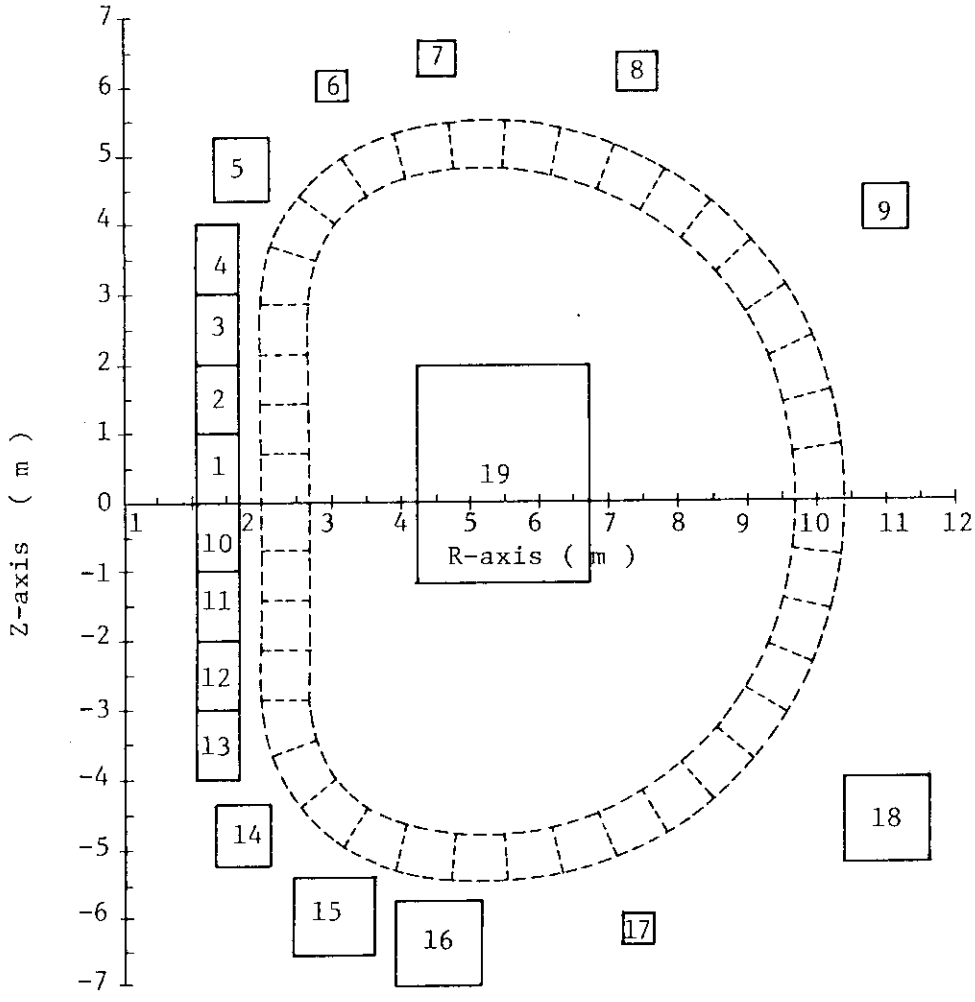

Fig. 5.4.5 Poloidal coil location for full-breeding blanket concept

Note: TF coil configuration indicates coil winding area

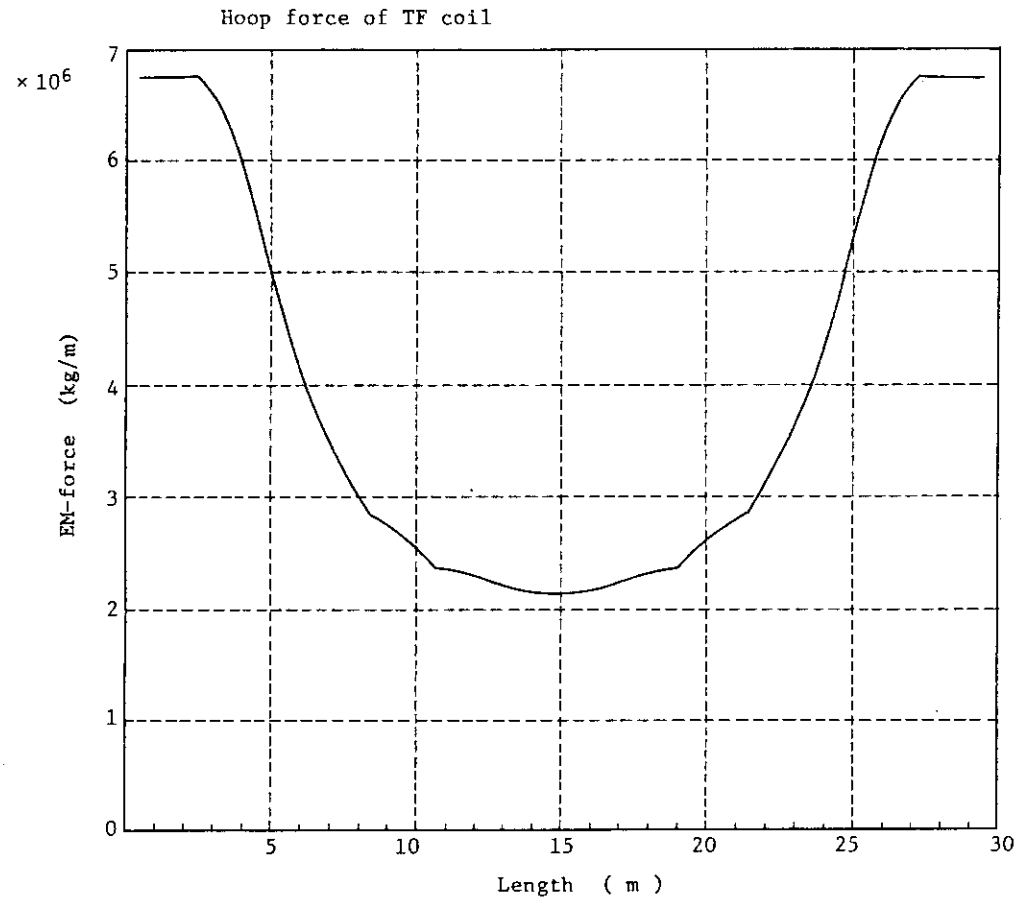

Fig. 5.4.6 In-plane force distribution for non-breeding blanket concept

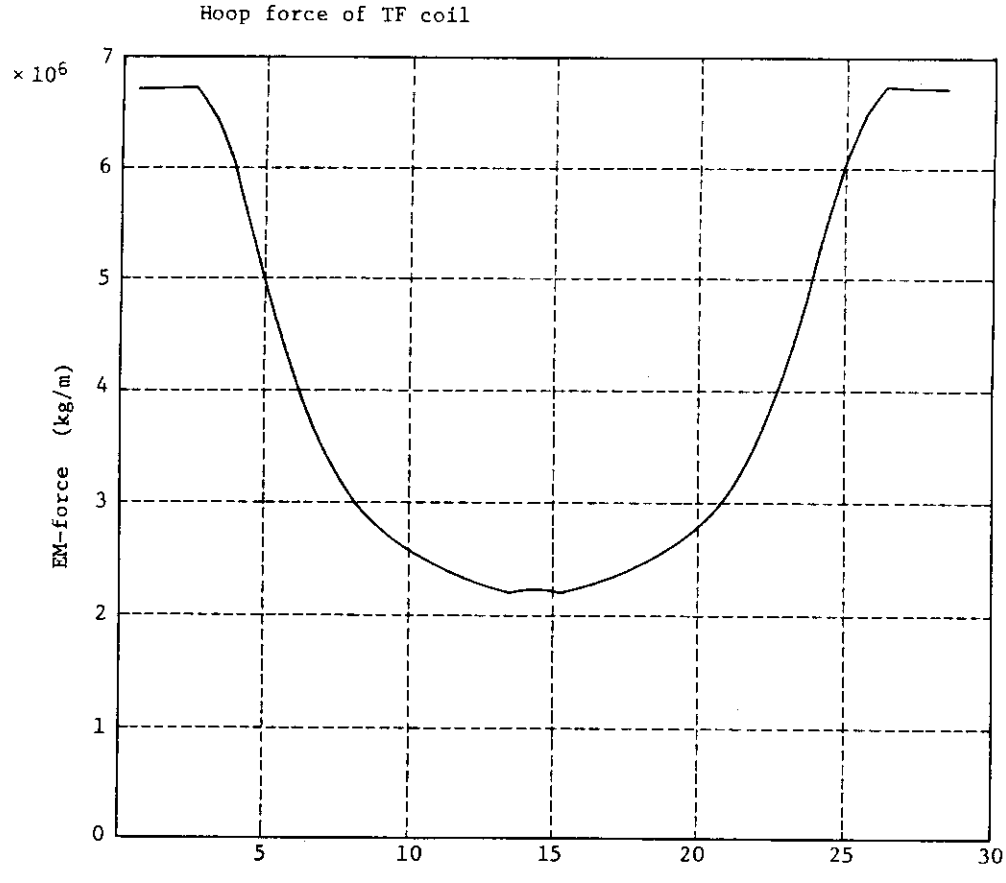

Fig. 5.4.7 In-plane force distribution for full-breeding blanket concept

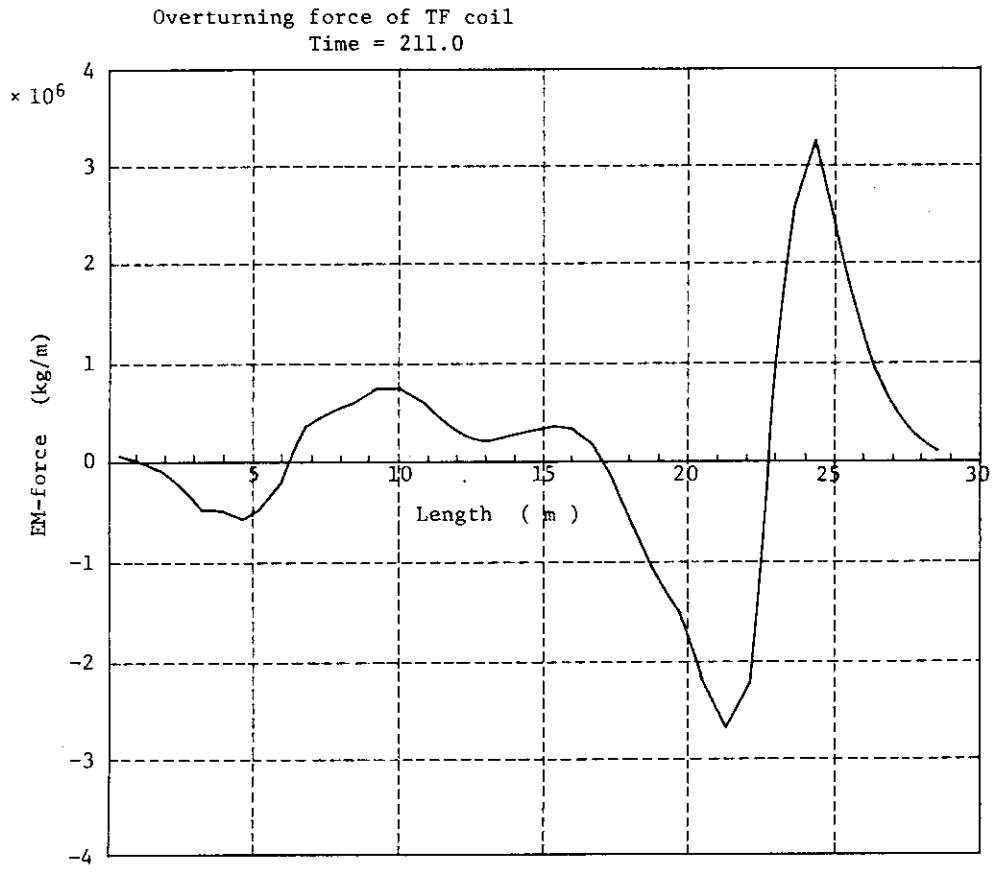

Fig. 5.4.8 Out-of-plane force distribution for non-breeding blanket concept

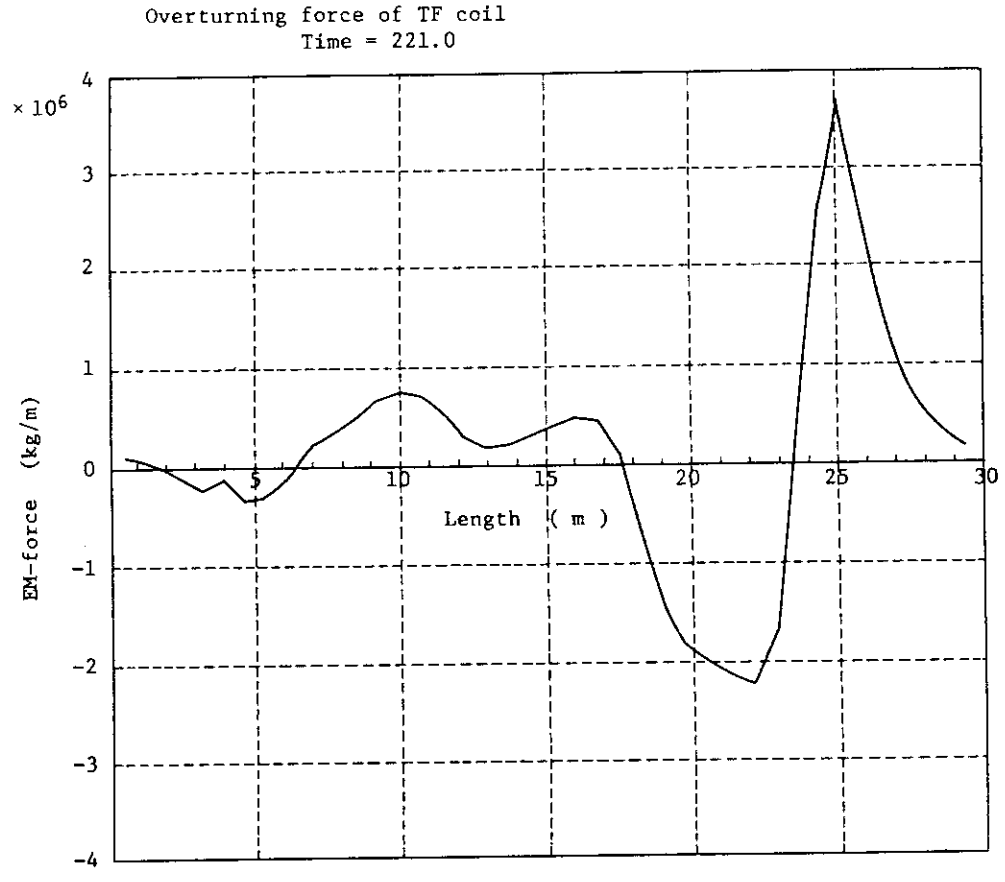

Fig. 5.4.9 Out-of-plane force distribution for full-breeding blanket concept

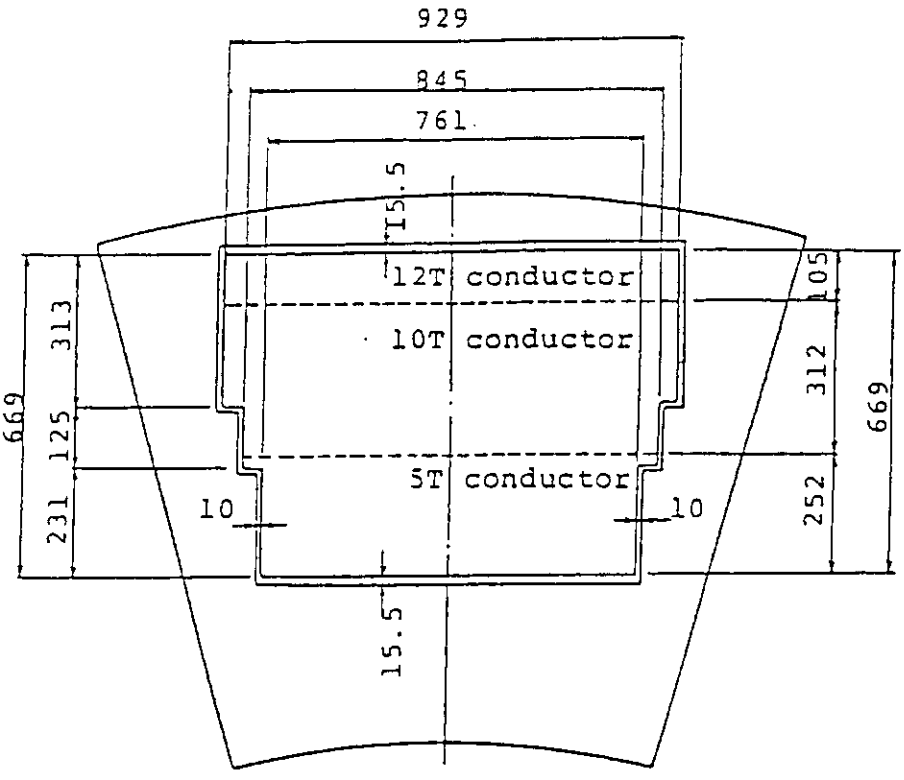

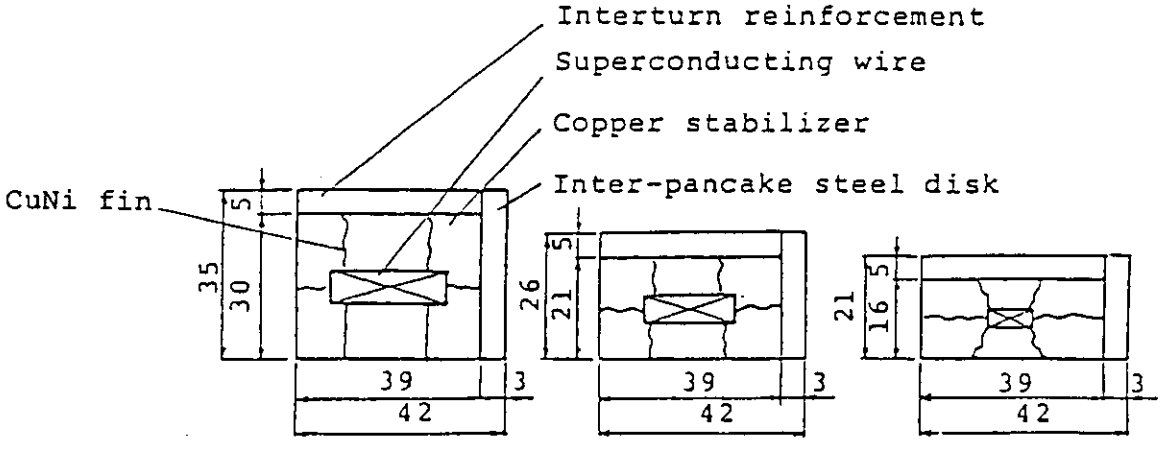

(1) 12T conductof (2) 10T conductor (3) 5T conductor

Fig. 5.4.10 TF coil winding concept and its conductors

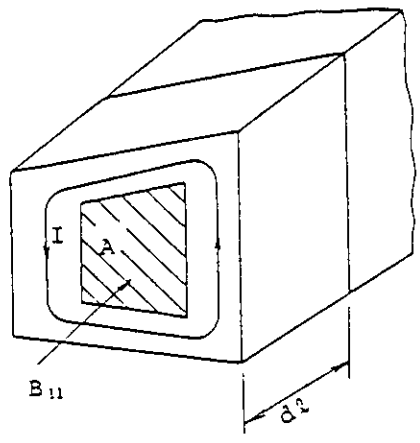

$$P_{\parallel} = \frac{A_2}{\langle R \rangle} \int_{\ell} \dot{B}_{\parallel}^2 \, d\ell$$

A : Crosssectional area

$\langle R \rangle$: Averaged resistance per unit length

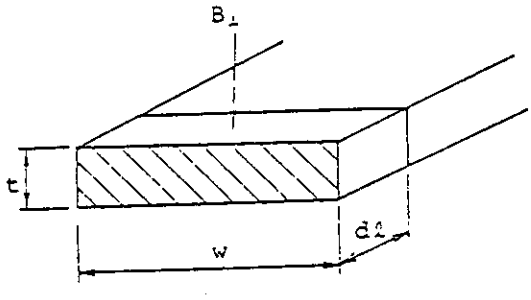

$$P_{\perp} = \frac{tw^3}{12\rho} \int_{\ell} \dot{B}_{\perp}^2 \, d\ell$$

t : Thickness

w : Width

ρ : Resistivity

Fig.5.4.11 The models for calculation of AC loss in TF vessel

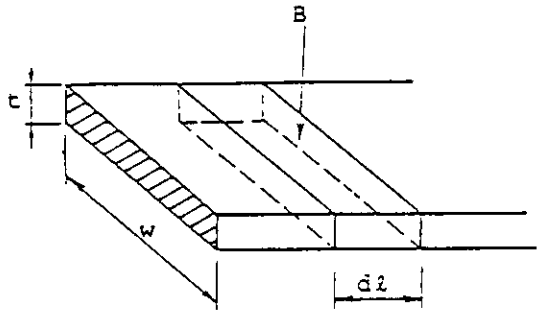

Fig.5.4.13 AC loss model

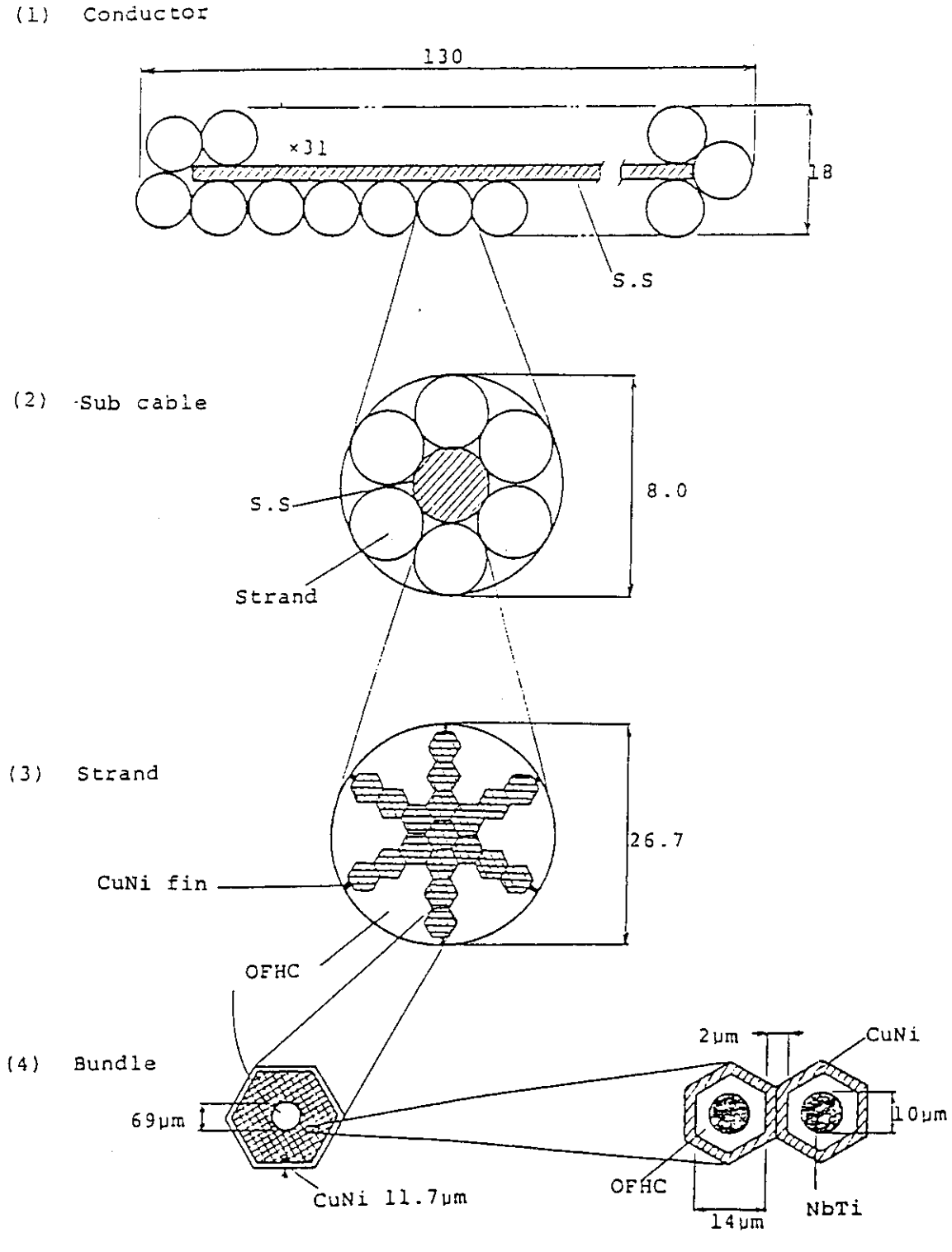

Unit: mm except noted above

Fig. 5.4.12 PF coil conductor

7. Impact on Availability Associated with Including a T-producing Blanket

Task 6 Evaluate the impact on availability associated with including a T-producing blanket.

T. Oikawa

N. Watanabe

T. Tobioka

H. Iida

T. Honda

1. Introduction.

The evaluations of availability associated with including a full T-producing blanket and with excluding T-producing blanket are carried out.

The comparison of availability between reference-blanket, full T-producing blanket and non-breeding blanket is shown from the estimation of MTBF and MTTR.

2. Estimation of Availability.

MTBF and MTTR of each system are listed in Table 1 ∿ 3 for reference-blanket, full T-producing blanket and for non-breeding blanket.

MTBF and MTTR of Coil system, Heating System and of Auxiliary Systems are same for three options. The difference consists only in Nuclean System.

The availability of each component is estimated as below,

$$A = \frac{MTBF}{MTBF+MTTR}, \qquad U = 1-A$$

excepting the systems where restant time is included such as Coil system, Cryogenic system and AC power system:

$$A = \frac{MTBF}{MTBF+MTTR+Restant}, \qquad U = 1-A$$

It is supposed that the AC power supply for TF coil system on PF coil system is independent from the AC Power supply system of auxiliary system as shown in Fig 1.

Therefore, Power supply system is included in availability estimation for TF coil system and for PF/OH coil system:

$$A_{TFCS} = 1-(U_{TFC} + U_{TFL} + U_{AC\ For\ TF})$$

$A_{PF/OHCS} = 1-(U_{OHC} + U_{OHL} + U_{EFC} + U_{EFL} + U_{AC\ For\ PF/OH})$

Availabilities of each component or system are listed in Table 4 ∿ 6.

Availability of INTOR, A_{INTOR}, is estimated under the assumption that the down of even one component listed in Fig. 2 leads to the down of INTOR:

$$A_{INTOR} = \prod_{i=1}^{n} Ai \ ,$$

3. Results

Above preliminary availability estimation shows that when tritium breeding blanket has same reliability as the first wall, the relative difference of the availability from the reference is calculated to be ±10 %. Since we have little information about tritium breeding blanket reliability, we cannot rely with full confidence on these values yet.

It is thought that the breeding blanket reliability larger than the first wall will be called for when we install them.

Table 1. MTBF/MTTR for outboard T-producing blanket

Component	MTBF(hrs)	MTTR(hrs)
Coil System		
TF Coil Winding	1×10^5	1×10^4
TF Power Leads	3×10^4	1.2×10^3
OH Coil Winding	1×10^5	1.0×10^4
OH Power Leads	3×10^4	1.2×10^3
EF Coil Winding	5×10^5	5×10^4
EF Power Leads	3×10^4	1.2×10^3
Cryostat Structure	2×10^6	1.5×10^3
Nuclear System		
Shield Structure	2×10^5	2.4×10^3
First Wall	1×10^4	1.24×10^3
Outboard T Producing Blanket	2×10^4*, 1×10^4**	1.24×10^3
Shield Blanket	2×10^5	1.24×10^3
Pumped Limiter Structure	2.7×10^3	4.5×10^2
Heating System		
ICRH Coaxial Cable	5×10^4	5×10^2
ICRH Antenna	5×10^3	5×10^2
LHRH Waveguide	5×10^4	5×10^2
Auxiliary Systems		
Vacuum Pumping System	5×10^4	20
Tritium Processing System	1×10^5	1×10^2
Cryogenic System	1×10^3	30
AC Power System	1×10^4	70
Heat Transport System	1×10^3	10
Fuel Storage System	1×10^4	50
Diagnostics	3×10^3	2×10^2
Instrumentation & Control System	2×10^3	10

* Estimated from the failure rate of a pipe (10^{-8} / y)

** Assumed to be same value as that for First Wall

Table 2. MTBF/MTTR for full T-producing blanket

Component	MTBF(hrs)	MTTR(hrs)
Coil System		
TF Coil Winding	1×10^5	1×10^4
TF Power Leads	3×10^4	1.2×10^3
OH Coil Winding	1×10^5	1.0×10^4
OH Power Leads	3×10^4	1.2×10^3
EF Coil Winding	5×10^5	5×10^4
EF Power Leads	3×10^4	1.2×10^3
Cryostat Structure	2×10^6	1.5×10^3
Nuclear System		
Shield Structure	2×10^5	2.4×10^3
First Wall	1×10^4	1.24×10^3
Inboard T-Producing Blanket	3×10^4*, 1.5×10^4**	1.24×10^3
Outboard T-Producing Blanket	2×10^4*, 1×10^4**	1.24×10^3
Pumped Limiter Structure	2.7×10^3	4.5×10^2
Heating System		
ICRH Coaxial Cable	5×10^4	5×10^2
ICRH Antenna	5×10^3	5×10^2
LHRH Waveguide	5×10^4	5×10^2
Auxiliary Systems		
Vacuum Pumping System	5×10^4	20
Tritium Processing System	1×10^5	1×10^2
Cryogenic System	1×10^3	30
AC Power System	1×10^4	70
Heat Transport System	1×10^3	10
Fuel Storage System	1×10^4	50
Diagnostics	3×10^3	2×10^2
Instrumentation & Control System	2×10^3	10

* Estimated from the failure rate of a pipe (10^{-8} / y)

** Assumed to be same value as that for First Wall

Table 3. MTBF/MTTR for non-breding blanket

Component	MTBF(hrs)	MTTR(hrs)
Coil System		
TF Coil Winding	1×10^5	1×10^4
TF Power Leads	3×10^4	1.2×10^3
OH Coil Winding	1×10^5	1.0×10^4
OH Power Leads	3×10^4	1.2×10^3
EF Coil Winding	5×10^5	5×10^4
EF Power Leads	3×10^4	1.2×10^3
Cryostat Structure	2×10^6	1.5×10^3
Nuclear System		
Shield Structure	2×10^5	2.4×10^3
First Wall	1×10^4	1.24×10^3
Non-Breeding Blanket	2×10^5	1.24×10^3
Blanket/First Wall Structure	5×10^3	1.24×10^3
Pumped Limiter Structure	2.7×10^3	4.5×10^2
Heating System		
ICRH Coaxial Cable	5×10^4	5×10^2
ICRH Antenna	5×10^3	5×10^2
LHRH Waveguide	5×10^4	5×10^2
Auxiliary Systems		
Vacuum Pumping System	5×10^4	20
Tritium Processing System	1×10^5	1×10^2
Cryogenic System	1×10^3	30
AC Power System	1×10^4	70
Heat Transport System	1×10^3	10
Fuel Storage System	1×10^4	50
Diagnostics	3×10^3	2×10^2
Instrumentation & Control System	2×10^3	10

Table 4 Availability for outboard T-producing blanket

Component		Availability	Unavailability
TF Coil Winding	TFC	0.84	0.1076
TF Power Leads	TFL		
OH Coil Winding	OHC	0.69	0.5635
OH Power Leads	OHL		
EF Coil Winding	EFC		
EF Power Leads	EFL		
Cryostat Structure	CRS	0.9993	0.0007
Shield Structure	SHD	0.9814	0.0186
First Wall	FS	0.8897	0.1103
Outboard T-Producing Blanket	OTB	0.9416*, 0.8897**	0.0584*, 0.1103**
Shield Blanket	SB	0.9938	0.0062
Pumped Limiter Structure	LIM	0.8343	0.1657
ICRH Coaxial Cable	ICC	0.9901	0.0099
ICRH Antenna	ICA	0.9091	0.0909
LHRH Waveguide	LHW	0.9901	0.0099
Vacuum Pumping System	VPS	0.9996	0.0004
Tritium Processing System	TPS	0.9990	0.001
Cryogenic System	CRG	0.82	0.18
AC Power System	AC	0.9268	0.0732
Heat Transport System	HTS	0.9901	0.0099
Fuel Storage System	FSS	0.9950	0.005
Diagnostics	DIA	0.9375	0.0625
Instrumentation & Control System	ICS	0.9950	0.005
Availability of INTOR		0.245, 0.232	

* Estimated from the failure rate of a pipe (10^{-8} / y)

** Assumed to be same value as that for First Wall

Table 5 Availability for full T-producing blanket

Component		Availability	Unavailability
TF Coil Winding	TFC	0.84	0.1076
TF Power Leads	TFL		
OH Coil Winding	OHC	0.69	0.5635
OH Power Leads	OHL		
EF Coil Winding	EFC		
EF Power Leads	EFL		
Cryostat Structure	CRS	0.9993	0.0007
Shield Structure	SHD	0.9814	0.0186
First Wall	FW	0.8897	0.1103
Inboard T-Producing Blanket	ITB	0.960*, 0.9236**	0.040*, 0.0764**
Outboard T-producing Blanket	OTB	0.942*, 0.8897**	0.058, 0.1103**
Pumped Limiter Structure	LIM	0.8343	0.1657
ICRH Coaxial Cable	ICC	0.9901	0.0099
ICRH Antenna	ICA	0.9091	0.0909
LHRH Waveguide	LHW	0.9901	0.0099
Vacuum Pumping System	VPS	0.9996	0.0004
Tritium Processing System	TPS	0.9990	0.001
Cryogenic System	CRG	0.82	0.18
AC Power System	AC	0.9268	0.0732
Heat Transport System	HTS	0.9901	0.0099
Fuel Storage System	FSS	0.9950	0.005
Diagnostics	DIA	0.9375	0.0625
Instrumentation & Control System	ICS	0.9950	0.005
Availability of INTOR		0.24, 0.21	

* Estimated from the failure rate of a pipe (10^{-8} / y)

** Assumed to be same value as that for First Wall

Table 6 Availability for non-breeding blanket

Component		Availability	Unavailability
TF Coil Winding	TFC	0.84	0.1076
TF Power Leads	TFL		
OH Coil Winding	OHC	0.69	0.5635
OH Power Leads	OHL		
EF Coil Winding	EFC		
EF Power Leads	EFL		
Cryostat Structure	CRS	0.9993	0.0007
Shield Structure	SHD	0.9814	0.0186
First Wall	FW	0.8897	0.1103
Non-Breeding Blanket	NBD	0.9938	0.0062
Pumped Limiter Structure	LIM	0.8343	0.1157
ICRH Coaxial Cable	ICC	0.9901	0.0099
ICRH Antenna	ICA	0.9091	0.0909
LHRH Waveguide	LHW	0.9901	0.0099
Vacuum Pumping System	VPS	0.9996	0.0004
Tritium Processing System	TPS	0.9990	0.001
Cryogenic System	CRG	0.82	0.18
AC Power System	AC	0.9258	0.0732
Heat Transport System	HTS	0.9901	0.0099
Fuel Storage System	FSS	0.9950	0.005
Diagnostics	DIA	0.9375	0.0625
Instrumentation & Control System	ICS	0.9950	0.005
Availability of INTOR		0.26	

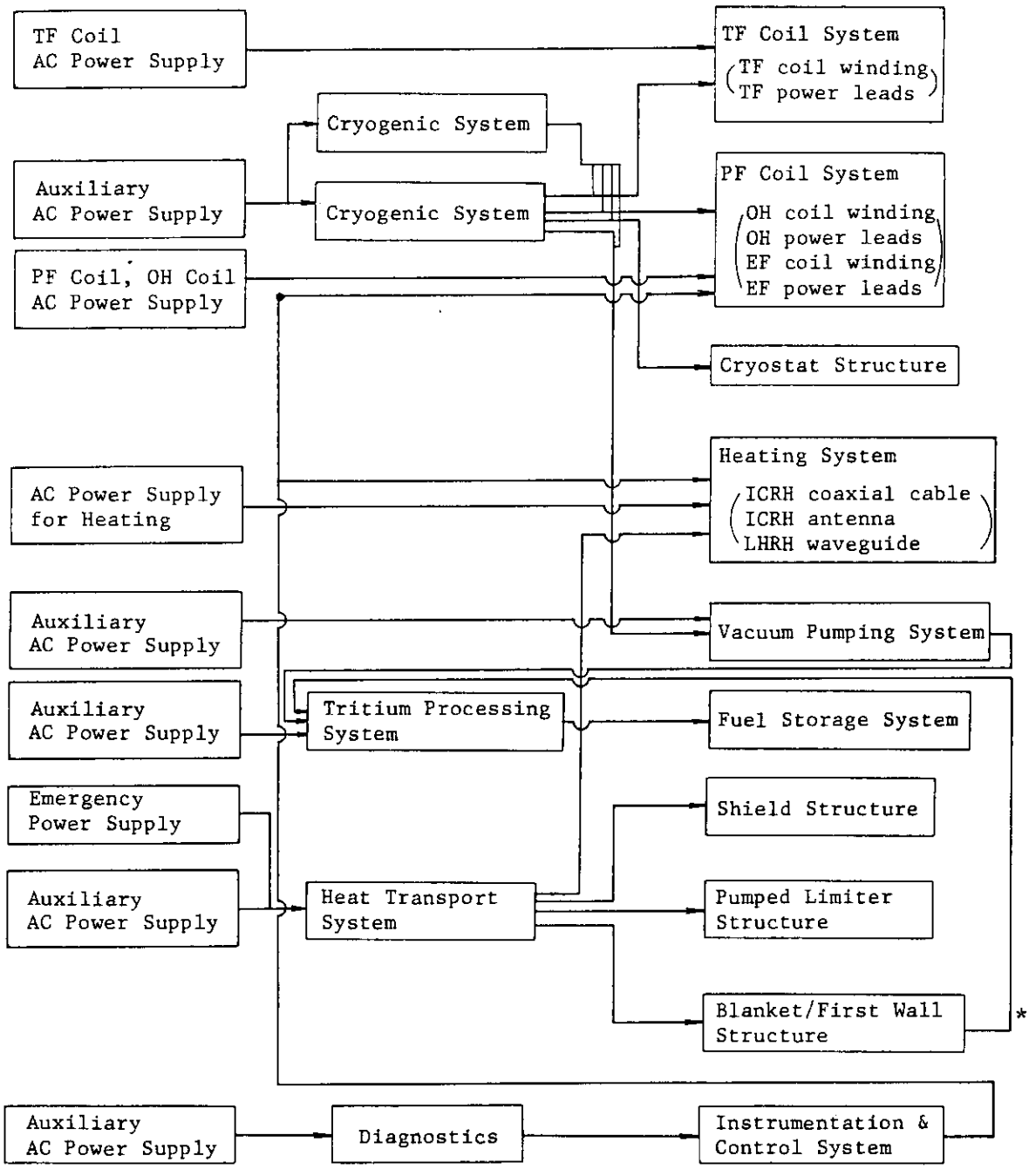

Fig. 1 System of each component

(* for non-breeding blanket, this route is omitted)

Component	Coil System / TF Coil Winding	TF Power Leads	OH Coil Winding	OH Power Leads	EF Coil Winding	EF Power Leads	Cryostat Structure	Nuclear System / Shield Structure	Blanket/First Wall Structure	Pumped Limiter Structure	Heating System / ICRH Coaxial Cable	ICRH Antenna	LHRH Waveguide	Auxiliary Systems / Vacuum Pumping System	Tritium Processing System	Cryogenic System	AC Power System	Heat Transport System	Fuel Storage System	Diagnostics	Instrumentation & Control System
Coil System / TF Coil Winding		✓	✓	✓	✓	✓	✓	✓	✓	✓	✓	✓	✓	✓	○	✓	○	○	○	✓	✓
TF Power Leads	✓		✓	✓	✓	✓	✓	✓	✓	✓	✓	✓	✓	○	○	✓	○	○	○	✓	✓
OH Coil Winding	✓	✓		✓	✓	✓	✓	✓	✓	✓	✓	✓	✓	✓	○	✓	○	○	○	✓	✓
OH Power Leads	✓	✓	✓		✓	✓	✓	✓	✓	✓	✓	✓	✓	○	○	✓	○	○	○	✓	✓
EF Coil Winding	✓	✓	✓	✓		✓	✓	✓	✓	✓	✓	✓	✓	✓	○	✓	○	○	○	✓	✓
EF Power Leads	✓	✓	✓	✓	✓		✓	✓	✓	✓	✓	✓	✓		○	✓	○	○	○	✓	✓
Cryostat Structure	✓	✓	✓	✓	✓	✓		✓	✓	✓	✓	✓	✓	✓	○	✓	○	○	○	✓	✓
Nuclear System / Shield Structure	✓	✓	✓	✓	✓	✓	✓		✓	✓	✓	✓	✓	✓	○	○	○	○	○	✓	✓
Blanket/First Wall Structure	○	○	✓	✓	✓	✓	○	✓		✓	✓	✓	✓	✓	○	○	○	○	○	✓	✓
Pumped Limiter Structure	○	○	✓	✓	✓	✓	○	✓	✓		✓	✓	✓	✓	○	○	○	○	○	✓	✓
Heating System / ICRH Coaxial Cable	○	○	✓	✓	✓	✓	○	✓	✓	✓		✓	✓	✓	○	○	○	○	○	✓	✓
ICRH Antenna	○	○	✓	✓	✓	✓	○	✓	✓	✓	✓		✓	✓	○	○	○	○	○	✓	✓
LHRH Waveguide	○	○	✓	✓	✓	✓	○	✓	✓	✓	✓	✓		✓	○	○	○	○	○	✓	✓
Auxiliary Systems / Vacuum Pumping System	○	○	✓	✓	✓	✓	○	✓	✓	✓	✓	✓	✓		×	○	○	○	×	✓	✓
Tritium Processing System	○	○	✓	✓	✓	✓	○	✓	✓	✓	✓	✓	✓	✓		○	○	○	×	✓	✓
Cryogenic System	×	×	×	×	×	×	×	✓	✓	✓	✓	✓	✓	×	✓		○	○	✓	✓	✓
AC Power System	×	×	×	×	×	×	×	×	×	×	×	×	×	×	×	×		○	×	×	×
Heat Transport System	○	○	✓	✓	✓	✓	○	×	×	×	×	×	×	○	○	○	○		○	✓	✓
Fuel Storage System	○	○	✓	✓	✓	✓	○	✓	✓	✓	✓	✓	✓	○	✓	○	○	○		✓	✓
Diagnostics	○	○	✓	✓	✓	✓	○	✓	✓	✓	✓	✓	✓	○	○	○	○	○	○		×
Instrumentation & Control System	○	○	×	×	×	×	○	✓	✓	✓	×	×	×	○	○	○	○	○	○	○	

Fig. 2 Condition of operation when a component in left column is down

×: down, ✓: stop, ○: run

8. Impact of Fulence and Burn Time on TFC Support Structure

Task 7 Evaluate the allowable reduction in TFC support structure that would result from reducing the fluence from 6.6 to 3 MW.y/m^2 and increasing the burn pulse from 200 to 1000s.

by

S. Nishio and

S. Itoh

Y. Itou

(1) The amplitude reduction of cyclic stress due to overturning force on TF coil by the quasi-steady state operation

If the plasma current drive by RF wave will be restricted in low density region even for future tokamak, one of the possible scenarios should be the quasi-steady state operation scenario. The advantages of the operation scenarios must be fully investigated since the mitigation of engineering difficulties can be expected. A typical scheme of this scenario is shown as a solid line in Fig. 1. This operation scenario is as follows. The plasma current is ramped up by the lower hybrid range of frequency wave (LHW) in the low density plasma during the start-up phase. Possible assistance by usual transformer coils (OH coils) and electron cyclotron heating for the current initiation and ramp-up can also be made available in this phase. Throughout the burning phase, the plasma current is sustained only by the usual OH coils. Long burning time can be established, since volt·second of OH coils can be economized by LHW start-up. After the burning is terminated, the plasma density is lowered (ramp-down phase). Also throughout this phase, the usual OH coils must work for sustaining the plasma current, since the plasma density is yet rather high and the volt·second is provided to plasma from equilibrium field (EF) coils by a variation of beta poloidal (β_p). After the plasma density is sufficiently reduced, the plasma current is sustained by LHW at a certain value (I_p^{RF}) which is not necessarily the same as burning plasma current. During this phase, the current in OH coils is reversed (recharging of OH coils) with the plasma current being kept at the certain value.

In general, a highly elongated divertor plasma requires much more magnetomotive force for the equilibrium field coils in low β_p phase than in high β_p phase. Because the equilibrium field is dominated not by the vertical field but by the shpaing field. Physically, the possible interpretation seems to be as follows. For the low β_p plasma much magnetomotive force is required in pressing down the null point at the designed position (near the plasma). On the other hand, the high β_p plasma with highly elongated shape has a tendency to become a circular shape by its internal pressure. Therefore, it is easier for high β_p plasma to press down the null point near plasma than for low β_p plasma. The plasma parameters employed here are as follows.

Fusion Power	440 MW
Major radius	5.5 m
Minor radius	1.1 m
Ellipticity	1.5 ~ 1.6
Triangularity	0.2
Plasma Current	5.3 MA
Poloidal beta	3.0
Limiter/Divertor	Double null poloidal divertor

The hybrid PF coils location are shown in Fig. 2. In this figure, the coils from H1 to H5 can produce the equilibrium field and the plasma current transformer field simultaneously, and the other coils, i.e. No. 4, 5, 6 produce only the plasma current transformer field. PF coils current for the equilibrium field are shown in Fig. 3 as a function of β_p. The range of the plasma beta value for LHW current drive is considered to be up to $\beta_p \approx 0.01$. Fortunately, the β_p dependency on EF coils current is very insensitive up to $\beta_p \approx 0.1$.

as shown in Fig. 3. Therefore, it is assumed that $\beta_p = 0.1$ is employed as a switching point from LHW operation phase to OH coil operation phase.

The TF coil structural design must follow a system design approach which allows it to meet not only its own requirements but also the requirements of the total device. The difficulties for supporting the super conducting TF coil of large tokamak like INTOR, however, are mainly caused by the overturning force which results from the interaction of the TF coil current and the equilibrium field. In the pulsed operation tokamak, this force acts cyclically on TF coils. The TF coil structural design criteria include conventional (primary) stress limits in addition to limits established for stress amplitude based on fatigue life consideration. It must be expected than the stress amplitude can be reduced considerably by introducing the quasi-steady state operation. It is our main concern to seek out a desirable transition of plasma current which corresponds to the EF coil current.

The overturning moment around the horizontal axis (R-axis) or the vertical axis (Z-axis) is usually proposed as the quantity which represents the out-of-plane force. The moment as a integrated quantity, however, is not necessarily useful information for the structural design. Because, the overturning force for the highly elongated plasma distributes along the TF coil perimeter from large plus region to large minus region as can be seen in Fig. 4. Then as can be seen in Fig. 5, the overturning moment integrated around R-axis becomes zero at $\beta_p \approx 1.5$.

Fig. 4 shows that the overturning force at low β_p phase is larger than at high β_p phase under the condition of same plasma current. This fact signify that the amplitude of the overturning force can be

reduced by sustaining the plasma current in OH coil recharging phase at lower value than the burning plasma current. Here, the point (between point B and C in Fig. 4) where the maximum overturning force acts is selected for evaluating the amplitude. The fore (f_{RF}) at this point in the OH coil recharging phase and that (f_B) in the burning phase has a relation which is $f_{RF}/f_B = 0.254\ I_P^{RF}(MA)$. The equivalent stress amplitude under existance of a mean stress is given by the following formula and is guaranteed by modified Goodman diagram.

$$\sigma_{eq} = \frac{\sigma_a}{1 - \frac{\sigma_{mean}}{\sigma_u}} \qquad \text{-------- (1)}$$

where,

σ_a : Cyclic stress amplitude

σ_{mean} : Mean stress

σ : Ultimate strength

The maixmum stress and minimum stress are denoted by σ_1 and σ_2 respectively. It is assumed that σ_1 does not exceed one of the ASME criteria for the primary stress. Therefore $\sigma_1 = \frac{1}{3}\sigma_u$ is assumed. Therefore equivalent stress amplitude for the pulsed operation (σ_{eq}^P) and the quasi-steady state operation (σ_{eq}^Q) are rewritten as follows.

$$\sigma_{eq}^P = \frac{3}{5}\sigma_1 \qquad \text{-------- (2)}$$

$$\sigma_{eq}^Q = \frac{\sigma_1 + \sigma_2}{2 - \frac{\sigma_1 + \sigma_2}{3\sigma_1}} \qquad \text{-------- (3)}$$

Unless both σ_{eq}^P and σ_{eq}^Q are so low that their lives exceed the

endurance limit ($\approx 10^6$), it is significant to define $\gamma = \sigma^P_{eq}/\sigma^Q_{eq}$ as a fatigue merit factor for the quasi-steady state operation, and γ is represented as follow.

$$\gamma = \frac{1}{5} \cdot \frac{5 - \sigma_2/\sigma_1}{1 - \sigma_2/\sigma_1} \qquad \text{-------- (4)}$$

If the force is in proportion to the stress, γ can be rewritten as follows by using f_{RF}/f_B.

$$\gamma = \begin{cases} \frac{1}{5} \cdot \frac{5 - f_{RF}/f_B}{1 - f_{RF}/f_B} & \cdots\cdots \quad 0 \leqq f_{RF}/f_B \leqq 1 \\ \frac{1}{5} \cdot \frac{5 - f_B/f_{RF}}{1 - f_B/f_{RF}} & \cdots\cdots \quad 1 < f_{RF}/f_B \end{cases} \qquad \text{-------- (5)}$$

Fig. 6 shows γ as the function of I_P^{RF} which is the sustained plasma current in OH coil recharging phase. The features of the fatigue merit factor are also shown schematically in Fig. 7.

Here we discussed the amplitude reduction of cyclic stress due to overturning force only at the most severe point for trial. Therefore even if the plasma current is sustained at about 4 MA in OH coil recharging phase, the fatigure problem may remain at another region. When a critical region appears after a detailed stress analysis including the TF coil support structure, however, the means of solving can be found by applying this way of thinking.

(2) The number of reactor operation during a life time will be decreased by a factor of $1/10^2 \sim 1/10^3$, in comparison with reference reactor (burn pulse 200 sec.) by the quasi-steady operation.

By means of the reduction of electromagnetic fatigue cycles, allowable stress intensities for TFC support structures are about 2~4 times value, compared with the case of reference reactor, so that TFC support structure designs are carried out with a large margin in the mechanical stress analysis.

In case of plasma scenario without transformer recharging,the number of reactor operation is estimated to be $\sim 1/10$ in comparison with the reference reactor and so the allowable stress intensity increases by ~20%.

In the concrete design, we should take into consideration not only electromagnetic fatigue of material but also limited strain of the superconductor and the insulation. Therfore, it is dangerous to increase easily the allowable stress according to the fatigue curve.

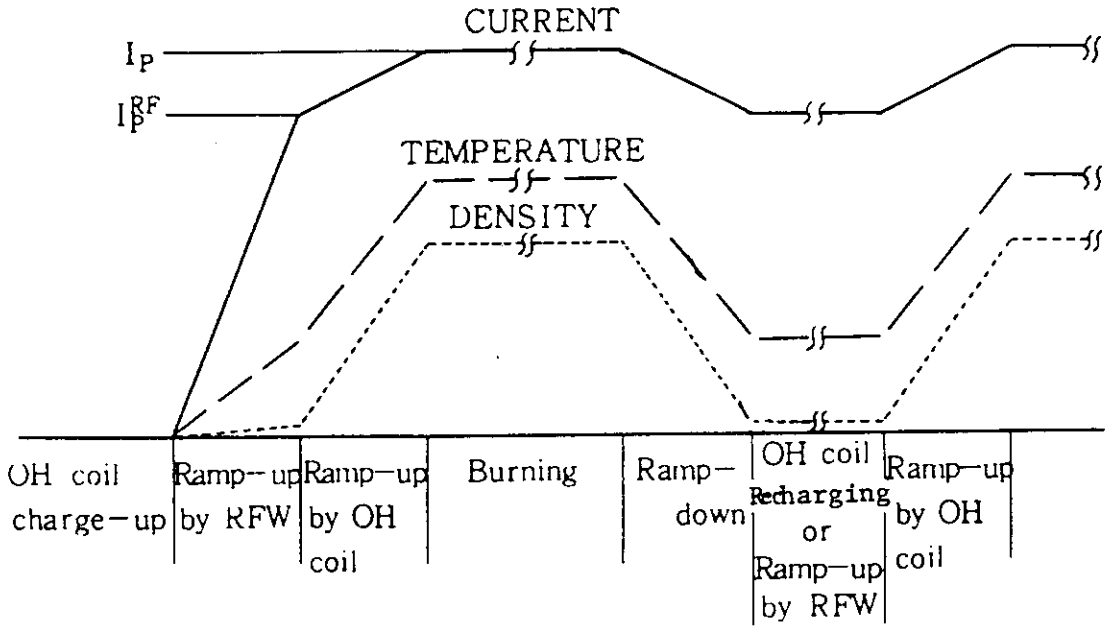

Fig. 1 Typical scheme of quasi-steady state operation scenario

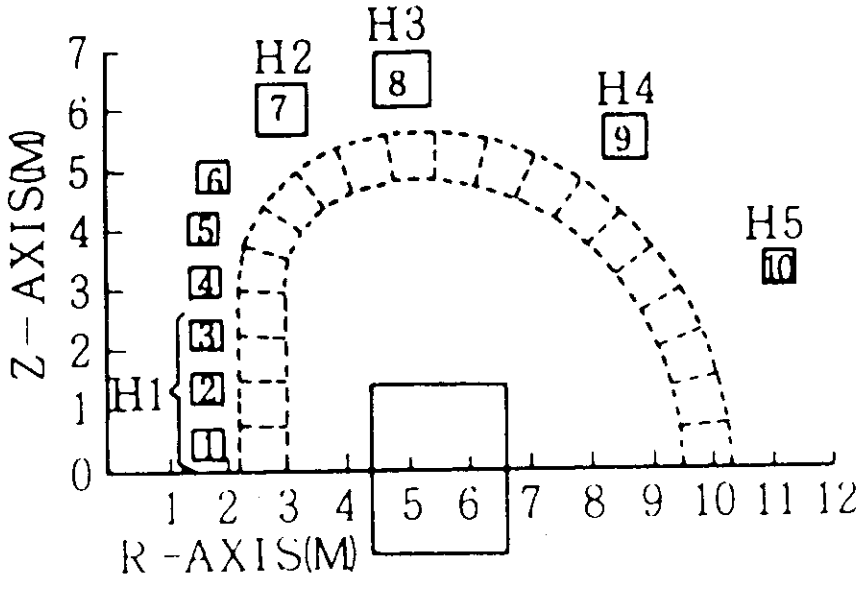

Fig. 2 Hybrid PF coils location

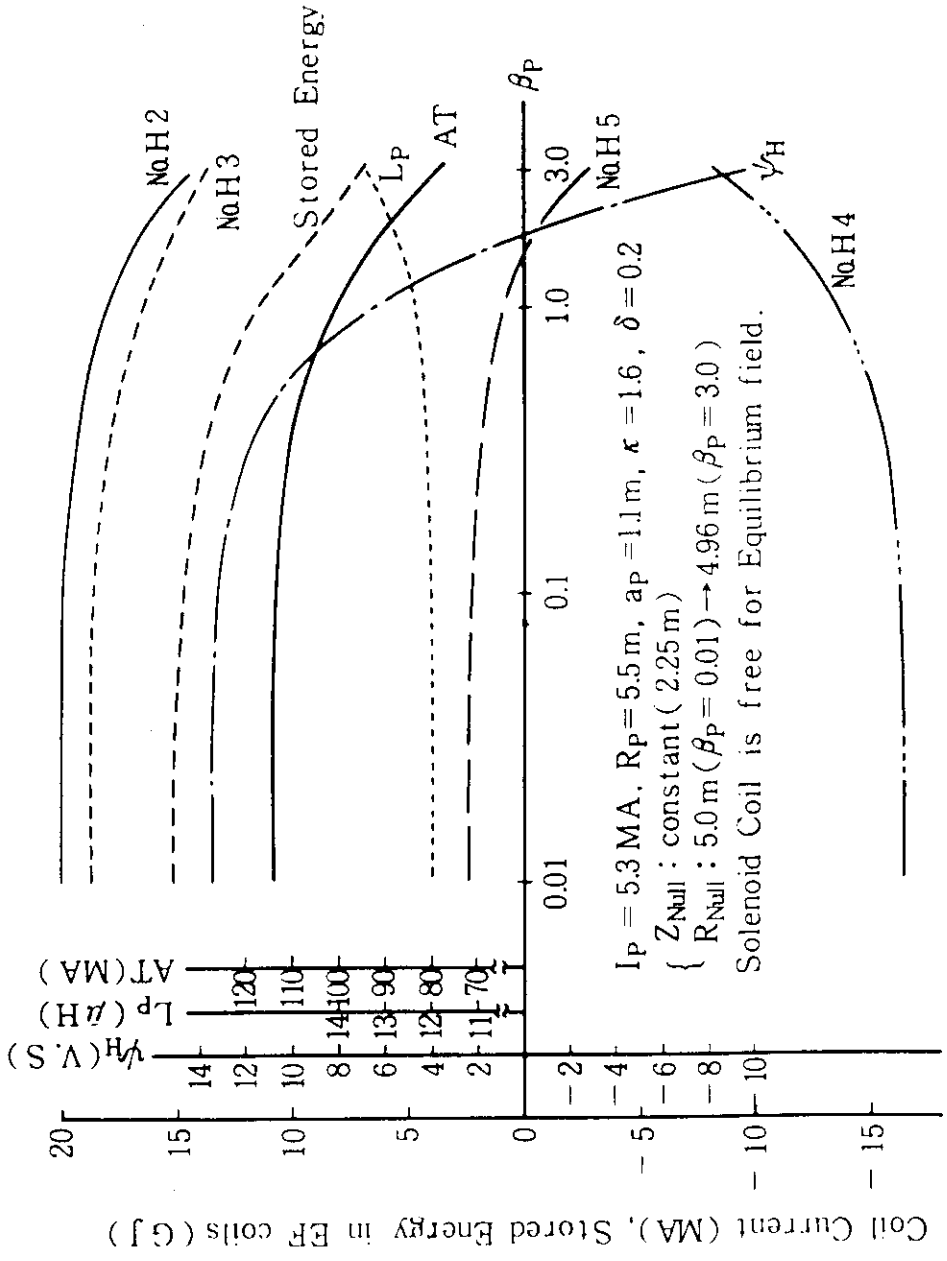

Fig. 3 Dependence of β_p on EF coils current

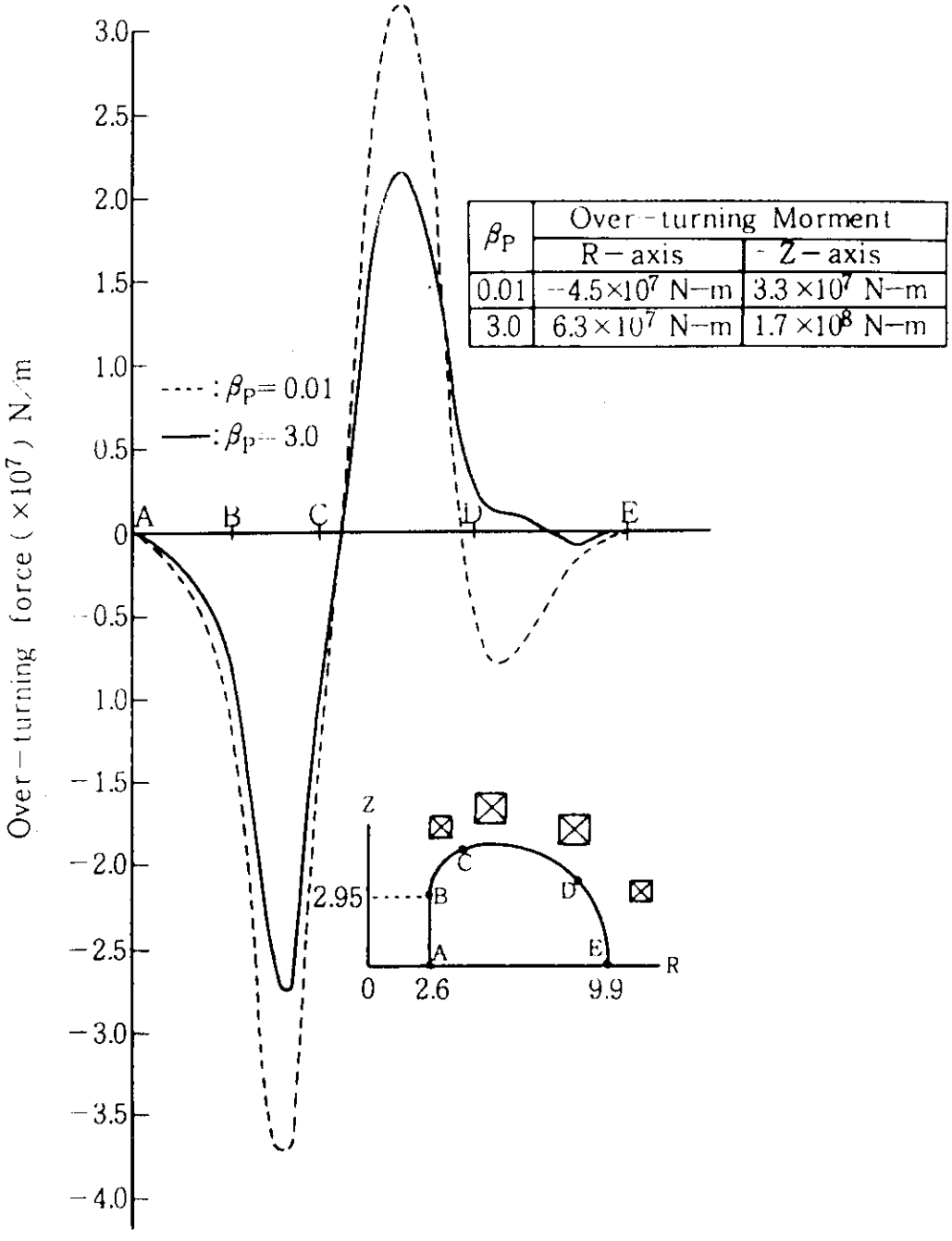

β_P	Over-turning Morment	
	R-axis	Z-axis
0.01	-4.5×10^{7} N-m	3.3×10^{7} N-m
3.0	6.3×10^{7} N-m	1.7×10^{8} N-m

Fig. 4 Overturning force distribution for low β_p and high β_p

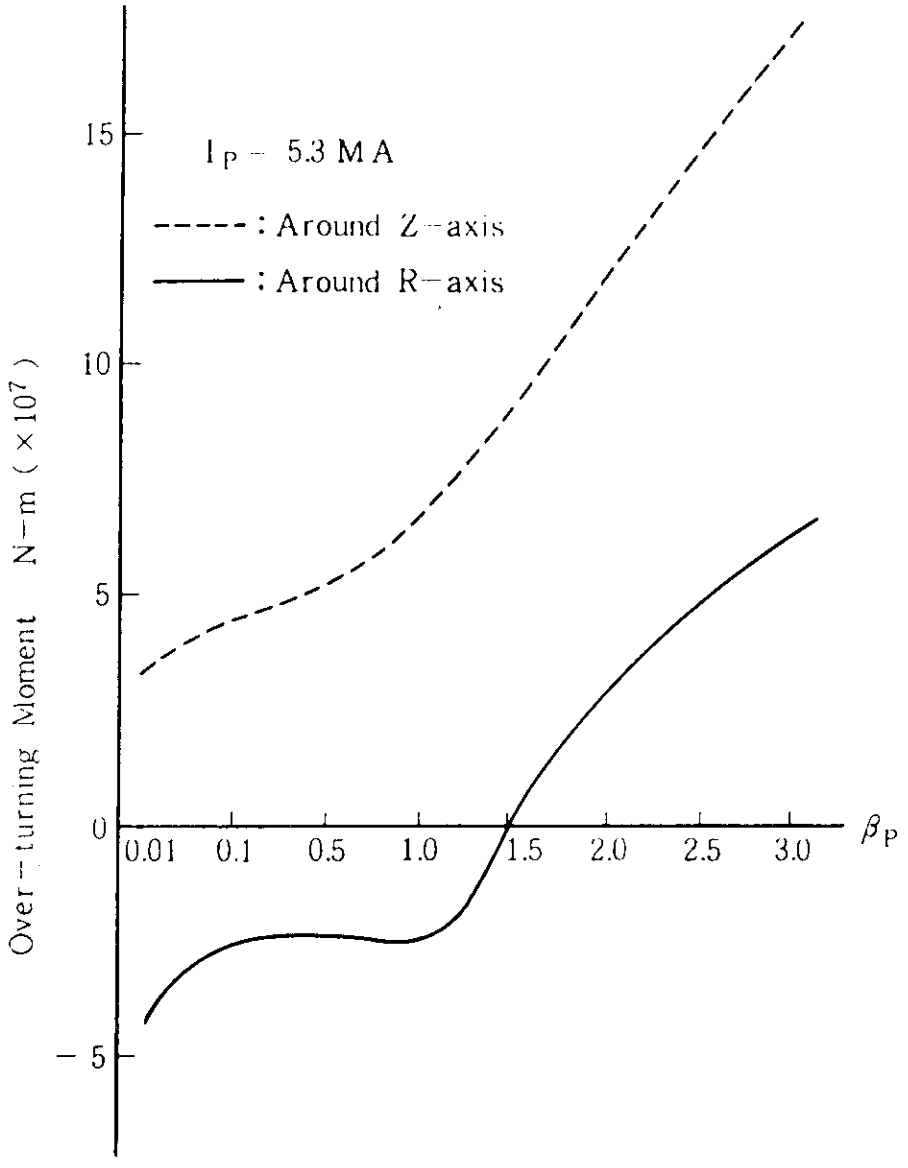

Fig. 5 Dependence of β_p on Overturning moment as an integrated quantity

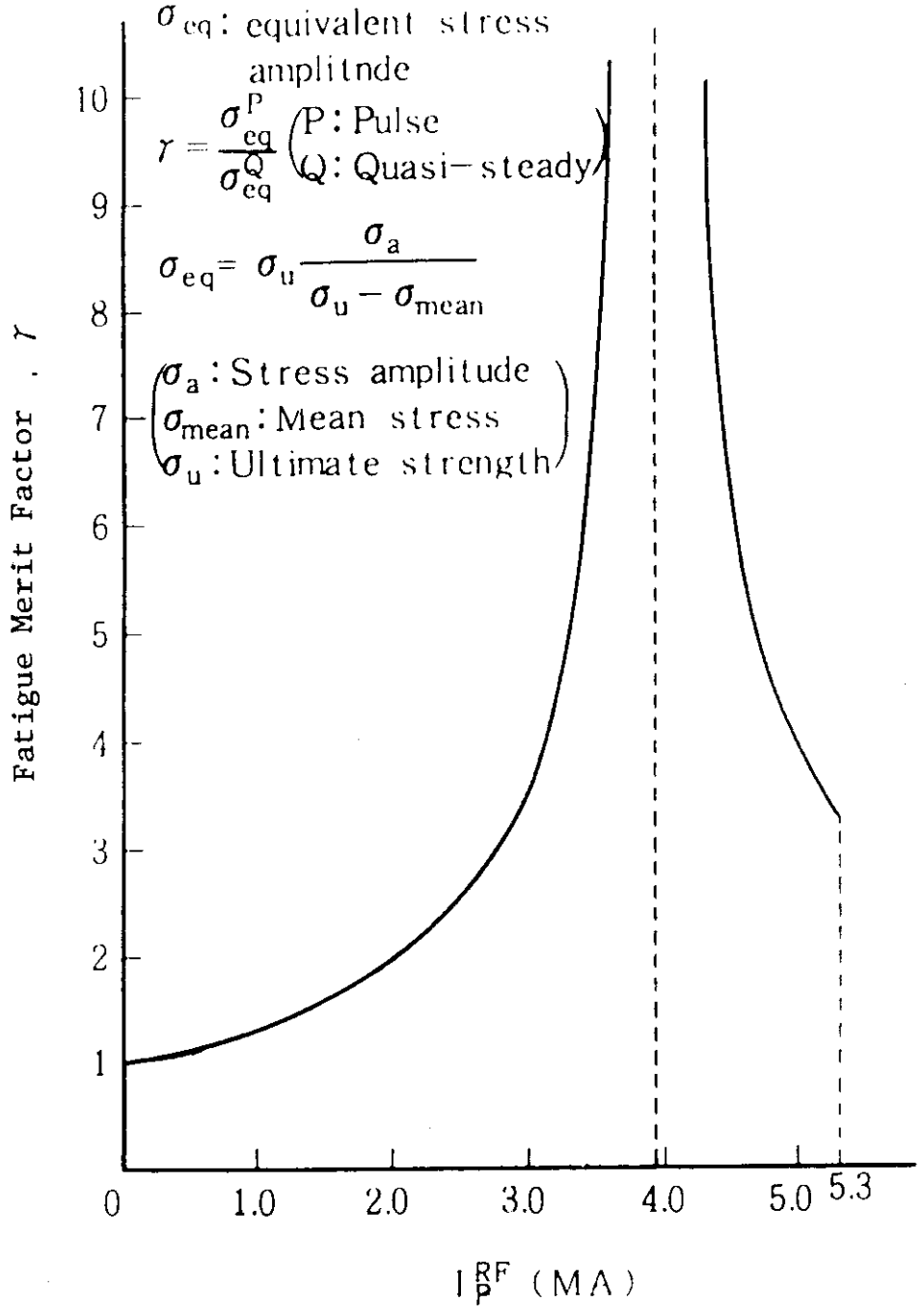

Fig. 6 Fatigue merit factor for quasi-steady state operation

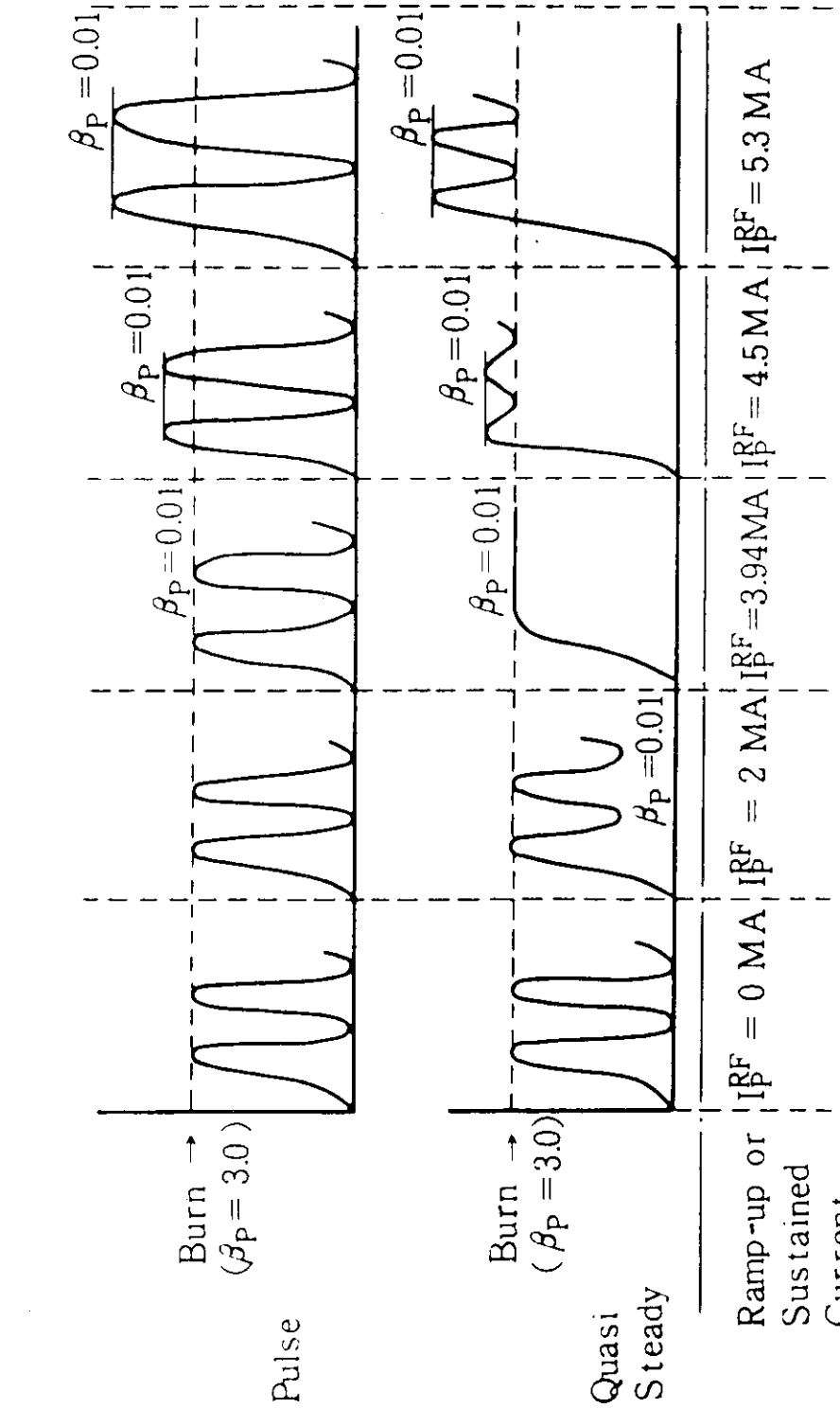

Fig. 7 Scheme of stress amplitude for pulsed operation and for quasi-steady state operation

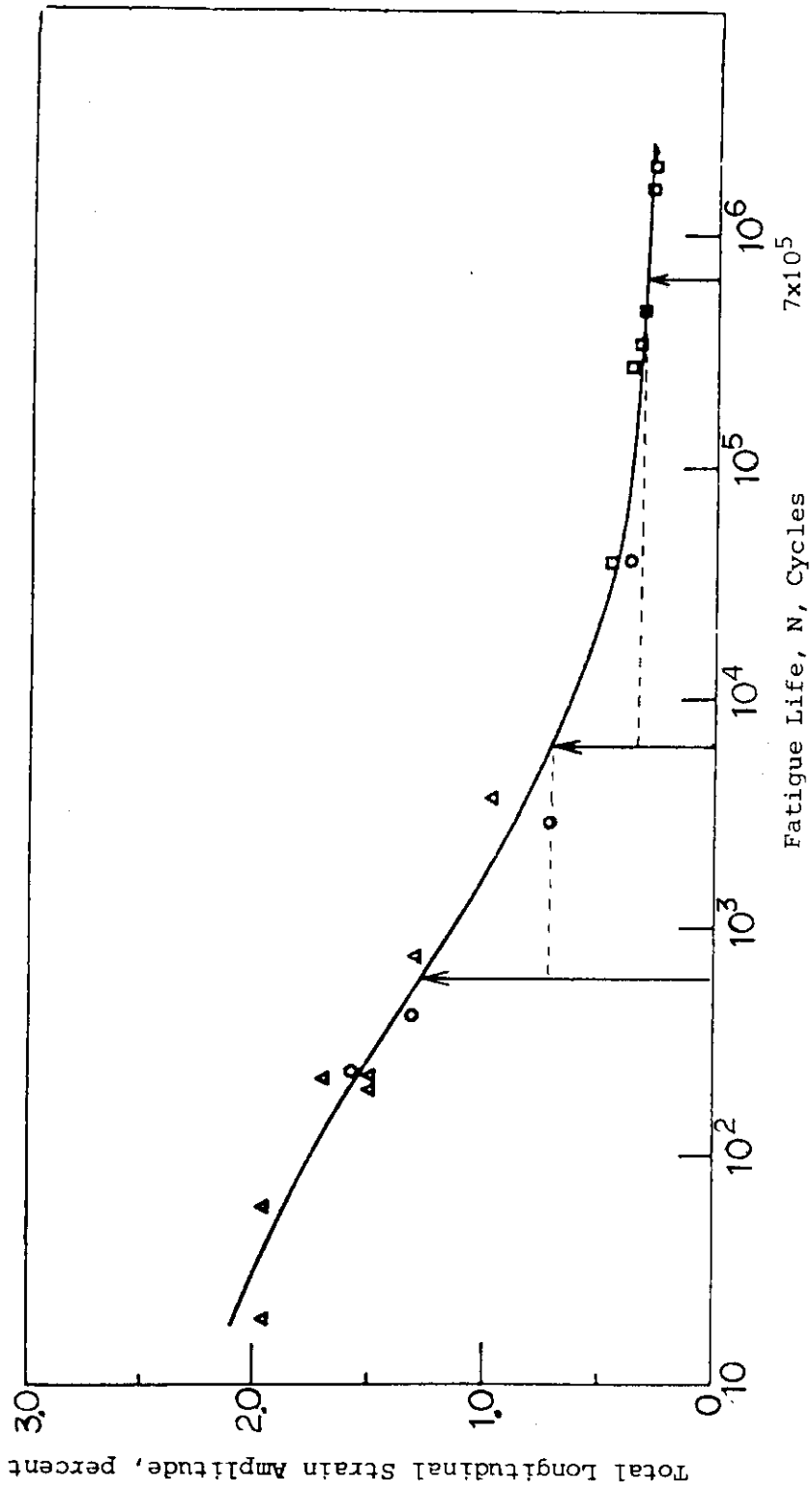

Fig. 8 Fatigue Life Curve for 304 at 4 K

9. Net Engineering Impact on the Device

Task 8 For all of the preceding suggested possible changes taken together in a consistent integrated way, evaluate the net engineering impact on the device (major radius, size of TF/PF coils, performance, cost, etc.)

Y. Sawada

T. Uchida

N. Miki

H. Iida

Task : For all of the preceding suggested possible changes taken together in a consistent integrated way, evaluate the net engineering impact on the device (major radius, size of TF/PF coils, performance, cost, etc.).

1. Introduction

Impacts of each possible change on INTOR reference design have been assessed in Task 1 to Task 7. The impacts studied here are for the case with these factors in a consistent integrated way in reactor design. Since engineering back-grounds and characteristics of impacts of these factors are fairly different from each other, the analyses are conducted taking into account these matters. The assessments conducted here are limited to the engineering features. So some comments are added for the design factors considered to need the discussions and judgements of other groups.

2. Scope of evaluation

Table 1 shows the conditions for evaluating in integnal way these design factors assessed individually in Task 1 to Task 7.

3. Evaluation

3.1 General

Table 2 shows the summary of results in Task 1 to Task 7 grouping into impacts on reactor size and performance. The factor which gives major impact on the reactor size is RF current drive and burn time length. Installation of tritium breeding blanket has the impact on the

reactor configuration and availability. Taking into account these results, the case studies are conducted for four cases shown in Table 3.

3.1 Machine size

The machine size (of INTOR) is evaluated with the parameters shown in Table 1. As the index of machine size, plasma major radius R_p, TF coil perimeter along the coil center line, the distance between TF coil outer leg and machine center R_{TF}, and the product of TF coil perimeter and coil ampere-turn, are considered.

The relationship of and TF coil perimeter is shown in Fig. 1 and that of R_p and R_{TF} depicted in Fig. 2. Both relations are shown with the parameters of TBR and burn-time. Since the short vertical build divertor is employed for all cases as shown in Table 1, vertical bore sizes of TF coils are shorter than the reference design by about 30 cm.

The followings can be said from Fig. 1.

1) INTOR reference design has approximately same R_p and TF coil perimeter as those in the case with RF current drive and ramp-up, burn-time of 2000 seconds and TBR of 0.6.
2) Under the condition of the same TBR, as the burn time is longer, TF coil perimeter becomes smaller. This is because that the plasma radius becomes smaller since R_p becomes larger with burn-time, then toroidal field on plasma axis becomes higher.
3) Comparing with the reference design the case with TBR of 0.6 and burn-time of 1000 seconds has slightly longer TF coil perimeter (2.4%) while plasma minor radius becomes smaller by 7%. The presence of T-breeding blanket has the impact on R_{TF} by 30 cm.

Figure 3 shows the relation between plasma major radius R_p and the product of TF coil perimeter and coil amper-turn which is

proportional to the TF coil volume. The latter increases almost linearly with the former. From the above-mentioned results, the adoption of RF current ramp-up has remarkable effect in extending burn time without the change of machine size, or in reducing machine size with the same burn-time. The vertical views of typical reactor concepts are illustrated in Fig. 4 to Fig. 8.

3.2 Performance

Table 2 summarizes the results of evaluation on the device performances, which are described as follow;

1) Compact divertor

The only major impact due to application of a compact divertor is a decrease in the hight of TF coils, while the decreases in TF coil overturning forces, PF coil stored energy and MG peak power are limited ones. Considerations are not required for the synergetic effects with other items.

2) Plasma current ramp-up by RF

As indicated in Table 2, plasma current ramp-up by RF enables to extend the burn-time of 200 sec for the reference design to 2000 sec, without changing the machine size. This extension of burn-time leads to easement of fatigue problems and reduction of AC losses and PF coil power supply capacities. As for the fatigue aspect, additional easement is expected with the synergetic effect with the decrease in fluence, which is discussed later.

3) RF assisted start-up

In this case, decreased OH coil voltages make the high-voltage power supply unnecessary, and, along with the reduced AC loss mentioned

above, make the superconducting PF coil design easier and more reasonable.

4) Impacts due to presence of tritium-breeding blanket

Impacts are expected to be on the machine size, and the availability because of the complexity of tritium-breeding blanket structures.

5) Fatigue

The number of fatigue cycles is largely decreased by combination of the extended burn-time (200 sec. → 1000 ~ 2000 sec.) with RF current ramp-up, reduced fluence (6.6 → 3 MW·y/m^2) and quasi-steady state operation mode, resulting in enhanced reliability of the integrity of structures. The support structures of superconducting coils can be designed more reasonably with the number of cycles decreased from 10^6 to 10^3~10^4 based on the application of quasi-steady state operation mode, of which details are described in Task 7.

i) This section describes the results of examination on thermal fatigues of the first wall and divertor plates for typical combinations of burn-time and fluence. Table 4 shows the conditions for each case. The loads to the first wall and divertor plates are of pulses even under quasi-steady state operation mode. Then the numbers of cycles for them are not decreased so much as for the coils. Yet the number of cycles is reduced to 1/20 for Case C with the longest burn-time.

ii) Tables 5 and 6 indicate the operating conditions and wall thickness requirements of the first wall, respectively. Fig. 9 and 10 show the temperature distributions and thermal stresses calculated based on the conditions. Fig. 12 illustrates the allowable first wall thickness as a function of fatigue cycles and the design points for each case. According to the figure, the designs for Case A, B,

C and D satisfy the allowable limit while the reference design exceeds it and needs some provisions such as grooving.

iii) Table 7 indicates the divertor operating conditions and Table 8 the results of life-time estimation for erosion and thermal fatigue (based on ASME evaluation). Case C with a 2000-sec burn-time results in a 5 times longer life than the reference. Fig. 15 and 16 show the analytical model and temperature and stress distributions calculated for Case C, respectively.

6) Others

In addition, the items of fluence, burn-time and tritium-breeding blanket, being associated with tests on tritium, neutronics and materials and tritium supply issues, should be evaluated systematically and totally, with reference to the discussion in Group H.

4. Conclusions and Recommendation

Among those mentioned above, the items which give largest impacts are plasma current ramp-up by RF, and presence of tritium-breeding blanket, which are described briefly as follows;

1) Plasma current ramp-up RF and RF assisted start-up

This option can yield either a longer burn-time or a more compact reactor.

(a) Longer burn-time

A burn-time of 2000 sec is possible with R_p similar to that of the reference (5.3 m), and yields the following merits;

- Sufficient experiments on plasma physics and verification of stable control of a reactor
- Reduction to ~1/10 at AC losses in superconducting magnets.

- Reliable SC magnet support structures due to low AC losses and fatigue
- Reasonable PF coil design due to low AC losses and voltages.
- Largely relaxed fatigue problems (first wall, divertor/limiter, and SC coils ← reduced numbers of cycles and quasi-steady operation mode)

(b) Compact reactor

The major radius, R_p, can be reduced by ~80 cm to ~4.5 cm, with a burn-time similar to that of the reference (~200 sec), and the conductor volume of TF coils can be decreased by approximately 30%.

Thus, plasma current drive/ramp-up by RF provide the INTOR design with large merits.

2) Presence of tritium-breeding blankets

Preliminary availability estimation of the cases with full (TBR=1.0), half (TBR=0.6) and no (TBR=0.0) tritium breeding blankets are made. When tritium breeding blanket has same reliability as the first wall, the relative difference of the availability from the reference is calculated to be ±10%. Since we have little information about tritium breeding blanket reliability, we can not rely much on these values.

3) Recommendation

Quasi-steady state operation mode based on plasma current ramp-up by RF (ECH assisted) with a burn-time of 2000 sec is recommended. This system can operate for 200 sec pulses with OH coils even when the current ramp-up by RF would not work.

Table 1 Parameters for the case study of evaluating the impacts on reactor design

NO.	Item	INTOR Reference	Scope of variation
1	Divertor	Ref. divertor	Divertor with short vertical build
2	Current drive	Inductive current drive	RF assist, RF Curr. ramp-up & Inductive Curr. Sustainment
3	Plasma position control	——	Active control coil
4	Tritium breeding blanket	T-breeding blanket in outboard and top TBR ≅ 0.6	① non T-breeding blanket TBR = 0 ② Outboard and top T-breed. blanket TBR ≅ 0.6 ③ Full T-breed. blanket TBR ≅ 1.0
5	Fluence	6.6 MW·Y/m^2	3.0 MW·Y/m^2
6	Burn time	200 sec.	200, 500, 1000, 2000 sec.

Table 2 Summary of Impacts by Design Alteration

Task No.	Items	Main Results	
		Impact on Size	Impact on Performance
1	Compact divertor	Reduction of TFC height by 30 cm	Small Reduction of TFC overturning force, PF stored energy, MG peak power
2	RF current Ramp-up (burn time 200 sec to 1000 sec)	1) Large effects on size reduction and on longer pulse operation	1) Reduction of stress cycles : 10^6 to 10^4 ~ 10^3 allowable stress intensity : multiplied by 2 ~ 4 2) AC loss of TFC : reduced to 1/10 3) Large reduction of PFC power supply 4) Reasonable structure of TFC bucking post 5) Number of thermal cycles for first wall and divertor : reduced to 1/5
3	Start-up by RF assist		1) Reduction by OH coil voltage : no use for high voltage power supply : enable reasonable installation for PFC (SC) 2) Reduction of peak power
4	Installation of plasma position control coil		1) If located inside TFC : Complicated support structure : Complicated assembling process 2) If located outside TFC : no large impact : need for passive coil with fairly large shell effect
5	No tritium breeding blanket vs. Full breeding blanket	Refernce / No / Full R_p 5.3m — 5.47 a 1.2m — 1.25 TFC bore 6.6×9.3m — 6.83×9.4	Refernce / No / Full TBR 0.6 / 0.0 / 1.0 PF energy 6.9GJ / ← / 7.81 MG peak power 1.77 / ← / 2.17
6	Impact of tritium breeding blanket installation on reactor availability		availability Reference 0.23 No blanket 0.26 Full blanket 0.21
7	Impact of reduction on TFC support : 6.6 to 3 MW·Y/m² : longer pulse 200 to 1000 sec		Reduction of number of cycles : 10^6 to 10^5 (pulse) 10^6 to 10^4 ~ 10^3 (Quasi-steady) : allowable stress intensity 1.2 (pulse) 2 ~ 4 (Quasi-steady)

Table 3 Parameters for case study

No \ case	Reference	A	B	C	D
1	reference divertor	compact divertor	compact divertor	compact divertor	compact divertor
2	Inductive Curr. ramp-up & sustain 200 sec	RF curr. ramp-up & 1000 sec Inductive Curr. sustain	← & ←	← & 2000 sec Inductive Curr. sustain	← & 200 sec Inductive Curr. sustain
3	no active control coil	active control coil	←	←	←
4	T blanket on Outboard and Top TBR ≈ 0.6	no T blanket TBR ≈ 0.0	Full T blanket TBR ≈ 1.0	no T blanket TBR ≈ 0.0	←
5	6.6 MWY/m^2	3.0 MWY/m^2	←	←	←

Table 4 Major operating parameters

		Ref.	A	B	C	D
Burn time	(S)	200	1000	1000	2000	200
Availability	(%)	50	50	50	50	50
Total fluence	($MW \cdot Y/m^2$)	6	3	3	3	3
Number of cycles	(/y)	7×10^4	1.4×10^4	1.4×10^4	7×10^3	7×10^4
	(Total)	7×10^5	7×10^4	7×10^4	3.5×10^4	3.5×10^5
Disruptions per pulse		10^{-3}	10^{-3}	10^{-3}	10^{-3}	10^{-3}

Table 5 First wall operating conditions

Total energy to first wall	37 MW
Surface heat flux	10 W/cm^2
Nuclear heating	13 W/cm^3
Coolant temperature	
Inlet/Outlet	50°C/100°C
Coolant velocity	4 m/s
Heat transfer coefficient	2.5×10^4 W/m^2 °C

Table 6 Wall thickness requirement for the first wall

	Ref. (mm)	A (mm)	B (mm)	C (mm)	D (mm)
Physical sputtering erosion[1]	3.8	1.9	1.9	1.9	1.9
Erosion during disruption[2]	9.8	1.0	1.0	0.5	4.9
Remarining wall thickness	3.0	3.0	3.0	3.0	3.0
Wall thickness required	16.6	5.9	5.9	5.4	9.8

(1) Erosion rate = 2.7×10^{-8} mm/s

(2) Assuming that the entire melt layer is lost

Table 7 Divertor operating conditions

Total power to plate		35.3 MW
Peak heat flux normal to plate[1]		2 MW/m^2
Nuclear heating	W	19 MW/m^3
	Cu	10 MW/m^3
	SS	8 MW/m^3
Coolant temperature Inlet/Outlet		50°C/80°C
Coolant velocity		7 m/s
Heat transfer coefficient		3.2×10^4 W/m^2 °C

(1) Collector plates are placed at 6° and 8° to magnetic field lines at outboard and inboard locations, respectively.

Table 8 Lifetime of divertor plate with 1 mm thick tungsten tiles

		Ref.	A	B	C	D
Life due to erosion						
Erosion by sputtering	(mm/y)	1.5	1.5	1.5	1.5	1.5
Life	(y)	0.7	0.7	0.7	0.7	0.7
Fatigue life of heat sink (Cu)						
Stress range	(MPa)	227	227	227	227	227
Life	(y)	0.14	0.7	0.7	1.4	0.14

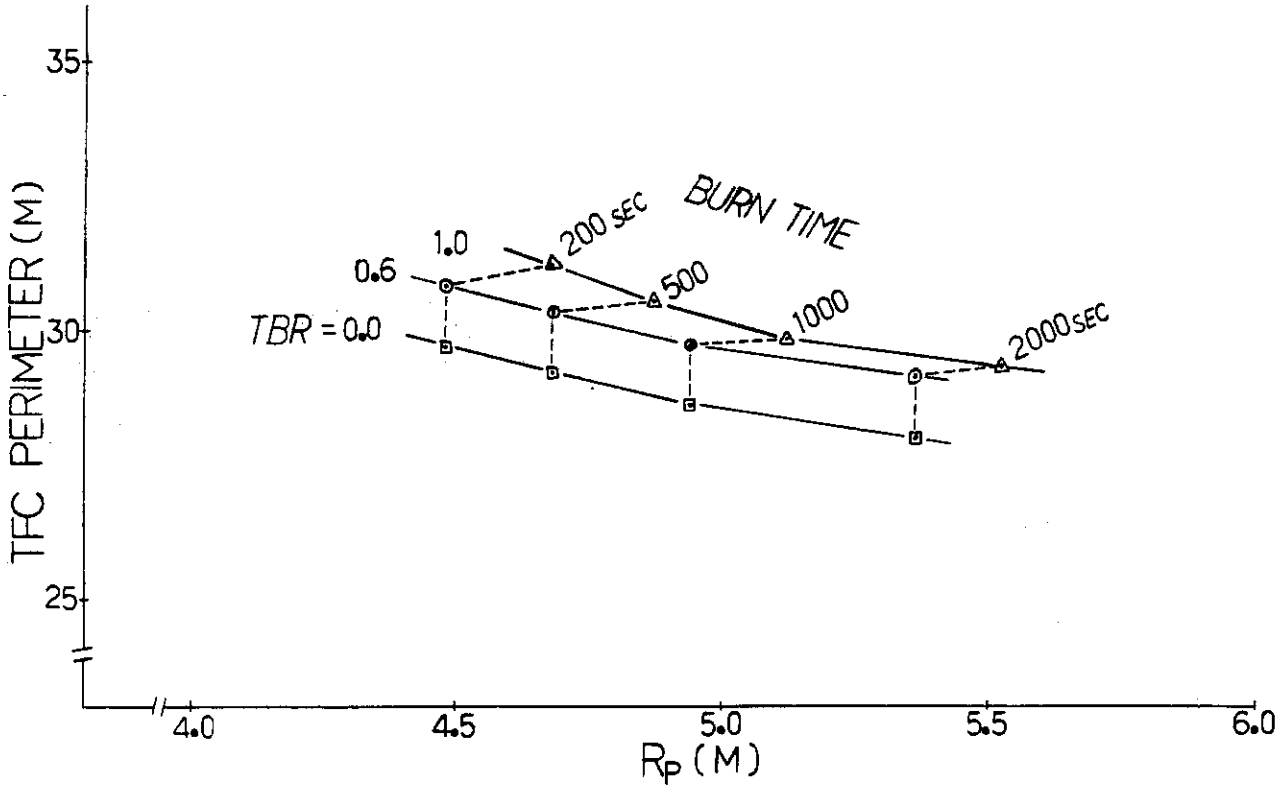

FIG. 1 MAJOR RADIUS VS. TFC PERIMETER

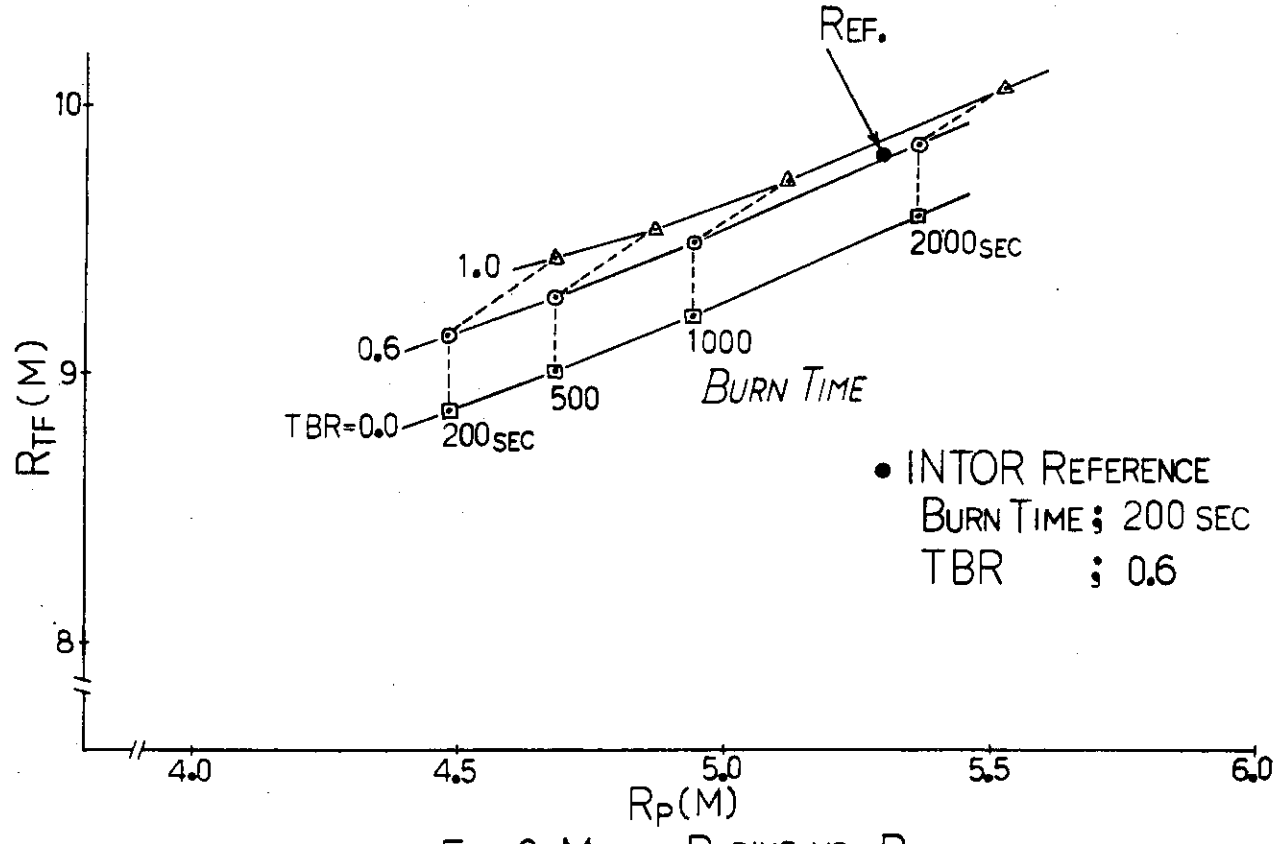

FIG. 2 MAJOR RADIUS VS. R_{TF}

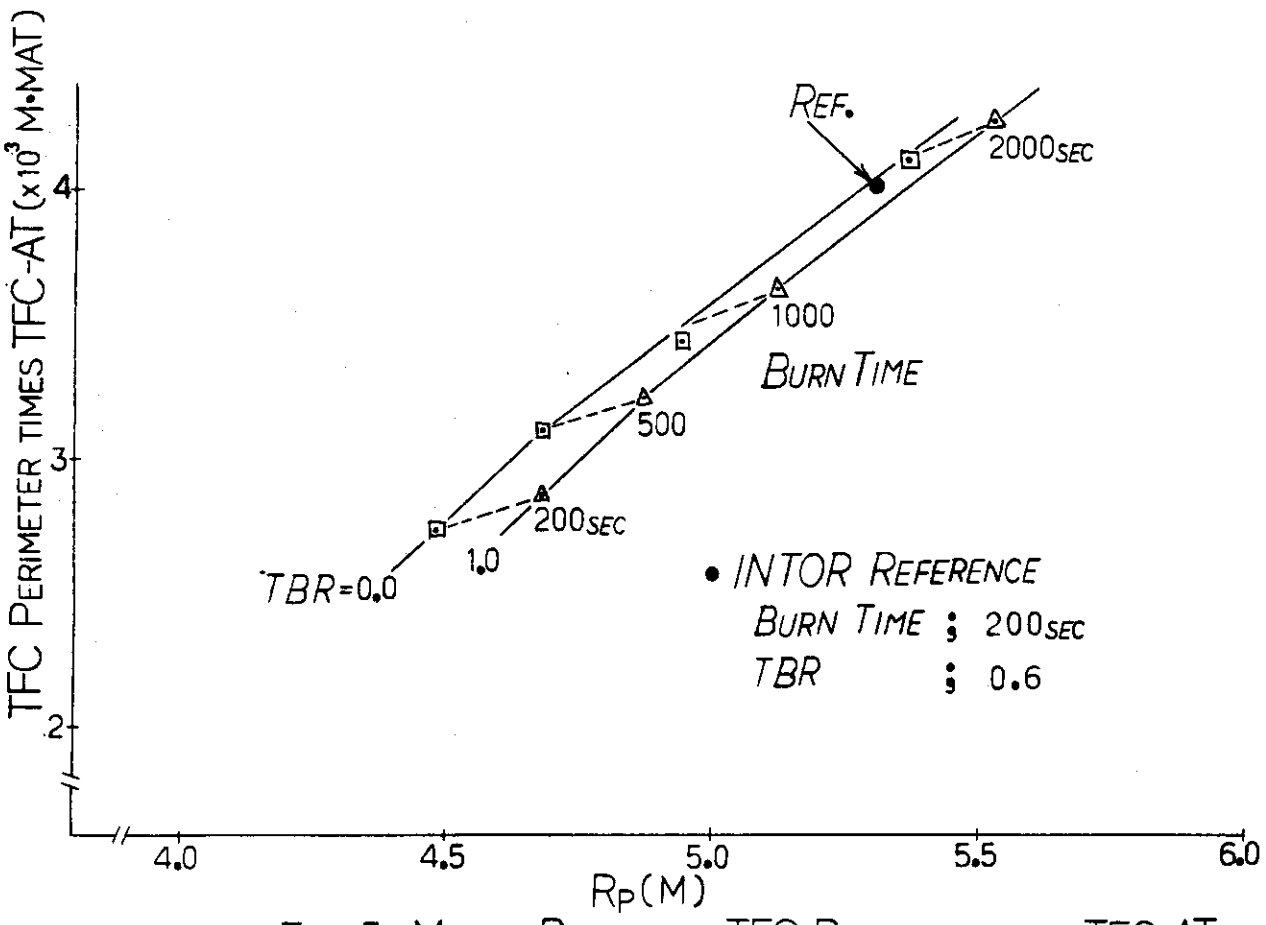

FIG. 3 MAJAR RADIUS VS. TFC PERIMETER TIMES TFC-AT

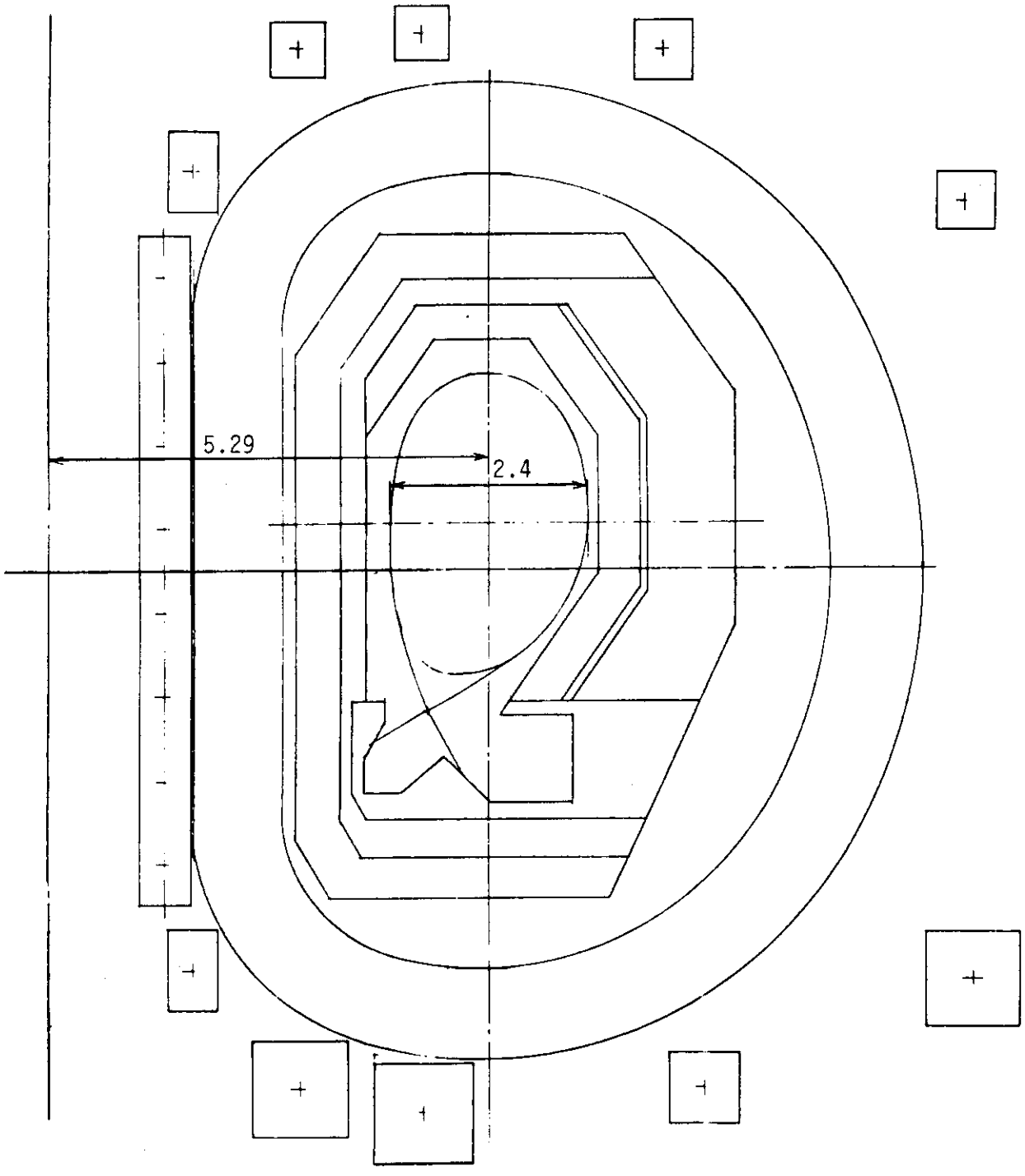

Fig.4 Case with TBR=0.6,
OH Current Ramp-up + 200 sec.OH,
Reference, TFC Bore : 6.6 x 9.6 m

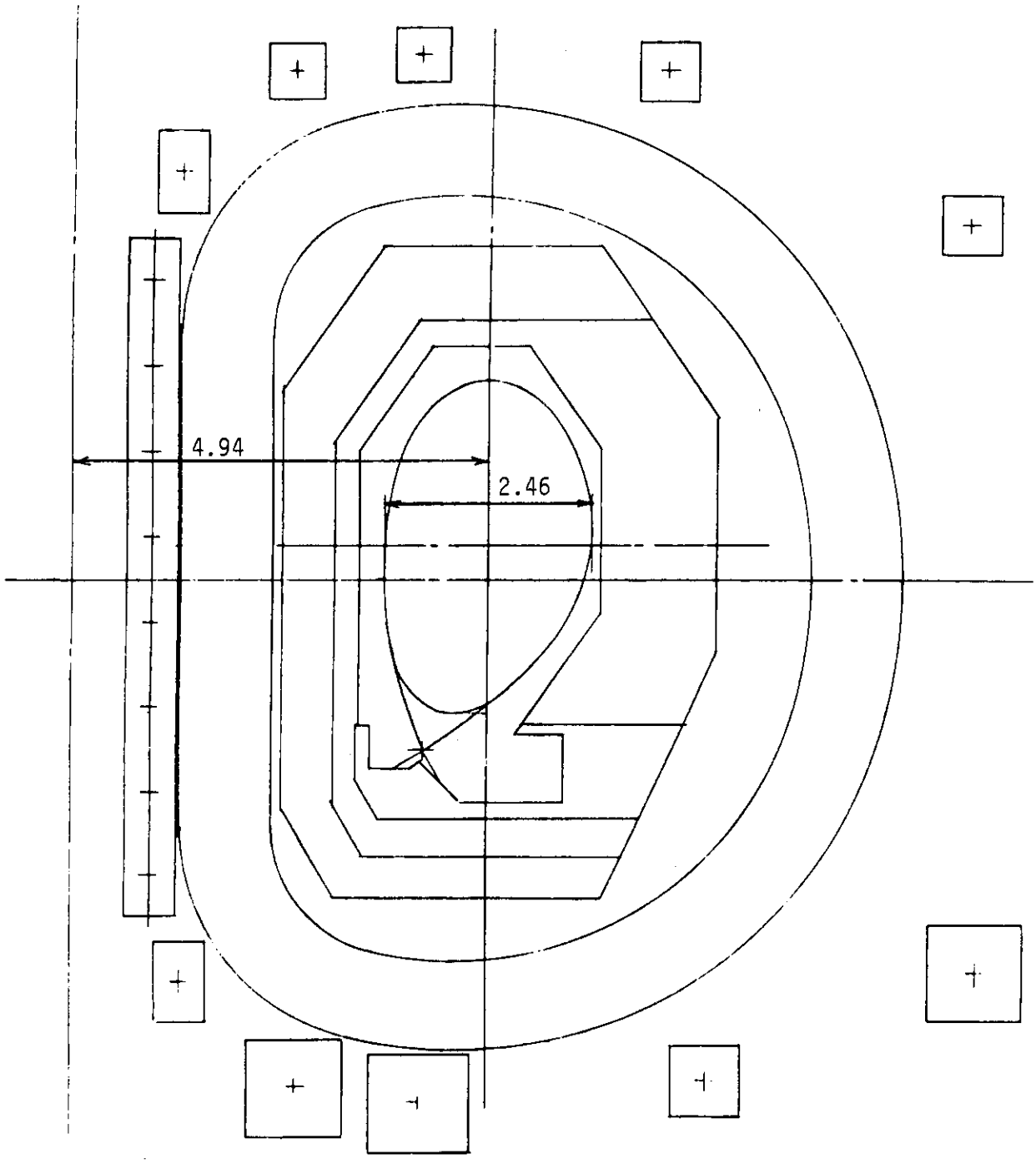

Fig.5 Case with TBR=0.0,
RF Current Ramp-up + 1000 sec.OH,
Option A, TFC Bore : 6.38 x 9.1 m

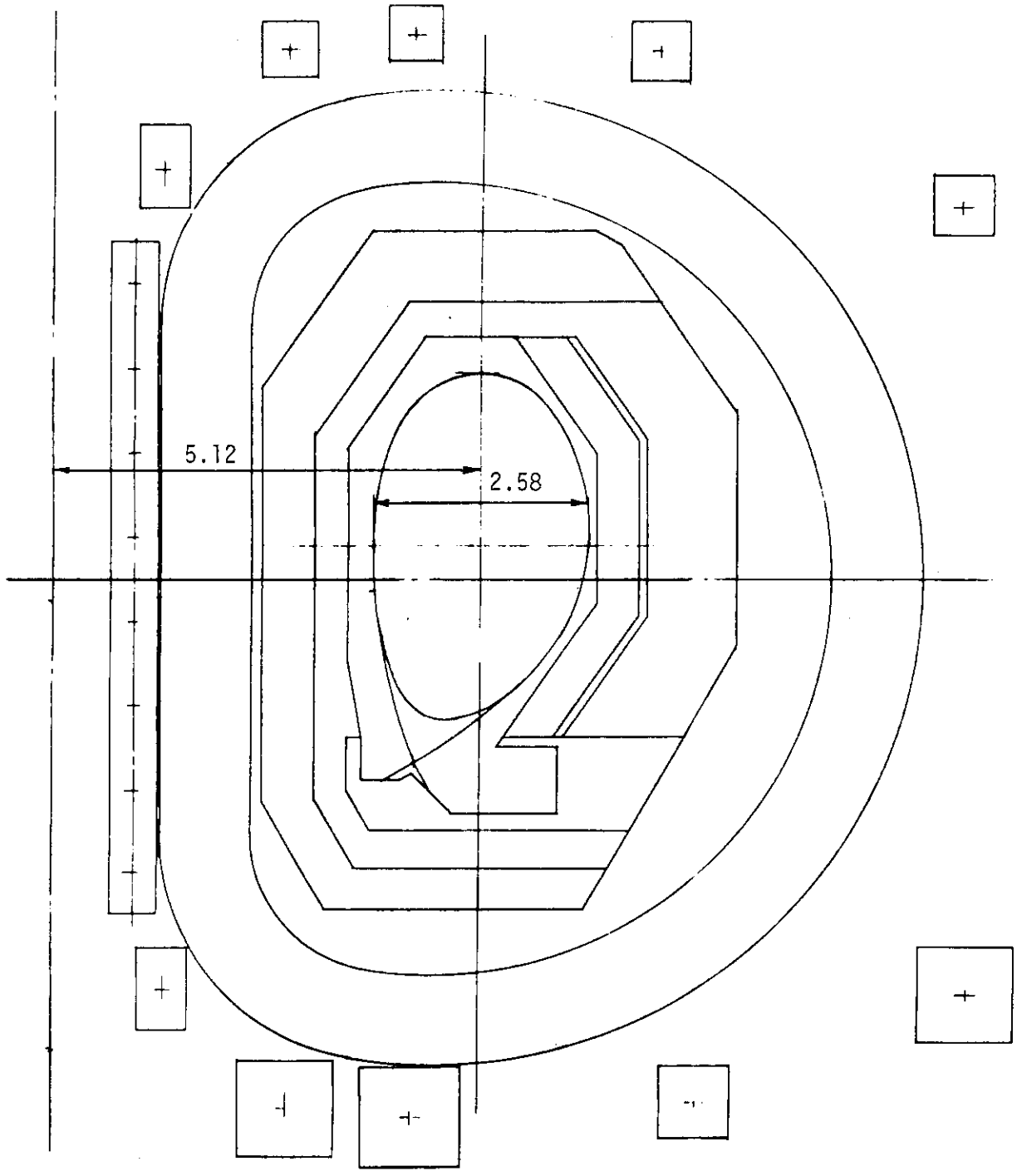

Fig.6 Case with TBR=1.0,
RF Current Ramp-up + 1000 sec.OH,
Option B, TFC Bore : 6.91 x 9.4 m

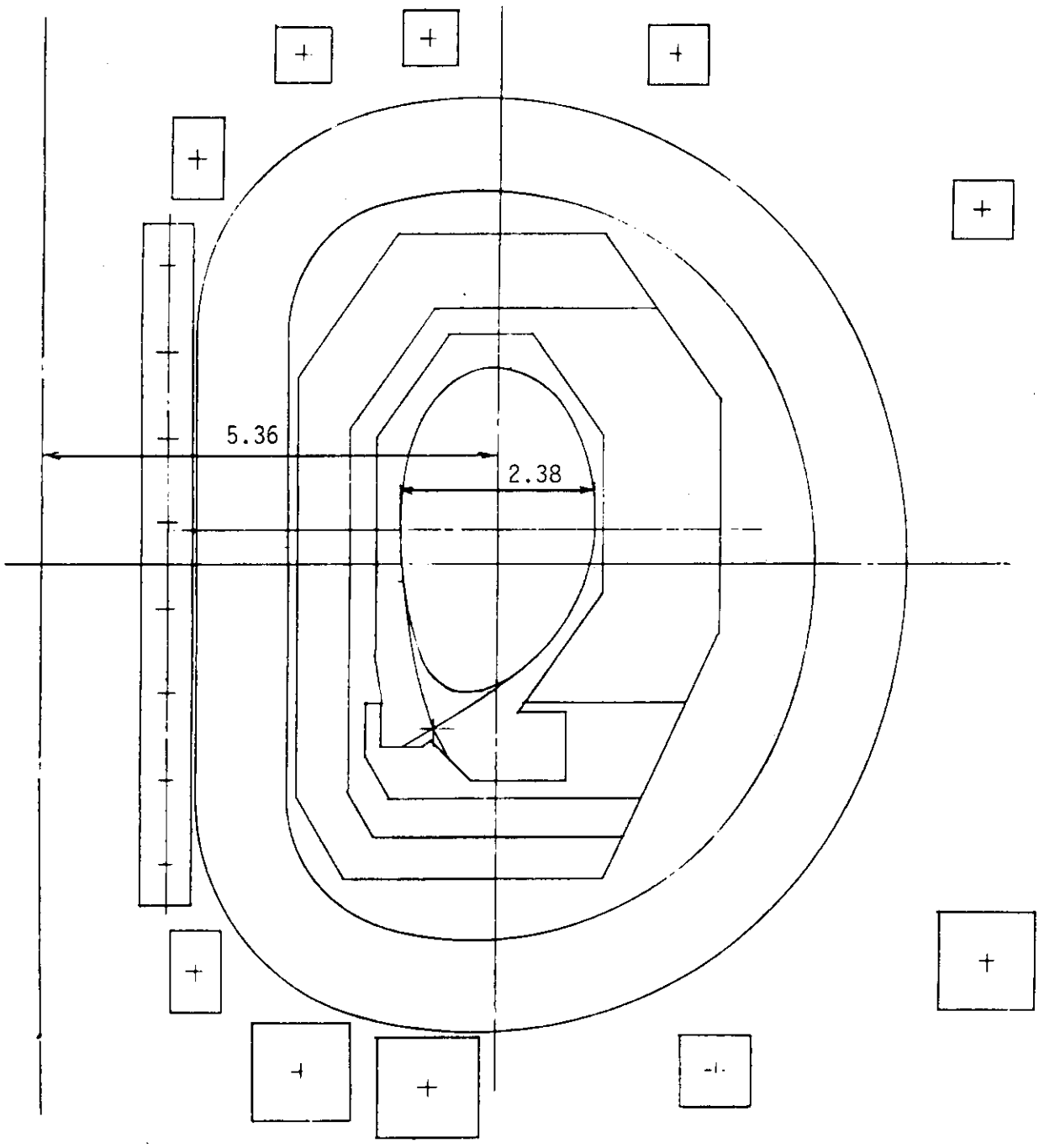

Fig.7 Case with TBR=0.0,
RF Current Ramp-up + 2000 sec.OH,
Option C, TFC Bore : 6.79 x 8.9 m

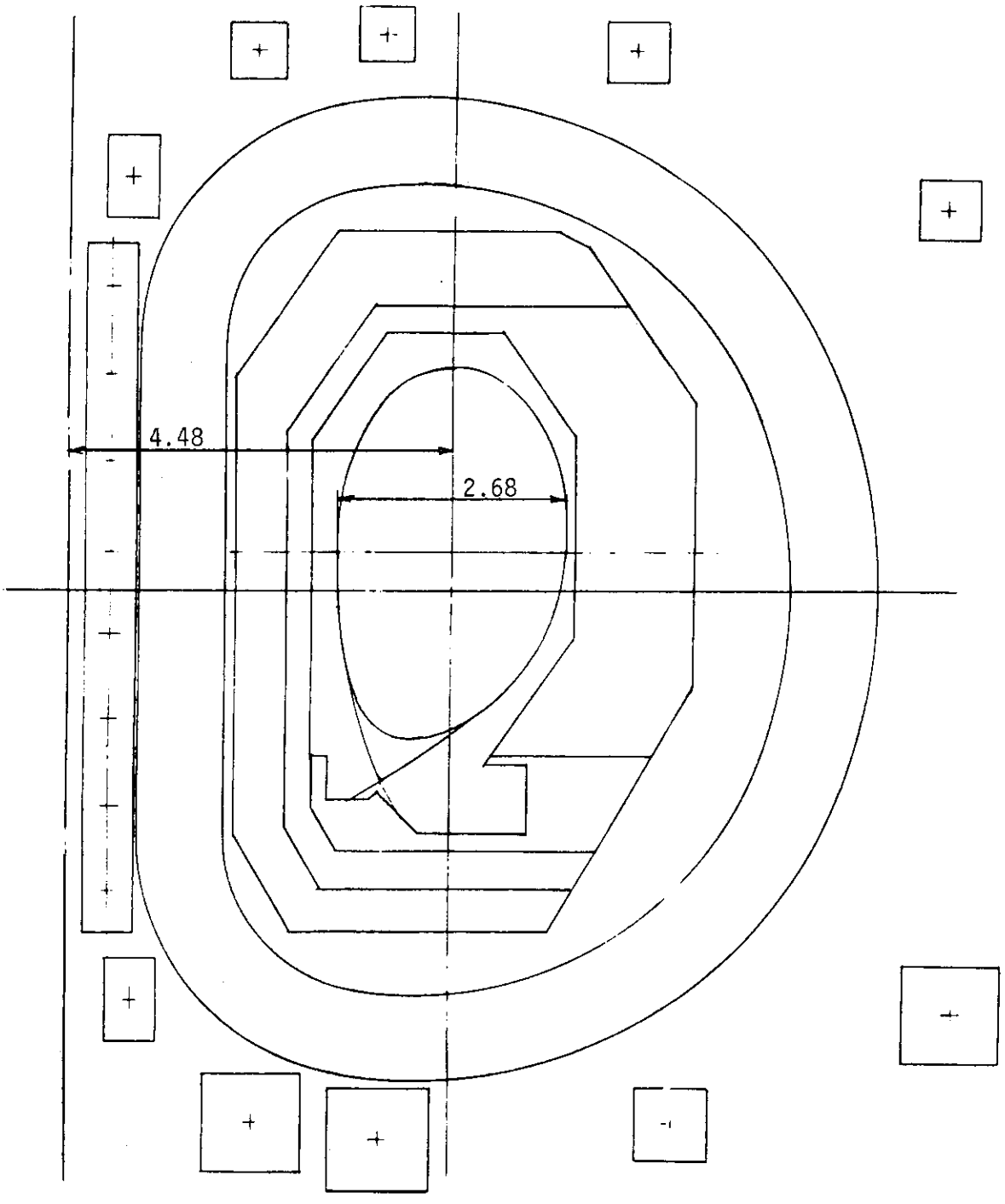

Fig.8 Case with TBR=0.0,
RF Current Ramp-up + 200 sec.OH,
Option D, TFC Bore : 6.6 x 9.5 m

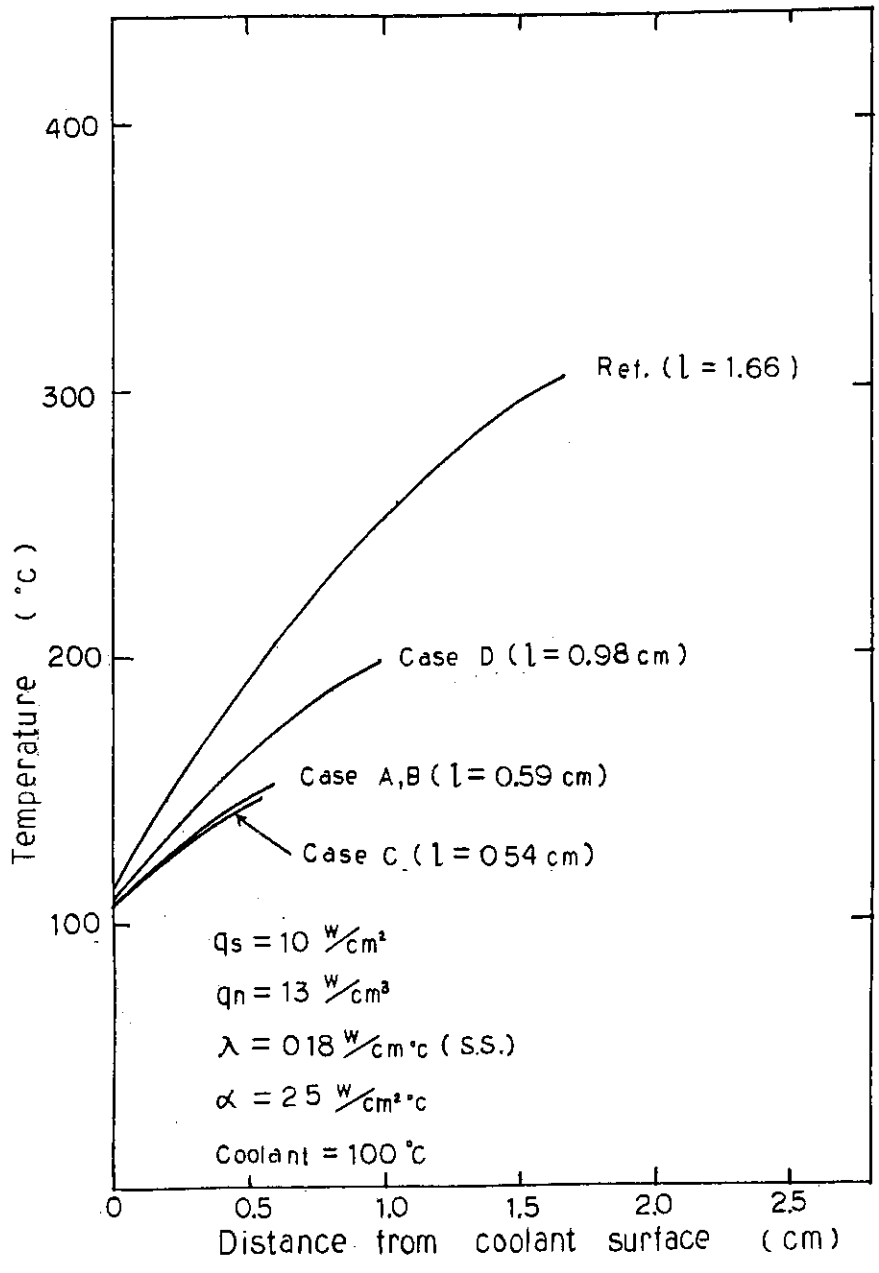

Fig. 9 Temprature distribution in first wall

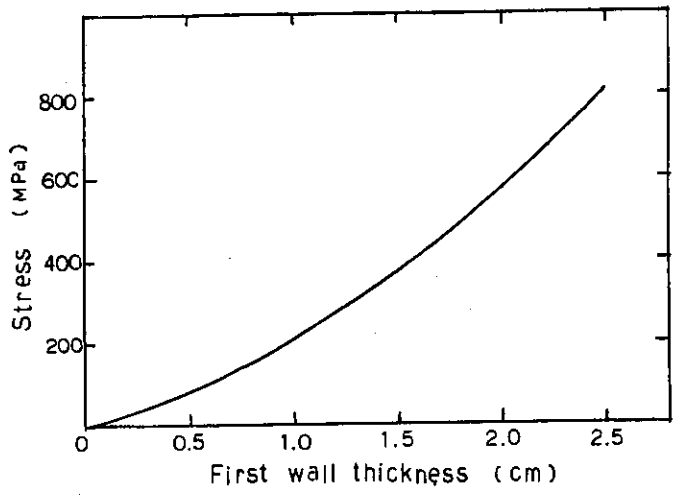

Fig. 10 Thermal stress in first wall

Cases of ASME boiler and pressure vessel code

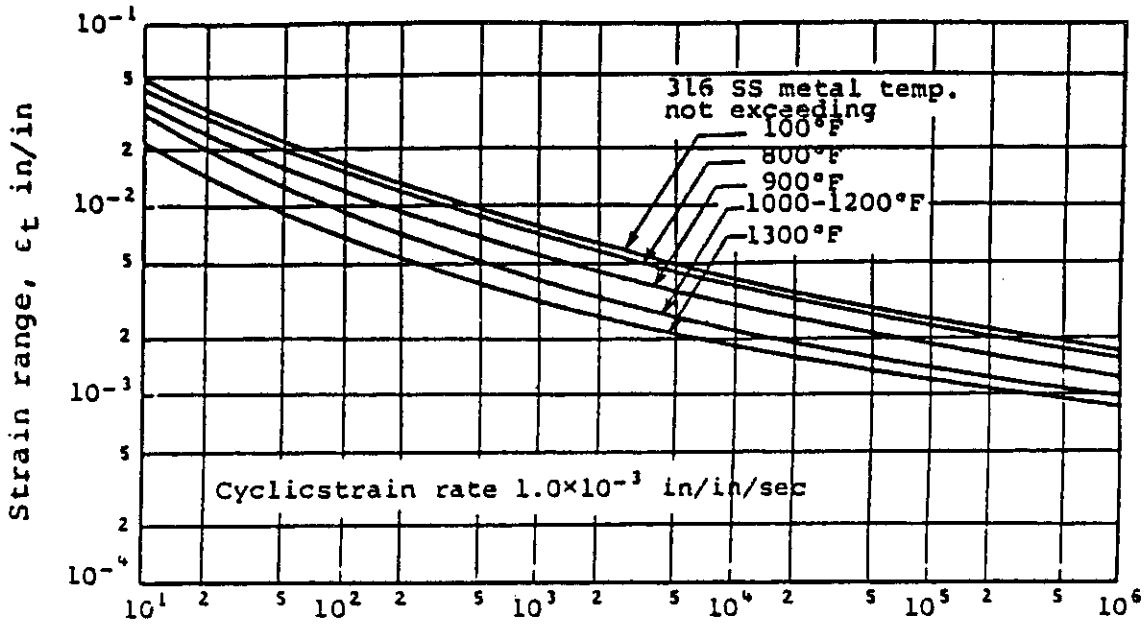

Nd Number of Cycles	εt, Strain range (in/in) at temperature				
	100F	800F	900F	1000-1200F	1300F
10^1	.0507	.0438	.0378	.0318	.0214
2×10^1	.0357	.0318	.0251	.0208	.0149
4×10^1	.026	.0233	.0181	.0148	.0105
$\times10^2$	.0177	.0159	.0123	.00974	.00711
2×10^2	.0139	.0125	.00961	.00744	.00551
4×10^2	.0110	.00956	.00761	.00574	.00431
10^3	.00818	.00716	.00571	.00424	.00328
2×10^3	.00643	.00581	.00466	.00339	.00268
4×10^3	.00518	.00476	.00381	.00279	.00226
10^4	.00403	.00376	.00301	.00221	.00186
2×10^4	.00343	.00316	.00256	.00186	.00162
4×10^4	.00293	.00273	.00221	.00161	.00144
10^5	.00245	.00226	.00182	.00136	.00121
2×10^5	.00213	.00196	.00159	.00121	.00108
4×10^5	.00188	.00173	.00139	.00109	.000954
10^6	.00163	.00151	.00118	.000963	.000834

Cyclic strain rate : 1×10^{-3}in/in/sec

Fig. 11 Design fatigue strain range, ε_t, for SS 316

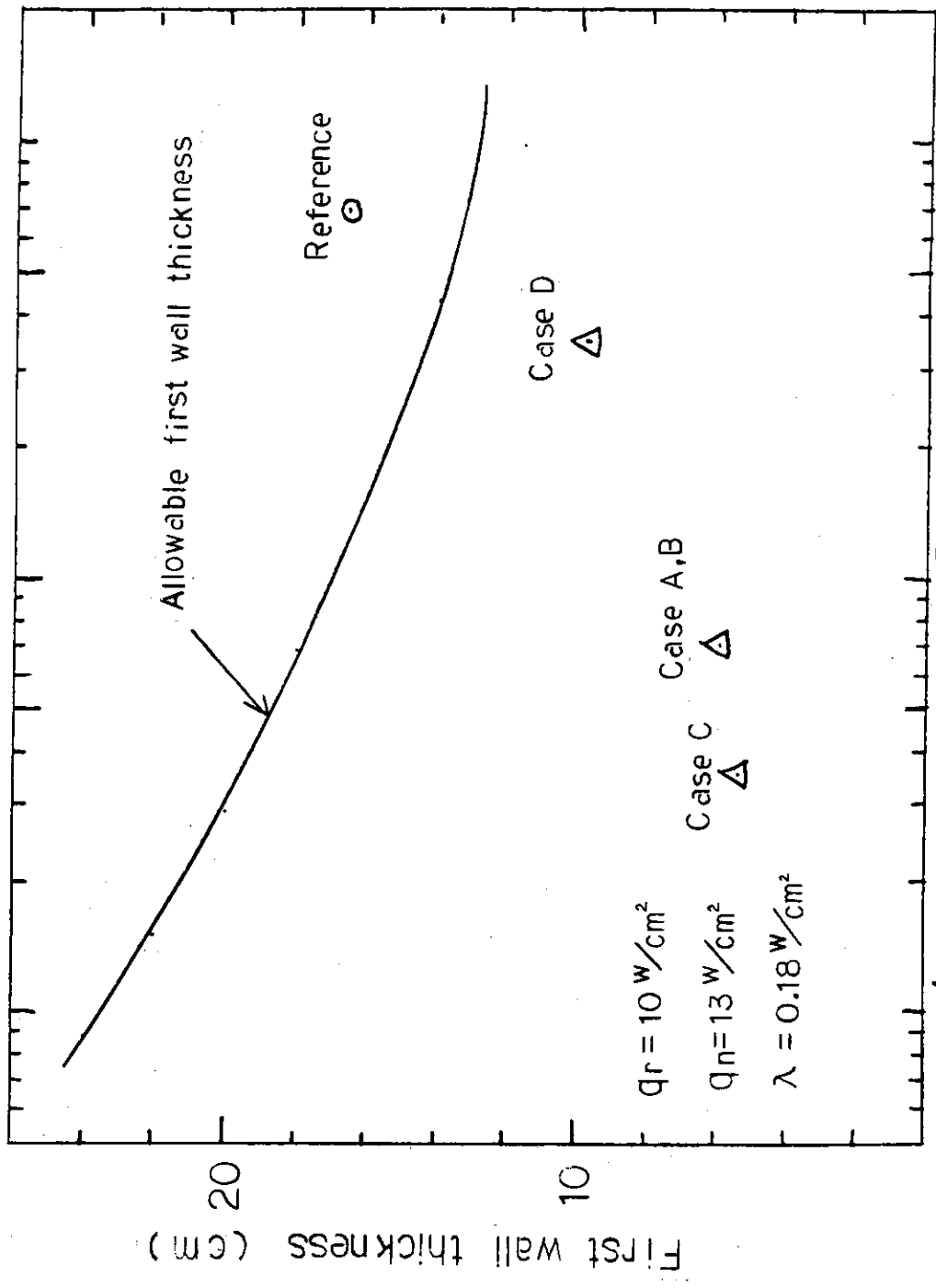

Fig.12 Allowable first wall thickness as a function of fatigue life

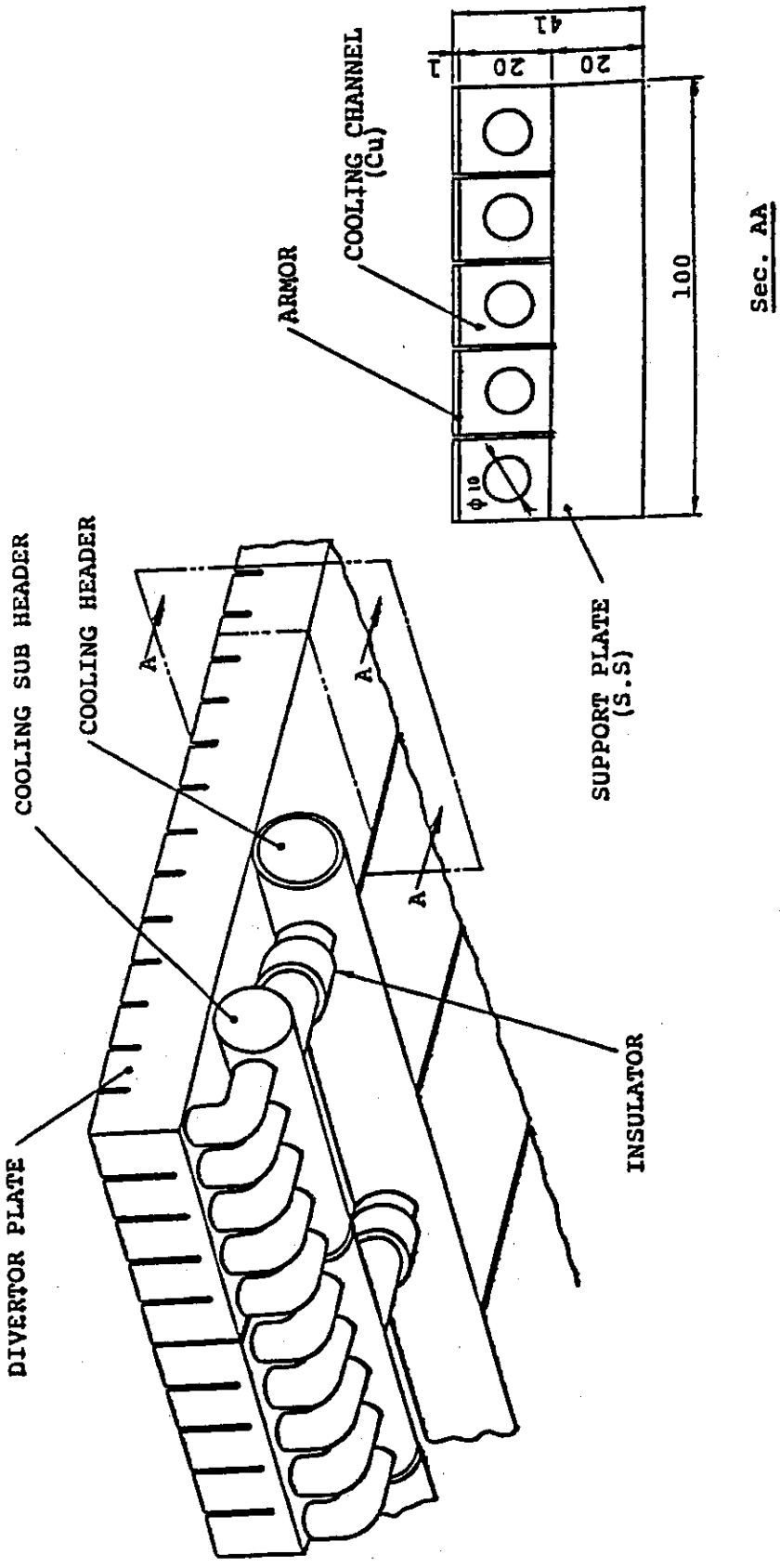

Fig. 13 Divertor plate

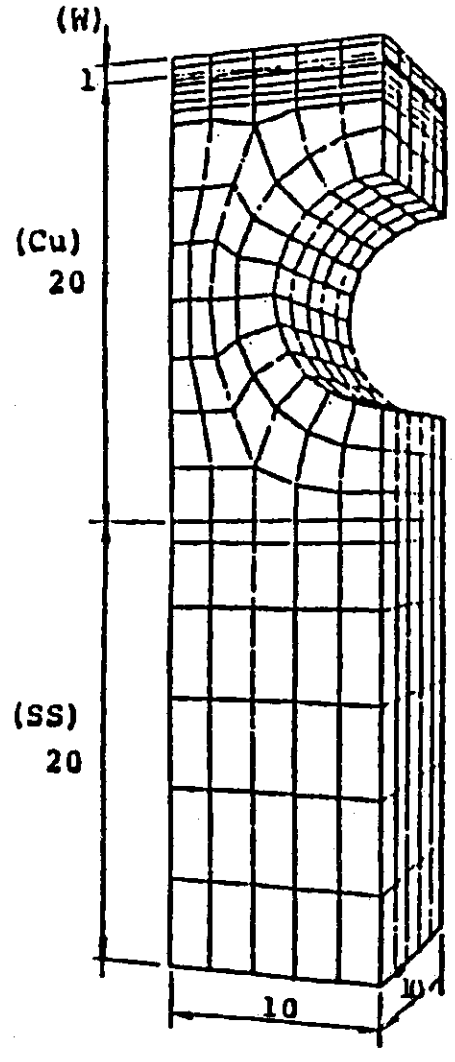

Fig.14. Geometry used for thermal hydraulics and stress analysis.

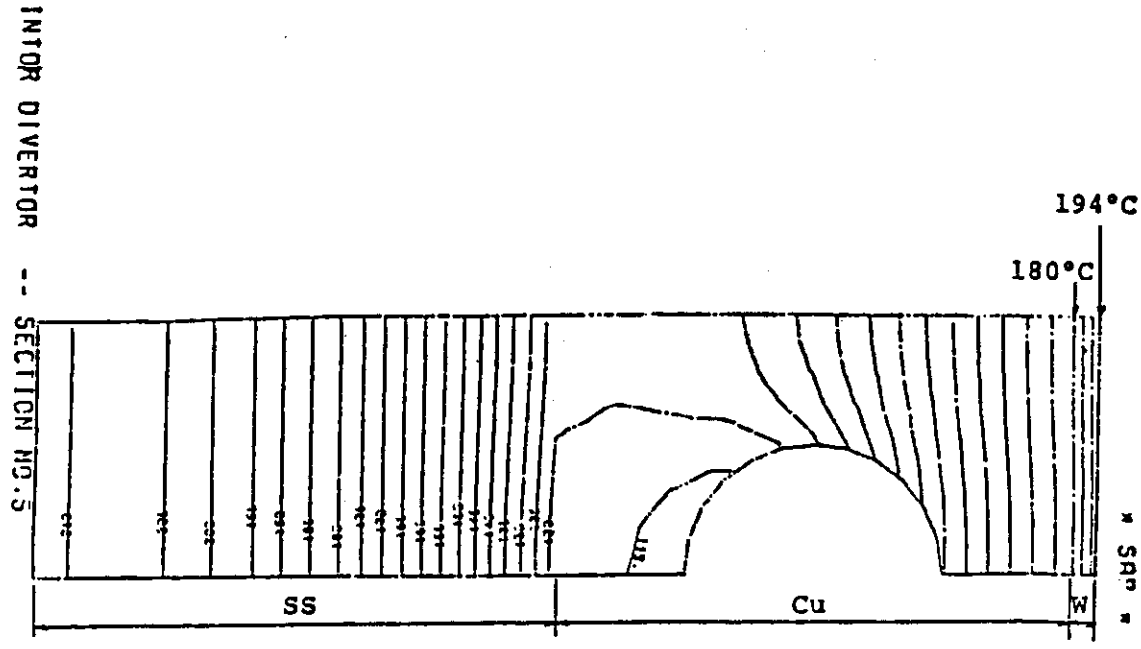

(a) Temperature distribution

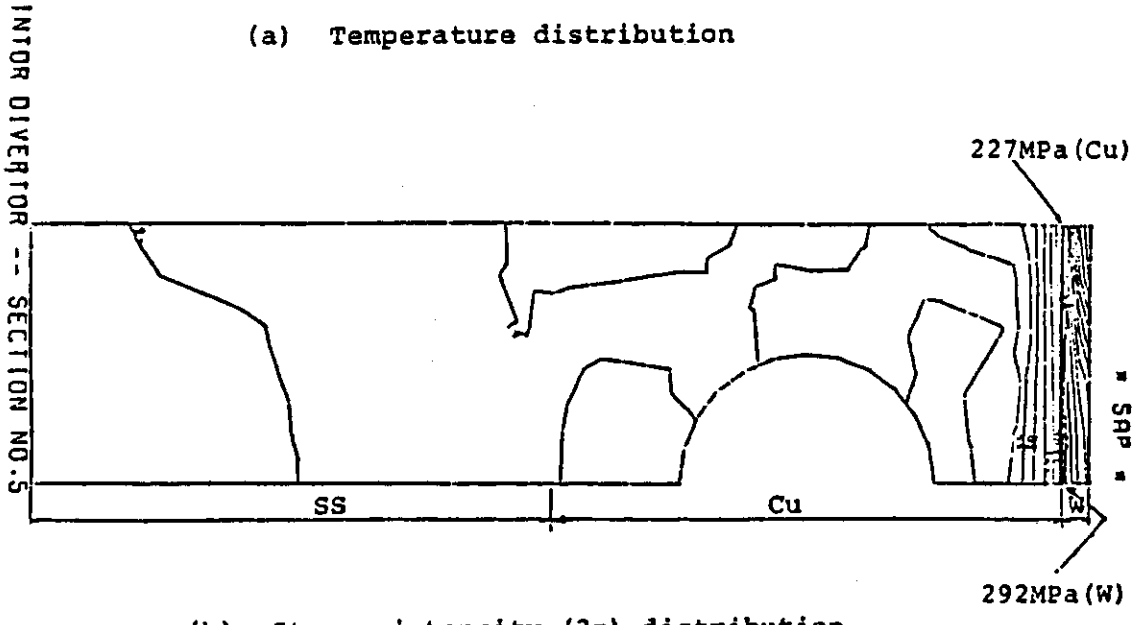

(b) Stress intensity (2τ) distribution

Fig. 15 Temperature and stress distribution of divertor plate with 1 mm thick tungsten tile on copper heat sink

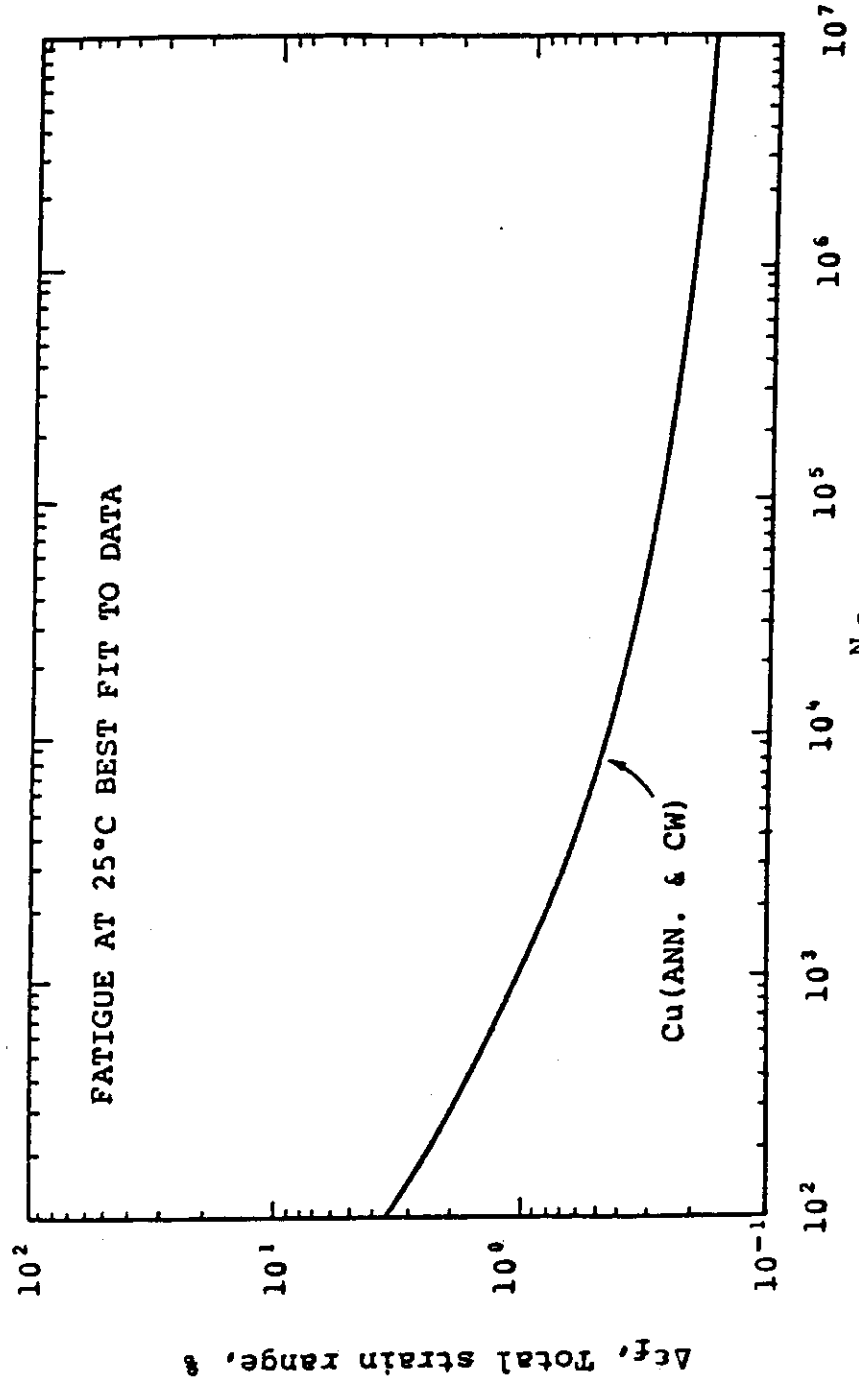

Fig. 16 Fatigue data for copper at room temperature